

*Studies of n-type doping and surface
modification of CVD diamond for use
in thermionic applications*



MUHAMMAD ZAMIR OTHMAN
UNIVERSITY OF BRISTOL
SCHOOL OF CHEMISTRY
BRISTOL

MARCH 2014

A dissertation submitted to the University of Bristol in accordance with the requirements of the degree of Doctor of Philosophy in the Faculty of Science, School of Chemistry

Word Count : 52, 223

Abstract

This thesis presents the investigation of potential shallow n-type donors that are candidates to be used as thermionic emitters for converting solar energy to electrical energy. Due to the various problems associated with current n-type dopants in diamond, the work has examined the use of Li-N codoping as a possible alternative doping strategy in chemical vapour deposition (CVD) of polycrystalline diamond films.

Lithium nitride (Li_3N) suspension in 1% w/v polyoxy in chloroform and N_2 or NH_3 gas were used as Li and N precursors, respectively, in preparing Li-N co-doped diamond films using a hot-filament CVD system. Using this system, high dopant concentrations of Li ($\sim 5 \times 10^{19} \text{ cm}^{-3}$) and N ($\sim 3 \times 10^{20} \text{ cm}^{-3}$) atoms were successfully incorporated into the diamond films. The addition of Li atoms into N-doped diamond films improved the resistance of the diamond film from $>200 \text{ M}\Omega$ to $<50 \text{ M}\Omega$. A resistance as low as $85 \text{ k}\Omega$ was recorded for Li-N co-doped diamond grown on a SCD type Ib substrate, however, these values and the overall electrical characteristics of the films were not sufficient for electronic devices.

Ab initio calculations predicted that a LiN cluster with a Li:N ratio of 1:4 should produce shallow donor characteristics with an energy level $\sim 0.1 \text{ eV}$ below the diamond conduction band minimum. The model only favours the formation of Li in substitutional sites rather than in interstitial sites due to its lower formation energy (4.88 eV and $>10 \text{ eV}$, respectively). This model also suggests that N atoms might act as traps to pin down Li atoms and reduced their mobility in diamond lattice.

The thermionic emission characteristics of Li-N co-doped diamond films were tested in Arizona State University, Arizona, USA. The films exhibited $121 \mu\text{A cm}^{-2}$ current density at 900 K with a threshold temperature at 800 K . The effective work function of the emitters varied from 2.87 eV to 3.62 eV . The presence of a negative electron affinity (NEA) surface is found to be crucial for increasing the electron emission from diamond.

H terminated diamond exhibits NEA and is usually prepared by exposing the diamond films in hydrogen plasma. However, desorption of H atoms between $925\text{--}1050\text{K}$ limits the application for these films for thermionic-based solar panels at higher temperature. Thus, various metal-oxygen-terminated diamond surfaces were examined to determine their thermionic electron yield and stability at high temperatures. Cr-O, Al-O and Ti-O terminated diamond surfaces exhibit NEA characteristics and were thermally stable at 650°C . However, only Cr-O terminated diamond showed true NEA characteristics while Al-O and Ti-O terminated diamond showed effective NEA.

Acknowledgments



In the name of The Almighty, the Most Gracious, the Most Merciful. First of all, I praise Allah for making this journey possible.

I would like to extend my gratitude to my supervisor, Professor Paul May for giving me this valuable opportunity to carry out my research work in his inspiring and interdisciplinary research group, Bristol University Diamond Group (BUDGies). His constant guidance, help, advices and supports throughout the course of my doctoral research are priceless and have broaden up my perspective in both scientific and education worlds.

I would also like to thank my co-supervisor, Dr. Neil Fox for the opportunity to work with School of Physics and the Interface Analysis Centre (IAC) and for guidance in the physics and electronics of the thermionic device.

In particular, I thank Professor Neil Allan, Dr. Kane O'Donnell and Dr. Judy Hart for their invaluable teaching, advice and helpful discussions of the diamond modelling and electronic structure analysis. Without them it will be impossible for the theoretical studies to be done within my degree time-frame. I also thank Dr. Peter Heard from the IAC, University of Bristol, for SIMS depth-profile analysis to determine the concentration of dopants in diamond. Thank you to my collaborators in Arizona State University (ASU), Arizona USA, Professor Robert Nemanich, Dr. Tianyin Sun and Mr. Franz Köeck for the fruitful discussion and experiences on XPS, UPS and thermionic emission studies during my visit in 2013.

I would also like to mention the expert help from Dr. James Smith and Mr. Keith Rosser for always being there when the instruments started to fail or when I failed to understand the instruments. Thanks to all the past and present members of the BUDGies: Raquel, James Richley, Tomas, Mark,

Ben, Gareth, Monika, Josh, Jeff, Hugo, Sarah, Cathy, Dan, Rabi, Yousheng and everyone else for their help, advice, and entertainment over the years.

I want to express my deepest gratitude to my parents, Othman Sadon and Zahrah Rameli, for their endless love and priceless advices, for always being there for me and trusting their son in achieving his dreams. Special thanks to my lovely siblings, Along, Ayi and Siti for the moral supports and unconditional loves while we are separated thousands miles away. Thanks also to my best friends, Amrulqays Maarof and Khalif Samsudin for the encouraging words of wisdom and for keep debating on my ideas throughout this journey.

Thanks also to my Malaysian friends in Bristol, Kak Hyda, Kak Anis, Kak Enny, Kak Kin, Kak Wan, Kak Farah, Kak Nora, Kak Fizah, Musbahiyah, Farihin, Azri, and Amirul for being by my side all these years, through thick and thin. Truly great friends are hard to find, difficult to leave, and impossible to forget.

Last but not least, I greatly appreciate and thank the Public Service Department (JPA), Malaysia for awarding me the King's scholarship to pursue my doctoral study at the University of Bristol.

*For my respectful supervisors, my beloved mother and father,
my siblings and my best friends.*

Declaration

I declare that the work in this dissertation was carried out in accordance with the requirements of the University's Regulations and Code of Practice for Research Degree Programmes and that it has not been submitted for any other academic award. Except where indicated by specific reference in the text, the work is the candidate's own work. Work done in collaboration with, or with the assistance of others, is indicated as such. Any views expressed in the dissertation are those of the author and in no way reflect those of the University of Bristol.

SIGNED:

DATE:.....

CHAPTER 1: INTRODUCTION.....	1
1.1 DIAMOND.....	1
1.2 TYPES OF DIAMOND	4
1.2.1 <i>Single-crystal diamond</i>	4
1.2.2 <i>Detonation nanodiamond</i>	4
1.2.3 <i>Chemical Vapour Deposition (CVD) diamond</i>	5
1.3 SYNTHETIC DIAMOND.....	8
1.3.1 <i>Details of Chemical Vapour Deposition</i>	8
1.3.1.1 Microwave Plasma CVD (MWCVD) system.....	9
1.3.1.2 Hot-Filament CVD (HFCVD) system	10
1.3.2 <i>Diamond Growth Mechanism</i>	11
1.3.2.1 Surface Mechanism of Diamond Growth	12
1.4 SUBSTRATE PRE-TREATMENT	15
1.4.1 <i>Manual Abrasion</i>	15
1.4.2 <i>Electrospray</i>	16
1.4.3 <i>Sonication in Diamond Suspension</i>	17
1.4.4 <i>Bias-Enhanced Nucleation (BEN)</i>	18
1.4.5 <i>Self-assembly of Diamond Particles</i>	18
1.5 IMPURITIES, DEFECTS AND DOPING	19
1.5.1 <i>P-type doping</i>	21
1.5.2 <i>N-type doping</i>	23
1.5.2.1 Nitrogen	23
1.5.2.2 Sulfur	24
1.5.2.3 Phosphorus.....	24
1.5.2.4 Sodium.....	26
1.5.2.5 Lithium	26
1.5.2.6 Lithium-Nitrogen Co-doping	28
1.6 THEORETICAL STUDIES OF LI-N DOPANTS IN BULK DIAMOND	29
1.6.1 <i>Density Functional Theory (DFT)</i>	29
1.7 APPLICATIONS.....	31
1.7.1.1 Thermionic Emission	32
1.8 DIAMOND SURFACE TERMINATION	35
1.8.1 <i>Negative Electron Affinity (NEA)</i>	37
1.9 THESIS OUTLINE & OBJECTIVES	38
1.10 REFERENCES	40
CHAPTER 2: INSTRUMENTATION AND TECHNIQUES	50
2.1 INTRODUCTION.....	50
2.2 HOT FILAMENT CHEMICAL VAPOUR DEPOSITION (HFCVD) SYSTEM.....	50
2.2.1 <i>Standard Diamond Growth Condition</i>	55

2.3	LASER RAMAN SPECTROSCOPY.....	56
2.4	SCANNING ELECTRON MICROSCOPY (SEM)	58
2.5	ENERGY-DISPERSIVE X-RAY SPECTROSCOPY (EDX)	59
2.6	SECONDARY ION MASS SPECTROSCOPY (SIMS)	61
2.7	ELECTRON EMISSION ANALYSIS	64
2.7.1	<i>X-Ray Photoelectron Spectroscopy (XPS)</i>	65
2.7.2	<i>Ultraviolet Photoelectron Spectroscopy (UPS)</i>	66
2.7.3	<i>Thermionic Emission Apparatus</i>	69
2.8	BELL JAR EVAPORATOR	71
2.9	SOFTWARE	72
2.9.1	<i>Limitations</i>	73
2.10	REFERENCES	73
CHAPTER 3: LITHIUM: A CHALLENGING PRECURSOR FOR DIAMOND DOPING		75
3.1	INTRODUCTION.....	75
3.2	EXPERIMENTAL	77
3.2.1	<i>Organic liquid selection</i>	77
3.2.2	<i>Polymer stabilisation</i>	80
3.2.3	<i>Melting Process under Growth Conditions</i>	82
3.2.4	<i>Preparation of lithium-doped diamond films</i>	83
3.2.5	<i>Determination of lithium content using SIMS</i>	84
3.3	RESULTS AND DISCUSSION	85
3.3.1	<i>Effect of liquids on suspension stability</i>	85
3.3.2	<i>Effect of Polymer addition</i>	87
3.3.3	<i>Li₃N melting process under Growth Conditions</i>	88
3.3.4	<i>Contamination and Limitations</i>	91
3.4	CONCLUSIONS	93
3.5	REFERENCES	94
CHAPTER 4: INCORPORATION OF LI & N IN CVD DIAMOND FILMS		98
4.1	INTRODUCTION.....	98
4.2	EXPERIMENTAL	99
4.2.1	<i>N-doped CVD Diamond Deposition with Different Nitrogen Precursors</i>	100
4.2.1.1	Nitrogen Gas.....	100
4.2.1.2	Hexamethylenetetramine (HMT).....	100
4.2.1.3	Ammonia Gas	102
4.2.2	<i>Addition of Li₃N into Diamond Films</i>	102
4.2.3	<i>Determination of Nitrogen and Lithium Content in Diamond Films</i>	103
4.2.4	<i>Two-Point Probe Measurement</i>	103
4.3	RESULTS AND DISCUSSION	104
4.3.1	<i>N-doped Diamond</i>	104

4.3.1.1	Nitrogen gas	104
4.3.1.2	HMT	107
4.3.1.3	Ammonia gas	108
4.3.1.4	Determination of N Atoms in N-doped Diamond Films	112
4.3.1.5	Conclusion	114
4.3.2	<i>Li-N Co-Doped Diamond Films</i>	115
4.3.2.1	Multiple layers	119
4.3.2.2	Effect of grain boundaries on dopants	121
4.3.2.3	Lithium Saturation Point	122
4.3.3	<i>Electrical Resistance</i>	125
4.4	CONCLUSIONS	126
4.5	REFERENCES	127
CHAPTER 5: THEORETICAL STUDY OF LI & N CLUSTERS IN DIAMOND		130
5.1	INTRODUCTION	130
5.2	DETAILS OF CALCULATIONS	133
5.2.1	<i>Geometry Optimisation</i>	133
5.2.2	<i>Formation Energy</i>	134
5.2.3	<i>K-point Optimisation</i>	135
5.2.4	<i>Band Structure Calculation</i>	136
5.2.5	<i>Density of State (DOS) Calculation</i>	136
5.2.6	<i>Dopants in Diamond</i>	137
5.3	RESULTS AND DISCUSSION	139
5.3.1	<i>Pure Diamond</i>	139
5.3.2	<i>Nitrogen in Diamond</i>	140
5.3.3	<i>Lithium in Diamond</i>	142
5.3.3.1	Interstitial Site	143
5.3.3.2	Substitutional Site	144
5.3.4	<i>Li-N Co-Doped Diamond</i>	147
5.3.4.1	1:1 Ratio of Li-to-N Atoms in Li-N Co-doped Diamond	147
5.3.4.1.1	Interstitial Lithium	147
5.3.4.1.2	Substitutional Lithium	150
5.3.4.2	1:2 Ratio of Li:N atoms in Li-N Co-doped Diamond	152
5.3.4.3	1:3 Ratio of Li:N Atoms in Li-N Co-doped Diamond	155
5.3.4.4	1:4 Ratio of Li:N Atoms in Li-N Co-doped Diamond	157
5.4	CONCLUSIONS	159
5.5	REFERENCES	160
CHAPTER 6: ELECTRON EMISSION STUDY OF LI-N CO-DOPED DIAMOND FILMS		163
6.1	INTRODUCTION	163
6.2	EXPERIMENTAL	165

6.2.1	<i>Preparation of Li-N Co-Doped Diamond</i>	165
6.2.2	<i>Thermionic Emission Measurements of Li-N Co-doped Diamond Films</i>	166
6.2.3	<i>UPS and XPS Analysis of Li-N Co-doped Diamond Films</i>	167
6.3	RESULTS AND DISCUSSION	168
6.3.1	<i>Thermionic Emission</i>	168
6.3.1.1	Effect of a Hydrogen Terminated Diamond Surface	168
6.3.1.2	Effect of Different Nitrogen Content in Li-N Co-doped Diamond Films	171
6.3.1.3	Effect of Different Substrates Used for Growing Li-N Co-doped Diamond Films	173
6.3.2	<i>Ultraviolet Photoemission of Li-N Co-doped Diamond Film</i>	177
6.3.3	<i>X-Ray Photoemission of Li-N Co-doped Diamond Film</i>	179
6.4	CONCLUSIONS	182
6.5	REFERENCES	183
CHAPTER 7: METAL-OXYGEN TERMINATION ON BORON-DOPED DIAMOND FILMS		186
7.1	INTRODUCTION	186
7.2	EXPERIMENTAL	189
7.2.1	<i>Thermal Deposition of Metal on Oxygen-Terminated BDD Films</i>	190
7.2.2	<i>Removing Excess Metal</i>	191
7.2.3	<i>Elemental Analysis using XPS</i>	193
7.2.4	<i>NEA Stability Determination using UPS</i>	194
7.3	RESULTS AND DISCUSSION	195
7.3.1	<i>Aluminium-Oxygen Termination</i>	199
7.3.2	<i>Chromium-Oxygen Termination</i>	203
7.3.3	<i>Titanium-Oxygen Termination</i>	207
7.3.4	<i>Zinc-Oxygen & Magnesium-Oxygen Termination</i>	212
7.4	CONCLUSIONS	213
7.5	REFERENCES	214
CHAPTER 8: THESIS SUMMARY		217
8.1	SUMMARY	217
8.2	FUTURE WORK	219
APPENDIX A.....		221
APPENDIX B.....		226
APPENDIX C.....		230
APPENDIX D.....		231
APPENDIX E.....		232
APPENDIX F.....		239

Chapter 1: Introduction

1.1 Diamond

Diamond has been renowned as one of the most remarkable materials of the past few decades, with applications ranging from sparkling gemstones to high-end mechanical and electrical devices [1-5]. It is the hardest known material, has the highest thermal conductivity at room temperature and it is inert to most chemical reagents [1,6]. With these properties, diamonds are employed for cutting, drilling, milling, grinding and polishing materials in mechanical applications [4,5]. After the development of diamond thin films, the applications were extended to electronic devices such as biosensors, surface acoustic wave filters (SAW), micro-electro-mechanical systems (MEMS), light emitting diodes (LEDs) and detectors [7-13]. The recent discovery of the bio-compatibility of diamond also enabled diamond to enter the biomedicine and biochemistry fields, to be used as a bio-tracker, a drug delivery agent, and as a substrate for cell growth [14-18]. Table 1.1 summarises some of the properties of diamond.

Table 1.1: Properties of diamond

Diamond Properties	
Hardness	90 GPa
Thermal conductivity	$2 \times 10^3 \text{ W m}^{-1} \text{ K}^{-1}$
Thermal expansion coefficient (25 °C)	$1.1 \times 10^{-6} \text{ K}^{-1}$
Band gap	5.45 eV
Carrier mobility (Electron & Hole)	$3800 \text{ cm}^2 \text{ V}^{-1} \text{ s}^{-1}$
Density	3.515 g cm^{-3}
Refractive index	2.42
Breakdown voltage	$100 \times 10^5 \text{ V cm}^{-1}$

Diamond is believed to have been discovered around 6,000 years ago in India [19]. Despite its apparent stability towards mechanical and chemical abrasion, diamond is actually a meta-stable form of carbon and less thermodynamically stable compared to graphite. Figure 1.1 shows three common allotropes of carbon: diamond, graphite and carbon nanotubes (CNTs), although various others exist, including graphene, fullerenes, carbon onions, and a multitude of different types of amorphous carbon (which can also be known as diamond-like carbon (DLC) depending on its structure).

Diamond has entirely sp^3 hybridised carbon bonded together in a tetrahedral structure and forming a three-dimensional crystal lattice. In contrast, graphite and CNTs have sp^2 hybridised carbon which are linked together into a hexagonal structure that forms sheets or layers. A single isolated layer is called graphene, and this material has received a lot of interest recently due to its remarkable electronic properties [20-22]. In graphite, weak van der Waals interactions bond many graphene sheets together, but these can slide easily over each other making graphite soft and useful as a lubricant. CNTs are composed of a graphene sheet that is rolled up to form a tube structure. Rolling up one graphene sheet produces single-walled carbon nanotubes (SWCNTs), whilst rolling up several sheets makes multi-walled carbon nanotubes (MWCNTs) [23,24]. The CNTs can have metallic or semiconducting properties depending upon the orientation in which graphene sheets are rolled up.

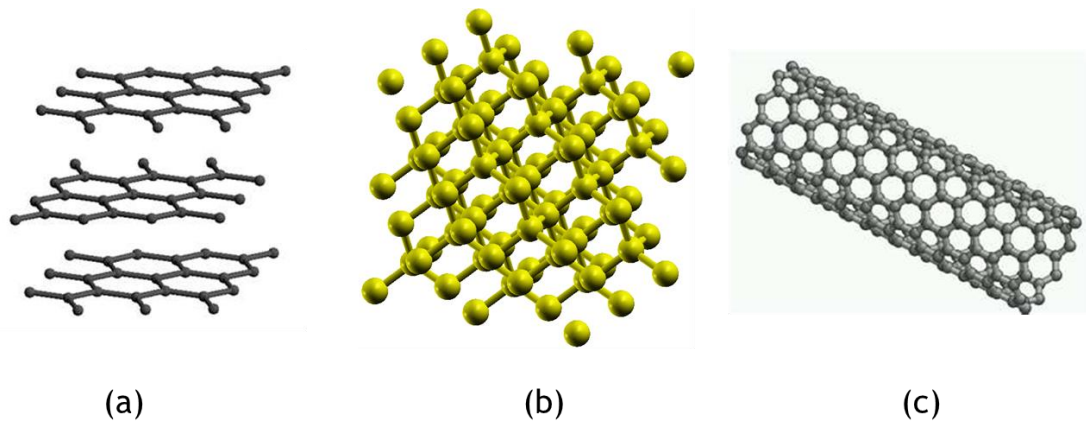


Figure 1.1: Common carbon allotropes; (a) graphite, (b) diamond and (c) carbon nanotubes

In order to produce diamond rather than graphite, more thermodynamically favourable conditions are required. Because these two materials are separated by a large activation energy barrier ($\sim 700 \text{ kJ mol}^{-1}$), the spontaneous interconversion of diamond and graphite at room temperature (25°C) and pressure (760 torr) is impossible. The first method reported to produce synthetic diamonds was using high temperature and high pressure (HPHT) technique [4,5], which mimics the way natural diamond is created in Earth's crust. In HPHT, carbon in the form of graphite powder is placed into a large hydraulic press along with a small amount of a metal catalyst, and then subjected to high pressure ($\sim 5 \text{ GPa}$) and temperatures about $1300\text{-}3000^\circ\text{C}$ [5]. After a few hours or days, single-crystal diamonds of size $\sim 1 \text{ mm}$ crystallise out. However, their purity and colour are not good enough for use as gemstones, so these 'industrial diamonds' are used in cutting and drilling applications - an industry which today is worth many millions of dollars.

In the late 1950's a breakthrough was made in synthesising diamond using a chemical vapour deposition (CVD) technique. With the advancement of diamond growth using CVD technique, researchers all over the world now had access to diamond in the form of thin films or coatings, and this allowed many of the unique properties of diamond to be utilised for the first time in novel scientific and engineering applications.

1.2 Types of diamond

1.2.1 Single-crystal diamond

Both natural diamonds and those produced by the HPHT process contain non-carbon impurities that have been trapped in the crystal during growth. Natural diamond often contain metals or minerals, along with elements such as hydrogen, nitrogen or boron which can create colour centres, turning the diamond from colourless into so-called ‘fancy’ diamonds, which appear yellow, red or blue. For example, the famous ‘Hope diamond’ in the Smithsonian museum in Washington DC is deep blue due to its high boron content.

The main impurity in HPHT diamond is nitrogen, which causes the crystals to appear yellow or brown. Both natural and HPHT diamond are classified depending upon the amount of N and B they contain [25]. Type I diamond contains N atoms, but this is then further divided into type Ia and type Ib. Type Ia diamond contains impurities of N atoms in aggregates while type Ib diamond consists of only single substitutional N atoms. Type II diamond contains less than 1 ppm of N atoms. This class is then divided further into two types: type IIa and type IIb. Type IIa diamonds do not contain any B atoms impurities while type IIb does contain B atoms, although the level of B is low and rarely exceeds 1 ppm.

1.2.2 Detonation nanodiamond

Detonation nanodiamond (DND) is the name given to diamond particles prepared from a detonation process in which a high explosive, such as TNT, is detonated inside an evacuated steel tank [26]. The shockwave produced travels through the carbon-rich explosive with such velocity and pressure that the carbon is converted to diamond particles sizes between 5 to 20 nm. However, the diamond cores are always covered with layers of graphitic material. These will aggregate to form larger

carbon clusters with size up to micrometer. Various methods have been suggested to remove the graphitic outer layers and disaggregate the clusters in order to prepare monodispersed diamond nanoparticles, including partial oxidation in air or hydrogen, filtration, ultracentrifugation and ultrasonic dispersion [27-29]. DND is often used as seeding material prior to diamond growth in a CVD system.

1.2.3 Chemical Vapour Deposition (CVD) diamond

Most diamond grown for electronic applications, coating materials and jewellery are nowadays prepared using a CVD technique. The versatility of this process enables the researchers to control the properties of the diamond produced. Nowadays, CVD diamond can be categorized into four different types, depending on the grain size of the diamond: single crystal diamond (SCD), microcrystalline diamond (MCD), nanocrystalline diamond (NCD) and ultra-nanocrystalline diamond (UNCD) [30-33]. SCD is typically grown from a single seed crystal, and is focused more on the jewellery industry due to its higher production cost [34,35]. Most seeds are carefully selected (100) orientation HPHT or natural diamonds. Homoepitaxial growth using this type of seed leads to less surface defects, so long as the growth parameter are very carefully controlled over the growth period, which may be several days or even weeks. [30]. Gemstones several mm in size have been prepared by this method, and these are now becoming commercially available via companies such as SCIO diamond and Gemesis [36,37]. For scientific applications, it is currently possible to buy flat, polished SCD substrates of size $\sim 8 \text{ mm} \times 8 \text{ mm} \times 0.5 \text{ mm}$ from Element Six [38] and in the next few years these dimensions are expected to increase. However, we are still several years away from the wafer-scale SCD substrates required for diamond to compete with Si or SiC.

Other types of diamond (MCD, NCD and UNCD) are grown heteroepitaxially using a non-diamond substrate that must be seeded or mechanically abraded to encourage initial diamond growth. The substrate

must be capable of surviving the harsh CVD conditions (temperatures of ~800 °C and a H₂ atmosphere), and form a thin carbide. If the substrate does not form a carbide (e.g. Ge, Cu) the diamond film does not adhere and simply delaminates upon cooling. Conversely, if the substrate material has too great an affinity for carbon (Ni, Fe, Co), the growing diamond film simply dissolves into the substrate forming a thick carbide. Thermal expansion mismatch between the substrate and diamond is also a problem, and often leads to compressive stresses, cracking or even delamination of the diamond film upon cooling after deposition. Materials which meet all these criteria include Si, Mo, W, and their carbides, and to some extent Ti [39-42].

Because of the random nature of the nucleation produced by manually abrasion and/or seeding, heteroepitaxial films are nearly always polycrystalline in nature. Even films grow on a diamond substrate and which start out epitaxial and single crystal, can often become polycrystalline due to renucleation processes during growth. The exact mechanism for renucleation is still a matter of debate, but it is thought that non-uniformities during growth cause defects in the growing diamond layer, which then lead to twins, dislocations, and ultimately a second crystallite growing misaligned to the first. The grain size thus depends upon the initial seeding density as well as the growth conditions. MCD films have crystals >0.5 μm, and are usually deposited using 1% CH₄ gas in H₂ atmosphere.

NCD films started to be popular in the early 21st century due to their small surface roughness compared to MCD films. The small surface roughness is due to the small crystallite size, between 10-500 nm. This small surface roughness made the production of transparent free standing polycrystalline diamond films possible following a series of polishing techniques [27,43,44]. NCD films can be made in two different ways, and the two types of NCD film have different properties. In the first type, a very high nucleation density is achieved by seeding with a densely packed monolayer of DND. Growth of diamond using 1% CH₄ in H₂ then occurs, producing a thin continuous NCD film. If growth were to continue for many

hours, this film would eventually become thicker and turn into an MCD film. However, stopping the growth while the film is $<1 \mu\text{m}$ thick produces an NCD film with faceted nano-crystallites. The second type of NCD film is deposited by simply increasing the methane content from 1% - 5% in the normal CVD gas mixture. The more methane is present in the mixture, the higher the rate of renucleation. NCD films produced this way often rounded grains of size 100 nm which have aggregated into ball-like (ballas) or cauliflower structures.

NCD films contain higher sp^2 carbon content compared to sp^3 carbon due to the increased number of grain boundaries present in the films [45,46], especially in cauliflower NCD where the grain boundaries can also be thicker. In certain electronic applications such as thermionic energy converters, the existence of grain boundaries is thought to improve the emission current produced [47-49]. However, usually the higher number of grain boundaries in the film detrimentally affects other diamond properties, such as the mechanical strength, thermal conductivity and optical transparency [30].

UNCD films are classified as diamond film with grain size less than 10 nm. They were originally developed at Argonne National Labs in the USA, and UNCD is actually their trade name - although it has now become the generic name for films of this type. Most UNCD films are grown in microwave CVD (MWCVD) systems in a hydrogen-poor atmosphere. The typical gas mixture used is 99%Ar with 1%CH₄, although sometimes (1%-3%) H₂ gas is added as well [30,32,50,51]. The deposition conditions allow renucleation to occur very frequently, and produce diamond films with very small grain size. Along with the increasing number of grains and grain boundaries comes a deterioration in properties, and UNCD possesses only a fraction of the values for many electronic and mechanical properties as SCD. Nevertheless, because the surface of UNCD films is smooth on a nm scale, this makes them useful for many electronic applications such as MEMS devices, biosensors and nanolithography. Due to their very small grain size, it has proved difficult to dope UNCD. N-type doping has been reported, but not in the conventional sense. In these films, doping using N

atoms during CVD will not substitute any C atoms inside the diamond lattice, but instead causes N to aggregate in the grain boundaries [30]. This leads to higher electrical conductivity of the UNCD films [52].

1.3 Synthetic Diamond

1.3.1 Details of Chemical Vapour Deposition

In a diamond CVD process, atomic hydrogen is known as the key factor which drives all the chemistry [53]. A hot filament or microwave plasma produces sufficient heat to dissociate the hydrogen molecules into H atoms, which then react with the other hydrocarbon components of the gas mixture to form a complicated chemical soup of atoms, radicals, ions and clusters positioned immediately above the growing diamond surface. In an atomic-H-rich environment, the etch rate of sp^2 carbon is between 10 to 100 times faster than that of sp^3 carbon [54]. Thus, any graphitic carbons are etched back into the gas phase, while the diamondlike sp^3 carbons remain attached to the substrate. In this situation it is kinetically stable to preferentially form the diamond structure.

A typical CVD system operates at a low pressure (10-200 torr), and a high substrate temperature (800-1000°C) with higher temperature of the activation region (2000-2500°C). The environment consists of an activated gas-phase mixture of hydrocarbons, H₂ and/or N₂. Plasma or thermal energy is commonly used as the hot activation region to dissociate the hydrocarbon (usually methane) into its radicals, and H₂ gas into atomic H. In modern diamond CVD, the two most commonly used systems are hot-filament CVD (HFCVD) and microwave-activated CVD (MWCVD). Both techniques are discussed in detail in the following section.

There are other CVD techniques used to prepare diamond films, such as DC-arc jet reactors and combustion flame CVD, but these are not

discussed here but have been mentioned in various papers in the past [55,56].

1.3.1.1 Microwave Plasma CVD (MWCVD) system

The first diamond films grown by MWCVD were reported in 1983 at NIRIM in Japan by Kamo and co-workers [57]. A MW-generated plasma ball with an excitation microwave frequency at ~2.4 GHz [58]. Figure 1.2 illustrates their linear-antenna MWCVD reactor, which remains one of the common setups used for diamond growth today. The microwaves enter the chamber through a quartz window, which separates the vacuum chamber from the atmospheric pressure air, igniting a plasma in the chamber directly above the substrate. The high temperature plasma ball (typically 2000-2500 °C) was generated from the collision of electrons, molecules, atoms and ions, and remains localised at one of the nodes in the microwave cavity. The power used to grow diamond films is reactor dependent and ranges from 800 W to 50 kW, although typical systems use 1-5 kW. The diamond growth rate using MWCVD varies from 0-100 $\mu\text{m}/\text{h}$, depending on the growth conditions [34,57,59,60].

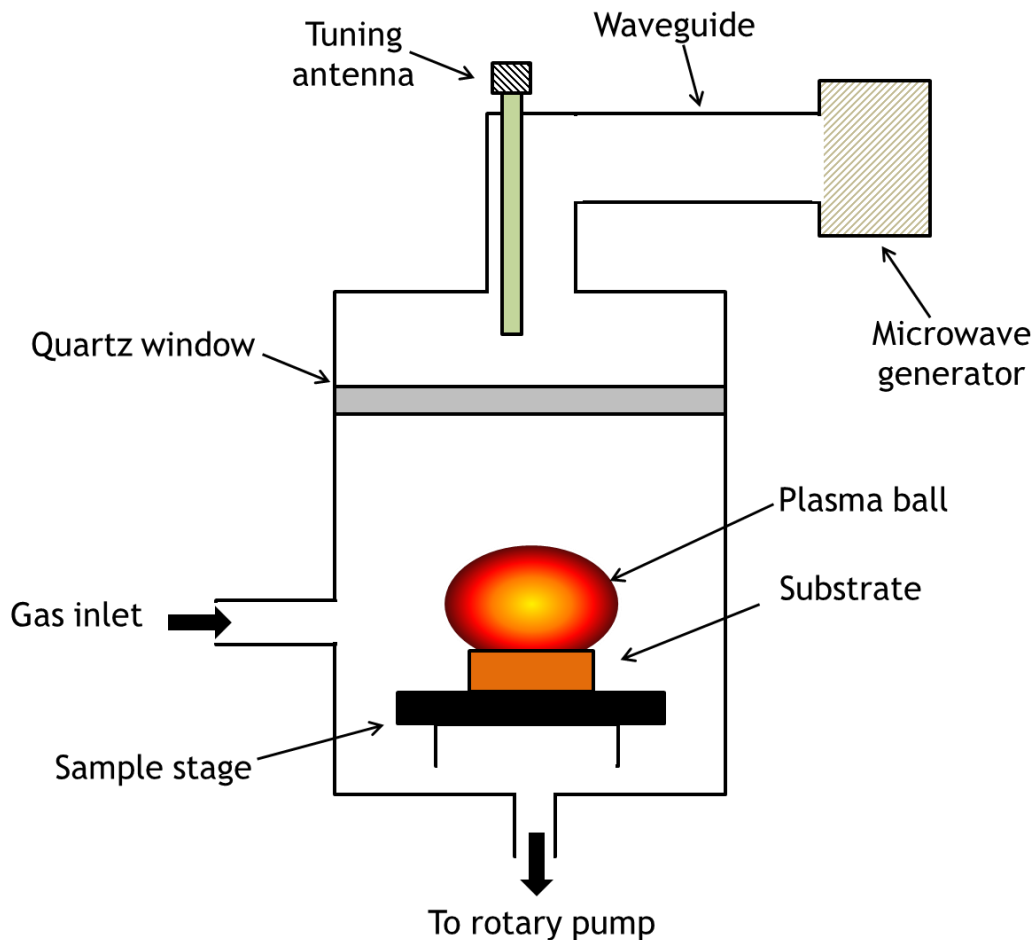


Figure 1.2: Schematic diagram of a linear antenna MWCVD reactor.

1.3.1.2 Hot-Filament CVD (HFCVD) system

HFCVD was chosen as the tool for diamond growth in this study due to their ability to deposit diamond films over large areas, along with their simplicity relative to MWCVD. In addition, HFCVD is one of the most established methods to date in growing thin films.

In this technique, a metal filament made from tungsten, tantalum or rhenium wire is typically used for the thermal activation of the gas mixture. The thin wire filament is positioned 3-5 mm above the substrate and then resistively heated to between 2000°C and 2500°C. The typical power used varies between 70 W to 300 W, at a process pressure of ~20 torr. The heat transfer from the filament through radiation usually is not

sufficient to heat the substrate temperature to the $\sim 850^\circ\text{C}$ required for diamond deposition. Hence, secondary heating is often used in the form of substrate heater to increase the substrate temperature to the desired value. The typical growth rate of a HFCVD system is $\sim 0.5 \mu\text{m/h}$. One disadvantage of HFCVD compared to MWCVD is that the filaments are sensitive to the presence of many gas-phase species, especially oxygen. If even trace amounts of oxygen are present, the filament lifetime is drastically reduced, often to seconds. This limits HFCVD gas mixtures to those that do not contain oxygen.

Details of the HFCVD setup and growth conditions used in this study are discussed in Chapter 2.

1.3.2 Diamond Growth Mechanism

Figure 1.3 illustrates the Bachmann diagram of C/H/O species for diamond and non-diamond growth. This diagram helps explain the growth conditions needed for CVD diamond films [61], and was created by comparing the quality of diamond produced by over 70 different CVD processes and gas mixtures. The diagram shows that good quality diamond is produced in only a small region of phase space, on the carbon-rich side of the CO tie line. Too much O or H and no films grow because all the carbon is in the form of gaseous species such as CO or CH_4 . Too little O or H and the C-containing molecules link together and deposit as non-diamond carbon forms, such as graphite or polymers.

The diagram shows that growing diamond films, either with C/H mixtures or C/H/O mixtures, is independent of the original precursor gases used. This suggests that the ‘chemical soup’ of reactants above the growing diamond surface is so well mixed that only the ratio of C:H:O matters for growth. It also emphasises the importance of H species in diamond growth process, as higher amounts of H species present help push the growth regime from non-diamond into diamond. In a HFCVD reactor, the presence

of oxygen causes the metal filaments to burn out within seconds. Thus, most of the Bachmann diagram is inaccessible to HFCVD. This is why there is a small region in the lower left-hand corner of the diagram (1-3% CH₄/H₂) which is used as the standard CVD conditions in HFCVD.

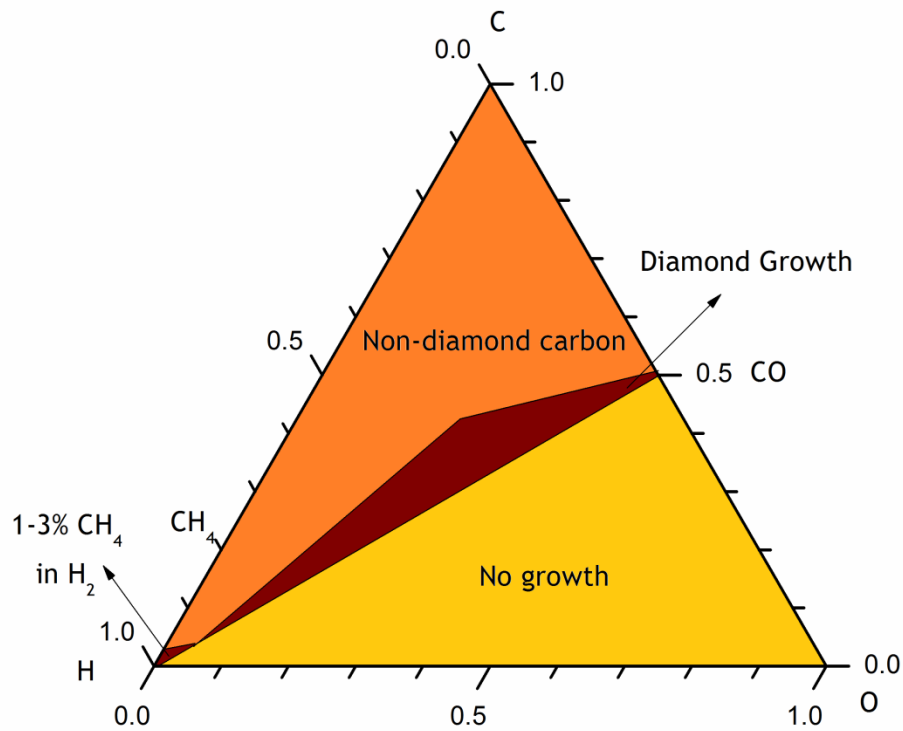


Figure 1.3: Bachmann diagram of C/H/O species for diamond and non-diamond growth.

1.3.2.1 Surface Mechanism of Diamond Growth

The gas mixture enters the process chamber, diffuses around, and at some point passes through the hot activation region (either the hot filament or the plasma ball), as depicted in Figure 1.4. Due to high temperature in this region (2000-2500°C), the gas molecules are dissociated. In particular, 1-40% of molecular hydrogen is split into atomic hydrogen which then starts a series of chemical reactions with the other hydrocarbon species present. CH₄ is typically used as the hydrocarbon source gas, but this series of reactions forms various other radicals such as

CH₃, CH₂, CH, C as well as C₂, C₂H, C₂H₂, C₂H₆ and higher hydrocarbons [32,50,62]. Of these, CH₃ is believed to be the main hydrocarbon radical that is crucial in determining the growth rate of diamond films due to its high concentration at the growing diamond surface.

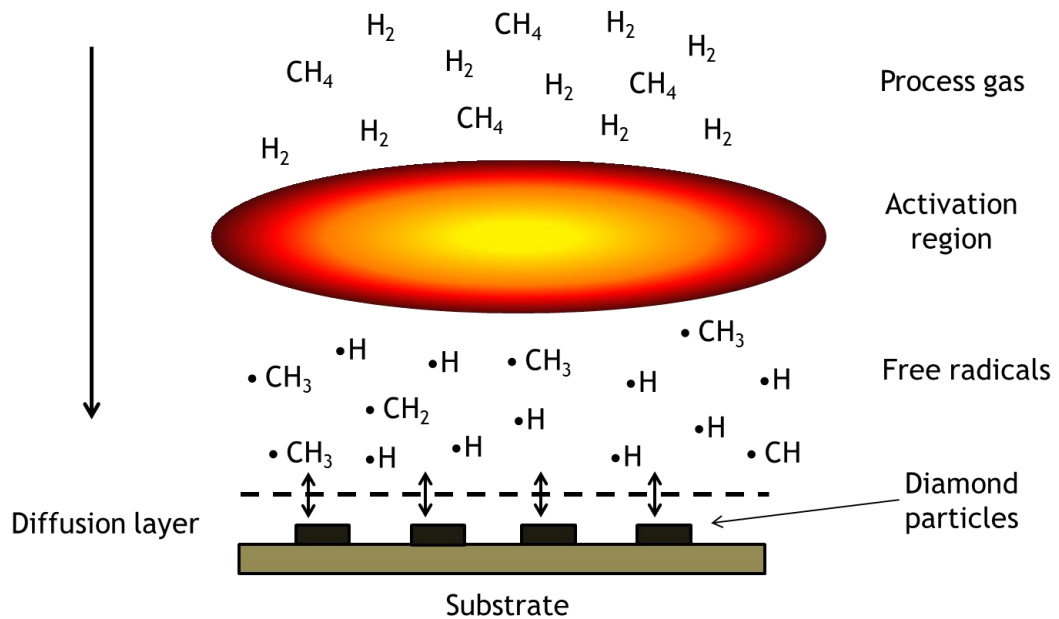


Figure 1.4: Schematic diagram of gas phase reaction pathway towards the substrate in the CVD diamond growth system. The activation region could be either a hot filament or plasma ball [1].

Figure 1.5 shows the simplified schematic diagram of the standard diamond growth model on a diamond surface. Theoretical calculations have shown that the formation of new layer of carbon atoms on a diamond surface is a rate-limiting process during growth. This consists of forming a four-C-atom nucleus on the {111} surface [63]. This nucleus is not only essential in growing the next layer of diamond by addition of another CH₃ but also as a reaction space for addition of any impurities to change the property of diamond. For example, CN and ·NH₂ species may be introduced during this step to produce N-doped diamond films.

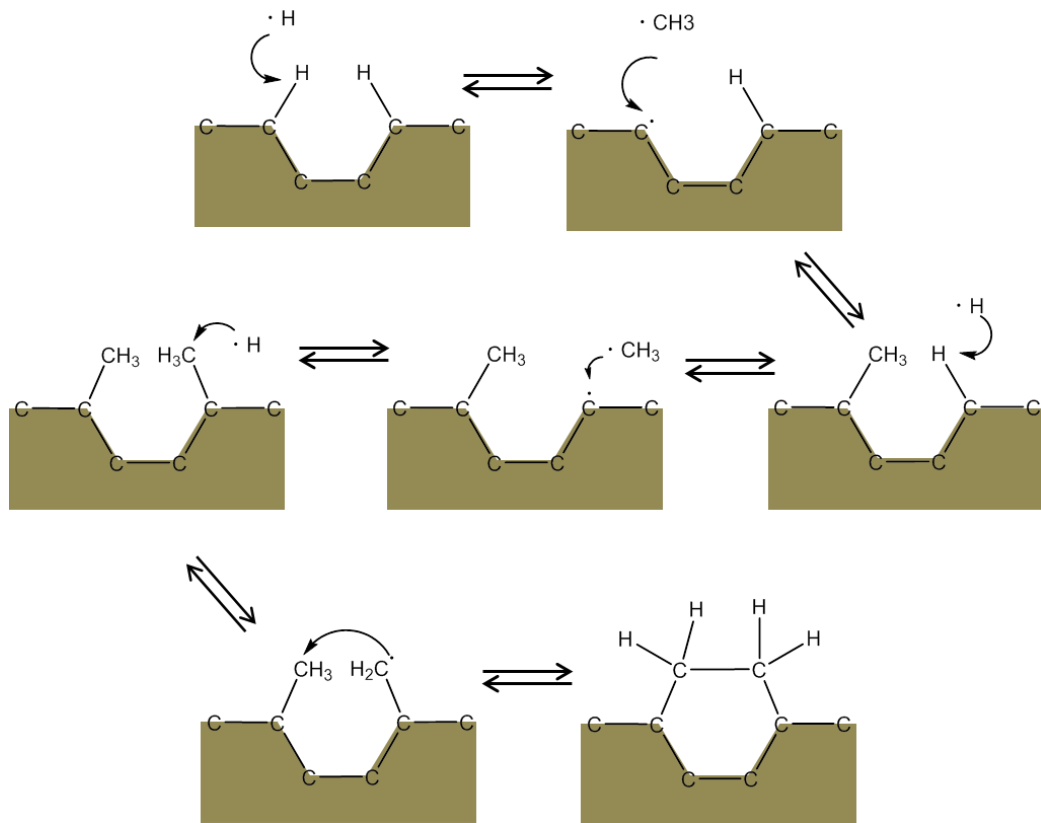


Figure 1.5: Simplified schematic diagram of the standard diamond deposition model [1,64].

The growth process is initiated by the abstraction of an H atom from the diamond surface to form a dangling bond, or surface radical site. Next, CH₃ will attack the dangling bond to form a new C-C bond. The process will be repeated on the next available C-H until it forms a complete 6-membered ring, so completing the diamond structure. This is a simplified surface mechanism of diamond growth because the model excludes the migration of C atoms, formation of nucleation sites and abstraction of C atoms from the surface to form gas phase hydrocarbon species.

If the diamond film is grown on a non-diamond substrate (heteroepitaxial growth), the initial mechanism differs slightly. When diamond films are grown heteroepitaxially, the first step is the formation of a metal-carbide or silicon-carbide [65-67]. The carbide layer acts as initial C layer for the H abstraction process and the subsequent formation of C-C bonds as depicted in Figure 1.5. Depending on the substrate material

and growth time, this carbide layer can be atomically sharp (Si), 10-100s of nm thick (Si, Mo), several μm thick (W) or 10-100 μm thick (Ti).

1.4 Substrate Pre-treatment

A pre-treatment process is essential for heteroepitaxial CVD as it reduces the nucleation time to form continuous diamond films. A wide range of seeding techniques are commonly used, such as simple manual abrasion using diamond powder, sonication in nanodiamond suspension, electrospray of diamond particles, self-assembly of a polymer-diamond suspension and applying a negative bias on the substrate during diamond growth in CVD reaction chamber (bias enhanced nucleation).

1.4.1 Manual Abrasion

This technique was the most simple and cost effective technique used in seeding diamond particles onto a substrate. Previously, hard grit such as SiC, c-BN and Al_2O_3 has been used in this technique [55,56,59,60,68,69]. However, diamond powder was proven to be the most effective [66]. In this technique, a small quantity of diamond powder (typically 1-3 μm in size) is applied between two substrate surfaces, which are then rubbed together to both scratch the surface and embed diamond particles onto both substrate surfaces. Excess diamond powder is then wiped away. The scratches formed on the surface due to abrasion create suitable defect sites to promote diamond growth. Also, fragments of diamond broken off from the abrasion grit are also embedded in the substrate surface - and these aid nucleation. The time taken for the process, the particle size of the diamond and abrasion procedure have been reported by others [39] and the reported optimised parameters were used in this study.

1.4.2 Electrospray

Figure 1.6 shows the electrospray system in the Diamond Laboratory, University of Bristol. This technique utilises an applied potential difference between a diamond-particle suspension and the grounded substrate as the driving force for the suspension to be attracted towards the substrate used. When a high potential (35 kV) is applied between the substrate and diamond suspension, the liquid suspension (usually nanodiamond in methanol) is attracted towards the substrate and pulled out of the syringe, and then vaporised into a spray which travels towards the substrate. The distance from the end of the nozzle to the substrate was optimised so that the liquid had enough time to nearly evaporate completely before striking the surface. If too much liquid hit the surface, splashing would occur, whereas if too little liquid (e.g. only the dry nanoparticles) hit the surface they would not stick properly. The substrate was rotated at a few rev/s to aid uniformity of deposition. After seeding, the seeds were only weakly bound to the surface and could easily be removed by sonication or friction from tweezers. Therefore, they were held carefully by the edge and either placed into the CVD reactor immediately, or stored in sample boxes. So long as the top surface was not touched these samples could be stored for many weeks before being used for CVD.



Figure 1.6: The electro spray instrument used in Diamond Laboratory, University of Bristol for diamond seeding process.

1.4.3 Sonication in Diamond Suspension

In this pre-treatment technique, diamond powder was dispersed in a liquid suspension. The most typical liquid used was water because the small surface charge on the nanodiamond interacts with the water molecule dipoles and creates a stable suspension [28]. Most commercially available detonation nanodiamond is supplied in this form. The substrate to be seeded was immersed in the diamond suspension and sonicated in an ultrasonic bath for between 30-60 minutes depending on the concentration of the suspension and the nanodiamond particle size [42,70,71]. The ultrasonication gently abraded the substrate surface with the diamond crystal and also embedded the diamond particles into the substrate surface. This technique was widely used to prepare thin NCD and UNCD diamond films with high nucleation density because manual abrasion produced scratches that were too deep or large for nanofilms. [72]. Similar pre-treatment processes using suspensions of diamond in various organic liquids have also been reported [73].

1.4.4 Bias-Enhanced Nucleation (BEN)

Bias-enhanced nucleation (BEN) is a technique whereby a negative DC bias (-70 to -250 V) is applied to the substrate during the first stages of the diamond growth process in a MWCVD reactor [74-76]. During this BEN stage, which usually lasts for about 10-30 minutes, the CH₄ concentration is usually increased from 1% to 4-10%. The negative bias will attract positive hydrocarbon ions (CH₃⁺, CH₂⁺, etc) from the plasma onto the substrate which they strike with high kinetic energy. This causes them to be implanted into the sub-surface region of the substrate (in a process called 'sub-plantation') creating few monolayers of carbon. Further impacts by ions cause thermal spikes to be sent through this layer, effectively annealing it and cause the carbon layer to register and align with the underlying Si lattice. This produces an almost epitaxial seed layer with high nucleation density [77]. After BEN, the growth conditions are switched back to normal and the bias is turned off, and CVD continues on the epitaxial seed layer, often forming a large area pseudo SCD coating. Although useful, this method requires a conductive substrate and only works with MWCVD.

1.4.5 Self-assembly of Diamond Particles

Self-assembly is one of the most recently developed pre-treatment techniques to seed diamond particle onto the substrate. It utilises the zeta potential charge (ZPC) of the substrate in a liquid medium, which is defined as the potential difference between the dispersion medium (liquid) and the stationary layer of fluid (surface species) attached to the substrate [78]. A Si wafer has a native oxide layer, and upon contact with water exhibits negative ZPC [28]. By manipulating the surface charge on nanodiamond particles (i.e. by giving them a positive ZPC), a spontaneous self-assembly mechanism was observed on the substrate with high nucleation density [28].

A different approach was used by previous Bristol researchers. Two different types of polymer, anodic and cathodic polymers, were used. First, the substrate was immersed in a positively charged cathodic polymer solution (polyethyleneimine - PEI or polydiallyldimethylammonium chloride - PDDA) to create a positive charge on the substrate surface. Then, the substrate was immersed in a mixture of a negatively charged anodic polymer (polystyrene sulfonate - PSS) with nanodiamond suspension. The negative nanodiamond-PSS were electrostatically attracted to the positively charged surface and adhered there, forming a stable, self-assembled nanodiamond monolayer. Lastly, a washing and drying process was performed to remove any excess polymers and nanodiamond from the surface of the substrate. Any remaining polymer is expected to be vaporised in gaseous hydrocarbons in the first few seconds of exposure to the reactive H atom atmosphere during CVD.

1.5 Impurities, Defects and Doping

The introduction of impurities into a diamond lattice may lead to various effects. It can either enhance or degrade the properties of the crystal. The introduction of metals such as iron, cobalt and nickel may degrade the properties of diamond while the introduction of oxygen, nitrogen, lithium, sodium or boron may lead to the enhancement of diamond's electrical properties [33,79-81]. By introducing these dopants, diamond can transform from being an electrical insulator into a semiconductor or even a semi-metal. Boron is responsible for transforming diamond into a p-type semiconductor while phosphorus and nitrogen (and theoretically, lithium) will transform diamond into an n-type semiconductor [82-84].

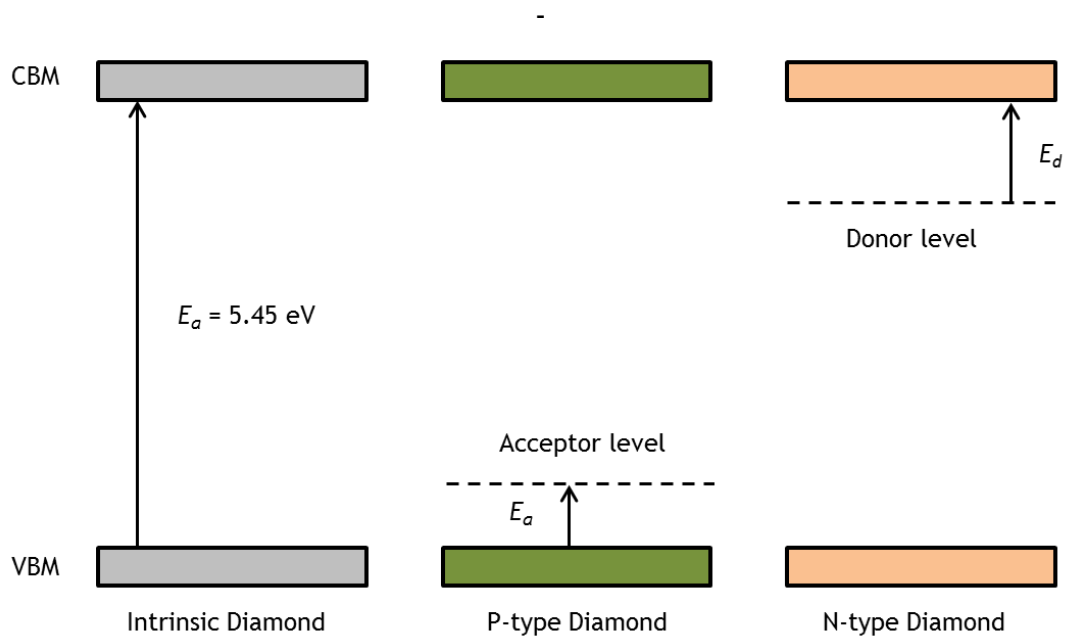


Figure 1.7: Band diagram of intrinsic diamond, p-type diamond and n-type diamond.

Figure 1.7 illustrates the band gap of intrinsic diamond, p-type diamond and n-type diamond. For intrinsic diamond, the energy for a single electron to be excited from the valence band maximum (VBM) to the conduction band minimum (CBM) is 5.45 eV. This high activation energy makes intrinsic diamond an electrical insulator. In contrast, p-type diamond has an acceptor energy level near the VBM. An acceptor is usually an element has one electron less than C, and is capable of substituting for a C atom in a diamond lattice. As a result of the missing electron, the dopant will generate a free positively charged hole, which will conduct the electrical current by accepting an electron from neighbouring carbon. Hence, a p-type dopant is also known as an acceptor in the diamond lattice.

The role of n-type dopants is the opposite of p-type material. Any element that has more electrons than C and has a capability to substitute for C atom in the lattice can be classified as a potential n-type dopant. However, the exception could also be made for any element that has the ability to be inserted into diamond lattice interstitially, such as lithium and magnesium. These elements have the potential to donate an electron into

the diamond lattice via an interstitial position. As depicted in Figure 1.7, n-type diamond has a donor level near the CBM of diamond. The extra electron from the donor atoms will be donated into the CBM of diamond to change the property of diamond from insulator to semiconductor.

1.5.1 P-type doping

P-type diamond has been widely researched, produced, used and samples are commercially available from Element Six, Ltd, and other synthetic diamond companies. Boron atoms are commonly used as the dopant giving an activation energy of 0.37 eV above the VBM of diamond [83]. This small activation energy is responsible for the low resistivity of boron-doped diamond films at room temperature and pressure.

In 1991, boron was first incorporated into SCD HPHT diamond *via* an ion-implantation method. p-type conductivity was observed in the SCD films due to the reduction of electrical resistance throughout the film, however, defects were created in the sample as result of the high energy ion beam (10-100 keV) [85] and it is possible that some of the improvement in electrical conductivity was due to increasing sp^2 carbon content in the films resulting from ion damage [86]. Some of this damage could be removed by post-annealing. $2 \times 10^{20} \text{ cm}^{-3}$ of B atoms was successfully implanted in the diamond films giving resistivity $< 10^{-2} \Omega \text{ cm}$ after post annealing treatment at 1450°C [87].

Forced diffusion has been done in the past using boron powder to incorporate boron atoms into SCD type II films. Boron powder was diffused between two SCD films under the influence of electrical bias. Higher concentrations of B atoms ($\sim 10^{18} \text{ cm}^{-3}$) were successfully incorporated when the sample was positively biased compared to $\sim 10^6 \text{ cm}^{-3}$ when negative bias was applied on the sample. This suggest that B atoms diffused into the sample as negative ions [88].

The most common method to prepare boron-doped diamond (BDD) is using CVD. Typical boron precursors used in this technique are diborane gas, boron trioxide and trimethylborane [86,89-92]. Extra precautions need to be taken into account while using these boron precursors due to their toxic nature. Higher concentrations of precursor gas used in the growth gas mixture leads to higher concentrations of boron atoms incorporated into the BDD. This allows the B concentration in the film to be readily controlled from $\sim 10^{17}$ to 10^{21} cm^{-3} [86,89,93].

The electrical conductivity of BDD increases with the amount of boron atoms incorporated, as illustrated in Figure 1.8. BDD starts to exhibit semi-metallic properties when the concentration of B increases $> 10^{21}$ cm^{-3} . Heavily doped BDD also becomes superconducting at 2-8 K and survives 3.5 T of magnetic field current [94].

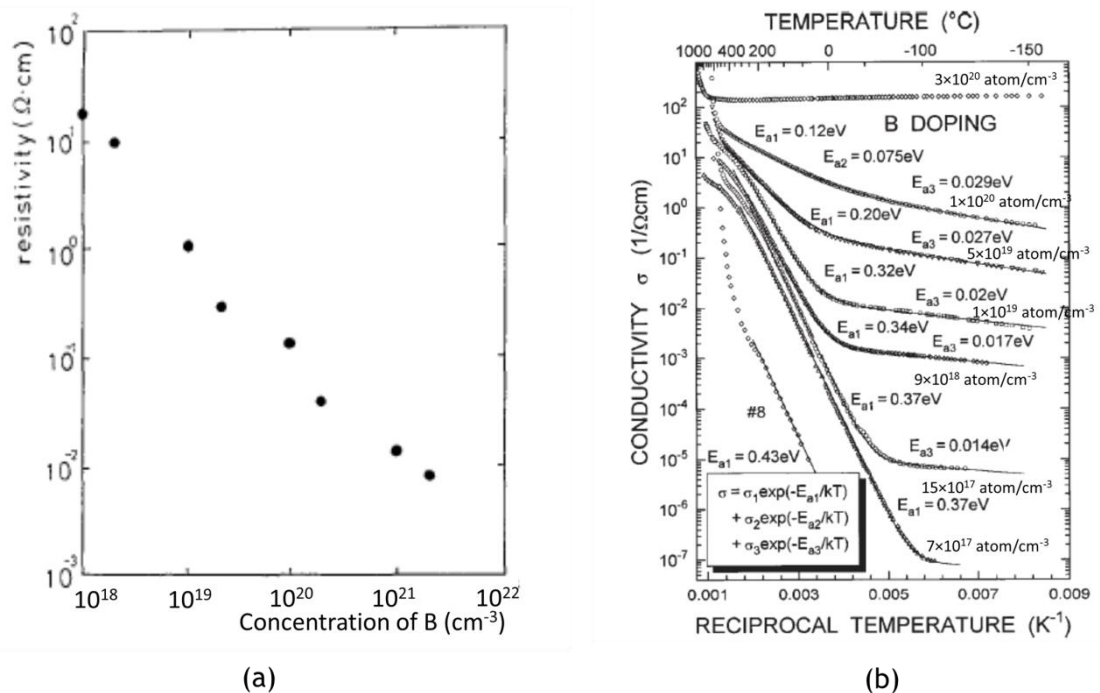


Figure 1.8: (a) Resistivity vs. concentration of B in boron-doped diamond films and (b) temperature dependent conductivity data at different temperature with different boron concentration incorporated in diamond films [89,93].

The ability to dope diamond with B has allowed a number of simple p-type devices to be constructed, such as UV detectors, simple sensors, electrochemical electrodes, photovoltaic cell and microplasmas [11,13,43,95-101].

1.5.2 N-type doping

Even though p-type semiconductor diamond films are widely available, to fully utilise diamond film technology, n-type semiconducting diamond is crucial, especially in making p-n junction for electronic devices. Moreover, the large band gap of diamond places the CBM of diamond near the vacuum level. To be able to excite electrons from the donor level into the CBM of diamond and then into the vacuum level will create a low work function material that will revolutionise the electron emission industry, potentially for the production of field emission and thermionic emission devices. A few n-type dopants have been suggested both experimentally and theoretically by other researchers, ranging from N, P, S, Li, Na, Sb and As but to date, none of these have provided useful n-type electronic characteristics at standard room temperature and pressure [33,40,102-105].

1.5.2.1 Nitrogen

N atoms are commonly found impurities in natural and synthetic diamond. Most HPHT type I diamonds contain N atoms either in aggregates or in a single substitutional site. N atoms are easily incorporated into diamond films grown using CVD. N₂ or NH₃ gas is mixed into the gas phase while growing the diamond films, and nitrogen-doped diamond have been successfully synthesised with a concentration of N atoms ranging between 10¹⁷ to 10¹⁹ cm⁻³ [106,107]. However, N atoms act as a deep donor in diamond, in which it requires 1.7 eV to excite an electron from the donor

level into the CBM of diamond. The high activation energy needed leads to high electrical resistance ($>200 \text{ M}\Omega$) throughout the diamond films at room temperature and pressure [81,108].

1.5.2.2 Sulfur

Sulfur atoms had the potential to be a shallow n-type dopant due to its two valence electrons. However, due to the larger covalent radius of sulfur (1.08 Å) compared to N and C, the solubility of S in diamond lattice will be low. Sulfur is usually incorporated into the diamond lattice using CVD with hydrogen sulfide (H_2S) gas used as the S precursor. Early reports said that the introduction of S into the growth process reduced the growth rate of the diamond film and also reduced the quality of the diamond films produced [33,79,109]. But in 1999 Sakaguchi and co-workers [103] claimed to have made an n-type diamond semiconductor containing $\sim 10^{16} \text{ cm}^{-3}$ of S atoms. The films had high carrier concentrations and a high mobility ($597 \text{ cm}^2 \text{ V}^{-1} \text{ s}^{-1}$ at 300 K) with an activation energy of 0.38 eV. However, the sample was later shown to be contaminated with B atoms due to the Type Ib SCD film used as the substrate [110]. The result of a boron-implanted sample with similar B concentration was proven to be consistent with the result for Hall measurement obtained by S-doped diamond films prepared by Sakaguchi [110]. Thus, S is currently not accepted as being an n-type dopant for diamond - although it does have the effect of increasing the graphitic grain boundaries which increases overall film conductivity.

1.5.2.3 Phosphorus

Apart from N and S atoms, P atoms are also candidates to promote n-type semiconductor properties in diamond films. Theoretical studies suggest that phosphorus-doped diamond had lower activation energy compared to nitrogen-doped diamond. Approximately 0.2 eV - 0.6 eV

energy is needed to excite an electron from the phosphorus donor energy level into the CBM of diamond, compared to ~1.2 eV - 1.7 eV energy needed in nitrogen-doped diamond [82,83,111]. However, the solubility of phosphorus in a diamond lattice remains as a great challenge. The large covalent radius of P atoms (1.13 Å) hinders the substitution of C atoms with P atoms and leads to a low solubility of P atoms in the diamond lattice [82]. This often leads to growth of non-uniform diamond films or diamond films grown with defects and re-nucleation sites on the grain itself [33,112-115].

Implantation of P atoms into diamond was reported to produce a high concentration ($2.8 \times 10^{18} \text{ cm}^{-3}$) of incorporated P atoms [116]. The n-type doping efficiency was at 10% for this sample with electron concentration at 900 K being $3 \times 10^{17} \text{ cm}^{-3}$. However, the electrical conductivity of this sample was small. Upon annealing, the conductivity reduced significantly. The annealing treatment caused an opposite effect compared to that caused in ion-implanted B-doped diamond films (see Section 1.5.1). The carrier mobility for the P-doped diamond film was low ($\sim 30 \text{ cm}^2 \text{ V}^{-1} \text{ s}^{-1}$) and was speculated to be limited due to the presence of defects.

The most common P-doped diamond today is prepared *via* CVD using phosphine gas, PH_3 . The amount of P atoms incorporated inside diamond can be controlled precisely between 1×10^{16} to $2.5 \times 10^{19} \text{ cm}^{-3}$ [41,42,117-119]. However, the quality of diamond films reduces greatly when higher concentrations of P are incorporated into the diamond films. Even though the growth conditions were those for standard MCD growth, analysis showed a higher than normal content of sp^2 carbon at the grain boundaries. This is due to the larger P atoms increasing the strain in the diamond lattice. The theoretical formation energy in substituting a C atom with P atom is predicted to be at 10.4 eV [82]. This large formation energy explained the low solubility of P atoms in diamond.

In addition to that, the carrier mobility in phosphorus-doped diamond films is too low (25 to $600 \text{ cm}^2 \text{ V}^{-1} \text{ s}^{-1}$) making them impractical in

creating n-type semiconductor electronics at room temperature [114,117,120].

1.5.2.4 Sodium

Sodium was also suggested as a potential donor in diamond due to its extra valence electron. However, after extensive theoretical calculations on Na behaviour in a diamond lattice, it was concluded that Na atoms substitute for the C atoms inside the diamond lattice, rather than insert themselves interstitially [80,83,121-123]. This position leads to the production of a p-type semiconductor rather than an n-type semiconductor. The Na atoms act as a deep acceptor. Experimental data also support the attribution of Na atoms as acceptors because Na atoms diffuse through diamond as negative ions under electric bias [88]. High concentrations of Na atoms ($2 \times 10^{19} \text{ cm}^{-3}$) were successfully incorporated *via* forced diffusion (negative bias) method, however the electrical resistance of Na-doped diamond films was still high; between $\sim 100 \text{ k}\Omega$ to $100 \text{ M}\Omega$ [105].

1.5.2.5 Lithium

Theoretical studies suggest that lithium can enhance the semiconductivity of diamond by introducing a shallow donor energy level in the band gap of diamond. The energy to excite an electron from the lithium donor level to the CBM of diamond should be less than 0.3 eV [83,121,122]. Unfortunately, experimental confirmation remains elusive. More research has been focused on trying to force lithium into the diamond lattice by implantation, diffusion and insertion during growth but the lithium remains inactive inside the diamond lattice [103,105,124].

In contrast with N, S and P doping, ion-beam implantation is preferable for Li compared to addition of the dopant precursor during CVD

growth. This is due to the limited availability of cheap, safe, gas-phase Li compounds. Various dosages of Li from 1×10^{14} - 4×10^{16} cm^2 were implanted into type IIa diamond substrates [105,125,126]. When 1×10^{14} cm^{-2} was used as the Li ion dosage, a maximum of 1×10^{19} cm^{-3} of Li were detected using SIMS [125]. The implantation followed a normal Gaussian distribution and spread across a depth of 600 nm beneath the diamond surface. High temperature implantation gave a lower sheet resistance by two orders of magnitude compared to room temperature implantation followed by annealing [126]. $100 \text{ M}\Omega \text{ cm}^{-2}$ sheet resistance was recorded at 850 K for the sample implanted with Li atoms at high temperature. Even though the activation energy of electrical conductivity of Li-doped diamond films is reported to be between 0.19-0.23 eV, the sheet resistance was too high for any practical application.

Forced diffusion was also used to incorporate Li atoms into diamond by applying an external voltage. 230-240 V was applied between a Li source sandwiched between two type IIa diamond substrates [88,127]. When Li metal was used, Li atoms diffused into the diamond lattice as negative ions and SIMS analysis recorded an average concentration of 1×10^8 cm^{-3} [88]. However, when Li_2CO_3 was used, the applied bias had no effect on the diffusion of Li. The concentration of Li atoms for the positively biased, negatively biased and non-electrical biased samples remained the same at $\sim 3 \times 10^{19}$ cm^{-3} [127]. In another series of diffusion experiments the initial concentration of Li atoms was as high as $\sim 10^{21}$ cm^{-3} . But this was later found to be an overestimation caused by the unwashed excess starting material. After a series of washing processes using mineral acids and deionised water the concentration of Li atoms reduced to $\sim 10^{17}$ cm^{-3} [103]. This serves as a cautionary warning about the pervasive nature of Li and how much care needs to be taken when using it to avoid false readings (see Section 3.3.4). Even though high concentrations of Li were successfully diffused into diamond, no significant results were obtained from Hall effect measurements.

Only a few attempts have been reported about attempts to incorporate Li atoms during diamond CVD. In one report, butyl-lithium,

C_4H_9Li , was dissolved in hexane and pressurised in Ar atmosphere at 1×10^4 Pa [128], and added into the CVD gas mixture. The maximum concentration of Li atoms observed 10 nm below the surface was $8 \times 10^{13} \text{ cm}^{-3}$ which reduced to $5 \times 10^{12} \text{ cm}^{-3}$ at 350 nm. Lithium-*t*-butoxide, $LiOC_4H_9$ powder was also used as Li precursor. The powder was heated in a different chamber (200°C) and connected to the CVD reactor with a stainless steel tube. Using this method, $2.49 \times 10^{16} \text{ cm}^{-3}$ of Li was successfully incorporated inside diamond films. Unfortunately, the Li-doped diamond films were also electrically inactive.

It was speculated theoretically that the high mobility of Li atoms in diamond at moderate temperatures, $\sim 550^\circ\text{C}$ might lead to the clustering of the Li atoms, and their mutual interaction/bonding would tie up their valence electrons, making them ineffective donors [80,82,83,123]. Goss and co-workers [123] simulated the formation of Li complexes in their theoretical models using the AIMPRO code. The clustering of interstitial and substitutional Li was found to be favourable due to the higher binding energy compared to incorporation of individual species. The clusters exhibit single and double acceptor energy levels at 1.8 eV and 3.1 eV above the VBM of diamond. These energy levels were considered to act as deep acceptors and will render them electrically inactive in diamond films.

1.5.2.6 Lithium-Nitrogen Co-doping

As N atoms in diamond act as a deep donor, Li atoms remain inactive due to cluster formation, and P has limited carrier mobility, the production of a suitable n-type semiconductor diamond is still an unresolved issue.

To attempt to solve this problem, Namba and co-workers [129] suggested that creating a defect site with a 1:1 ratio of lithium and nitrogen will enhance the conductivity of the diamond as an n-type donor. In this case, the Li atoms must be inserted interstitially while N atoms replace one of the carbon atoms to form a substitutional dopant. It is

suggested that the Li atom will be pinned down by the N atom, so its mobility will be reduced, with the electron from the Li atom being transferred through the N atom directly into the diamond lattice through the Li-N bond. Thus, this co-doping process could create n-type semiconducting diamond with a shallow donor level and high electron mobility. The original report of Li-N codoping came from Namba et al's US patent, but this included no experimental evidence showing the codoping actually worked. Much of the work in this thesis (Chapters 4 & 5) was performed to try to verify the co-doping idea and to optimise the Li:N ratio and electrical properties.

1.6 Theoretical Studies of Li-N Dopants in Bulk Diamond

The complexity and multiple variations in doping diamond with potential dopant atoms will lead to a large number of trial and error experiments if the approach is being done by experimentation alone. Thus, computational calculations have also been used to ease the complexity in determining the best structure, stoichiometry, and predict the electrical properties of the dopants in diamond. Density Functional Theory (DFT) was chosen as the best approach to calculate the energy of the doped diamond structure due to its accuracy in solid state calculations.

1.6.1 Density Functional Theory (DFT)

Density Functional Theory (DFT) was developed to solve the Schrödinger equation for systems with many electrons, and to deduce the ground-state of the electrons in the material of interest. The ground-state behaviour is best described and explained using a first-principle approach due to the inclusion of electron-electron interactions.

The complexity of solving the Schrödinger equation requires approximations and simplifications to be made to reduce the time needed to perform the calculations. The Born-Oppenheimer approximation [130] is used to exclude the nuclei-electron interactions and to simplify the calculation to only calculate the electronic wavefunction. The concept of pseudopotentials is also applied in the DFT calculation in order to treat the core electrons as fixed potentials due to the strong interaction of the core electrons and the nuclei that will make them behave independently in the chemical environment. Hence, only valence electrons are included when solving the Schrödinger equation. The pseudopotentials are constructed prior to the calculation and are done automatically by the software used.

Before the discovery of the DFT concept, the most popular technique used in *ab initio* calculations was Hartree-Fock (HF) theory. However, HF theory over complicates the calculation by calculating the entire wavefunction of all the electrons in many-electron systems, which increases the computational time greatly. In contrast, DFT utilises the concept of electron density rather than the wavefunction of electrons. The electron charge density will determine the electronic structure of the material and the many-electron wavefunction does not need to be solved explicitly. The basic concept behind DFT was that the minimum charge density calculated would be identical to the true ground-state charge density.

The advancement of computer power allowed DFT to gain popularity, with much more user-friendly software being used by biologists, chemists and engineers. By having a minimum understanding of quantum mechanics, the researchers were still able to utilise the DFT software in predicting the properties of materials.

1.7 Applications

Diamond is known to have wide range of applications due to its mechanical properties and chemically inertness in harsh conditions. In addition to that, its high thermal conductivity and high electrical resistance make diamond films good candidates for heat-sink applications [1,5,85]. P-type and n-type diamond have been created using various dopants (see above), and the semiconducting diamond used in various devices such as SAW [11,12], MEMS [7,8] and LEDs [13]. In addition to that, the wide band gap of diamond (5.45 eV) and its high carrier mobility ($\sim 10^4 \text{ cm}^2 \text{ V}^{-1} \text{ S}^{-1}$) allow photoelectron and electron emission applications. The wide band gap of diamond places the CBM of diamond near the vacuum level, and by introducing an n-type donor into the diamond film, the work function of this material will be reduced greatly. This allows the diamond to be used as an efficient source of electrons in vacuum, because the electrons can be emitted from the surface with only a very low barrier to overcome. The emission process can occur as a result of excitation by various methods.

Secondary electron emission used a high energy primary electron beam to knock out electrons from the diamond surface. For diamond the yield of secondary electrons is greater than one, leading to electron multiplication. This can be useful in photomultiplier devices or dynodes [2,131].

Alternatively, the electrons may be emitted as a result of a high potential difference applied between the diamond and a collector electrode. This is known as field emission, and diamond has a threshold field for field emission of a few $\text{V}/\mu\text{m}$, comparable with carbon nanotubes and better than most other materials. The electron current increases with applied field, and the electrons can be accelerated to strike a phosphor screen (for use in flat panel displays), a metal electrode (for use in X-ray generation), or a diamond anode (to form a fast-response vacuum valve device) [132-135].

The electrons can also be emitted as a result of thermal energy - simply heating the diamond in vacuum causes electrons to be ejected from the surface in a process called thermionic emission. The electrons can be captured by a collector electrode, and by completing the circuit a self-bias is produced which can be used to drive a load. This effectively converts heat into electricity, and has been suggested as a method for solar energy generation [136-139].

1.7.1.1 Thermionic Emission

Thermionic emission is a heat-induced process that emits electrons from a hot emitter (cathode) over an energy barrier and collects them on a colder collector (anode), as depicted in Figure 1.9. Most common applications of this process can be found in electron microscopes (the hot filament used to generate the electrons operates by thermionic emission) and power generation in space-borne devices. When enough heat is supplied to the emitter to overcome the work function of the material, electrons will be emitted from its surface. However, an electron cloud will be generated near the emitter surface, and this space-charge effect will inhibit further electron emission. To overcome this, a small positive bias is usually applied to the collector to attract the electron cloud and reduce the space-charge effect near the emitter surface. The emitter and collector are connected to ground to ensure the electron flow is kept continuous.

The first thermionic converter used to generate energy was reported in 1957 [140] and the common working temperature for thermionic emission applications are between 1000°C to 2000°C for emitter metals such as W, Mo and Ta. High working temperatures inhibits the usage of this application for many Earth-based devices, but have been used to power satellites and spacecraft.

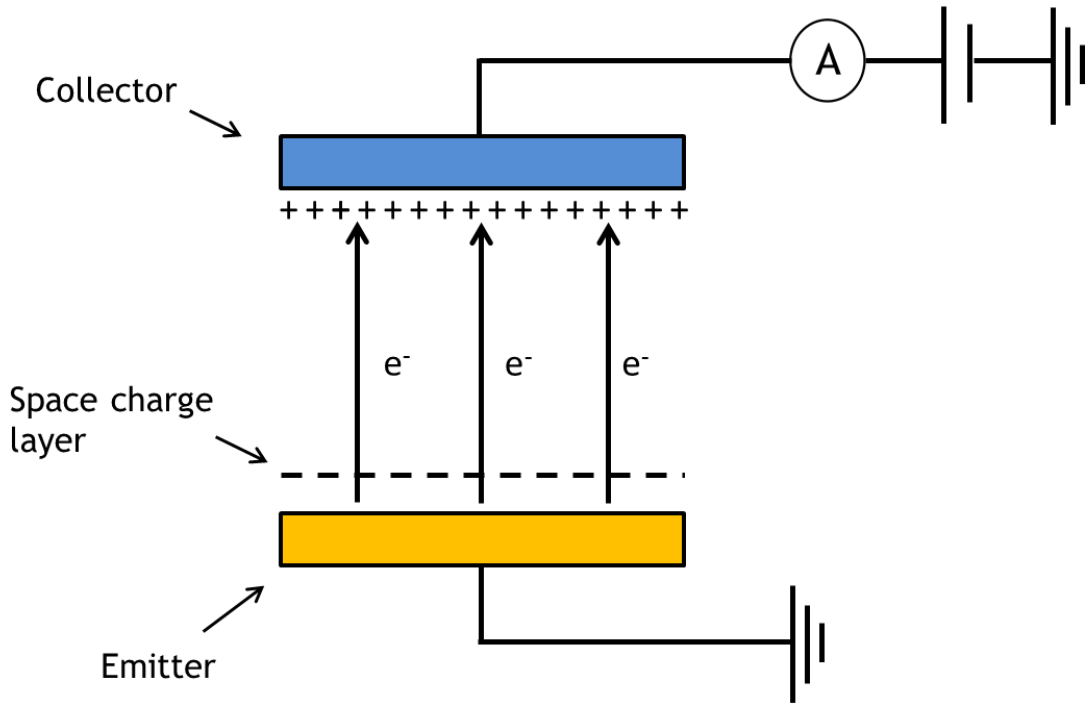


Figure 1.9: Schematic diagram of thermionic emission consisting of an emitter and collector. Both electrodes were grounded and a positive bias was applied to the collector to overcome the space-charge effect near the emitter surface.

Thermionic emission from diamond was first reported in 1991 [141] with working temperature less than 1000°C. The threshold temperature for diamond based emitters was reported at between 250°C and 550°C, with a low effective work function measured during the emission ranging from 0.9 eV to 4.43 eV [42,48,71,136,142]. These low temperatures suggest that diamond could form the basis of a very efficient solar thermionic converter, even on cloudy days.

The Richardson-Dushman described in Equation (1.1) is used to describe thermionic emission [143]:

$$J = A_R T^2 e^{\frac{-\phi}{kT}} \quad (1.1)$$

where J is the current density measured at the collector, A_R is the Richardson constant with the theoretical value of $120 \text{ A m}^{-2} \text{ K}^{-2}$, T is the working temperature, k is the Boltzmann constant and ϕ is the effective work function of the material.

The group at Arizona State University, led by Robert Nemanich, has been leading the field of thermionic emission from diamond. They tested various types of diamond films with different type of dopants for thermionic emission. They found that a high current density was typically generated by nitrogen-doped NCD films compared to other SCD and MCD films. The value ranges from 0.12 to 0.70 mA cm^{-2} depending on the substrate used and type of dopant incorporated inside the diamond films [48,138,144]. The high sp^2 carbon content in the NCD films were believed to be the contributing factor in increasing the current density produced due to the increased film conductivity. Different types of dopant were investigated by other groups using B, N, and P as the dopant element grown in an MCD film. Boron-doped diamond showed the poorest emitter characteristic with the current density of 0.6 nA cm^{-2} at 1390 K [142]. Phosphorus-doped diamond films prepared with a doping concentration of $5 \times 10^{18} \text{ atoms cm}^{-3}$ exhibited the lowest work function ever reported with the value of 0.9 eV [42]. However, the current density of the films collected at 900 K was $\sim 70 \text{ }\mu\text{A cm}^{-2}$ [42]. Nitrogen-doped MCD films grown by Paxton and co-workers showed a lower current density collected at the same working temperature with the value of $\sim 2 \text{ }\mu\text{A cm}^{-2}$ [145]. The work function of the materials produced was between 2.22 eV and 2.25 eV . The lower current density recorded on nitrogen-doped diamond can be explained due to the deep donor attribute of N atoms in a diamond lattice compared to phosphorus-doped diamond.

Apart from the low working temperature and low work function of diamond based thermionic emitters, another variable that was suggested might play an important role for electron emission was the nature of the diamond surface. It was found that the negative electron affinity (NEA) (see Section 1.8) generated by H-termination on the diamond surface was essential [48,136,145]. When the working temperature of the emitter

reached 973 K, the H atoms started to desorb from the diamond surface and degradation of current density was observed [49,136,145-147]. When the experiments were repeated without the regeneration process of the H-termination surface, the diamond emitter failed to produce a high current density even at lower working temperatures.

Currently, the best diamond-based thermionic emitter with the lowest work function and high current density was produced using mixture of UNCD/NCD films grown on a Mo substrate with H-termination present on the surface [138]. However, by having higher sp^2 carbon content in the film, it reduced some of the other desirable properties of diamond, such as hardness, robustness, thermal conductivity, which may reduce the device lifetime. Thus, it is important to have MCD or SCD films that can produce high current density and low work function without jeopardising much of the diamond properties.

To date and within the knowledge of the author, there is no literature published discussing the effect of Li atoms as dopant in diamond for thermionic emission applications. Hence, one of the aims of this thesis is to investigate the potential of Li-N co-doped diamond films as a diamond-based thermionic emitter material. If the addition of Li atoms into the existing nitrogen-doped MCD films increases the current density and reduces the work function of the material, it would open up a new perspective for thermionic energy conversion.

1.8 Diamond Surface Termination

Diamond is known to possess a H-terminated surface upon growing in CVD system. In each step during diamond growth process from the surface mechanism depicted in Figure 1.5, C-H bonds will always be present and any C dangling bonds will form C-H bonds due to the abundance of atomic H present in the system relative to other species. The substitution of H atoms with other species such as O atoms and N atoms initiate further

chemical reactions to functionalised organic moieties onto the surface for biomarkers and biosensor applications [15,17,148,149].

The ability to change the surface termination of diamond films is closely related to the electrostatic interaction of the C atoms and the surface species due to the dipole moment created between both species. For instance, a H-terminated surface is believed to yield a negative electron affinity (NEA) due to the surface dipole created by the difference in electronegativity between the H atoms (2.20) relative to the C atoms (2.55) [150-154]. Upon further investigation, this surface charge was not only responsible for attracting other molecules towards the diamond surface, but it changes the way electrons are transported from the bulk diamond into the surface for further reactions.

Figure 1.10 illustrates the band diagram of an NEA and a positive electron affinity (PEA) surface for pristine diamond. PEA occurs when the vacuum level is situated above the CBM of the material, and it what is usually found in most non-metals. This requires additional energy to excite electrons from the CBM of diamond into the vacuum level, before the electron can be used in any chemical reaction or in electron emission applications. A typical example of PEA surface is the O-termination surface of diamond [153,155,156]. The higher electronegativity of O atoms relative to C atoms creates a dipole moment between the C-O bonds with the negative pole outermost. O atoms will have partial negative charged thus repel any electrons near the surface of the diamond back into the bulk, preventing them from escaping into the vacuum level.

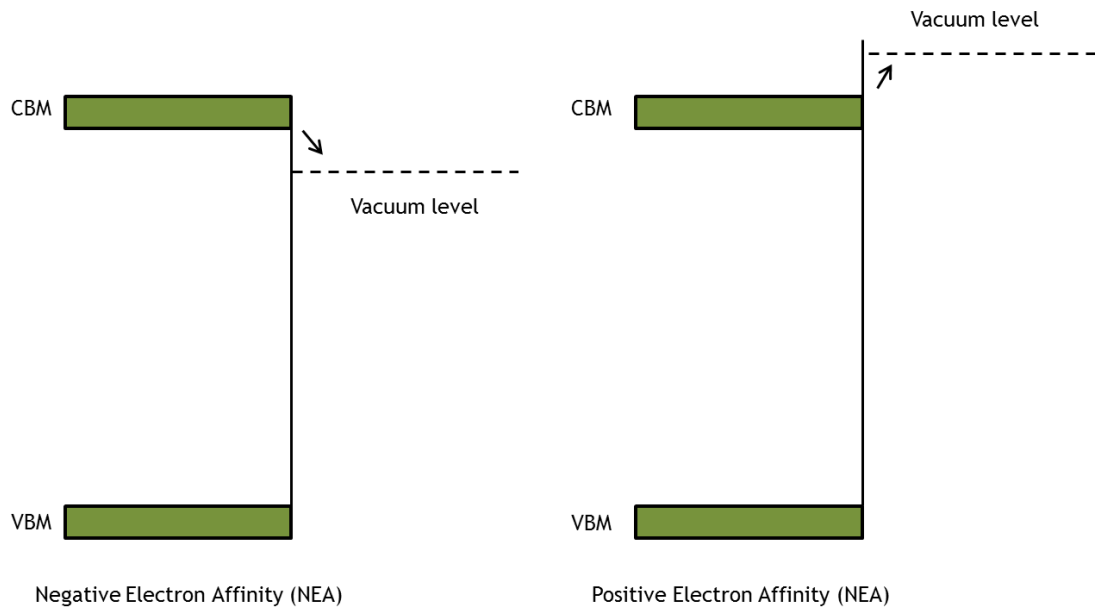


Figure 1.10: Schematic band structure of (a) a negative electron affinity surface and (b) a positive electron affinity surface of diamond.

1.8.1 Negative Electron Affinity (NEA)

The most basic form of NEA on diamond surface was the H-termination surface. In this case, the surface dipole is such that the positive pole is at the outermost. This has the effect of increasing the CBM so it lies above the vacuum level. Now, any electrons that enter the CB can fall into vacuum (i.e. be ejected from the surface) with no barrier. However, electrons still need to be promoted from the VB into the CB by some process, such as electron impact, thermal energy, or photo excitation.

Almost all diamond films grown using CVD are produced with the H-terminated surface due to the rich H environment during the growth process. However, the H atoms are easily desorbed from the diamond surface when heated between 650°C - 800°C in vacuum. Due to the importance of the NEA surface in allowing the electrons to be excited into the vacuum level, it is important to have a thermally stable NEA, especially for high temperature electronic devices such as thermionic energy

converters [145,146,153]. Thus, an alternative NEA termination which is stable at high temperatures is greatly sought after.

Apart from H-termination, other terminations using metals and non-metal elements have been explored in order to replace the weakly bonded H atoms on the diamond surface. Cl, F and Br were investigated but the low adsorption energy of the species made the surface termination process difficult to be done experimentally [157]. Another way to create the correct surface dipole is to first oxidise the diamond surface, and then attach a monolayer of a highly electropositive metal, such as Cs, Na or Li [152,158-160]. In these cases, the dipole again has its positive pole outermost. However, CsO⁻ and NaO⁻ terminations show good NEA and electron emission properties, but they decompose at temperatures as low as 500°C [161].

Other metals such as Ti, Ni, Co, Zr were deposited as thin layer films (<1 nm) on top of a diamond surface [151,152,162,163]. When the metal atoms were coupled with oxygen on diamond films, it changed the PEA of O-terminated diamond surface into an NEA surface.

In this study, various potential metal-oxygen termination surfaces were developed to understand further the effect of the metal-oxygen termination on diamond surface. This was found to be important in order to provide higher working temperature for the diamond-based thermionic emitter.

1.9 Thesis Outline & Objectives

The challenge in understanding and preparing n-type semiconducting diamond is crucial for the advancement of electronics using diamond-based materials. The aims for the experiments described within this thesis were:

- To investigate the potential of co-doped diamond with high dosage of Li and N atoms.

- To propose theoretical models of Li-N co-doped diamond for better understanding the effect of N atoms as trapping elements for immobilising the Li atoms to enhance the n-type electrical properties of diamond.
- To identify the optimum Li:N ratio using the theoretical models proposed.
- To study the potential of thermionic electron emission of Li-N co-doped diamond.
- To synthesise a thermally stable NEA surface on diamond films using a combination of various metal-oxygen termination techniques.

In **Chapter 2**, the common instruments and techniques used are introduced including their standard operating procedure, data analysis and basic concepts used in characterising the material produced.

Chapter 3, the first experimental chapter. It discusses the methods used to prepare the Li precursor for growing Li-N co-doped diamond films. The challenges and precautions that need to be taken while handling the compound to avoid introducing any unnecessary contamination are also mentioned in this chapter.

Chapter 4 reports the results for preparing Li-N co-doped diamond films. It also includes the limitations of SIMS analysis and effects of Li_3N on diamond materials.

Chapter 5 reports the result for the theoretical calculation of various Li-N clusters and their electronic structure.

Chapter 6 reports the thermionic emission study of Li-N co-doped diamond with various growth conditions.

Chapter 7 reports the preparation of various metal-oxygen terminations on boron-doped diamond and the analysis of the surface

species using X-ray Photoelectron Spectroscopy (XPS) and Ultraviolet Photoelectron Spectroscopy (UPS).

Chapter 8 summarises the results presented in this thesis and explores the potential for further improvement of Li-N co-doped diamond for electron emission applications.

1.10 References

- [1] P.W. May, *Philos. Trans. R. Soc. London. Ser. A Math. Phys. Eng. Sci.* **358** (2000) 473-495.
- [2] J.S. Lapington, D.P. Thompson, P.W. May, N.A. Fox, J. Howorth, J. Milnes, & V. Taillandier, *Nucl. Instruments Methods Phys. Res. Sect. A* **610** (2009) 253-257.
- [3] C. Wild, & E. Worner, *The CVD Diamond Booklet*, Germany, (2008).
- [4] M.H. Nazare, & A.J. Neves, *Properties, Growth and Applications of Diamond*, INSPEC, (2001).
- [5] J.E. Field, *The Properties of Natural and Synthetic Diamond*, Academic Press, (1992).
- [6] P.W. May, *Science* **319** (2008) 1490-1491.
- [7] E. Sillero, O.A. Williams, V. Lebedev, V. Cimalla, C.-C. Röhlig, C.E. Nebel, & F. Calle, *J. Micromechanics Microengineering* **19** (2009) 115016.
- [8] O.A. Williams, A. Kriele, J. Hees, M. Wolfer, W. Müller-Sebert, & C.E. Nebel, *Chem. Phys. Lett.* **495** (2010) 84-89.
- [9] C.G. Specht, O.A. Williams, R.B. Jackman, & R. Schoepfer, *Biomaterials* **25** (2004) 4073-8.
- [10] O.A. Williams, V. Mortet, M. Daenen, & K. Haenen, *Appl. Phys. Lett.* **90** (2007) 063514.
- [11] O.A. Williams, V. Mortet, M. Daenen, & K. Haenen, *J. Nanosci. Nanotechnology* **8** (2009) 1-4.
- [12] V. Mortet, O.A. Williams, & K. Haenen, *Phys. Status Solidi* **205** (2008) 1009-1020.

- [13] A.A. Melnikov, A. V. Denisenko, A.M. Zaitsev, A. Shulenkov, V.S. Varichenko, A.R. Filipp, V.A. Dravin, H. Kanda, & W.R. Fahrner, *J. Appl. Phys.* **84** (1998) 6127.
- [14] P.W. May, E.M. Regan, A. Taylor, J. Uney, A.D. Dick, & J. McGeehan, *Diamond Relat. Mater.* **23** (2012) 100-104.
- [15] P.-H. Chung, E. Perevedentseva, J.-S. Tu, C.C. Chang, & C.-L. Cheng, *Diamond Relat. Mater.* **15** (2006) 622-625.
- [16] A.P. Puzyr', I.O. Pozdnyakova, & V.S. Bondar', *Phys. Solid State* **46** (2004) 761-763.
- [17] K. Liu, W. Zheng, & C. Wang, *Nanotechnology* **21** (2010) 315106.
- [18] H. Huang, E. Pierstorff, E. Osawa, & D. Ho, *Nano Lett.* **7** (2007) 3305-3314.
- [19] W. Hershey, *The Book of Diamonds*, Hearthsides Press, (1940).
- [20] K.S. Novoselov, Z. Jiang, Y. Zhang, S. V Morozov, H.L. Stormer, U. Zeitler, J.C. Maan, G.S. Boebinger, P. Kim, & A.K. Geim, *Science* **315** (2007) 1379.
- [21] K.S. Kim, Y. Zhao, H. Jang, S.Y. Lee, & J.M. Kim, *Nature* **457** (2009) 706-710.
- [22] Y. Zhang, T.T. Tang, C. Girit, Z. Hao, & M.C. Martin, *Nature* **459** (2009) 820-823.
- [23] S. Iijima, & T. Ichihashi, *Nature* **363** (1993) 603-605.
- [24] S. Iijima, *Nature* **354** (1991) 56-58.
- [25] I.A. Dobrinets, V.G. Vins, & A.M. Zaitsev, *HPHT - Treated Diamonds*, Springer New York, (2013).
- [26] V. Danilenko, *Phys. Solid State* **46** (2004) 595-599.
- [27] M. Daenen, O.A. Williams, J. D'Haen, K. Haenen, & M. Nesládek, *Phys. Status Solidi* **203** (2006) 3005-3010.
- [28] O.A. Williams, J. Hees, C. Dieker, W. Jäger, L. Kirste, & C.E. Nebel, *ACS Nano* **4** (2010).
- [29] A. Krüger, F. Kataoka, M. Ozawa, T. Fujino, Y. Suzuki, A.E. Aleksenskii, A.Y. Vul', & E. Osawa, *Carbon N. Y.* **43** (2005) 1722-1730.
- [30] P.W. May, *Chemical Vapour Deposition - A Route to Microcrystalline, Nanocrystalline. Ultrananocrystalline and Single Crystal Diamond*

- Films, in: A.Ochsner and W. N. Ali Ahmed, Carbon Based Nanomater. Mater. Sceince Found., 1st ed., Trans Tech, Switzerland, (2010): pp. 145-176.
- [31] S. Bhattacharyya, O. Auciello, J. Birrell, J.A. Carlisle, L.A. Curtiss, A.N. Goyette, D.M. Gruen, A.R. Krauss, J. Schlueter, A. Sumant, & P. Zapol, *Appl. Phys. Lett.* **79** (2001) 1441-1443.
- [32] J.E. Butler, Y.A. Mankelevich, A. Cheesman, Jie, & M.N.R. Ashfold, *J. Phys. Condens. Matter* **21** (2009) 364201-364220.
- [33] R. Haubner, *Diam. Relat. Mater. Diam. 2004, 15th Eur. Conf. Diamond, Diamond-Like Mater. Carbon Nanotub. Nitrides Silicon Carbide* **14** (2005) 355-363.
- [34] Q. Liang, C. Yan, Y. Meng, J. Lai, S. Krasnicki, H. Mao, & R.J. Hemley, *Diamond Relat. Mater.* **18** (2009) 698-703.
- [35] A. Tallaire, A.T. Collins, D. Charles, J. Achard, R. Sussmann, A. Gicquel, M.E. Newton, A.M. Edmonds, & R.J. Cruddace, *Diamond Relat. Mater.* **15** (2006) 1700-1707.
- [36] Gemesis lab-created diamonds, <http://gemesis.com/> (2012).
- [37] SCIO Diamond Technology Corporation, <http://www.sciodiamond.com/> (2011).
- [38] Element six, <http://www.e6cvd.com/cvd/page.jsp?pageid=100&lang=en> (2014).
- [39] W. Ahmed, C.A. Rego, R. Cherry, A. Afzal, N. Ali, & I.U. Hassan, *Vacuum* **56** (2000) 153-158.
- [40] P. W. May, M. Davey, K. N. Rosser, & P.J. Heard, *Mater. Res. Soc. Symp. Proc.* **1039** (2007) 101-1039.
- [41] S. Koizumi, M. Kamo, Y. Sato, S. Mita, A. Sawabe, A. Reznik, C. Uzan-Saguy, & R. Kalish, *Diamond Relat. Mater.* **7** (1998) 540-544.
- [42] F.A.M. Koeck, R.J. Nemanich, A. Lazea, & K. Haenen, *Diamond Relat. Mater.* **18** (2009) 789-791.
- [43] W. Gajewski, P. Achatz, O.A. Williams, K. Haenen, E. Bustarret, M. Stutzmann, & J. Garrido, *Phys. Rev. B* **79** (2009) 045206.
- [44] O.A. Williams, M. Nesladek, M. Daenen, S. Michaelson, A. Hoffman, E. Osawa, K. Haenen, & R.B. Jackman, *Diamond Relat. Mater.* **17** (2008) 1080-1088.
- [45] J. Filik, *Spectrosc. Eur.* **17** (2005).

- [46] J. Loader, Basic Laser Raman Spectroscopy, Heyden & Son, London, (1970).
- [47] F.A.M. Koeck, J.M. Garguilo, & R.J. Nemanich, Diamond Relat. Mater. **13** (2004) 2052-2055.
- [48] M. Suzuki, T. Ono, N. Sakuma, & T. Sakai, Diamond Relat. Mater. **18** (2009) 1274-1277.
- [49] F.A.M. Köck, J.M. Garguilo, B. Brown, & R.J. Nemanich, Diamond Relat. Mater. **11** (2002) 774-779.
- [50] P.W. May, J.A. Smith, & Y.A. Mankelevich, Diamond Relat. Mater. **15** (2006) 345-352.
- [51] J. Birrell, J.E. Gerbi, O. Auciello, J.M. Gibson, D.M. Gruen, & J.A. Carlisle, J. Appl. Phys. **93** (2003) 5606.
- [52] F. Koeck, & R. Nemanich, J. Appl. Phys. **112** (2012) 113707.
- [53] S. Matsumoto, Y. Sato, M. Tsutsumi, & N. Setaka, J. Mater. Sci. **17** (1982) 3106-3112.
- [54] J.C. Angus, & C.C. Hayman, Science **241** (1988) 913-21.
- [55] K. V. Ravi, C.A. Koch, H.S. Hu, & A. Joshi, J. Mater. Res. **5** (2011) 2356-2366.
- [56] K. Suzuki, A. Sawabe, H. Yasuda, & T. Inuzuka, Appl. Phys. Lett. **50** (1987) 728.
- [57] M. Kamo, Y. Sato, S. Matsumoto, & N. Setaka, J. Cryst. Growth **62** (1983) 642-644.
- [58] E. Brillas, & C.A. Huitle-Martinez, Synthetic Diamond Films: Preparations, Electrochemistry, Characterization and Applications, John Wiley & Sons, New Jersey, (2011).
- [59] A. Sawabe, & T. Inuzuka, Thin Solid Films **137** (1986) 89-99.
- [60] C.-P. Chang, D.L. Flamm, D.E. Ibbotson, & J.A. Mucha, J. Appl. Phys. **63** (1988) 1744.
- [61] P. Bachmann, D. Leers, & H. Lydtin, Diamond Relat. Mater. **1** (1991) 1-12.
- [62] P.W. May, & Y.A. Mankelevich, J. Phys. Chem. C **112** (2008) 12432-12441.

- [63] J.E. Butler, & I. Oleynik, *Philos. Trans. A. Math. Phys. Eng. Sci.* **366** (2008) 295-311.
- [64] S.J. Harris, *Appl. Phys. Lett.* **56** (1990) 2298.
- [65] B. Stoner, G. Ma, S. Wolter, & J. Glass, *Phys. Rev. B. Condens. Matter* **45** (1992) 11067-11084.
- [66] L. Demuynck, C. Arnault, C. Speisser, R. Polini, & F. Le Normand, *Diamond Relat. Mater.* **6** (1997) 235-239.
- [67] X. Jiang, & C. Jia, *Appl. Phys. Lett.* **1197** (1995) 13-16.
- [68] W.A. Yarbrough, *Applications of Diamond Films and Related Materials*, Elsevier, (1991).
- [69] P.C. Yang, W. Zhu, & J.T. Glass, *J. Mater. Res.* **9** (1994) 1063-1066.
- [70] F.A.M. Köeck, J.M. Garguilo, & R.J. Nemanich, *Diamond Relat. Mater.* **14** (2005) 704-708.
- [71] F.A.M. Koeck, & R.J. Nemanich, *Diamond Relat. Mater.* **14** (2005) 2051-2054.
- [72] A.A. Smolin, V.G. Ralchenko, S.M. Pimenov, T. V. Kononenko, & E.N. Loubnin, *Appl. Phys. Lett.* **62** (1993) 3449.
- [73] D.M. Gruen, O.A. Schenderova, & A.Y. Vul', *Synthesis, Properties and Applications of Ultrananocrystalline Diamond*, Springer, (2005).
- [74] S. Yugo, T. Kimura, & T. Muto, *Vacuum* **41** (1990) 1364-1367.
- [75] X. Jiang, R. Six, C. Klages, & R. Zachai, *Diamond Relat. Mater.* **2** (1993) 407-412.
- [76] S. Yugo, T. Kanai, T. Kimura, & T. Muto, *Appl. Phys. Lett.* **58** (1991) 1036.
- [77] J.-C. Arnault, S. Saada, S. Michaelson, N.K. Hangaly, R. Akhvlediani, & A. Hoffman, *Diamond Relat. Mater.* **17** (2008) 377-382.
- [78] R.J. Hunter, *Zeta Potential in Colloid Science: Principles and Applications*, Academic Press, (1981).
- [79] R. Haubner, & D. Sommer, *Diam. Relat. Mater. Eur. Conf. Diamond, Diamond-Like Mater. Carbon Nanotub. Nitrides Silicon Carbide* **12** (2003) 298-305.
- [80] E.B. Lombardi, A. Mainwood, & K. Osuch, *Phys. Rev. B* **76** (2007) 155203.

- [81] N. Jiang, A. Hatta, & T. Ito, *Japanes J. Appl. Phys.* **37** (1998) L1175-L1177.
- [82] S.A. Kajihara, A. Antonelli, J. Bernholc, & R. Car, *Phys. Rev. Lett.* **66** (1991) 2010.
- [83] A. Mainwood, *J. Mater. Sci. Mater. Electron.* **17** (2006) 453-458.
- [84] J.P. Goss, P.R. Briddon, R. Jones, & S. Sque, *Diamond Relat. Mater.* **13** (2004) 684-690.
- [85] I.M. Buckley-Golder, R. Bullough, M.R. Hayns, J.R. Willis, R.C. Piller, N.G. Blamires, G. Gard, & J. Stephen, *Diamond Relat. Mater.* **1** (1991) 43-50.
- [86] J. Mort, D. Kuhman, M. Machonkin, M. Morgan, F. Jansen, K. Okumura, Y.M. LeGrice, & R.J. Nemanich, *Appl. Phys. Lett.* **55** (1989) 1121.
- [87] R. Kalish, *Carbon N. Y.* **37** (1999) 781-785.
- [88] G. Popovici, T. Sung, & M. Prelas, *J. Chem. Vap. Depos.* **3** (1994) 115-131.
- [89] K. Okano, T. Kiyota, T. Kurosu, & M. Iida, *Diamond Relat. Mater.* **3** (1993) 35-40.
- [90] M.S. Alexander, M.N. Latto, P.W. May, D. Jason Riley, & G. Pastor-Moreno, *Diamond Relat. Mater.* **12** (2003) 1460-1462.
- [91] T. Teraji, K. Arima, H. Wada, & T. Ito, *J. Appl. Phys.* **96** (2004) 5906.
- [92] M. Nesládek, D. Tromson, C. Mer, P. Bergonzo, P. Hubik, & J.J. Mares, *Appl. Phys. Lett.* **88** (2006) 232111.
- [93] K. Thonke, *Semicond. Sci. Technol.* **20** (2003) S20-S26.
- [94] E.A. Ekimov, V.A. Sidorov, E.D. Bauer, N.N. Mel'nik, N.J. Curro, J.D. Thompson, & S.M. Stishov, *Nature* **428** (2004) 542-5.
- [95] G. Popovici, A. Melnikov, V. V Varichenko, T. Sung, M.A. Prelas, R.G. Wilson, & S.K. Loyalka, *J. Appl. Phys.* **81** (1997) 2429-2431.
- [96] N.G. Ferreira, L.L. Mendonça, V.J.T. Airoidi, & J.M. Rosolen, *Diam. Relat. Mater. Eur. Conf. Diamond, Diamond-Like Mater. Carbon Nanotub. Nitrides Silicon Carbide* **12** (2003) 596-600.
- [97] J.-F. Hochedez, P. Bergonzo, M.-C. Castex, . Dhez, O. Hainaut, M. Sacchi, J. Alvarez, H. Boyer, A. Deneuille, P. Gibart, B. Guizard, J.-

- P. Kleider, P. Lemaire, C. Mer, E. Monroy, E. Munoz, P. Muret, F. Omnes, et al., *Diam. Relat. Mater.* **10** (2001) 673-680.
- [98] D. Gandini, E. Mahé, P.A. Michaud, W. Haenni, A. Perret, & C. Comninellis, *J. Appl. Electrochemistry* **30** (2000) 1345-1350.
- [99] E. Brillas, I. Sirés, C. Arias, P.L. Cabot, F. Centellas, R.M. Rodríguez, & J.A. Garrido, *Chemosphere* **58** (2005) 399-406.
- [100] J. Iniesta, P. Michaud, M. Panizza, & G. Cerisola, *Electrochim. Acta* **46** (2001) 3573-3578.
- [101] S. Mitea, M. Zeleznik, M.D. Bowden, P.W. May, N. a Fox, J.N. Hart, C. Fowler, R. Stevens, & N.S. Braithwaite, *Plasma Sources Sci. Technol.* **21** (2012) 022001.
- [102] H. Sternschulte, M. Schreck, B. Stritzker, A. Bergmaier, & G. Dollinger, *Diamond Relat. Mater.* **9** (2000) 1046-1050.
- [103] C. Uzan-Saguy, C. Cytermann, B. Fizgeer, V. Richter, R. Brener, & R. Kalish, *Phys. Status Solidi* **193** (2002) 508-516.
- [104] G. Popovici, R.G. Wilson, T. Sung, M.A. Prelas, & S. Khasawinah, *J. Appl. Phys.* **77** (1995) 5103-5106.
- [105] S. Praver, C. Uzan-Saguy, G. Braunstein, & R. Kalish, *Appl. Phys. Lett.* **63** (1993) 2502-2504.
- [106] J. Mort, M.A. Machonkin, & K. Okumura, *Appl. Phys. Lett.* **59** (1991) 3148-3150.
- [107] S. Jin, & T.D. Moustakas, *Appl. Phys. Lett.* **65** (1994) 403-405.
- [108] V. Baranauskas, B.B. Li, A. Peterlevitz, M.C. Tosin, & S.F. Durrant, *J. Appl. Phys.* **85** (1999) 7455-7458.
- [109] J.R. Petherbridge, P.W. May, G.M. Fuge, G.F. Robertson, K.N. Rosser, & M.N.R. Ashfold, *J. Appl. Phys.* **91** (2002) 3605-3613.
- [110] R. Kalish, A. Reznik, C. Uzan-Saguy, & C. Cytermann, *Appl. Phys. Lett.* **76** (2000) 757.
- [111] G. Popovici, & M.A. Prelas, *Diamond Relat. Mater.* **4** (1995) 1305-1310.
- [112] S. Koizumi, M. Kamo, Y. Sato, H. Ozaki, & T. Inuzuka, *Appl. Phys. Lett.* **71** (1997) 1065-1067.
- [113] K. Haenen, K. Meykens, M. Nesládek, G. Knuyt, L.M. Stals, T. Teraji, S. Koizumi, & E. Gheeraert, *Diamond Relat. Mater.* **9** (2000) 952-955.

- [114] S. Koizumi, T. Teraji, & H. Kanda, *Diamond Relat. Mater.* **9** (2000) 935-940.
- [115] K. Haenen, A. Lazea, J. Barjon, J. D'Haen, N. Habka, T. Teraji, S. Koizumi, & V. Mortet, *J. Phys. Condens. Matter* **21** (2009) 364204.
- [116] R. Kalish, *Carbon N. Y.* **37** (1999) 781-785.
- [117] M. Nesládek, K. Haenen, J. D'Haen, S. Koizumi, & H. Kanda, *Phys. Status Solidi* **199** (2003) 77-81.
- [118] H. Ken, L. Andrada, B. Julien, D. Jan, H. Nada, T. Tokuyuki, K. Satoshi, & M. Vincent, *J. Phys. Condens. Matter* **21** (2009) 364204.
- [119] K. Okano, & K. Gleason, *Electron. Lett.* **31** (1995) 74-75.
- [120] M. Nesladek, *Semicond. Sci. Technol.* **20** (2005) R19-R27.
- [121] E.B. Lombardi, & A. Mainwood, *Diamond Relat. Mater.* **17** (2008) 1349-1352.
- [122] E.B. Lombardi, & A. Mainwood, *Phys. B Condens. Matter* **401-402** (2007) 57-61.
- [123] J.P. Goss, & P.R. Briddon, *Phys. Rev. B* **75** (2007) 75202.
- [124] R. Zeisel, C.E. Nebel, M. Stutzmann, H. Sternschulte, M. Schreck, & B. Stritzker, *Phys. Status Solidi* **181** (2000) 45-50.
- [125] C. Cytermann, R. Brener, & R. Kalish, *Diamond Relat. Mater.* **3** (1994) 677-680.
- [126] R. Job, A. Denisenko, A. Zaitsev, W.R. Fahrner, & M. Werner, *Diamond Relat. Mater.* **5** (1996) 757-760.
- [127] G. Popovici, T. Sung, S. Khasawinah, M.A. Prelas, & R.G. Wilson, *J. Appl. Phys.* **77** (1995) 5625-5629.
- [128] M. Nesládek, K. Meykens, L.M. Stals, C. Quaeyhaegens, M. D'Olieslaeger, T.D. Wu, M. Vanecek, & J. Rosa, *Diamond Relat. Mater.* **5** (1996) 1006-1011.
- [129] A. Namba, Y. Yamamoto, H. Sumiya, Y. Nishibayashi, & T. Imai, *Process for producing n-type semiconductor diamond and n-type semiconductor diamond*, US 2006/0177962 A1, (2006).
- [130] M. Born, & R. Oppenheimer, *Ann. Phys.* **84** (1927) 457.
- [131] A. Shih, J. Yater, P. Pehrsson, J. Butler, C. Hor, & R. Abrams, *J. Appl. Phys.* **82** (1997) 1860-1867.

- [132] A.T. Sowers, B.L. Ward, S.L. English, & R.J. Nemanich, *J. Appl. Phys.* **86** (1999) 3973-3982.
- [133] J.B. Cui, J. Ristein, M. Stammer, K. Janischowsky, G. Kleber, & L. Ley, *Diamond Relat. Mater.* **9** (2000) 1143-1147.
- [134] M.W. Geis, J.C. Twichell, N.N. Efremow, K. Krohn, & T.M. Lyszczarz, *Appl. Phys. Lett.* **68** (1996) 2294.
- [135] P.W. May, J.C. Stone, M.N.R. Ashfold, K.R. Hallam, W.N. Wang, & N.A. Fox, *Diamond Relat. Mater.* **7** (1998) 671-676.
- [136] M. Kataoka, C. Zhu, F.A.M. Köeck, & R.J. Nemanich, *Diamond Relat. Mater.* **19** (2010) 110-113.
- [137] P. Shefsiek, *IEEE Trans. Plasma Sci.* **38** (2010) 2041-2047.
- [138] F.A.M. Koeck, & R.J. Nemanich, *Diamond Relat. Mater.* **18** (2009) 232-234.
- [139] F.A. M. Koeck, R.J. Nemanich, Y. Balasubramaniam, K. Haenen, & J. Sharp, *Diamond Relat. Mater.* **20** (2011) 1229-1233.
- [140] K.G. Hernqvist, M. Kanefsky, & N.F. H., *RCA Rev.* **19** (1958) 224.
- [141] B.C. Djubua, & N.N. Chubun, *IEEE Trans. Electron Devices* **38** (1991) 2314-2316.
- [142] W.F. Paxton, T. Wade, M. Howell, N. Tolk, W.P. Kang, & J.L. Davidson, *Phys. Status Solidi* **209** (2012) 1993-1995.
- [143] O.W. Richardson, *Thermionic Emission From Hot Bodies*, Wexford College Press, (2003).
- [144] F.A.M. Koeck, & R.J. Nemanich, *Diam. Relat. Mater. Appl. Diam. Conf. 2005 - ADC/NanoCarbon 2005* **15** (2006) 217-220.
- [145] W.F. Paxton, M. Howell, W.P. Kang, & J.L. Davidson, *J. Vac. Sci. Technol. B Microelectron. Nanom. Struct.* **30** (2012) 021202.
- [146] W.F. Paxton, A. Steigerwald, M. Howell, N. Tolk, W.P. Kang, & J.L. Davidson, *Appl. Phys. Lett.* **101** (2012) 243509.
- [147] F. Köck, J. Garguilo, & R. Nemanich, *Diamond Relat. Mater.* **10** (2001) 1714-1718.
- [148] Y. Coffinier, S. Szunerits, B. Marcus, R. Desmet, O. Melnyk, L. Gengembre, E. Payen, D. Delabouglise, & R. Boukherroub, *Diamond Relat. Mater.* **16** (2007) 892-898.

- [149] S. Szunerits, & R. Boukherroub, *J. Solid State Electrochem.* **12** (2007) 1205-1218.
- [150] J. Ristein, M. Riedel, M. Stammler, B.F. Mantel, & L. Ley, *Diamond Relat. Mater.* **11** (2002) 359-364.
- [151] J. Van der Weide, & R. Nemanich, *Phys. Rev. B* **49** (1994).
- [152] W. Pickett, *Phys. Rev. Lett.* **73** (1994).
- [153] D. Takeuchi, S.G. Ri, N. Tokuda, & S. Yamasaki, *Diamond Relat. Mater.* **18** (2009) 206-209.
- [154] D. Takeuchi, S.G. Ri, H. Kato, C.E. Nebel, & S. Yamasaki, *Phys. Status Solidi* **202** (2005) 2098-2103.
- [155] R.E. Thomas, R.A. Rudder, & R.J. Markunas, *J. Vac. Sci. Technol. A Vacuum, Surfaces, Film.* **10** (1992) 2451-2457.
- [156] C.K. Fink, & S.J. Jenkins, *J. Phys. Condens. Matter* **21** (2009) 264010.
- [157] K. Larsson, & S. Lunell, *J. Phys. Chem. A* **101** (1997) 76-82.
- [158] K.M. O'Donnell, T.L. Martin, N.A. Fox, & D. Cherns, *Phys. Rev. B* **82** (2010) 115303.
- [159] K. M. O'Donnell, & T. L. Martin, *Mater. Res. Soc. Symp. Proc.* **1282** (2011).
- [160] G. Popovici, A.A. Melnikov, V.S. Varichenko, S. Khasawinah, T. Sung, M.A. Prelas, A.B. Denisenko, N.M. Penina, V.A. Martinovich, E.N. Drozdova, A.M. Zaitsev, W.R. Fahrner, J.W. Farmer, H. White, & J. Chamberlain, *Diamond Relat. Mater.* **5** (1996) 761-765.
- [161] K.P. Loh, X.N. Xie, S.W. Yang, J.S. Pan, & P. Wu, *Diamond Relat. Mater.* **11** (2002) 1379-1384.
- [162] J. Van der Weide, & R. Nemanich, *J. Vac. Sci. Technol. B Microelectron. Nanom. Struct.* **10** (1992) 1940-1943.
- [163] P.K. Baumann, & R.J. Nemanich, *J. Appl. Phys.* **83** (1998) 2072.

Chapter 2: Instrumentation and Techniques

2.1 Introduction

This chapter discusses the basic concept, standard procedure and data analysis for the related instrumentation or techniques used during the study. The aim of this chapter is to provide a brief understanding on how the instruments work or how the data is processed and reported in the following chapters.

2.2 Hot Filament Chemical Vapour Deposition (HFCVD) System

A custom-built Hot-Filament Chemical Vapour Deposition (HFCVD) system was used to prepare all the diamond films grown in this study. Figure 2.1 shows a schematic diagram of the HFCVD system used at the University of Bristol. The system consists of three main components; the gas system, reaction chamber and process gases exhaust.

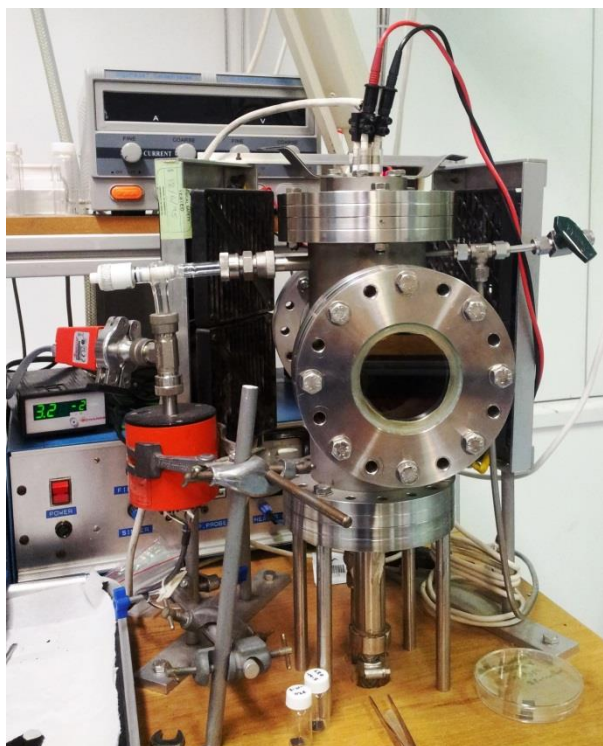
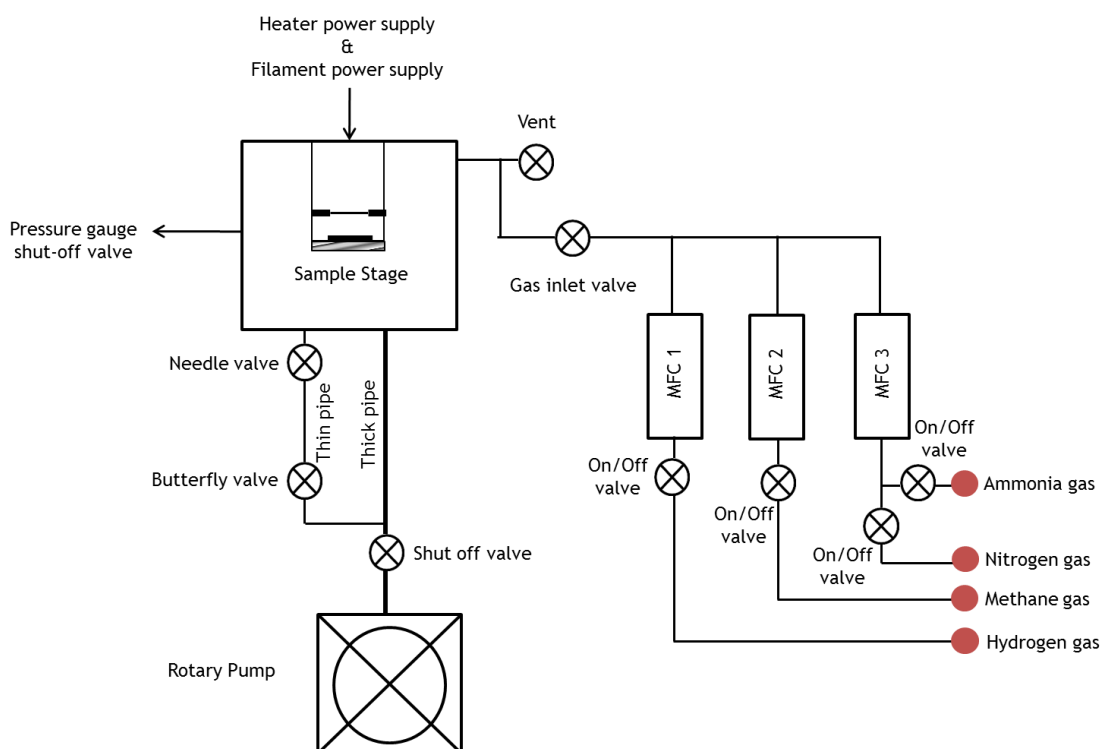


Figure 2.1: Schematic diagram (above) and photograph (below) of the HFCVD in the School of Chemistry, University of Bristol.

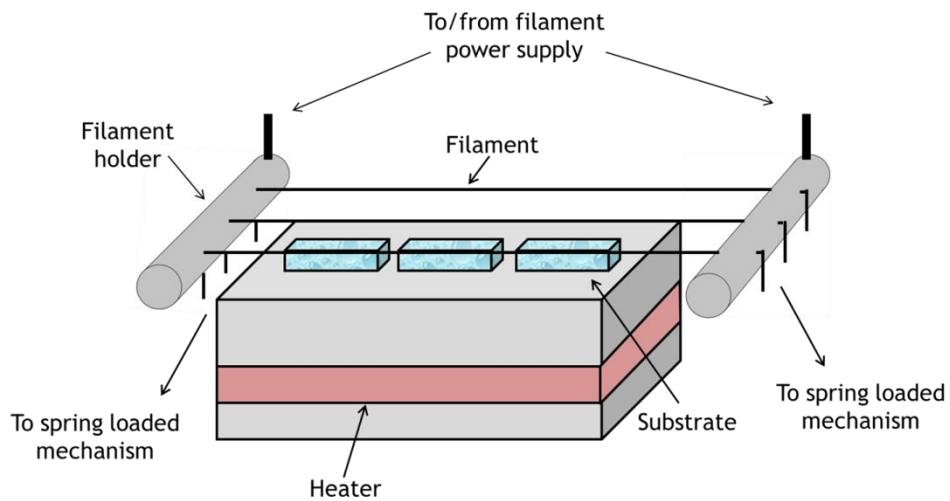
The chamber is a stainless steel vacuum vessel attached to a rotary pump by means of two pipes. A viewport at the front allows the user to

see inside the chamber during operation. The substrate holder assembly is mounted onto the removable top flange, which contains the electrical feedthroughs to power both the substrate heater and filament. Two pressure gauges are attached to a side-arm on the chamber: a capacitance manometer (Vacuum General, CMLB-21, 0-100 torr) to measure the pressure during CVD, and a Pirani (Edwards, PG100-XM, 0-1 torr) to measure the base pressure. The process gas mixture enters the chamber by means of another sidearm, which also incorporates a vent valve to allow the system to be brought up to atmosphere for sample removal.

Pumping is achieved with a rotary pump (Leybold Vacuum GMBH, D10E) which attains a base pressure of ~18 mtorr. To achieve base pressure in minimal time, pumping occurs through the thick pipe. For CVD, this pipe is blocked, and pumping occurs through the thinner pipe. This makes it easier to control the pressure in the chamber by use of a manual needle valve which partially obstructs the thin pipe. Exhaust gases (mostly hydrogen) are removed from the pump into a pumped extract and diluted 1000× by mixing with air before being expelled out of a chimney in the roof.

Figure 2.2 illustrates the sample stage inside the HFCVD system. The stage consists of a Mo plate, stainless steel platen (housing an internal Ni/Cr coil) and filament holder. The platen was heated by passing 4 A DC from a home-built power supply through the NiCr resistance wire. The thin Mo plate on top of the platen diffuses the heat evenly throughout the sample stage while protecting the platen and coil assembly from the direct radiation of the filament and reactive CVD gas mixture. The platen temperature was previously calibrated using a thermocouple, and found to reach ~400°C without the filaments being turned on.

Tantalum wires (Advent Research Material Ltd, 99.9% purity, 0.25 mm diameter) were used as the filaments and the distance between the filaments and the substrate was fixed at 3 mm.



(a)



(b)

Figure 2.2: (a) Schematic diagram of the sample stage and (b) photograph of the sample stage taken out from the HFCVD chamber.

Three filaments were held by the filament holder using a spring loaded mechanism. Each filament was attached to a spring that was shielded by hollow curved-stainless steel tube to protect the spring from the reactive gases during the growth process. A small amount of tension was applied to the spring by pulling the other end of the filament, which was then secured with another hollow stainless tube and locked with a bolt. At high temperature, the filament will expand due to the heat and the expansion will be taken up by the spring. This ensures that the filament

will remain straight and taut, and will not bend, droop, or distort during the CVD run.

The filaments were supplied with 25 A of DC current from an external power supply (Digimess, SM3040) using the electrical feedthroughs. The three filaments were wired in parallel, with each sharing 1/3rd of the 25 A current at a common applied voltage of ~10 V. The arrangement allows a uniform deposition area of ~two 1 cm² samples side-by-side.

A carburisation process may occur during diamond growth due to the reaction of the filament surface with carbon species. This process converts the Ta filament surface into TaC. As a result, the filament become brittle after each diamond growth cycle and usually break during the cooling down process. Other metals, such as Re, could be used to replace Ta because Re will not form a carbide. However, the price of Re wire is much more expensive compared to Ta and so is only used for special deposition experiments where carburisation might be an issue.

All process gases used in this study except NH₃ gas were stored in the gas cylinder cabinet in the Gas Room. NH₃ gas (Sigma-Aldrich, Anhydrous - lecture bottle, 99.99%) was stored in a lecture bottle and attached next to the HF-CVD reactor. H₂ gas (Air Liquide, CP grade, 99.995%), CH₄ gas (BOC, Research grade, 99.99%) and N₂ gas (BOC, OFN, CP grade, 99.99%) were transported using stainless gas lines from the gas cylinders in the Gas Room into the HF-CVD reactor. The flow rate of the gases was controlled by individual mass flow controllers, MFC (Tylan, FC260). MFC1 (see Figure 2.1) was calibrated with H₂ gas while MFC2 and MFC3 were calibrated using N₂ gas. These were operated *via* an MFC control box which allowed the flow rate of each gas (in standard cubic cm per minute, sccm) to be automatically controlled and monitored.

2.2.1 Standard Diamond Growth Condition

Diamond films were grown in a hydrogen rich environment with a small amount of CH₄ gas and/or dopant precursors such as N₂ or NH₃ present. Table 2.1 shows the standard gases used in this study with their respective mass flow controller (MFC) offset, gas correction factor, gas volume recorded on the MFC controller in standard cubic centimetre per minute (sccm) and percentage of each gas relative to the H₂ atmosphere.

Table 2.1: Standard gases used for growing diamond films with their respective MFC offset, gas correction factor, gas volume shown on the MFC controller and the percentage of the gases relative to the H₂ atmosphere.

Gases	MFC offset	Gas Correction Factor	Gas volume (on MFC controller)	Percentage relative to H ₂ atmosphere
H ₂	-6.00	1.00	200.00	-
CH ₄	-0.34	0.72*	2.00	0.82%
N ₂	-0.17	1.00	0.75	0.45%
NH ₃	-0.17	0.74*	0.75	0.33%

*relative to the N₂ gas

A silicon wafer (100) (Si Mat, B-doped, 1-30 ohm, one -side polished) was used as the main substrate in this study. These were then cleaved into substrates about 1 cm² in size. Before CVD, the substrates were manually abraded with 1-3 μm diamond powder (Diadust) in order to scratch the surface and to seed it with diamond particles. The substrate was then placed into the reaction chamber. The HFCVD system was pumped down to a base pressure of 1.8×10^{-2} torr. Prior to the growth process, the sample stage was heated up resistively using the coil for 15 to 20 minutes to ~400°C. Next, for standard growth of MCD films, 0.82% of CH₄/H₂ gases were passed into the chamber. The pressure of the reaction chamber was set at 20 torr. The filament power supply was set to 25 A. From previous calibration using a 2-colour pyrometer the temperature of the filament at

the current was known to be between 2100 K to 2300 K. These conditions resulted in a growth rate of $\sim 0.5 \mu\text{m h}^{-1}$ of MCD film.

2.3 Laser Raman Spectroscopy

The laser Raman spectrometer depicted in Figure 2.3 (Renishaw 2000) was used in this study. The instrument consists of three types of laser with different excitation wavelengths; 325 nm (UV, He:Cd), 514 nm (Green, Ar⁺) and 785 nm (IR, diode laser).

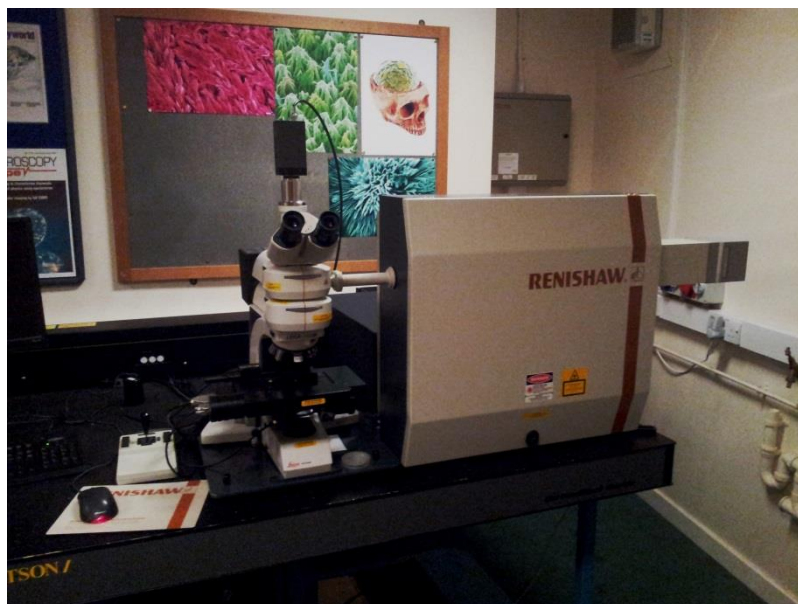


Figure 2.3: Laser Raman Spectroscopy instrument in Diamond Laboratory, School of Chemistry, University of Bristol

When monochromatic light illuminates a solid material, it scatters. When this scattered light is passed through a spectrometer, a series of emission lines are detected [1]. The highest intensity line observed is due to Rayleigh scattering, and this elastic scattering scattered in all directions observed at the same wavenumber as the light source excitation. Rayleigh scattering is usually removed using a filter. Raman scattering is light

scattered inelastically by the atoms/molecules, and is also generated but at much smaller intensity compared to Rayleigh scattering. This Raman effect gives information regarding the vibrational energy levels, rotational energy levels and phonon behaviour of the structure of interest. Raman scattering creates emission lines on both sides of the Rayleigh line, symmetrically. The lines on the lower frequency side are called Stokes shifted and have high intensity. While, the lines observed at higher frequency side are called anti-Stokes shifted and have lower intensity. All of the spectrum lines observed using Raman spectrometry are generated from the Stokes line, and result in some of the laser energy being absorbed by the diamond into particular phonons.

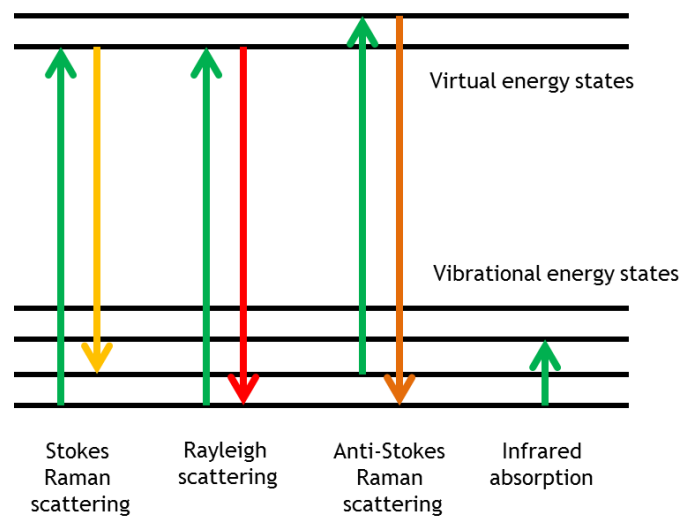


Figure 2.4: Energy level diagram showing the states involved in Raman signal.

For diamond film analysis, different excitation wavelengths of laser were essential. UV excitation is sensitive to sp^3 C (diamond) giving a strong peak at 1332 cm^{-1} while green excitation and IR excitation are more favourable to sp^2 C peaks between 1550 cm^{-1} to 1580 cm^{-1} [2,3]. Diamond is >65% transparent between 400 nm - $100\text{ }\mu\text{m}$ [4]. This transparency reduces the scattering effect during Raman spectroscopy measurement, so the sp^3 C peak detection is less sensitive. In contrast, green and IR excitation

wavelength, are sensitive towards sp^2 C peak due to the higher scattering effect on low-transparency graphite material. Thus, for determination of the quality of the MCD films in this study, UV excitation was used to identify the presence of small amounts of diamond in a large sp^2 background while green/IR excitation was used to study sp^2 impurities in a largely diamond material.

2.4 Scanning Electron Microscopy (SEM)

SEM is a powerful tool to characterise surface morphology. Figure 2.5 shows two SEM instruments at the University of Bristol. The first (JEOL JSM 5600LV) is a low resolution (100 nm) machine used for day-to-day microscopy. The second (JEOL JSM 6330F) uses a field emission gun (FEG) as its electron source, and is very high resolution (<10 nm) microscope used for studying samples <100 nm in size.

Both systems work by focusing electron beam on to the sample in vacuum, which generates secondary electrons from the surfaces. These secondary electrons were passed through filters, and the current detected was analysed. By rastering the beam across the sample and monitoring the current, a real-time image of the sample surface can be seen on the monitor.

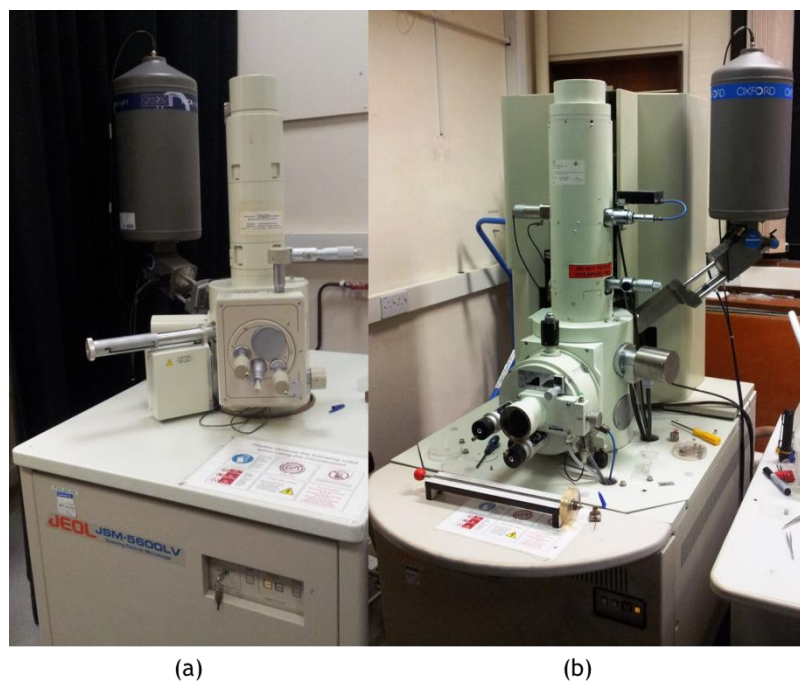


Figure 2.5: Electron microscopes, (a) JEOL JSM 5600LV and (b) JEOL JSM 6330F in the Electron Microscope Unit, School of Chemistry, University of Bristol.

These instruments were used to observe the morphology of CVD diamond films, especially the type of facets produced on the diamond films and the morphology changes with respect to the dopant concentrations. The crystal qualities observed were compared with Raman spectra obtained from similar samples.

All diamond samples were analysed using 13 kV external voltages with spot size of 21 nm, working distance of 15 mm and current was maintained at 12 μA .

2.5 Energy-dispersive X-ray Spectroscopy (EDX)

Energy-dispersive X-ray spectroscopy is another type of analytical technique used to investigate the elemental composition of a solid sample. The fundamental concept in this technique is the unique atomic structure in each element. In this study, the EDX detector was attached to SEM

instrument. When the primary electron beam hits the sample surface, core electrons can be knocked out of surface atoms leaving a vacancy. This vacancy can be filled by relaxation of a higher-energy electron. The energy difference between the two electron levels is released in the form of an X-ray with wavelength specific to the individual element. However, due to the material used to make the window used for the detector, this instrument cannot detect elements with atomic number less than or equal to three (*i.e.* H, He or Li). Furthermore, due to the residual air in the chamber (even at high vacuum), it was problematic to analyse oxygen or nitrogen contents properly.

An Oxford Instruments EDX analyser (INCAx-sight) was used in the experiment as illustrated in Figure 2.6. The analyser was attached to the JEOL JSM 5600LV SEM instrument. Measurements were taken immediately after recording the morphology of the diamond films, using the parameters: 20 kV electron gun external voltage, spot size 40 nm, working distance 15 mm, and current 12 μ A.



Figure 2.6: EDX analyser attached to JEOL JSM 5600LV in the Electron Microscope Unit, School of Chemistry, University of Bristol.

2.6 Secondary Ion Mass Spectroscopy (SIMS)

Secondary ion mass spectroscopy (SIMS) was used to characterise the diamond samples with the help of Dr. Peter Heard from the Interface Analysis Centre (IAC), University of Bristol. SIMS utilised a beam of primary ions (Ga^+) to etch the material surface, and to sputter off secondary ions composed of fragments of the surface composition [5]. The secondary ions were collected by a mass spectrometer and mass separated using a magnetic field. The continuous etching process by Ga^+ ions creates a depth profile analysis of the material. This analysis was crucial to identify different layers inside the materials (metallic coating, diamond film or

silicon) and the position of the incorporated dopant atoms inside diamond films.

Even though qualitative analysis was the primary usage of SIMS, certain modifications were done to obtain quantitative data. In this study, it was essential to know the concentrations of dopant atoms. To do so, the SIMS signal needed to be calibrated for each dopant type. A specially commissioned SCD sample implanted with a known concentration of dopant (Li or N) was prepared by the University of Surrey, and then used as calibration samples for the quantitative analysis using SIMS. Detail of these processes are discussed further in Appendix A (Li atoms) and Appendix B (N atoms).

When using SIMS to analyse diamond films containing Li, N (and H at the grain boundaries), the different species were detected in different ways. The Li signal was detected as Li^+ with a minimum detection limit of $2.03 \times 10^{17} \text{ cm}^{-3}$. The N signal was detected as CN^- , however, because CVD diamond may contain hydrogen at the grain boundaries, it is possible that some of the CN^- SIMS signal at mass 26 might be due to contributions from C_2H_2^- . To determine the magnitude of this contribution, an N-doped CVD diamond film was deposited onto an undoped diamond film, and the relative signal at mass 26 compared for both layers in the SIMS depth profile as depicted in Figure 2.7. The mass-26 signal for the undoped layer was lower than the limit of detection for N detection at $1.15 \times 10^{19} \text{ cm}^{-3}$, while the signal for the N-doped layer was ~100 times higher. Thus, it was relatively easy to distinguish the CN^- signal from the background due to C_2H_2^- . All graphs plotted in this study were plotted after subtracting the C_2H_2 background signal to obtain the concentration of N atoms with an uncertainty of ~5%.

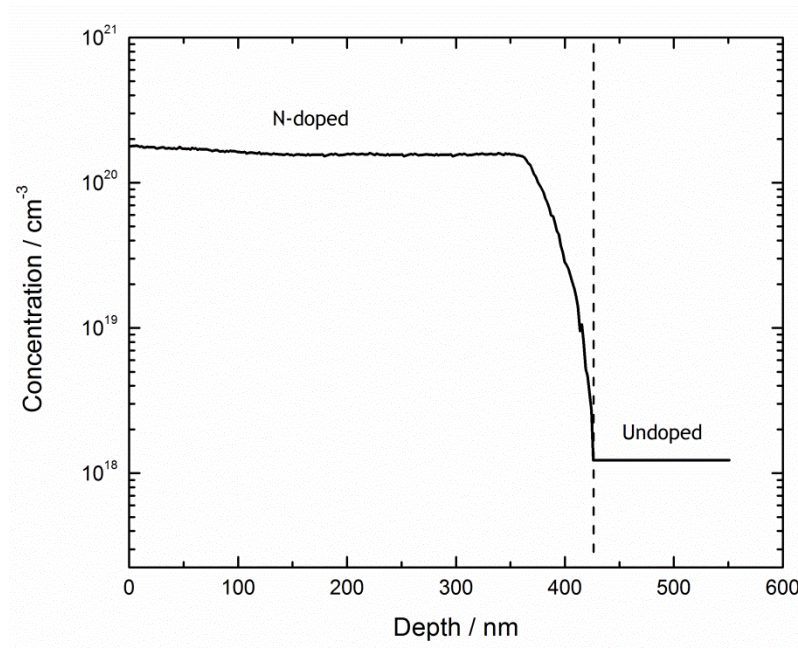


Figure 2.7: Depth profile analysis of an N-doped CVD diamond film that was deposited onto an undoped diamond film. The concentration of undoped diamond film was below the detection limit of the instrument ($1.15 \times 10^{19} \text{ cm}^{-3}$).

Another potential problem with using SIMS for depth profiling on non-flat samples is that large variations in the surface roughness might affect the sharpness of any layer boundaries. This problem is machine-dependent: etching/depth-profiling in some SIMS instruments planarises the initial surface morphology making the problem negligible, whereas in some SIMS instruments, the height difference of surface features becomes magnified as etching proceeds, severely broadening the layer profiles. To determine if this was a problem in our SIMS, two CVD films were grown with approximately the same thickness (3 μm) but with different morphologies. The first was an MCD film with surface grain size (and hence approximate r.m.s. surface roughness) of $\sim 1 \mu\text{m}$ as measured by SEM. The second was a smoother nanocrystalline diamond (NCD) film with grain size and surface roughness $\sim 100 \text{ nm}$. Both films were grown onto a Si substrate known to support a native-oxide layer of thickness $\sim 100 \text{ nm}$. SIMS depth profiles were performed on both samples depicted in Figure 2.8, and the full-width half-maximum of this oxide layer was measured after etching through the overlying diamond film. The two measured values were 98.4 nm and

103.4 nm for the MCD and NCD film, respectively, which is the opposite of what might be expected if surface roughness blurred layer boundaries. Therefore, we conclude that in our SIMS system the initial surface morphology is not a problem when measuring the sharpness of layer boundaries and the reproducibility of the system due to SIMS mixing and other effects is ± 10 nm in diamond samples.

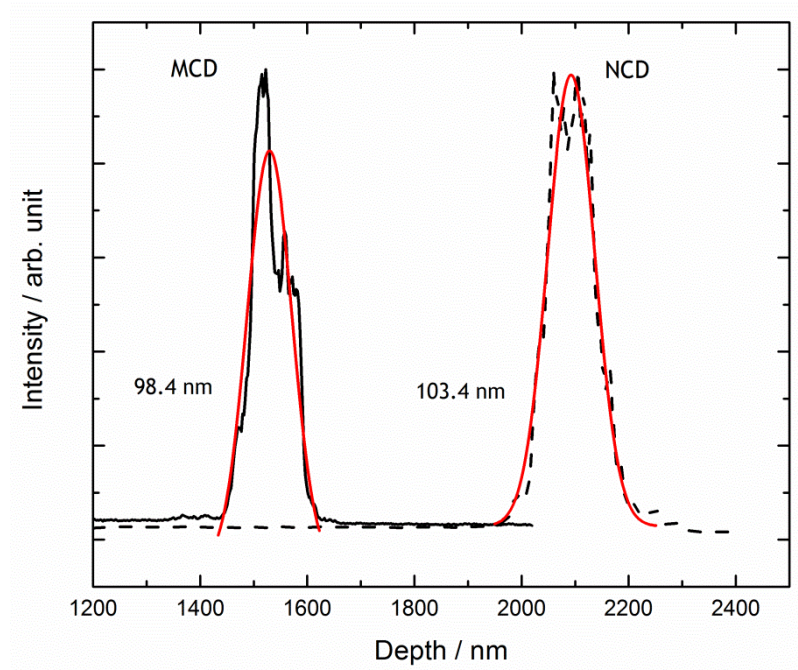


Figure 2.8: SIMS analysis on O^- at the oxide interface layer between the diamond film and silicon substrate.

2.7 Electron Emission Analysis

Electron emission is a study whereby electrons released from the surface of a material are captured and analysed. Electrons can be emitted as a result of an applied high positive potential (field emission), or high temperature (thermionic emission) or bombardment with a high energy particle beam (secondary electron emission). All electron emission analysis in this study were measured at Arizona State University (ASU), Tempe,

Arizona, USA with help from Prof. Dr. Robert Nemanich, Dr. Tianyin Sun and Mr. Franz Köeck.

2.7.1 X-Ray Photoelectron Spectroscopy (XPS)

X-ray photoelectron spectroscopy is a technique that utilises an x-ray source to determine the elemental species present at a surface and sub-surface region (1 - 10 nm). This method is surface sensitive therefore any surface contamination will affect the data interpretation. Hence, all measurements were done in ultra-high vacuum (UHV) conditions with a base pressure of 1×10^{-9} torr. XPS is a non-destructive test as the X-ray source only excites the electrons in the material without changing the chemical composition or structure of the material.

High energy X-rays produced by an X-ray source (typically a Mg $K\alpha$ source at 1256.6 eV photon energy correspond to wavelength of 0.987 nm) supply enough energy to the core electrons in the surface atoms that the electrons are emitted. The binding energy of the electrons in elements was determined using Equation 2.1.

$$E_{binding} = E_{photon} - (E_{kinetic} + \varphi) \quad (2.1)$$

$E_{binding}$ is the binding energy of the electron, E_{photon} is the energy of the X-ray source used, $E_{kinetic}$ is the kinetic energy of the electron measured by the instrument and φ is the work function of the detector used. The φ of the detector always remains constant after the calibration process. The binding energy is characteristic of a particular element, although slight shifts in energy can occur due to variations in chemical bonding (e.g. sp^2 or sp^3 C).

XPS analysis was performed using the 1256.6 eV Mg $K\alpha$ line of a VG XR3E2 dual anode source and a VG microtech Clam II analyser operated at a resolution of 0.1 eV. Initially, a low resolution, wide energy range 'survey scan' was performed on each sample from 0 eV to 600 eV to identify the elements present in the sample. This was crucial because any surface contamination was easily spotted during this scan. Next, individual element scans were taken with a 20 eV scan window at a resolution of 0.1 eV. 20 scan accumulations were sufficient to improve the signal-to-noise ratio for both C and O. Some metal elements required up to 60 accumulation scans to confirm the present of the element on the diamond surface. Spectra collected by XPS was referenced to the Fermi level of the metallic sample holder in which were calibrated against a standard gold sample.

2.7.2 Ultraviolet Photoelectron Spectroscopy (UPS)

Ultraviolet Photoelectron Spectroscopy (UPS) initially is a technique used to investigate the molecular-orbital energies of molecules from the kinetic-energy spectra of the photoelectron produced [6]. The advancement of UPS technique created an opportunity to investigate negative electron affinity (NEA) on diamond surface [7-9]. A He discharge lamp generated He I ions and UV light at 21.2 eV which illuminated the sample surface.

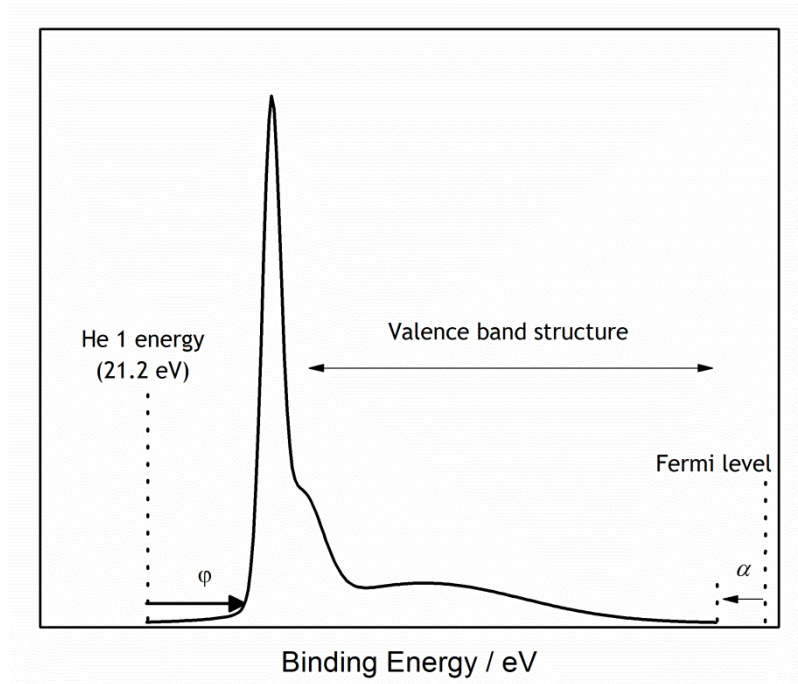


Figure 2.9: Example of a UPS spectrum of a diamond film.

Figure 2.9 shows an example photoelectron spectrum of diamond film obtained from the UPS instrument. The cut-off energy on the right of the graph is the value between the valence band maximum (VBM) of diamond and the Fermi level, denoted as, α . The value between the He I energy and the cut-off energy on the left of the spectrum is the work function, φ of the material. Diamond can form an NEA or positive electron affinity (PEA) surface. The affinity can be calculated using Equation 2.2 below.

$$\chi = \varphi + \alpha - E_g \quad (2.2)$$

where χ is the electron affinity, E_g is the band gap of diamond (5.45 eV), α is the difference between the Fermi level and valence band maximum and φ is the work function of the material obtained from the photoelectron spectrum. If the value of χ is positive, the diamond possesses a PEA surface, and if χ is negative, the diamond has an NEA surface.

$$E_V = E_{CL} - E_{VBM} \quad (2.3)$$

Band-offset analysis (discussed in Chapter 7) was done based on the analysis method derived by Koide and co-workers [10]. This analysis determines the band bending of the VBM in bulk material towards the surface of the material. When C atoms on the diamond surface form new bonds with surface species (*i.e.* H, O, Br or Li), the binding energy observed for the C 1s core peak in XPS shifts. This shift can be calculated using Equation 2.3. This equation was used to determine the valence band offset (E_V) after the introduction of metal-oxygen surfaces in Chapter 7. E_{CL} is the value for the C 1s core peak of the diamond sample obtained from XPS measurements and E_{VBM} is the valence band maximum of the diamond film measured using UPS.

UPS spectra were obtained using He I line at 21.2 eV generated from a He discharge lamp. The spectra were recorded by a VSW HA50 hemispherical analyser and a VSW HAC300 lens controller that operated at a resolution of 0.1 eV. A negative bias (8 V) was applied to the substrate to overcome the work function of the analyser. Spectra collected by UPS were referenced to the Fermi level of the metallic sample holder, which itself was calibrated against a standard gold sample. Two set of analyses were done using UPS. The first analysis was a survey scan from 0 eV to 21.2 eV to obtain the electronic structure of the sample. The scan was repeated five times to ensure the consistency of the data. The second analysis focused on the lower energy regime. This was important to deduce the VBM value of the sample. Higher resolution (0.15 eV) with a slower scan rate was employed to achieve higher accuracy during this analysis.

2.7.3 Thermionic Emission Apparatus

Thermionic emission converts heat into electricity energy. The heat was used to excite electron from the material into the vacuum level, later collected by an anode (collector) that was separated from the hot cathode by small vacuum gap (0.1 - 1.0 mm). The technique utilised the Richardson-Dushman equation shown in Equation 2.4

$$J = A_R T^2 e^{\frac{-\phi}{kT}} \quad (2.4)$$

where J is the current density measured by the instrument, A_R is the Richardson constant, T is the working temperature, ϕ is the work function of the material and k is the Boltzmann constant.

Thermionic emission measurement was done in a different laboratory at ASU. This setup was not connected to another surface analysis instrument *via* the ultra-high vacuum transfer line. Figure 2.10 illustrates the thermionic emission apparatus used to measure the thermionic emission properties of Li-N co-doped diamond film (Chapter 6) at ASU. The setup consists of a UHV with base pressure 1.8×10^{-10} torr. The working pressure of the chamber during the measurement was $\sim 2.0 \times 10^{-8}$ torr. The sample stage inside the chamber was radiatively heated by a W coil. The anode (collector) was a mirror-polished Mo disk which was movable in all three spatial directions. The anode was cooled with a 20 mm copper rod attached to the back of the anode. The electrical contact of the anode was made through the back of the Mo disk. The current produced was measured using Keithley 2000 and was connected to external power supply (Mastech, HY3003D) in series in the electrical circuit. The surface area of diamond sample exposed to the anode was 0.50 cm^2 .

The sample was mounted onto a custom-made sample holder using Ta wires, and inserted into the chamber. The sample holder and the sample

stage were made from Mo metal. The diamond-based emitter (cathode) was grounded through the sample stage. The distance between the anode and cathode was fixed at 0.75 mm. Degassing was done at 120°C for 30 minutes to remove any trapped gases and moisture. Then the temperature was increased to 330°C to begin the thermionic emission experiment. The temperature was increased slowly and the emission current was recorded using a Kiethley 2000 at every 10°C interval. The first set of experiments increased the temperature to 450°C in order to clean the surface of any gases that were adsorbed when the sample was exposed in air during the sample transport and preparation processes. After the sample was cooled down to approximately 250°C, the second run started and finished after the sample temperature reached 620°C. The temperature was recorded using a two-colour pyrometer and calibrated against the thermocouple attached under the cathode (emitter).

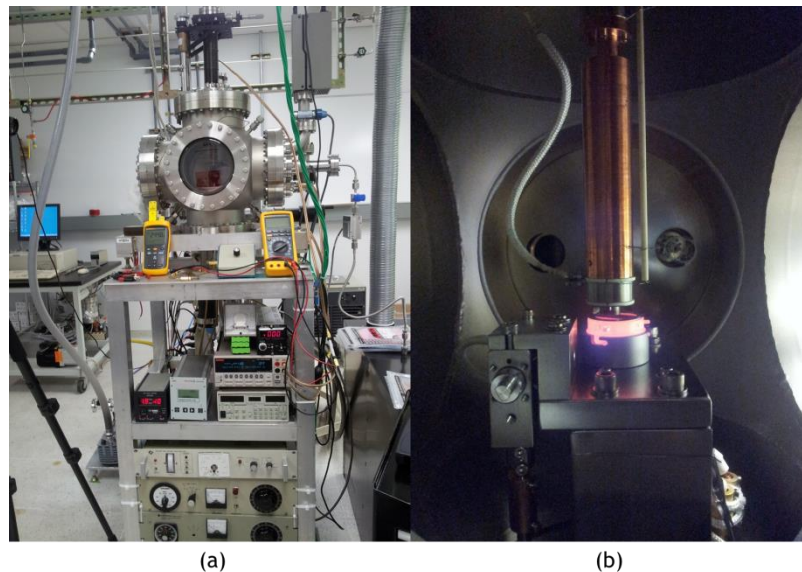


Figure 2.10: (a) Thermionic emission kit and (b) sample stage inside the thermionic emission kit in ASU, Arizona, USA.

2.8 Bell Jar Evaporator

A bell jar evaporator (Edwards Coating System E306A) was used to vaporise various metals to form thin layers, either to fabricate metal contacts or to make the metal-oxygen terminated surfaces (see Chapter 7).



Figure 2.11: Bell jar evaporator in the Diamond Laboratory, School of Chemistry, University of Bristol.

Figure 2.11 shows the bell-jar evaporator used in this study. The samples (oxygen-terminated boron doped diamond films) were placed ~10 cm away from the W cage or W filament. The metal of interest (Cr, Mg, Ti, Au, etc) in the form of a wire or foil was placed inside the W cage or wrapped around the W filament. Next, the glass bell jar was sprayed with polymeric spray (Bell Bright) to ease the bell-jar cleaning process after the deposition was completed. Then, the vacuum chamber was pumped down

to a base pressure $<5.0 \times 10^{-6}$ torr. Once it reached the base pressure, 18 A to 30 A current was passed through the W cage or W filament depending on the metal that was used for the deposition process. Low melting point metals required less current. The thickness of the metal film deposited was monitored *in situ* using an Agar quartz crystal resonator. For making the metal-oxide surface terminations, a standard 20 nm coating was used on every set of metal deposition experiment. Once the film reached the desired thickness, the instrument was switched off and cooled down to room temperature.

2.9 Software

The Cambridge Serial Total Energy Package (CASTEP) software [11,12] was used in this study to calculate the ground-state energy of the electrons that will lead to the value of formation energy of the doped-diamond structure, band structure and density-of-states of the diamond and its dopant. Further analysis was described in detail in Chapter 5. CASTEP is a DFT software packaged developed by the researchers at the Universities of Cambridge, Durham, York and St. Andrews with collaborations with the Rutherford Laboratory. It uses the Born-Oppenheimer approximation to explain the nuclear and electrons interaction and pseudopotentials for the core electrons to reduce computational time.

Other than CASTEP, theoreticians in the UK and Europe also developed their own DFT codes that were flexible to their style and understanding. Goss and co-workers in Newcastle, UK developed AIMPRO, while Mainwood's group in London used SIESTA, CASTEP and AIMPRO to predict dopant behaviour in diamond structures [13-17].

2.9.1 Limitations

Even though predicting electronic properties using computational methods is easier than producing the material in laboratories, it has a few drawbacks due to the approximations used and also the limitations of the software in solving the Schrödinger equation. The approximations in the theory cannot be improved much without significant cost in terms of longer computational time. However, care needs to be taken with the limitations of the software. For instance, most of the DFT calculations used to predict the electronic structure of various dopants in diamond only used 64 atoms per unit cell. If one C atom was substituted with one N atom, the doping level of the diamond structure was calculated to be ~1.59% with the concentration of dopant in the real diamond film would be in the range of 1.5×10^{21} atoms cm^{-3} . The dopant level was greatly overestimated as the highest concentration of N atoms detected in diamond films only ranges between 10^{19} and 10^{20} atoms cm^{-3} . Thus, it is important to understand that the result generated by the theoretical calculations are relative values and can only be used to understand the pattern of dopants in diamond films.

CASTEP is also capable of calculate a larger unit cell, such as 215 atoms, but the computational time needed to solve the Schrödinger equation will increase significantly. Other software has the capability to calculate even larger unit cells, 500 - 2000 atoms, such as Order-N Electronic Total Energy Package (ONETEP), but due to the complexity of the operating procedure, it was not chosen for this study [18]. In addition, due to the limitation in computational capability and time constraint, the work here focused on using CASTEP with a 64-atom unit cell.

2.10 References

- [1] J. Loader, Basic Laser Raman Spectroscopy, Heyden & Son, London, (1970).

- [2] J. Filik, *Spectrosc. Eur.* **17** (2005) 10-17.
- [3] R.G. Buckley, T.D. Moustakas, L. Ye, & J. Varon, *J. Appl. Phys.* **66** (1989) 3595.
- [4] C. Wild, & E. Worner, *The CVD Diamond Booklet*, Germany, (2008).
- [5] V.T. Cherepin, *Secondary Ion Mass Spectroscopy of Solid Surfaces*, VNU Science Press BV, Utrecht, (1987).
- [6] T.A. Carlson, *Photoelectron and Auger Spectroscopy*, Plenum Press, (1975).
- [7] K.M. O'Donnell, M.T. Edmonds, J. Ristein, A. Tadich, L. Thomsen, Q.H. Wu, C.I. Pakes, & L. Ley, *Adv. Funct. Mater.* **23** (2013) 5608-5614.
- [8] J. Van der Weide, & R. Nemanich, *J. Vac. Sci. Technol. B Microelectron. Nanom. Struct.* **10** (1992) 1940-1943.
- [9] P.K. Baumann, & R.J. Nemanich, *Surf. Sci.* **409** (1998) 320-335.
- [10] J.W. Liu, M.Y. Liao, M. Imura, & Y. Koide, *Appl. Phys. Lett.* **101** (2012) 252108.
- [11] S.J. Clark, M.D. Segall, C.J. Pickard, P.J. Hasnip, M.I.J. Probert, K. Refson, & M.C. Payne, *Zeitschrift für Krist.* **220** (2005) 567-570.
- [12] M.D. Segall, P.J.D. Lindan, M.J. Probert, C.J. Pickard, P.J. Hasnip, S.J. Clark, & M.C. Payne, *J. Phys. Condens. Matter* **14** (2002) 2717.
- [13] J.P. Goss, P.R. Briddon, R. Jones, & S. Sque, *Diamond Relat. Mater.* **13** (2004) 684-690.
- [14] J.P. Goss, & P.R. Briddon, *Phys. Rev. B* **75** (2007) 75202.
- [15] Z.M. Shah, & A. Mainwood, *Diamond Relat. Mater.* **17** (2008) 1307-1310.
- [16] E.B. Lombardi, A. Mainwood, & K. Osuch, *Phys. Rev. B* **76** (2007) 155203.
- [17] E.B. Lombardi, & A. Mainwood, *Phys. B Condens. Matter* **401-402** (2007) 57-61.
- [18] P.D. Haynes, A.A. Mostofi, C.-K. Skylaris, & M.C. Payne, *J. Phys. Conf. Ser.* **26** (2006) 143.

Chapter 3: Lithium: A Challenging Precursor for Diamond Doping

3.1 Introduction

Despite recent developments in doping diamond films with phosphorus, antimony, arsenic and sulfur, the production of n-type semiconducting diamond with useful electronic properties remains elusive [1-10]. Nitrogen is another possible dopant, and nitrogen-doped diamond has been successfully synthesised using hot-filament chemical vapour deposition (HFCVD) and microwave plasma CVD (MWCVD) techniques [3,11-16]. However, due to its high activation energy (1.7 eV), nitrogen-doped diamond is an insulator at room temperature, and only becomes semiconducting at high temperatures which makes it impractical for use in most devices.

Recently, lithiated diamond surfaces were suggested as a method to produce low-work-function materials [17-19], and theoretical studies have predicted that interstitial lithium should act as a shallow donor [20]. The energy to excite an electron from the lithium donor level to the conduction band of diamond is calculated to be less than 0.3 eV [21], however this has proved difficult to obtain experimentally, partly due to the low solubility of Li in diamond [22]. Research has been focused on trying to force Li into the diamond lattice by implantation [23-27], diffusion [28-30] and addition of Li species to the gas phase during CVD [31-34]. Although Li was incorporated inside the diamond lattice to values as high as $1 \times 10^{21} \text{ cm}^{-3}$ [32], in all cases the Li remained electrically inactive. The proposed explanation for this is the high mobility of Li in diamond at high temperature, which causes diffusion and aggregation of the Li into inactive clusters [30]. To overcome this, it has been suggested [35] that Li diffusion can be prevented by simultaneously adding nitrogen together with Li, with the N acting as a trap to pin down the Li in the diamond lattice and reduce its mobility. The co-doped system will be further discussed in Chapter 4

One problem limiting the study of Li doping is the lack of sources of Li that are suitable for use as a precursor during diamond CVD. Ideally, to be compatible with the CVD process, a gas-phase lithium-containing compound would be preferable, as this could then be metered into the CVD chamber using standard MFCs. However, although some organo-lithium compounds exist which are gases or volatile liquids, they are nearly all extremely expensive, hazardous and explosive [36].

The next best choice is to use a solid compound of lithium which can vaporise at a controlled rate when placed in the high temperature CVD environment. The compound needs to be relatively safe to handle, air stable (so that it can be added to the chamber easily), not react with any of the CVD process gases, and have a melting/boiling point consistent with the substrate temperatures during CVD (850°C). Lithium metal itself is known to be reactive and corrosive. But it forms lithium oxide when exposed to humid air, making handling difficult. Having oxygen-containing compounds in a HF-CVD reactor is a problem due to them vaporising, then reacting with the hot filaments, which then oxidise and break prematurely. This problem exists for other oxygen-containing Li compounds such as nitrates, carbonates and sulfates. Some of these concerns are less important if MW-CVD is used rather than HF-CVD, but it would be preferable to find a Li precursor that was not reactor dependent [32,34,37,38].

Other common lithium salts, such as lithium chloride and bromide, were also taken into consideration. The chlorine-containing gases (HCl, Cl₂) and similar bromine-containing gases that may be produced as by-products of the CVD process would not harm the filaments but they have health and safety issues as well being corrosive to the vacuum system and pumps.

Two other potential lithium precursors are lithium carbide (Li₂C) and lithium nitride (Li₃N), which can be purchased commercially as powders from chemical suppliers. Li₂C has a lower melting point (~550°C) [39] compared to Li₃N (~850°C) [40]. Both compounds will melt during the standard diamond growth procedure, and then vaporise slowly and

uniformly at a rate dependent upon the temperature. Li_3N was chosen as the precursor because its higher melting point gave it a lower vapour pressure at the growth temperature, slowing its vaporisation rate, and preventing the precursor evaporating away too rapidly. Furthermore, because the eventual aim of the project was to co-dope the diamond with Li and N, having N present in the Li precursor was not a problem - in fact, it may actually help with the co-doping process.

3.2 Experimental

Li_3N is a flammable compound which is moisture sensitive. Extra precautions were taken to ensure the safe use of this material. First, to minimise risk, only small amounts (<10 mg) of Li_3N were used in each set of experiments. In order to introduce Li_3N inside the HF-CVD chamber, it is essential to have it in a form that is compact and controllable, ideally in solution form. However, Li_3N does not dissolve readily in water or any common organic solvent. Indeed, it spontaneously reacts with water to form lithium hydroxide and ammonia gas. To solve this, Li_3N was introduced into the chamber by preparing Li_3N powder as a suspension in an organic liquid which could then be drop-cast onto the substrate using a pipette.

3.2.1 Organic liquid selection

A stable suspension is essential to ensure that the Li_3N formed a uniform, repeatable layer when drop-cast onto a surface. As such, the liquid medium plays an important role to prolong the stability of the suspension. Thus, to investigate the effect of the liquid on the stability of the Li_3N suspension, trials were carried out using the liquids listed in Table 3.1.

Table 3.1: List of liquids and their density at 20 °C.

Liquids	Chemical Formula	Density at 20 °C / (g ml ⁻¹)
Hexane	C ₆ H ₁₄	0.65
Heptane	C ₇ H ₁₆	0.68
Acetone	C ₃ H ₆ O	0.79
Methanol	CH ₃ OH	0.79
Cyclohexane	C ₆ H ₁₂	0.78
Toluene	C ₆ H ₅ (CH ₃)	0.87
Paraffin oil	<i>n</i> -alkane	0.80
Chloroform	CHCl ₃	1.48

All liquids used in the experiment were dried using a molecular sieve to remove all traces of water for a week prior to the experiment. 5 mg of Li₃N powdered crystals (CERAC, 99.5% purity, <250 μm) was used for this experiments. The compound consists of small crystallites in a powder form. Initially, trials were done to grind this powder further in a mortar and pestle to reduce the grain size. However, this appeared to make no difference to the stability of the subsequent suspension and therefore all further experiments used the compound straight from the bottle with no further processing.

The Li₃N powder was mixed with 5 ml of the liquid under test in a 10 ml glass vial. The mixture was sonicated in an ultrasonic bath for an hour to produce an opaque black/maroon suspension. A drop of this freshly prepared suspension was drop-cast on a microscope slide, allowed to dry, and observed under an optical microscope to see the size and uniformity of coverage of the crystallites. The remaining suspension was set aside for a day. Each day, the suspension was sonicated for five minutes, and a drop from the suspension was again drop-cast on a microscope slide and observed as before. Any changes due to oxidation or other reactions were recorded. Similar procedures were repeated for the other liquids in Table 3.1.

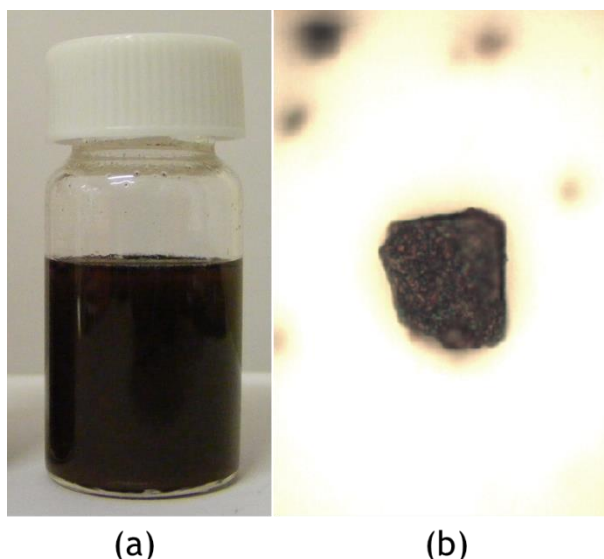


Figure 3.1: (a) Li_3N suspension in hexane solution and (b) optical micrograph of Li_3N crystals obtained from the Li_3N suspension in (a).

Figure 3.1(a) shows a freshly prepared Li_3N suspension in hexane solution, and in (b) its crystals observed under an optical microscope after evaporation of the hexane in air. After an hour of sonication, a black/maroon colour suspension was successfully prepared. Under the optical microscope, the Li_3N crystals could be recognised easily based on their maroon/black colour as shown in Figure 3.1(b). The time taken for vaporisation of the liquid varied, depending on the liquid used for creating the stabilised suspension. The size of the particles ranges from $1\ \mu\text{m}$ to $20\ \mu\text{m}$. The particles distributed uniformly but the crystallites separate on average of $30\ \mu\text{m}$.

The Li_3N crystallites oxidised/hydrolysed when exposed to humid air or to water dissolved in the liquid, which was undesirable. Figure 3.2 shows an example of an oxidised Li_3N crystal. The crystal was taken from a Li_3N suspension in hexane solution after 48 hours. From the micrograph, only a small fraction of maroon/dark areas were observed in the crystals. These are the remaining unreacted/non-oxidised Li_3N crystals. The larger clear areas surrounding the dark crystals were consistent with them being lithium oxide (Li_2O) or lithium hydroxide (LiOH).

We required the Li_3N to be stable in a chosen solution for several days, without oxidising/hydrolising, and therefore stability tests were performed with various liquids and the results are given in Section 3.3.1.



Figure 3.2: Micrograph of Li_3N suspension in hexane solution after 48 hours showing clear crystallites of Li_2O or LiOH .

3.2.2 Polymer stabilisation

Polymer addition often leads to prolonging the stability of suspensions [41]. Two polymers (polyoxyethylene oleyl ether (polyoxy) and Polysorbate-20) were chosen as suitable candidates to investigate for this purpose. Both of the polymers are non-toxic and are soluble in water, but contain a number of hydroxyl groups capable of bonding to the Li_3N crystallites, protecting them from oxidation and from coalescing with other crystals. Polysorbate-20 (Figure 3.3) is a polyoxyethylene ether derived from sorbitan monolaurate. It contains a carbonyl group, multiple branches of ethyl ether groups and three hydroxyl groups. In contrast, polyoxy only has one hydroxyl group, with straight-chain ethyl ether groups attached to the alkyl chain. In short, Polysorbate-20 can be described as a multiply

branched polymer while polyoxy can be classified as a straight-chain polymer.

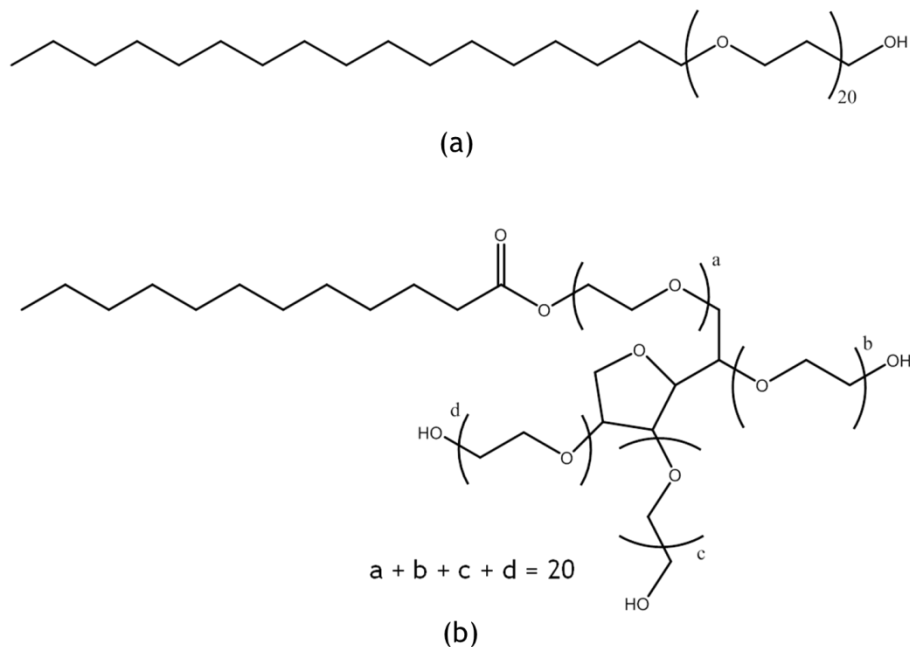


Figure 3.3: Skeleton structure of (a) Polyoxy and (b) Polysorbate-20.

To introduce the polymer, 1% v/v of Polysorbate-20 in chloroform was prepared by adding 50 μ l of Polysorbate-20 in 5 ml of chloroform in a glass vial. The mixture was sonicated for 5 minutes in an ultrasonic bath. 50 mg of Li_3N was added into the solution and sonicated for a further hour to ensure a uniform dispersion of the Li_3N crystals. The same procedures were repeated to prepare 1% w/v of polyoxy in chloroform. Both solutions were set aside and observed for any changes.



Figure 3.4: (a) 1% w/v Polyoxy in chloroform and (b) Li_3N suspension in 1% w/v Polyoxy in chloroform.

Figure 3.4 shows the solution of (a) 1% w/v polyoxy in chloroform and (b) Li_3N suspension in 1% w/v polyoxy in chloroform. Both polymers dissolve completely in chloroform and create a black/maroon coloured Li_3N suspension similar to the suspension prepared without the polymer.

The experiment was also repeated with toluene as the solvent replacing chloroform to confirm that chloroform is the best solvent to stabilise Li_3N suspension after the addition of polymer into the solution.

3.2.3 Melting Process under Growth Conditions

After creating a stable Li_3N suspension, the next stage was to check whether the Li_3N crystals melted during CVD in the reactor. If the Li_3N did

not melt, diffusion of lithium into the diamond lattice would be limited or not occur at all. In addition, unmelted Li_3N crystals would create a rough surface hindering the growth of the next layer of diamond.

200 μl of Li_3N suspension in 1% polyoxy in chloroform were dropped onto a silicon (100) substrate and placed into the hot filament reactor. The melting procedure was similar to standard diamond growth condition (see Section 2.2.1) except only using hydrogen gas. The substrate heater and filament were turned on, and the substrate temperature rose to ~ 850 C. The sample was heated in hydrogen (20 torr) in this manner for one hour and then cooled down to room temperature. The experiment was repeated with 100 μl of the same suspension. The results of these experiments are given in Section 3.3.3.

3.2.4 Preparation of lithium-doped diamond films

Lithium-doped diamond films were grown in a HFCVD system in the Diamond laboratory at the University of Bristol. Single-crystal silicon wafers (100) were used as the substrate and manually abraded as described in Section 2.2. Diamond was deposited in a HF reactor using standard CVD conditions with the distance between the substrate and the tantalum filaments (99.9%, 0.25 mm diameter) fixed at 3 mm. Undoped diamond was deposited using a standard ratio of 0.82% CH_4 in H_2 . The pressure of the chamber was set at 20 torr while the filament temperature was measured using 2-coloured optical pyrometer and maintained between 2100 and 2250 K with 25.0 A passing through the filaments. These conditions fabricated faceted microcrystalline diamond at a rate of $\sim 0.5 \mu\text{m h}^{-1}$.

100 μl of Li_3N polymer-stabilised suspension were drop cast onto the surface of a freshly prepared undoped diamond film that had been grown in the same reactor. The sample was then placed back inside the HF-CVD chamber. The film was heated using the substrate heater and filament in a hydrogen atmosphere for 1 hour at 20 torr. The filament temperature was

maintained at 2100 K and monitored using an optical pyrometer. This was to ensure the Li₃N melted completely and began the diffusion process into the underlying diamond layer. A colour change was observed during the melting process of Li₃N. The film began with a dark surface; once exposed to atomic hydrogen it started changing into a white surface almost instantaneously may due to the conversion of Li₃N to LiH in H-rich atmosphere. Then, it slowly changed back to a darker surface indicating melting process had begun. The time taken to observe the second colour change varied from 10 to 20 minutes. The remaining exposure time was done to ensure sufficient time for the diffusion process of lithium atoms into the diamond layer. After an hour of hydrogen treatment, CH₄ was added to the process gas in order to recommence diamond growth to fully encapsulate the lithium layer. The layer was grown for an hour. The prepared diamond film was cooled down to room temperature and further analysis was carried out using laser Raman spectrometry and SIMS.

3.2.5 Determination of lithium content using SIMS

The concentration of dopants was characterised using SIMS in the Interface Analysis Centre, University of Bristol. For SIMS, the Li signal was detected as Li⁺ while the nitrogen signal was detected as CN⁻. The absolute concentrations of N and Li in the diamond were quantified using exemplar single-crystal diamond samples previously implanted with known concentrations of Li and N for use as SIMS calibration (see appendix A).

From the calibration report in Appendix A, the calibration factor was calculated:

$$\frac{Li(\text{cps})}{C(\text{cps})} \times 1.80 \times 10^{19} = \text{Concentration/cm}^3$$

Based on the calibration experiment, the limit of detection of lithium atoms in diamond using SIMS was 2.03×10^{17} atoms/cm³. In addition, SIMS was also able to produce a depth-profile analysis. The combination of qualitative and quantitative analysis identified which elements are present and also how many atoms were successfully incorporated. Furthermore, SIMS was used to obtain the diffusion profile of the dopant at a certain depth. It determined whether the diffusion of the dopant followed a Gaussian profile or a constant doping level throughout the diamond film.

3.3 Results and Discussion

3.3.1 Effect of liquids on suspension stability

A series of liquids were tested in order to create stable Li₃N suspensions (see Section 3.2.1) and the observations are tabulated in Table 3.2.

Table 3.2: Observations after the addition of Li₃N into the liquids followed by ultrasonication.

Liquids	Chemical formula	Addition of Li ₃ N crystals into the liquids	Stability of Li ₃ N in the suspension
Acetone	C ₃ H ₆ O	Instantly dissolved	-
Methanol	CH ₃ OH	Instantly dissolved	-
Hexane	C ₆ H ₁₄	Black suspension formed	< 24 hours
Heptane	C ₇ H ₁₆	Black suspension formed	< 12 hours
Cyclohexane	C ₆ H ₁₂	Black suspension formed	< 12 hours
Toluene	C ₆ H ₅ (CH ₃)	Black suspension formed	< 48 hours
Paraffin oil	<i>n</i> -alkane	Did not mix well	-
Chloroform	CHCl ₃	Black suspension formed	< 72 hours

For all the suspensions prepared eventually sedimentation and coalescence occurred. The stability shown in Table 3.2 refers to elapsed

time after which most of the Li_3N crystals completely sedimented from the suspension and the liquid reverted back to colourless, i.e. that of the pure liquid.

Li_3N crystals dissolved completely in both acetone and methanol after an hour of ultrasonication. As Li_3N should not be able to dissolve in any common organic solvent, certain reactions were occurring during the ultrasonication process. Figure 3.5 shows optical micrographs of Li_3N crystals in (a) acetone and (b) methanol. Clear crystals were observed from both solvents which indicated reaction of Li_3N to form LiOH . High water solubility in both solvents may have caused this as during the ultrasonication treatment, water vapour in air could be trapped and dissolved into the liquid. This led to the formation of LiOH .

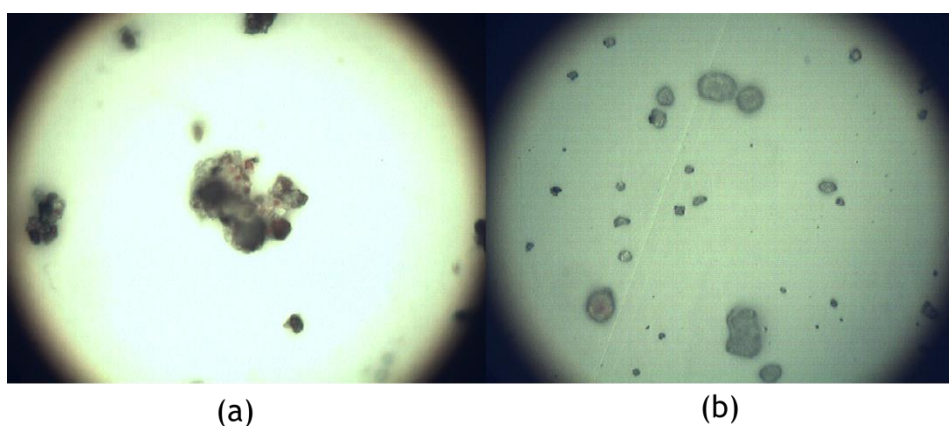


Figure 3.5: Optical micrographs of Li_3N crystals in (a) acetone solution and (b) methanol solution after ultrasonication.

For hexane, toluene and chloroform, it was observed that the more polar the molecule, the longer the stability of the Li_3N suspension. By increasing the polarity of the liquid, the stability of the Li_3N suspension increased from 24 hours to 72 hours. The reason for this may be that the stability of a suspension increases if the individual particles are prevented from colliding and coalescing. The Li_3N particles are slightly charged, and in a non-polar liquid they can overcome this small repulsive barrier (zeta

potential charge) relatively easily, leading to a rapid increase in the particle size and ultimately sedimentation. Conversely, in a polar liquid, the liquid molecules can orient themselves so that the part of the molecule with the opposite charge to the Li_3N faces the particles. Thus, the particles are surrounded in a protective layer of liquid molecules, which prevent the particles colliding and coalescing.

After these experiments, it was decided that chloroform was the best liquid from which to make the suspension, as this could remain stable for nearly 3 days.

3.3.2 Effect of Polymer addition

From the experiments described in section 3.2.2, we found that addition of a polymer successfully enhanced the stability of the Li_3N /chloroform suspension from 72 hours up to 120 hours. Some evidence of coalescence and sedimentation after Day-3 was seen, but the rate was much slower compared with the suspension prepared without the addition of the polymer. Apart from being polar, the polymer also increased the density of the solution. By having a denser solution with higher polarity, it further reduced the coalescence process that led to sedimentation of the Li_3N crystals.

The Polysorbate-20 suspension showed better stability compared to polyoxy with stability up to 200 hours. The branched ethyl ether groups in Polysorbate-20 were probably responsible for enhancing the stability. Branched polymers are more flexible compared to straight-chain structures. This fact, together with the larger dipoles from the ethyl ether functional group in Polysorbate-20 gave it a higher tendency to entangle the Li_3N crystals better than the rigid straight-chain polyoxy structure. This entanglement effect reduced the probability for the Li_3N crystals to interact with each other. Hence, it reduced the rate of coalescence of Li_3N crystals in the suspension.

However, the steps in making the solution were crucial. An attempt to make the solution in one step by mixing the polymer and Li_3N crystal simultaneously in chloroform resulted in an unstable suspension. The sedimentation process was completed within 12 hours after the ultrasonication process. This suggests that the polymer must be added into the suspension prior to the addition of the Li_3N crystals to ensure the entanglement process took place adequately.

When the experiment was repeated by replacing the chloroform with toluene, the stability of the Li_3N suspension increased compared to Li_3N suspension without the addition of the polymer. However, the suspension started to sediment after 72 hours. Thus, it can be concluded that chloroform was most suited to be used for the preparation of a stabilised Li_3N suspension.

3.3.3 Li_3N melting process under Growth Conditions

Figure 3.6 shows silicon substrates coated with of 200 μL and 100 μL of Li_3N after the melting process described in section 3.2.3. It is clearly seen that 200 μL is not an ideal amount of Li_3N to be used for the introduction of lithium into diamond films. The presence of a large lump of solid can be seen on top of the silicon wafer. In contrast, a smooth surface can be observed for the sample coated with 100 μL of Li_3N .

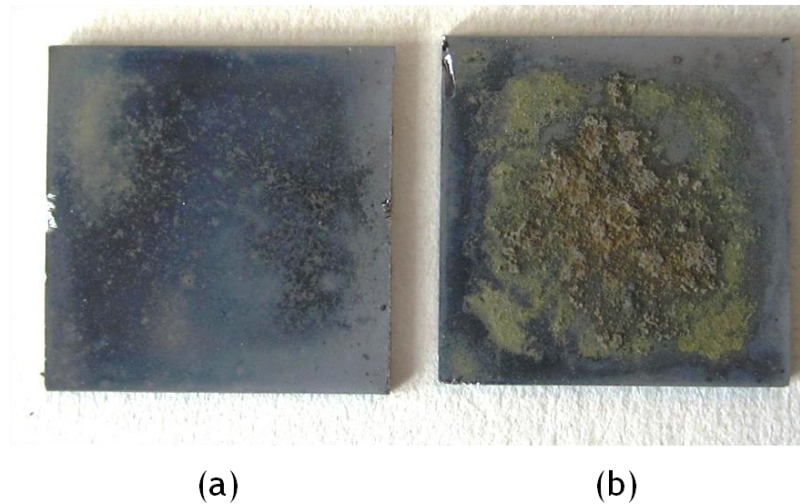


Figure 3.6: Silicon substrate with (a) 100 μl and (b) 200 μl of Li_3N suspension after melting in hydrogen and cooling down to room temperature.

Further analysis using EDX was done to determine if there was contamination present in these samples. Figure 3.7 shows EDX analysis of the samples coated with both 200 μl and 100 μl of Li_3N , respectively. From the analysis, both samples show the presence of tantalum on the surface of the material. This indicates that the temperature of the filaments during the melting process was high enough to vaporise the tantalum filaments. The tantalum atoms then diffused into the cooler area around the substrate and coated the sample at the same time as the lithium melted. To avoid this contamination by Ta, the experiment was repeated using carburised filaments (see Section 2.2).

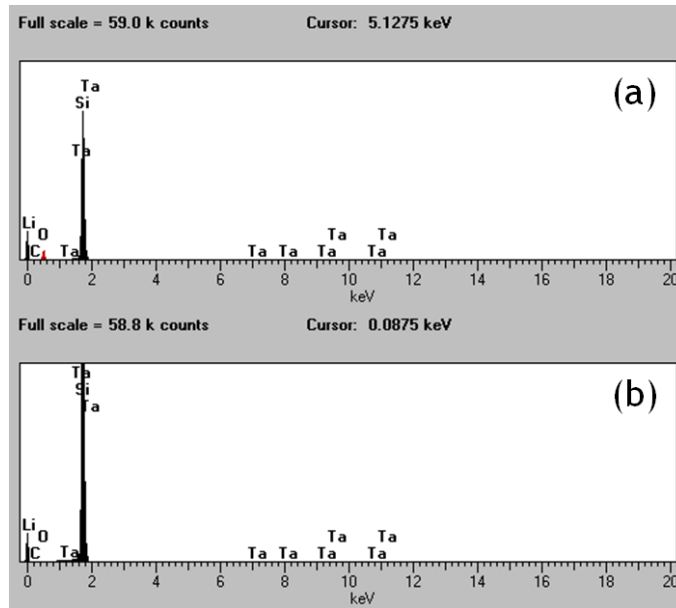


Figure 3.7: EDX analysis of silicon wafers coated with (a) 200 μl and (b) 100 μl of Li_3N after the melting process with a new Ta filament.

Figure 3.8 illustrates the EDX analysis of a 100 μl thin layer of Li_3N coated on top of silicon wafer after being melted using the carburised filament. There is no evidence of tantalum on the surface of the sample, suggesting that the TaC layer on the surface of the filament inhibited the vaporisation of tantalum.

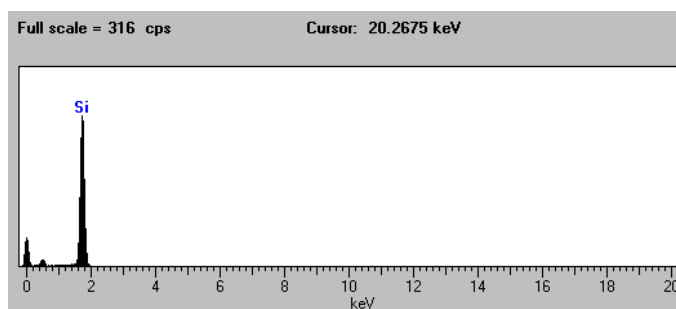


Figure 3.8: EDX analysis of a Li_3N thin layer coated on top of a silicon wafer after the melting process using a carburised filament.

3.3.4 Contamination and Limitations

A few microcrystalline diamond (MCD) samples were successfully grown using 100 μl of Li_3N in 1% w/v Polyoxy in chloroform. When further analysis was done using SIMS we discovered, surprisingly, that the control sample (undoped diamond) apparently also contained large amounts of lithium as illustrated in Figure 3.9.

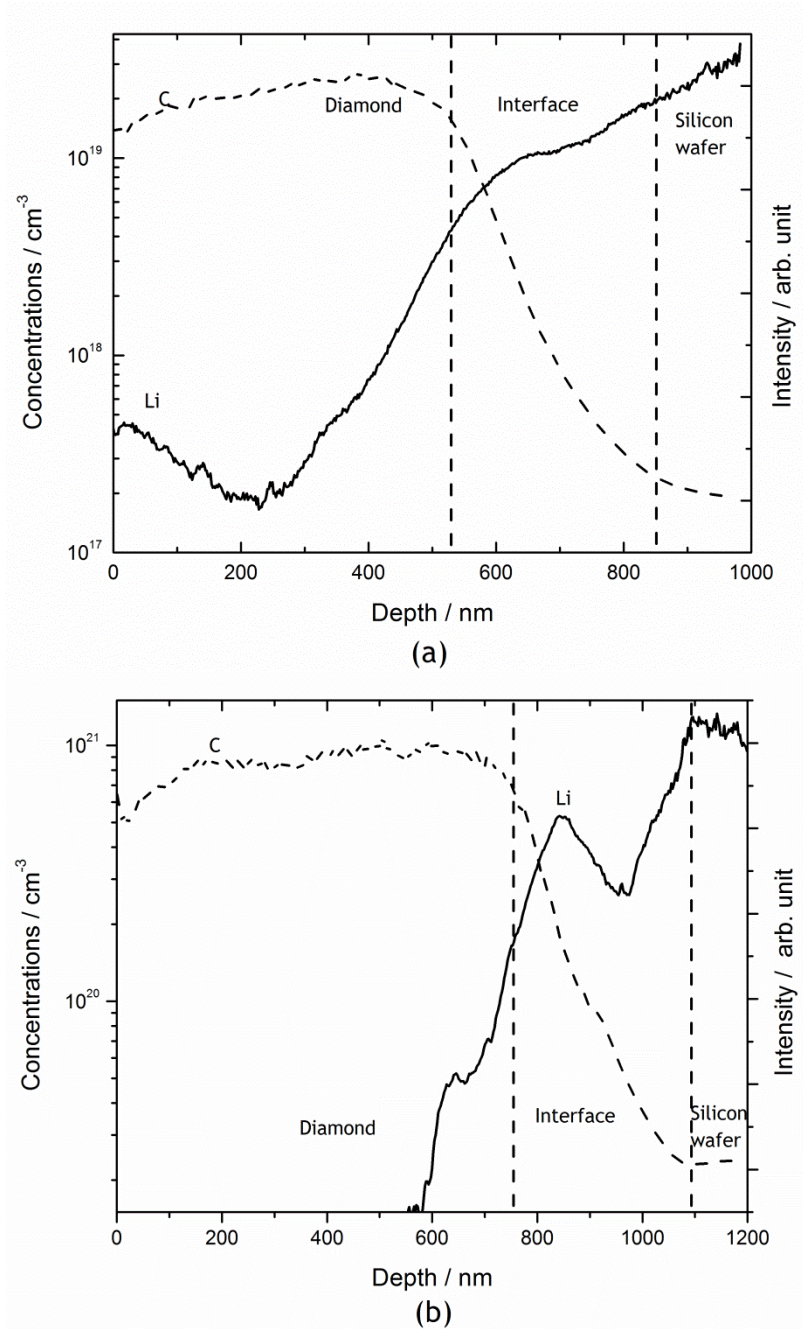


Figure 3.9: Depth profile as measured by SIMS of the (a) undoped diamond thin film and (b) lithium-doped diamond thin film. The undoped film had the following layered structure,

indicated by the dashed vertical lines, starting from the Si substrate, interface and $\sim 0.5 \mu\text{m}$ of undoped diamond. The lithium-doped diamond film had the following layered structure, indicated by the dashed vertical lines, starting from the Si substrate, interface and $\sim 0.75 \mu\text{m}$ of lithium-doped diamond. Shown on the plot are the absolute calibrated concentrations of Li and C intensity (used as the baseline from which the other concentrations were calculated), as a function of depth beneath the diamond surface.

Figure 3.9 shows the depth profile measured by SIMS for both undoped diamond and also lithium-doped diamond thin films. The interface between the silicon wafer and the diamond thin film were determined as the point at which the carbon signal started to decrease, because this layer did not consist of pure diamond. At the interface, a mixture of silicon carbide and carbon was present [42,43]. Hence, any lithium concentration calculated at the interface and towards the silicon wafer region will be unreliable and could not be deemed as the true concentration of lithium in the structure due to the nature of the calibration method. The calibration was based on the Li/C signal ratio. Changes in the carbon signal will affect the reliability of the calculated concentrations. In addition, the calibration was done on a diamond substrate. The concentrations calculated using the calibrated method will be compromised if the materials analysed were other than diamond itself. Thus, the concentration calibrated using SIMS could only be used to determine the amount of lithium atoms inside a diamond structure and could not be used to determine the lithium content in any other carbon compounds.

Based on Figure 3.9, it is clear that the Li preferred to diffuse towards and into the Si substrate rather than upwards into the diamond film. This is probably due to the higher diffusion rate of Li in Si and SiC (which is present at the interface) than diamond. This is a problem for doping experiments, as a large, uncontrolled and unknown percentage of the Li is lost into the Si and does not go into the diamond. For this reason, in all subsequent experiments, a thin ($1\text{-}2 \mu\text{m}$) diamond layer was deposited onto a Si wafer before Li doping experiments were performed.

A surprising result from Figure 3.9 (a), was that the undoped diamond film showed a high content of lithium just before the interface

between the diamond film and silicon wafer, when there should have been no Li present in this sample. Indeed, 7×10^{18} atoms of lithium per cm^2 were detected near the interface and started to diffuse ~ 110 nm towards the diamond film.

Further investigation was done in order to track down and understand the mysterious lithium SIMS signal in the supposedly undoped diamond film. Throughout the sample preparation process, the source of lithium (Li_3N) was always kept far away from the sample to avoid any cross-contamination. Different tweezers and sample vials were used to reduce the probability of cross-contamination but the results remained unchanged. Thus, we deduced that the contamination must occur during the sample preparation itself.

To unveil the introduction of the mysterious lithium, SIMS was used as the primary tool for characterisation. At every step of the process, the sample was taken and analysed using SIMS to detect the first appearance of lithium with the sample. Surprisingly, lithium was found at the very beginning of the sample-cleaning process. It is a common practice in the laboratory to wipe any received silicon wafers with methanol using methanol-soaked cotton buds to remove any unnecessary organic moieties such as fingerprints. After lengthy investigation it was determined that the source of the Li was the cotton buds, which are composed of cellulose fibres. These are processed in the factory using a LiCl solution [44-46]. Having discovered this unlikely source of Li contamination, it was easy to eliminate it by simply not using cotton buds in subsequent sample cleaning, and instead use cellulose-free lens-cleaning tissues.

3.4 Conclusions

Li_3N suspension was successfully prepared in 1% w/v polyoxy in chloroform. The black suspension remained stable for more than 120 hours before showing any sign of coalescence and sedimentation. Chloroform was

chosen as the liquid medium due to its high polarity which is believed to help prevent particle coalescence. Addition of the polymer also increased stability time, and branched polymers such as Polysorbate-20 were able to wrap around the particles more efficiently than straight-chained polymers, further preventing particle coalescence. Only a limited number of liquids were tested, along with only two polymers, due to time limitations. This means there is a great deal of scope for future optimisation of both the liquid used to make the suspension, and the choice of stabilising polymer.

Li_3N suspension was drop-cast onto the diamond film surface and heated in hydrogen using a Ta filament (which had been pre-carburised to prevent Ta contamination). This caused the Li_3N crystallites to melt and Li to diffuse into the diamond lattice. 100 μl of Li_3N suspension was determined to be an appropriate amount for substrates of size 1 cm^2 .

A 1 - 2 μm barrier layer of CVD diamond was found to be necessary before the introduction of Li_3N suspension to prevent the Li reaching the Si substrate. This is important as SIMS has difficulty quantifying the lithium content at the diamond/Si interface, and because Si acts as a sink for Li and would readily absorb much of the Li from the diamond.

Finally, it is important to avoid using cotton buds or any other cellulose material to clean any apparatus involved in lithium based experiments. A considerable amount of lithium could be detected on a Si wafer after simply wiping it with a wet cotton bud. To avoid this in subsequent experiments, all the apparatus used were cleaned using lens cleaning tissues to lower the probability of cross-contamination from lithium compounds that exist in commercial cellulose products.

3.5 References

- [1] R. Kalish, Carbon N. Y. **37** (1999) 781-785.
- [2] P. W. May, M. Davey, K. N. Rosser, & P.J. Heard, Mater. Res. Soc. Symp. Proc. **1039** (2007) 101-1039.

- [3] V. Baranauskas, B.B. Li, A. Peterlevitz, M.C. Tosin, & S.F. Durrant, *J. Appl. Phys.* **85** (1999) 7455-7458.
- [4] S. Koizumi, T. Teraji, & H. Kanda, *Diamond Relat. Mater.* **9** (2000) 935-940.
- [5] J.R. Petherbridge, P.W. May, G.M. Fuge, G.F. Robertson, K.N. Rosser, & M.N.R. Ashfold, *J. Appl. Phys.* **91** (2002) 3605-3613.
- [6] K. Haenen, K. Meykens, M. Nesládek, G. Knuyt, L.M. Stals, T. Teraji, S. Koizumi, & E. Gheeraert, *Diamond Relat. Mater.* **9** (2000) 952-955.
- [7] M. Nesládek, K. Meykens, K. Haenen, L.M. Stals, T. Teraji, & S. Koizumi, *Phys. Rev. B* **59** (1999) 14852-14855.
- [8] K. Haenen, A. Lazea, J. Barjon, J. D'Haen, N. Habka, T. Teraji, S. Koizumi, & V. Mortet, *J. Phys. Condens. Matter* **21** (2009) 364204.
- [9] F.A.M. Koeck, R.J. Nemanich, A. Lazea, & K. Haenen, *Diamond Relat. Mater.* **18** (2009) 789-791.
- [10] S. Koizumi, M. Kamo, Y. Sato, S. Mita, A. Sawabe, A. Reznik, C. Uzan-Saguy, & R. Kalish, *Diamond Relat. Mater.* **7** (1998) 540-544.
- [11] S. Jin, & T.D. Moustakas, *Appl. Phys. Lett.* **65** (1994) 403-405.
- [12] A.J. Eccles, T.A. Steele, A. Afzal, C.A. Rego, W. Ahmed, P.W. May, & S.M. Leeds, *Thin Solid Films* **343-344** (1999) 627-631.
- [13] J. Mort, M.A. Machonkin, & K. Okumura, *Appl. Phys. Lett.* **59** (1991) 3148-3150.
- [14] A. Badzian, T. Badzian, & S.T. Lee, *Appl. Phys. Lett.* **62** (1993) 3432-3434.
- [15] R. Locher, C. Wild, N. Herres, D. Behr, & P. Koidl, *Appl. Phys. Lett.* **65** (1994) 34-36.
- [16] W. Muller-Sebert, E. Worner, F. Fuchs, C. Wild, & P. Koidl, *Appl. Phys. Lett.* **68** (1996) 759-760.
- [17] K. M. O'Donnell, & T. L. Martin, *Mater. Res. Soc. Symp. Proc.* **1282** (2011).
- [18] K.M. O'Donnell, T.L. Martin, N.A. Fox, & D. Cherns, *Phys. Rev. B* **82** (2010) 115303.
- [19] K.M. O'Donnell, M.T. Edmonds, J. Ristein, A. Tadich, L. Thomsen, Q.H. Wu, C.I. Pakes, & L. Ley, *Adv. Funct. Mater.* **23** (2013) 5608-5614.

- [20] J.P. Goss, R.J. Eyre, & P.R. Briddon, *Theoretical Models for Doping Diamond for Semiconductor Applications*, Wiley-VCH Verlag GmbH & Co. KGaA, (2008).
- [21] E.B. Lombardi, & A. Mainwood, *Diamond Relat. Mater.* **17** (2008) 1349-1352.
- [22] G. Popovici, T. Sung, & M. Prelas, *J. Chem. Vap. Depos.* **3** (1994) 115-131.
- [23] S. Praver, C. Uzan-Saguy, G. Braunstein, & R. Kalish, *Appl. Phys. Lett.* **63** (1993) 2502-2504.
- [24] R. Job, A. Denisenko, A. Zaitsev, W.R. Fahrner, & M. Werner, *Diamond Relat. Mater.* **5** (1996) 757-760.
- [25] C. Cytermann, R. Brener, & R. Kalish, *Diamond Relat. Mater.* **3** (1994) 677-680.
- [26] M. Restle, K. Bharuth-Ram, H. Quintel, C. Ronning, H. Hofsaß, S.G. Jahn, & U. Wahl, *Appl. Phys. Lett.* **66** (1995) 2733.
- [27] I.M. Buckley-Golder, R. Bullough, M.R. Hayns, J.R. Willis, R.C. Piller, N.G. Blamires, G. Gard, & J. Stephen, *Diamond Relat. Mater.* **1** (1991) 43-50.
- [28] C. Uzan-Saguy, C. Cytermann, B. Fizeer, V. Richter, R. Brener, & R. Kalish, *Phys. Status Solidi* **193** (2002) 508-516.
- [29] G. Popovici, T. Sung, S. Khasawinah, M.A. Prelas, & R.G. Wilson, *J. Appl. Phys.* **77** (1995) 5625-5629.
- [30] G. Popovici, R.G. Wilson, T. Sung, M.A. Prelas, & S. Khasawinah, *J. Appl. Phys.* **77** (1995) 5103-5106.
- [31] K. Okumura, J. Mort, & M. Machonkin, *Appl. Phys. Lett.* **57** (1990) 1907-1909.
- [32] R. Zeisel, C.E. Nebel, M. Stutzmann, H. Sternschulte, M. Schreck, & B. Stritzker, *Phys. Status Solidi* **181** (2000) 45-50.
- [33] H. Sachdev, R. Haubner, & B. Lux, *Diamond Relat. Mater.* **6** (1997) 494-500.
- [34] H. Sternschulte, M. Schreck, B. Stritzker, A. Bergmaier, & G. Dollinger, *Diamond Relat. Mater.* **9** (2000) 1046-1050.
- [35] A. Namba, Y. Yamamoto, H. Sumiya, Y. Nishibayashi, & T. Imai, *Process for producing n-type semiconductor diamond and n-type semiconductor diamond*, US 2006/0177962 A1, (2006).

- [36] P.G. Urben, Bretherick's Handbook of Reactive Chemical Hazards, 7th Ed., Academic Press, (2007).
- [37] J.R. Petherbridge, P.W. May, S.R.J. Pearce, K.N. Rosser, & M.N.R. Ashfold, *J. Appl. Phys.* **89** (2001) 1484.
- [38] M. Elliott, P. May, & J. Petherbridge, *Diamond Relat. Mater.* **9** (2000) 311-316.
- [39] American Elements, MSDS of Lithium Carbide, <http://www.americanelements.com/lic.html>. (2013).
- [40] Sigma-Aldrich, MSDS of Lithium Nitride, <http://www.sigmaaldrich.com/catalog/product/aldrich/399558?lang=en®ion=GB>. (2013).
- [41] R.J. Hunter, *Zeta Potential in Colloid Science: Principles and Applications*, Academic Press, (1981).
- [42] B. Stoner, G. Ma, S. Wolter, & J. Glass, *Phys. Rev. B. Condens. Matter* **45** (1992) 11067-11084.
- [43] X. Jiang, & C. Jia, *Appl. Phys. Lett.* **1197** (1995) 13-16.
- [44] D. Anne-Laurence, *Polymer (Guildf)*. **44** (2003) 4117-4126.
- [45] C.L. McCormick, P.A. Callais, & B.H. Hutchinson, *Macromolecules* **18** (1985) 2394-2401.
- [46] C.L. McCormick, & P.A. Callais, *Polymer (Guildf)*. **28** (1987) 2317-2323.

Chapter 4: Incorporation of Li & N in CVD Diamond Films

4.1 Introduction

Li-doped diamond films are believed to be the key to create n-type semiconducting diamond with low resistivity at room temperature (see previous Chapter). However, the high mobility of lithium atoms in diamond at the CVD growth temperature leads to cluster formation that hinders the shallow donor properties [1-3]. In addition, theoretical studies suggest Li atoms are situated either in interstitial positions or substitutional positions [4,5]. Both positions exhibit different properties. Li atoms situated at interstitial positions will behave as shallow n-type donors while Li atoms in substitutional positions act as deep acceptors [6]. Having both acceptors and donors in a diamond system will cause them to compensate each other, and this will not enhance the n-type properties in diamond films [2]. Therefore, it seems that Li doping performed by diffusion, implantation and/or addition during growth processes, will always lead to compensating defects, and therefore to uncontrolled and unreliable doping.

However, recent developments in computational models suggest that substitutional Li can become more favourable if there are vacancies or other atoms nearby in the diamond lattice that will spontaneously pin Li into the substitutional position [6]. Nitrogen atoms have been suggested as the possible way to do this, with the N atoms acting as traps to pin lithium atoms that would otherwise be mobile during the growth process. In such a system, the electrons from the pinned interstitial Li are transferred through a substitutional N atom directly into the diamond lattice. It is suggested [7] that if a suitable co-doping process can create defect sites with a 1:1 ratio of Li:N, this could produce n-type semiconducting diamond with a shallow donor level and high electron mobility. More recent theoretical work has suggested that shallow donor states may be also created using LiN_4 clusters [8], requiring a 1:4 ratio of Li:N in the diamond lattice. However, no experimental work has yet been reported to test these hypotheses.

Even though N-doping studies grown with various precursors are well established in the literature [9-19], a comprehensive study was done in the Bristol Diamond Laboratory to ensure the quality of N-doped diamond films grown was optimised and comparable with those in the literature. The aim of the N incorporation studies was to choose the best N precursor to incorporate high concentrations of N atoms ($\sim 10^{20}$ atoms/cm³) in diamond films without jeopardising the crystal quality and morphology. It is important to have a higher number of N atoms inside the diamond crystal prior to the addition of Li atoms into the films. This will ensure the Li trapping process occurs before the Li starts to aggregate and form clusters.

Two types of substrate were used for the diamond growth in this chapter, either 1 cm² single-crystal Si wafers (100) which were pre-treated by a manual abrasion technique using 1-3 μ m diamond particles, or high-pressure high-temperature (HPHT) single-crystal diamond (2.5×2.5 mm²) type 1b (100) (purchased from Element Six, Ltd.).

The optimised Li precursor (a suspension of Li₃N powder in 1% w/v polyoxy in chloroform) was used as described in Chapter 3. All precautions regarding the limitation of SIMS, contamination by Ta due to the use of a non-carburised filament, and Li compounds found in cotton buds discussed in Chapter 3 were taken into consideration when investigating the Li-N co-doped system.

4.2 Experimental

HFCVD was used to grow MCD diamond films using standard growth conditions described in Section 2.2. Laser Raman Spectrometry in the Diamond Laboratory was used to characterise the quality of the films. SEM in the Electron Microscopy Unit in School of Chemistry was used to analyse the morphology and thickness of the diamond films. A SIMS instrument that was based in the Interface Analysis Centre, University of Bristol, was used

to determine the amount of Li and N atoms incorporated in the diamond films.

4.2.1 N-doped CVD Diamond Deposition with Different Nitrogen Precursors

Three types of nitrogen precursors were used in this study. Two of the precursors were in the gas state; nitrogen gas and ammonia gas, while the third precursor was white solid crystals, hexamethylenetetramine.

4.2.1.1 Nitrogen Gas

Nitrogen gas was introduced into the system using a separate mass flow controller, and was then mixed with the methane and hydrogen process gases in the manifold before entering the CVD chamber. The amount of nitrogen gas introduced into the system varied from 0.32% - 1.04% with respect to H₂ flow. The film morphology, quality and concentration of dopants were characterised using SEM, laser Raman spectrometry and SIMS.

4.2.1.2 Hexamethylenetetramine (HMT)

HMT (Sigma-Aldrich, ACS Reagent, ≥99% purity) was chosen as N-containing precursor due to its adamantane structure that consists of C-N bonds as depicted in Figure 4.1. It was thought that having pseudo-tetrahedral C-N bonds already present within the molecule might improve the N incorporation process because of the similarity with the diamond structure.

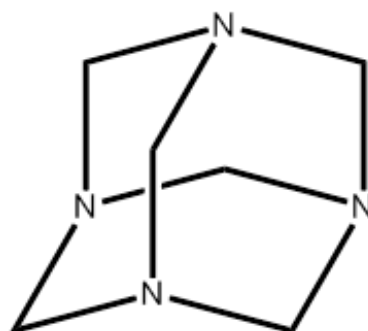


Figure 4.1: Skeletal structure of HMT.

HMT exists as white crystals at room temperature and pressure. The common properties of this compound are tabulated in Table 4.1.

Table 4.1: Common properties of HMT crystals.

Boiling point	Sublimation at 280 °C (in vacuum)
Vapour pressure	<0.01 mmHg (20 °C)
Hazards	Highly flammable
Solubility	Water & polar organic solvents
Appearance	White crystalline solid

To prepare HMT solution, 0.58 mg of HMT crystals were dissolved in 5 ml of chloroform. Next, the mixture was sonicated for 30 minutes in an ultrasonic bath which resulted in a colourless solution of HMT of concentration ~0.83 M.

As discussed in Section 3.3.4, CVD diamond films were grown in layers, with the doping varied between layers to see the effects of diffusion. To protect the Si substrate and to give a controlled starting surface, an initial layer of undoped/N-doped diamond (0.56% N₂ gas) was grown for six hours in the HF-CVD reactor. Then, 50 µl of the HMT solution were drop-cast on top of the freshly grown diamond film. When the solvent evaporated, this resulted in white uniform layer of HMT lying on the

surface of the diamond. SEM analysis showed that the average distance between the HMT crystals was 1-3 μm . Then, a diamond capping layer was grown on top of the HMT layer to ensure the HMT was encapsulated inside the diamond film. The capping layer was either an undoped diamond film or an N-doped diamond film (grown with the presence of N_2 gas), for one hour in the HFCVD chamber, resulting in a layer $\sim 0.5 \mu\text{m}$ thick. The film morphology, quality and concentration of dopants were characterised using SEM, laser Raman spectrometry and SIMS.

4.2.1.3 Ammonia Gas

Ammonia gas was introduced into the HFCVD system using the same gas line used by the nitrogen gas, with the amount varying from 0.19% to 1.24% with respect to H_2 . Due to the corrosive nature of NH_3 gas, bellow valves were used to avoid leakage from the seal and the vacuum pump was purged with air every week for 10 to 15 minutes to extend the life-time of the vacuum oil. The standard growth procedure of growing CVD diamond films was used as discussed in Section 2.2. The film morphology, quality and concentration of dopants were characterised using SEM, laser Raman spectrometry and SIMS.

4.2.2 Addition of Li_3N into Diamond Films

To incorporate Li into the diamond film, the Li_3N suspension prepared in Chapter 3 was drop-cast onto the surface of the diamond, heated in the HF reactor to cause the Li to diffuse into the layer below, and then embedded within the diamond using a CVD capping layer, as described in detail in Section 3.2.4.

4.2.3 Determination of Nitrogen and Lithium Content in Diamond Films

In SIMS the Li signal was detected as Li^+ while the nitrogen signal was detected as CN^- . The absolute concentrations of N and Li in the diamond were quantified using exemplar single-crystal diamond samples previously implanted with known concentrations of Li and N for use as SIMS calibration as discussed in section 3.4.2, Appendix A and Appendix B. The calibration parameter for Li was discussed in Section 3.2.5 and the N calibration parameter was calculated as:

$$\frac{N(\text{cps})}{C(\text{cps})} \times 3.40 \times 10^{20} = \text{Concentration}/\text{cm}^3$$

The minimum detection limits for Li and N in the instrument were $2.03 \times 10^{17} \text{ cm}^{-3}$ and $1.15 \times 10^{19} \text{ cm}^{-3}$, respectively.

4.2.4 Two-Point Probe Measurement

Electrical resistance measurements were performed using a two-point probe method. All samples underwent ozone treatment to change the hydrogen-terminated surface of the as-grown diamond to an oxygen-terminated surface in order to eliminate any possible surface conductivity [18]. Two $1 \times 1 \text{ mm}^2$ silver contacts were evaporated on top of the diamond film at the diagonal corners of each sample allowing the bulk electrical resistance to be measured.

4.3 Results and Discussion

4.3.1 N-doped Diamond

N-doped diamond was successfully prepared using HFCVD and appeared as a grey film, similar to standard undoped MCD thin films. This section discusses the studies of different N precursors introduced into the reactor to obtain the best growth condition with the highest amount of N atoms incorporated into the diamond films without jeopardising the crystal and structure quality of the diamond.

4.3.1.1 Nitrogen gas

Figure 4.2 illustrates the morphology of N-doped diamond thin films grown on Si wafers using N₂ gas as the N precursor (Section 4.2.1.1). The amount of N₂ gas introduced into the hydrogen atmosphere varied from 0.32% to 1.04% N₂/H₂. When 0.56% N₂/H₂ was introduced into the gas phase, the diamond crystal grains observed (1.02 μm) were bigger than when 0.32% N₂/H₂ was introduced (0.63 μm). The increase in grain size and growth rate with N₂ addition have also been reported by previous workers [10,15,18]. It is believed that the HCN species produced during the addition of N₂ gas help the rearrangement of carbon atoms on the surface and the abstraction of H atoms to create more readily available sites for the formation of C-C bonds on the diamond surface [15]. This process increases the growth rate and quality of the diamond films produced up to a certain N₂ concentration. When higher amounts of N₂ gas were introduced (0.80% N₂/H₂) the diamond did not form a continuous film. This was due to scavenging of the C to form stable CN radicals in the gas phase. [14]. With a lower concentration of methyl radicals in the system, the growth rate of diamond films was reduced [20]. When still higher N₂ amounts were introduced (1.04%) into the gas phase, the film became more discontinuous and the average grain size reduced to ~400 nm. A small number of larger

grains (μm sized) could be observed. This was due to the diamond growth rate decreasing so much that the growth of new crystallites was now determined by the efficiency of nucleation. Pre-existing diamond crystallites would grow much faster than new one could nucleate, leading to growth of isolated crystals rather than a continuous close-packed film.

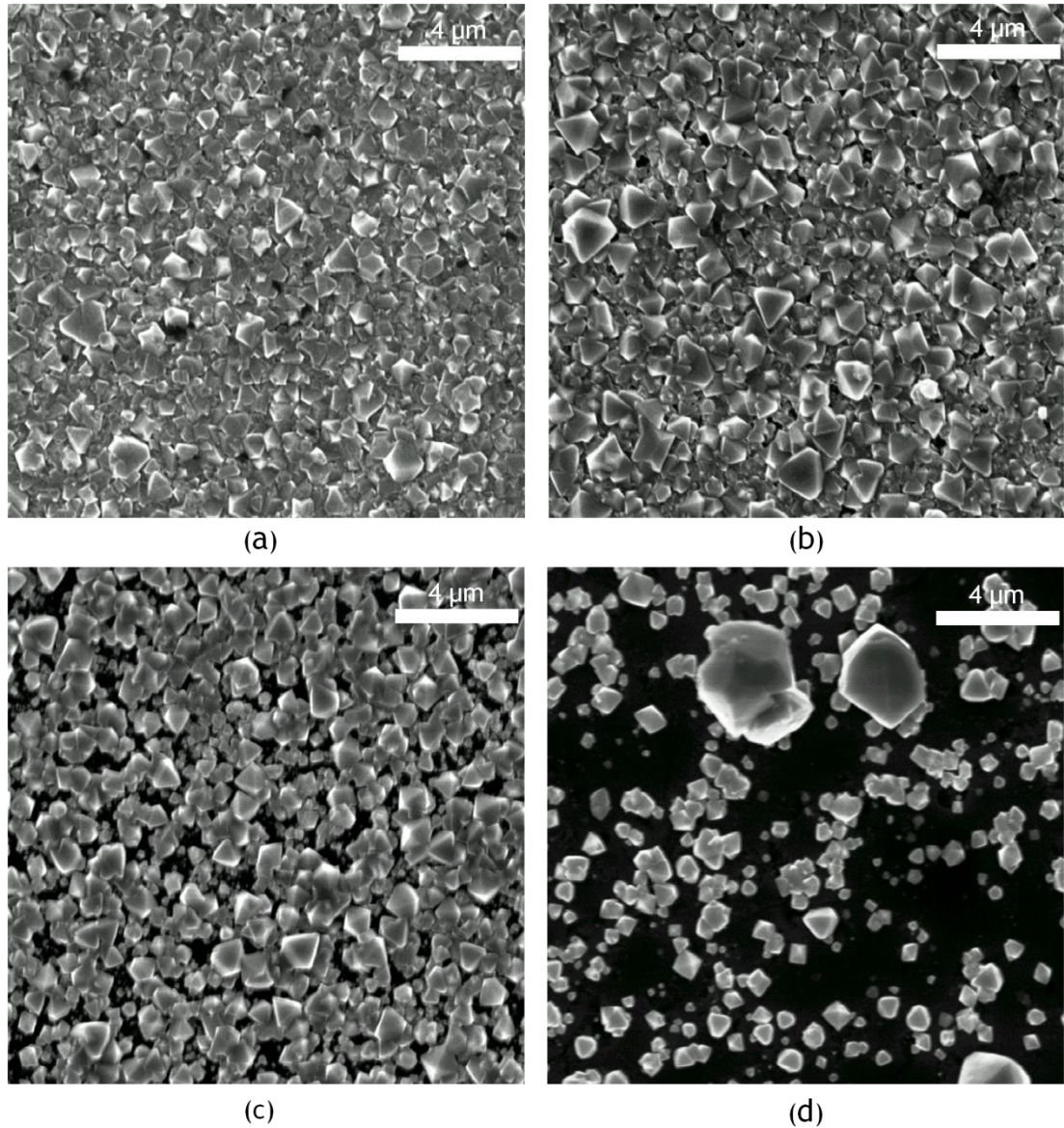


Figure 4.2: SEM micrographs of N-doped diamond grown on Si wafers with (a) 0.32%, (b) 0.56%, (c) 0.80% and (d) 1.04 N_2 w.r.t H_2 .

Figure 4.3 shows the Raman spectra obtained using a He-Cd laser as the excitation source for N-doped diamond films grown on Si wafers with different gas-phase N₂ concentrations. The spectra were normalised to the 1332 cm⁻¹ peak for easier evaluation of the changes of the *sp*² graphitic peak at 1580 cm⁻¹. There were no changes on the width of diamond peak at 1332 cm⁻¹ for all samples, suggesting there was no significant change in phonon-lifetime [21-23]. Diamond film grown with 0.32% N₂ gas showed the largest *sp*² graphitic peak. This suggested that the film had a higher amount of *sp*² carbon at the grain boundaries if compared to other films prepared in richer N₂ atmospheres. These results were consistent with those reported by others; when more N₂ gas is introduced into the gas phase, the quality of the film increased [15,18].

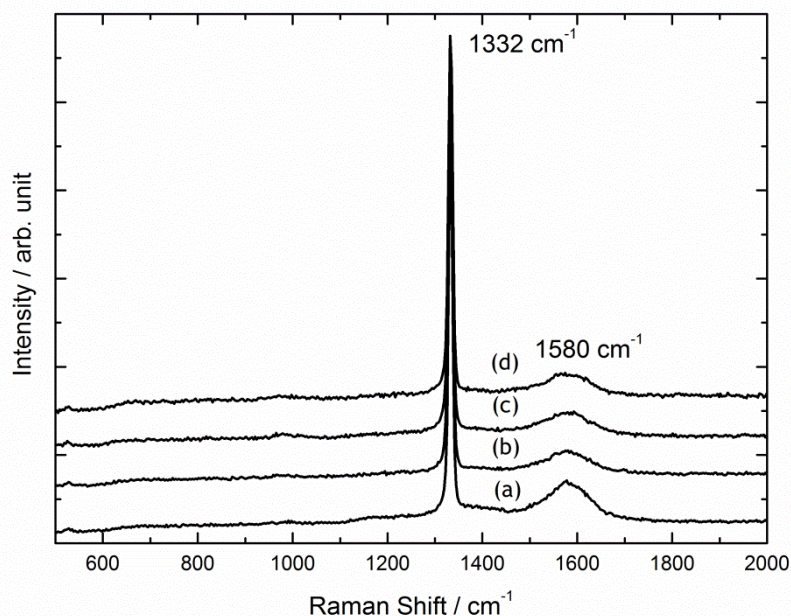


Figure 4.3: Raman spectra (325 nm He-Cd laser excitation) of N-doped diamond films grown on Si wafers with (a) 0.32%, (b) 0.56%, (c) 0.80% and (d) 1.04% of nitrogen gas w.r.t. H₂. The spectrum was normalised to the 1332 cm⁻¹ peak.

Based on results obtained from SEM and laser Raman spectroscopy, the sample grown with 0.56% N₂ gas introduced into the gas phase was chosen as the optimum N-doped diamond film. The sample showed high

quality and a uniform diamond coating. This sample was characterised using SIMS to determine the amount of N atoms that were successfully incorporated into the film. The result is discussed in Section 4.3.1.4 together with other N-doped diamond films grown with different N precursors.

4.3.1.2 HMT

Figure 4.4 shows the morphology of N-doped diamond films grown using HMT as the N precursor. Figure 4.4(a) depicts the film grown with the HMT layer sandwiched between two undoped diamond layers, while Figure 4.4(b) shows the film grown with HMT sandwiched between two N-doped layers (0.56% N₂). SEM images from other samples described in Section 4.2.1.2 can be seen in Appendix C.

Both samples illustrated in Figure 4.4 exhibit (100) facets. Normally, undoped diamond grown using HFCVD produce random facets [24-27] but after the introduction of HMT, (100) facets started to appear as shown in Figure 4.4(a). Interestingly, when HMT was introduced, the morphology changed drastically compared to the morphology depicted in Figure 4.2(b). Most of the (111) facets observed on the N-doped diamond film disappeared and were replaced by (100) facets. Theoretical calculations suggested that the growth of (100) facets was possible when the temperature of the diamond surface was reduced below 1073 K [28]. Once the (100) facets were grown, even if the temperature of the surface rose above 1073 K, the (100) facets will remain dominant. The addition of HMT crystals and the melting process may reduce the temperature at the diamond surfaces and promote the formation of (100) facets.

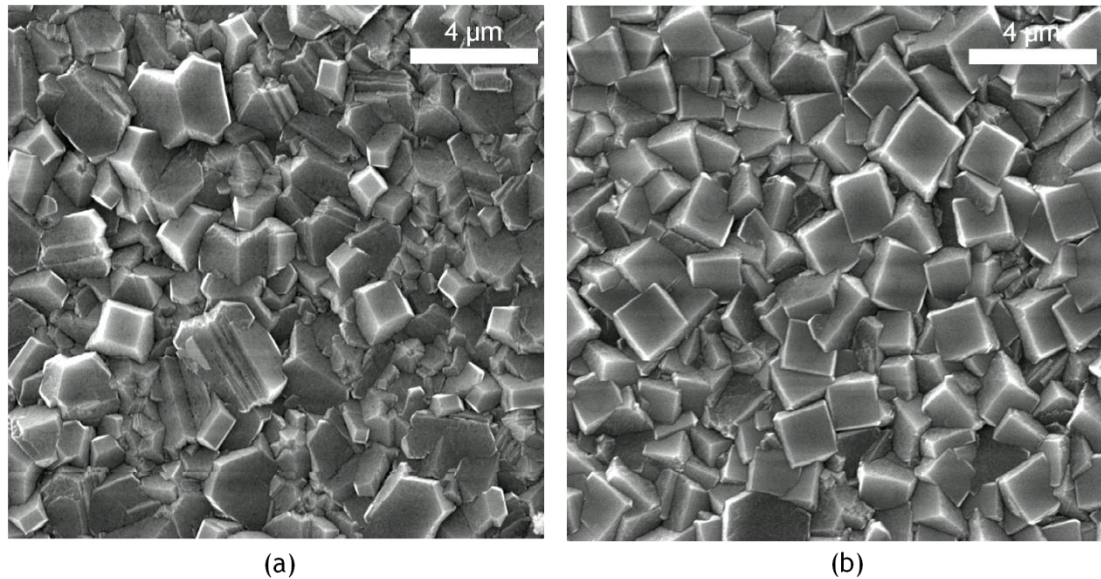


Figure 4.4: SEM micrographs of diamond films grown with addition of HMT sandwiched in between two diamond layers grown with (a) undoped diamond and (b) N-doped diamond, with N_2 gas used as the N precursor.

Laser Raman spectroscopy (Appendix D) confirmed that there were no changes in both the diamond sp^3 peak and the graphitic sp^2 peak for the entire range of samples grown with the addition of HMT sandwiched between two diamond films. The presence of HMT only changed the facets on the diamond surface and did not improve the overall quality of the diamond films produced. The sample grown with 0.56% N_2 in the gas phase was further analysed using SIMS. The effect of HMT on N atom incorporation into diamond was investigated and the results are discussed in Section 4.3.1.4.

4.3.1.3 Ammonia gas

Figure 4.5 shows the morphology of N-doped diamond grown with addition of NH_3 gas in the standard hydrogen/methane growth conditions. When 0.19% of NH_3 w.r.t. H_2 was introduced, evidence of (100) facets was clearly observed. At higher percentages (0.27% NH_3), the diamond films changed drastically into a cauliflower-like nanodiamond structure while

maintaining some microstructure features. The nanodiamond features were expected due to high concentration of HCN species in the gas phase [14,16] which enhanced the re-nucleation process. Interestingly, when even higher amount of ammonia gas were introduced into the gas phase (0.50% NH₃ and 0.68% NH₃), the (100) facets started to reappear. At 0.68% NH₃, the average size of the (100) grains and its amount increased if compared to when 0.50% NH₃ was introduced. It is believed that in richer ammonia gas atmospheres, the concentrations of HCN species increased further, leading to the decreasing of both concentrations of atomic H and •CH₃ [14]. High concentrations of HCN molecules reduced the gas-phase temperature due to the stability of these molecules. The substrate temperature and filament temperature also decreased, because HCN molecules acted as a 'heat sink' in the HF-CVD system [14]. The dissociation processes of CH₄ gas to form •CH₃ were reduced due to the reduction of the filament temperature. The dissociation processes of H₂ gas to form atomic H, however, were not as affected due to the lower dissociation energy of H₂ gas (240 kJ/mol) [14] compared to that of CH₄ (439 kJ/mol) [29]. The higher ratio of atomic H relative to •CH₃ reduced the rate of re-nucleation process and produced a higher quality of diamond crystals as the occurrence of re-arrangement mechanism. This led to formation of MCD films as illustrated in Figure 4.5(c) & (d)

However, when the ratio of NH₃/H₂ was increased still further (0.87% NH₃), another interesting phenomenon was observed. The morphology of the diamond films changed completely. The structure remained as MCD but most of the facets were randomised and less (100) facets were observed. In addition, the facets were covered with nanocrystalline diamond clusters or step-growth features. The details can be seen clearly in the inset in Figure 4.5(e). Further increases in the NH₃ concentration (1.24%) led to the same observation obtained using high concentrations of N₂ gas, discussed in Section 4.3.1.1. The films started to become discontinuous and non-uniform. This is probably due to the effects of the formation of HCN species in the reaction chamber, as discussed previously.

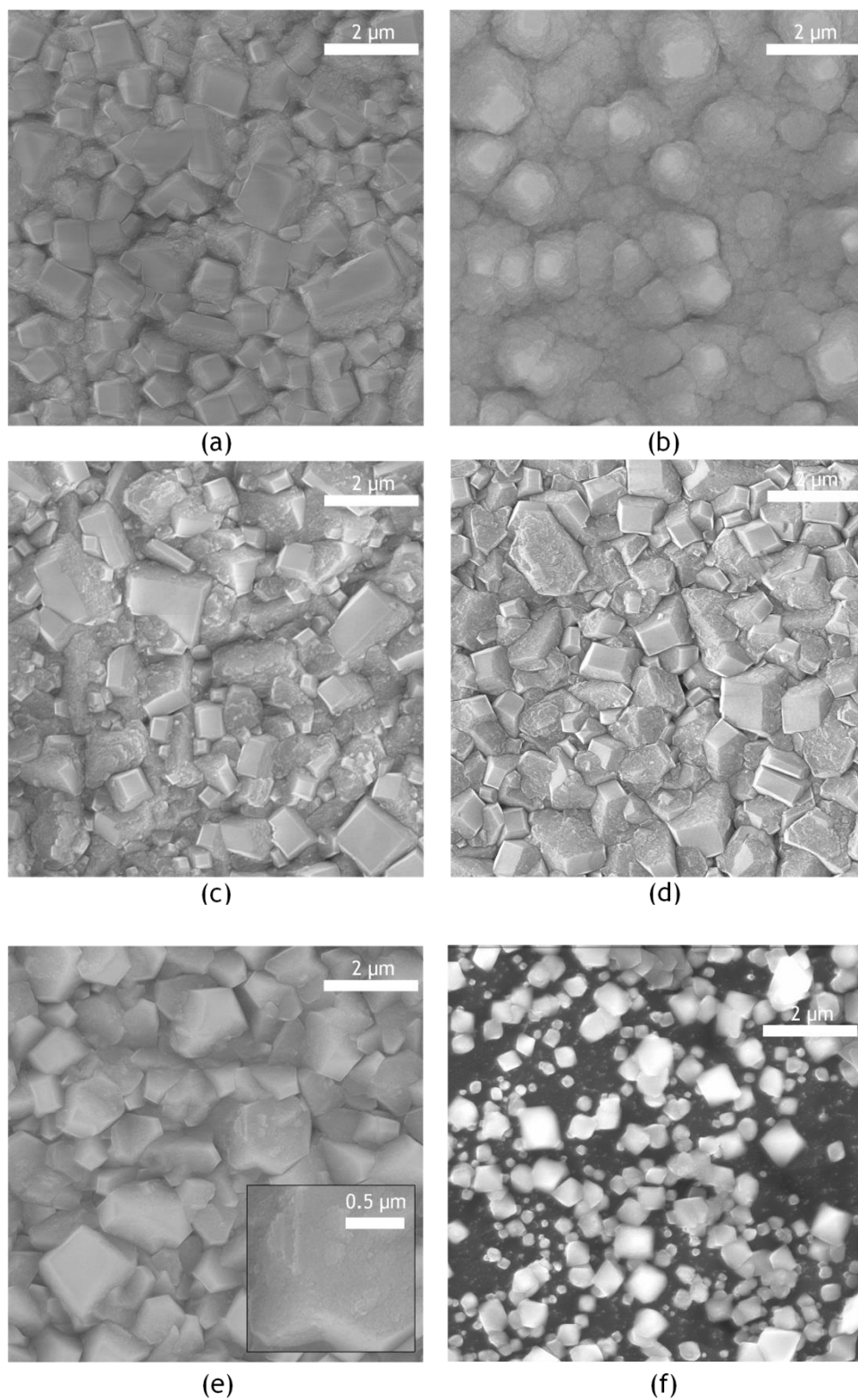


Figure 4.5: SEM micrographs of N-doped diamond grown on Si wafers with (a) 0.19%, (b) 0.27%, (c) 0.50%, (d) 0.68%, (e) 0.87% and (f) 1.24% in NH₃ w.r.t H₂. The inset in (e) is at higher magnification.

Figure 4.6 depicts the Raman spectra of N-doped diamond films grown on Si substrates with 0.19% to 1.24% of NH_3 in the gas phase. The spectra suggest that the diamond film that grew with 0.27% of NH_3 had the highest sp^2 graphitic content. This is consistent with the nanostructure features observed in the SEM micrograph in Figure 4.5(b). Typical NCD films have higher percentage of grain boundaries compared to MCD films [30,31]. The increased sp^2 signal was due to the increasing number of grain boundaries in the diamond films. When excessive amounts of ammonia are introduced into the gas phase (1.24% NH_3), there were no diamond peaks or graphitic peaks observed in the Raman spectrum. The crystals formed could be SiC as this is believed to be formed in the initial stages of growing CVD diamond on Si wafer [32]. All the other N-doped diamond films grown possessed typical MCD crystal structure with a small sp^2 graphitic peak observed in their Raman spectra. Surprisingly, the sample grown with 0.87% NH_3 , (Figure 4.5(e)), suggests the existence of NCD structure on the diamond surface but it exhibit the smallest sp^2 graphitic peak in Figure 4.6. These nanocrystal features may only exist on the surface and not throughout the bulk, which explained the small graphitic peak observed in the Raman spectrum.

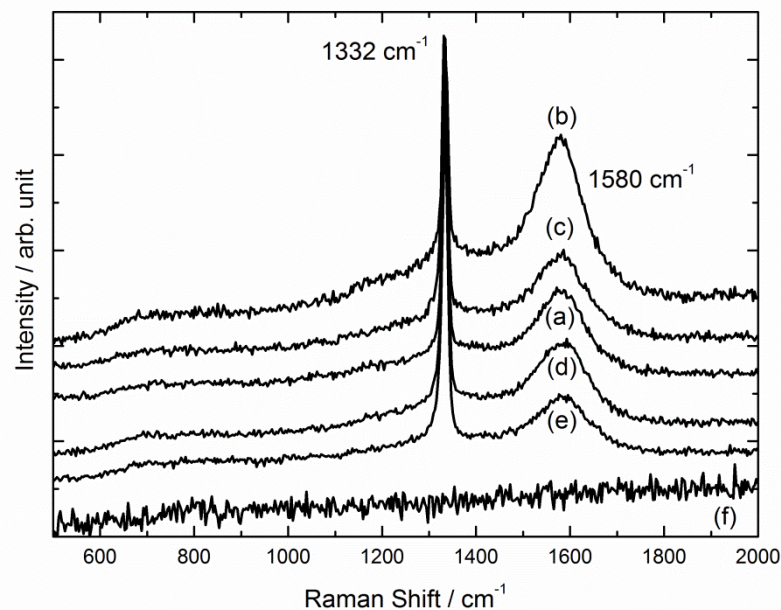


Figure 4.6: Raman spectrum (325 nm He-Cd laser excitation) of N-doped diamond grown on Si wafers with (a) 0.19%, (b) 0.27%, (c) 0.50%, (d) 0.68%, (e) 0.87% and (f) 1.24% NH₃. The spectra were normalised to the 1332 cm⁻¹ peak.

From both Raman spectra and SEM micrographs, the diamond film grown in 0.68% of NH₃ was chosen as the optimum sample. The film morphology and crystal quality is typical of N-doped MCD films with (100) facets as reported by others [16-18,33]. The N-doped diamond film was further analysed with SIMS to determine the amount of N atoms incorporated inside the material.

4.3.1.4 Determination of N Atoms in N-doped Diamond Films

Figure 4.7 shows the SIMS depth profile of N-doped diamond films grown with various nitrogen precursors and a standard HPHT type 1b diamond substrate purchased from Element Six Ltd. Nitrogen atoms were successfully incorporated in all diamond samples grown using the HF-CVD method. N-doped diamond films grown with 0.56% of N₂ in the gas phase had a constant doping of N atoms throughout the film with an average concentration of 2.84×10^{19} N atoms/cm³, depicted in Figure 4.7(a). An increase of N content was observed near the surface of the films. The existence of defect structure in graphitic carbon formed at the surface increased the uptake of N atoms due to higher solubility of N atoms in *sp*² compared to *sp*³ carbon [34].

When HMT was used, Figure 4.7(b) clearly depicts the increase in N atoms concentration. A maximum value of 2.09×10^{19} N atoms/cm⁻³ was detected using SIMS. After the introduction of HMT, an encapsulated layer was grown using standard growth conditions without the presence of N₂ gas. From the SIMS depth profile, it was confirmed that HMT alone was not sufficient to provide constant N doping due to a reduction of N concentration in the encapsulated diamond layer near the surface. In contrast, when NH₃ was used as an N precursor an abrupt increase in the N

atom concentration was detected using SIMS, as shown in Figure 4.7(c). An average of 2.05×10^{20} N atoms/cm³ was detected from SIMS depth profile. The doping level using NH₃ was constant throughout the film, similar to when using N₂ gas. However, 10 times the amount of N atoms were incorporated inside diamond films grown using NH₃ gas compared to the film grown using N₂ gas. This is because the energies available in a hot filament system are not sufficient to efficiently dissociate the strong triple bonds in N₂ gas (914 kJ mol⁻¹) compared to the weaker NH bonds (414 kJ mol⁻¹) in NH₃ gas [14], although this is less of an effect in higher power microwave plasma systems.

All three N-doped diamond films grown with different precursors were compared with HPHT single crystal type Ib diamond substrates produced by Element Six, Ltd. The general N content described by Element Six in their HPHT diamond substrates was <200 ppm. Figure 4.7(d) shows that the concentration of N atoms in a HPHT substrate remains constant, with an average N concentration of 5.56×10^{19} atoms/cm². This value is slightly more than was achieved in our experiments using N₂ gas, but ~4 times less than achieved using NH₃. Unfortunately, the concentrations of N atoms differ from one HPHT diamond substrate to the others. A wide range of N atom concentration was detected from various diamond type 1b substrates, from as low as 1.35×10^{19} atoms/cm² to 1.54×10^{20} atoms/cm². Therefore, we conclude that with such a wide variability in N content, HPHT substrates cannot be used as a reliable electronic material.

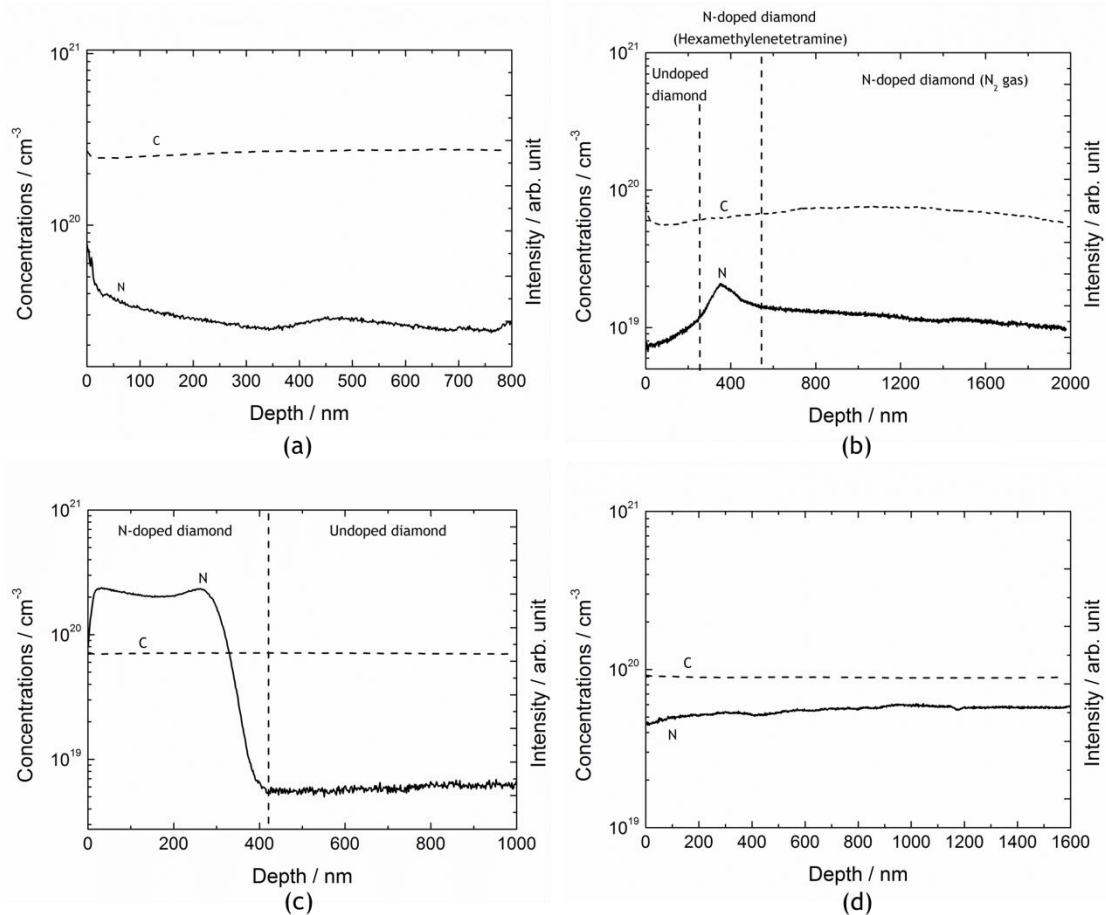


Figure 4.7: SIMS depth profile analysis of (a) N-doped diamond film grown with N_2 gas, (b) N-doped diamond film with N_2 gas and addition of HMT, (c) N-doped diamond film (Initial layer was grown as undoped diamond film followed by an additional layer grown with NH_3 gas) and (d) single-crystal HPHT SCD type Ib substrate purchased from Element Six, Ltd. Shown on the plots are the absolute calibrated concentrations of N, and the C intensity (used as the baseline from which the other concentrations were calculated), as a function of depth beneath the diamond surface.

4.3.1.5 Conclusion

From the observations on the morphology, crystal quality and N content in the diamond films, NH_3 gas was determined to be the optimal dopant to be used for subsequent Li-N co-doping experiments. The use of HMT resulted in homogenous and uniform (100) facets that could be utilised in the future. However, the film had only a low concentration of N atoms present in the diamond structure. N_2 gas is much less effective at producing

N incorporation in a hot filament reactor due to the strength of the N-N triple bond.

4.3.2 Li-N Co-Doped Diamond Films

Li-N co-doped diamond films were successfully synthesised following the procedure described in Section 4.2.2. Laser Raman spectra taken from the three types of diamond layer grown on Si substrates are shown in Figure 4.8. The Li-N-co-doped diamond layer exhibited a typical Raman spectrum that was very similar to that from undoped CVD diamond films grown with the same CH_4 content. The diamond peak at 1332 cm^{-1} and graphitic G-band at $\sim 1580\text{ cm}^{-1}$ are present, as expected for microcrystalline films, but no new peaks corresponding to N or Li are observed.

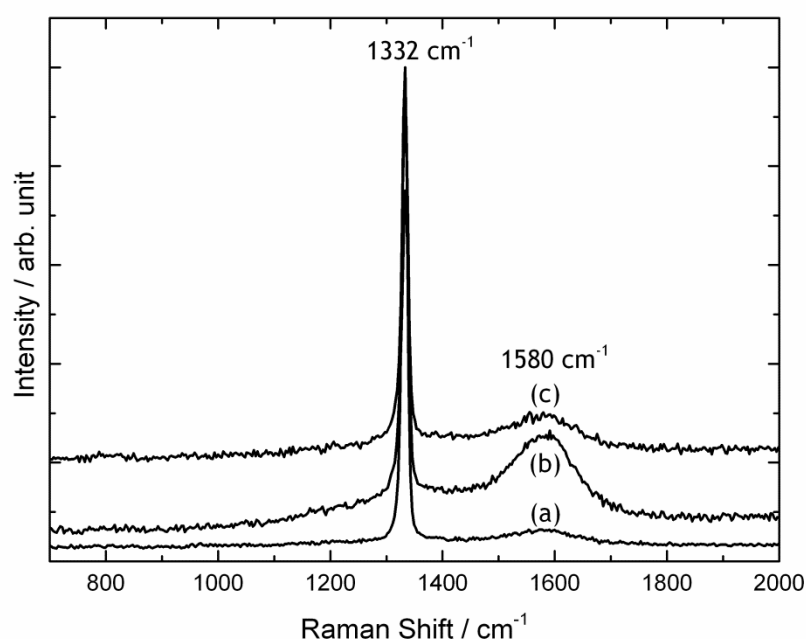


Figure 4.8 : Laser Raman spectrum (325 nm He-Cd excitation) obtained from different layers of the microcrystalline diamond films grown on Si. (a) Undoped diamond, (b) N-doped diamond, and (c) Li/N-co-doped diamond. The spectra have been normalised to the 1332 cm^{-1} peak.

Figure 4.9 shows the morphology of the microcrystalline diamond layers before and after the addition of lithium nitride. The undoped and N-doped diamond exhibited microcrystalline facets (Figure 4.9(a,b)), as expected. After addition of Li_3N the facets became much rougher (Figure 4.9(c,d)), suggesting new nucleation sites had been created, possibly as a result of localised etching of the surface by Li [35]. The etching and surface modification only occurred on the surface in a layer less than 100 nm in thickness (Figure 4.9(e)). Based on the micrographs and Raman spectra in Figure 4.8, we suggest that the Li preferentially etches the graphitic carbon at the grain boundaries of the diamond thin film. This might explain the reduction of the graphitic feature at 1580 cm^{-1} in Figure 4.8 suggesting the improvement in diamond quality was due to the etching and re-nucleation of diamond surfaces.

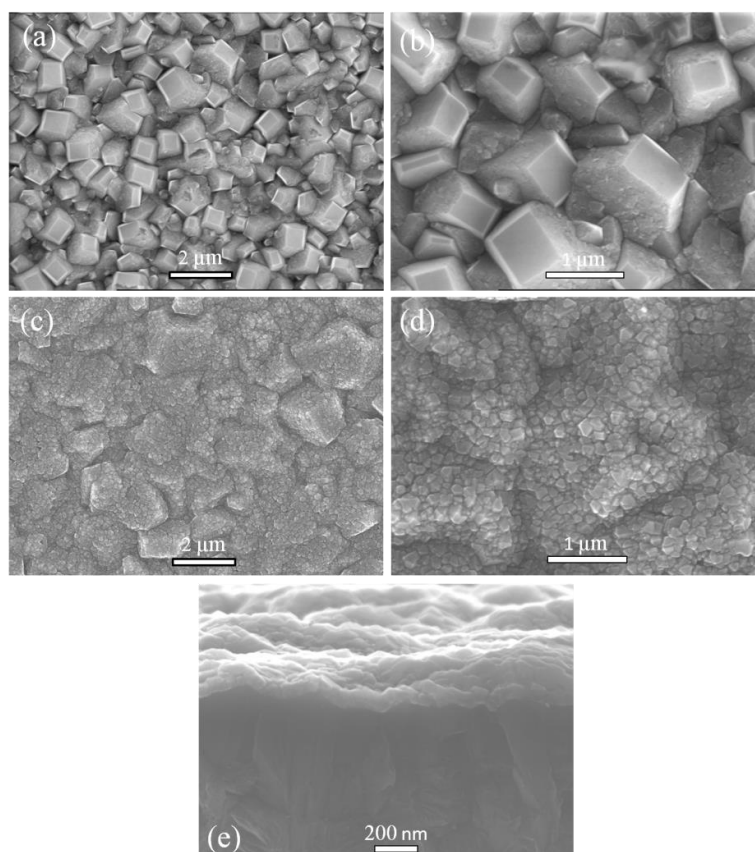


Figure 4.9: SEM micrographs showing the morphology of the two types of diamond film grown on Si substrates. (a) & (b) N-doped microcrystalline diamond. (c), (d) & (e) Li-N-co-doped diamond with (e) showing a cross-section through the film.

Further evidence for this theory comes from Figure 4.10, which shows the morphology of the N-doped diamond capping layer grown on top of the Li-N co-doped layer on a HPHT substrate. Figure 4.10(a) shows the surface of the single-crystal HPHT diamond substrate before the diamond growth process, with no visible defects or etch pits observed. Figure 4.10(b) shows that after deposition of Li_3N followed by $\sim 1\ \mu\text{m}$ of N-doped diamond capping layer, the diamond surfaces did not show any signs of significant renucleation and/or new crystal formation - the new diamond layers appear to be homoepitaxial with the HPHT substrate. There are some new superficial discolorations visible on the surface, in the form of stripes and lines, but these are $\ll 1\ \mu\text{m}$ in thickness and are probably due to variations in secondary electron emission yield from non-uniform H-termination. Raman spectra (not shown) show no sign of sp^2 carbon formed at new grain boundaries, indicating the new layers remain essentially single crystal. Similar surface effects were also observed on diamond films grown on the other HPHT substrates. These results are consistent with the idea mentioned above - because HPHT substrates are single crystal, there are no grain boundaries to be etched by the Li, and so the film growth is more uniform with no secondary nucleation.

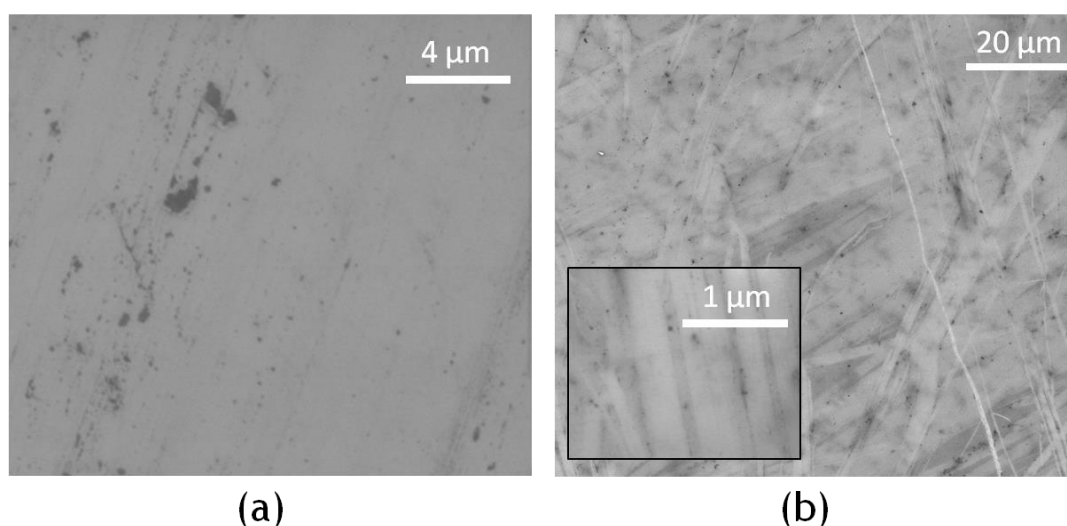


Figure 4.10: SEM micrographs of a HPHT substrate (a) before growth and (b) after growth of a 1- μm -thick N-doped diamond capping layer on top of a Li/N co-doped layer. The inset is at higher magnification. There are no obvious growth features on the surface, showing that the film was essential homogeneous. The dark marks are believed to be artefacts of the SEM showing regions

of lower secondary electron emission due to localized variation in H termination, and not due to changes in surface topology.

Figure 4.11 shows the SIMS depth-profile analysis of a multilayered Li-N-co-doped diamond thin film. The carbon signal remains constant for all the layers and serves as the baseline from which to calculate the concentrations of Li and N. The Li signal is centred at a depth of ~200 nm beneath the diamond surface, with a spread of ~ 100 nm either side due to diffusion, with a possible contribution of ± 20 nm due to SIMS mixing. The maximum concentration of Li detected was $5.02 \times 10^{19} \text{ cm}^{-3}$ with a total integrated dose of $3.73 \times 10^{21} \text{ cm}^{-3}$ of Li was detected throughout the diffusion region. The N signal was detected only in the first 500 nm inside the diamond thin film, as expected. The maximum concentration of nitrogen atoms embedded in the film was $4.42 \times 10^{20} \text{ cm}^{-3}$ which is ~9 times more than the Li content. This over-doping with N had been done to ensure all that all the Li atoms inside the diamond film were adjacent to at least one N and so were immobilised within the diamond lattice. It can be seen that the N-doped NCD diamond that grew on the outer surface (topmost 50 nm) still contains a considerable amount of Li, and a reduction in N. This may be due to the high solubility of Li in sp^2 carbon structures compared to diamond [34], which may have displaced some of the nitrogen.

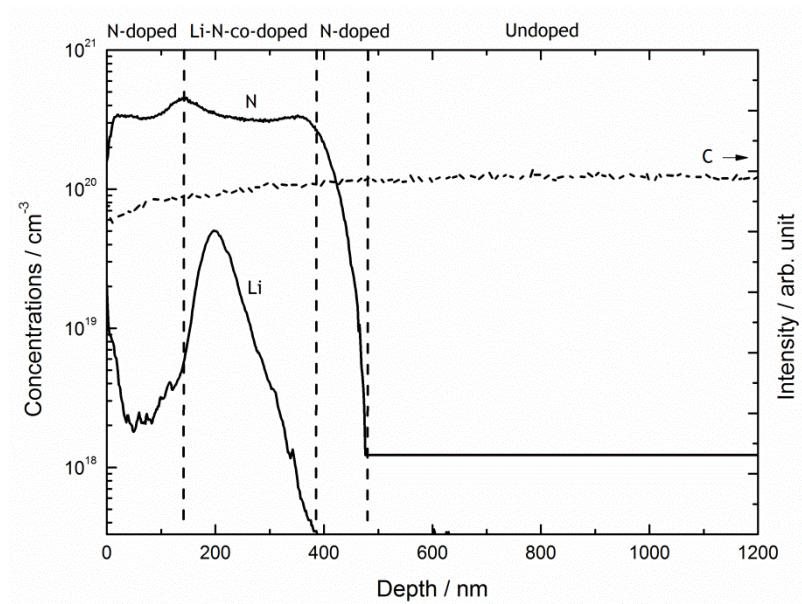


Figure 4.11: SIMS depth profile of a multilayered Li-N-co-doped diamond film grown on a Si substrate. This film had the following layered structure, indicated by the dashed vertical lines, starting from the Si substrate: $\sim 2 \mu\text{m}$ of undoped diamond, $\sim 0.5 \mu\text{m}$ of N-doped diamond (grown using NH_3), $\sim 200 \text{ nm}$ Li-N co-doped layer, $\sim 150 \text{ nm}$ N-doped diamond capping layer. Shown on the plot are the absolute calibrated concentrations of (i) Li and (ii) N, and (iii) C intensity (used as the baseline from which the other concentrations were calculated), as a function of depth beneath the diamond surface. The horizontal line for the N concentration in an undoped diamond region shows the lower limit of detection when the mass 26 signal is due entirely to C_2H_2 .

These results confirm that the Li_3N diffusion process followed by encapsulation produced a well-defined layer of diamond that contains localised high concentrations of N and Li. However, electrical testing showed that the 2-point resistivity of these films remained high ($\sim 15\text{-}50 \text{ M}\Omega$) suggesting either that the Li or its associated LiN_x defect centre were electrically inactive or that it has been overcompensated by too much N.

4.3.2.1 Multiple layers

In order to test whether it was possible to grow a diamond film with multiple embedded Li-rich layers, a sample was grown using the standard

procedures outlined above, but with ammonia gas acting as the nitrogen precursor, and repeated application of the Li_3N followed by an embedding layer. Figure 4.12 shows the SIMS depth profile for a film that had the following deposition sequence: Si substrate, 1st addition of Li_3N to form 300 nm of Li-N co-doped diamond layer, 2nd addition of Li_3N to create 250 nm of Li-N co-doped diamond layer, 3rd addition of Li_3N to produce 80 nm of Li-N co-doped diamond layer, and finally 20 nm of capping layer consisting of undoped diamond. As expected, the Li atoms are present in three localised layers within the diamond film. The first two additions have the same maximum Li concentration of $\sim 1.0 \times 10^{19} \text{ cm}^{-3}$ while the final addition has concentration up to $\sim 6.0 \times 10^{19} \text{ cm}^{-3}$. The minimum amount of Li detected was $\sim 1.0 \times 10^{18} \text{ cm}^{-3}$ while the concentration of N atoms inside the film during all three additions remained constant at $\sim 1.8 \times 10^{20} \text{ cm}^{-3}$. The concentration of the N dropped near the diamond surface due to the capping layer being grown without ammonia being present. This is essential to avoid any amine or other nitrogen derivatives terminating the diamond surface which may affect the conductivity of the film. However, the N:Li ratio was still 18:1, meaning that the dominant dopant of the film was nitrogen. Interestingly, the resistance of the film did not resemble the values obtained from typical N-doped diamond films ($>200 \text{ M}\Omega$ at room temperature [19,21]), being 10-20 $\text{M}\Omega$ at room temperature. This suggests that the incorporation of lithium and nitrogen in this way may enhance the conductivity of the film slightly but it is not yet sufficient for the film to be used in any semiconductor devices.

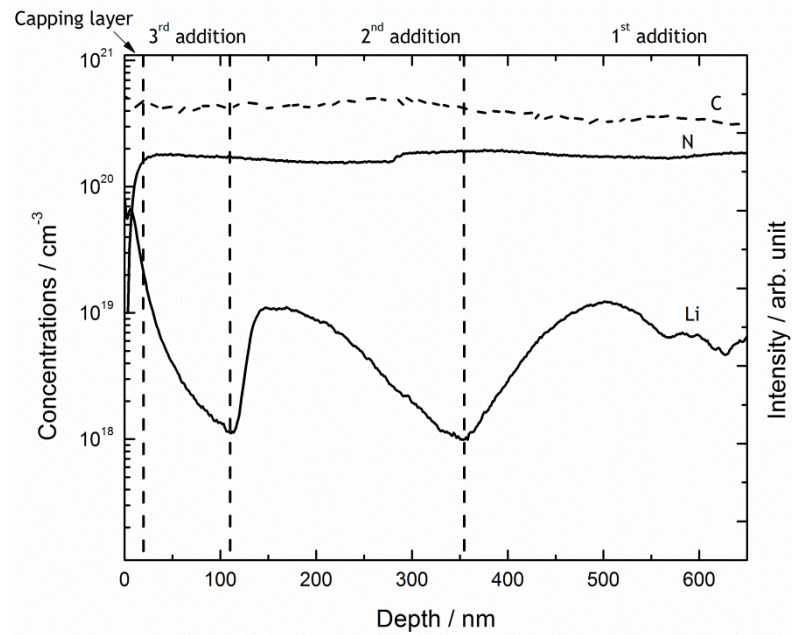


Figure 4.12: SIMS depth profile of a multi-layered Li-N co-doped diamond film grown on a Si substrate. This film had the following layered structure starting from the Si substrate: 1st layer of Li-N co-doped diamond, 2nd layer of Li-N co-doped diamond and then 3rd layer of Li-N co-doped diamond. The capping layer (~20 nm) was grown without the addition of ammonia into the gas phase. Shown on the plot are the absolute calibrated concentrations of Li and N, and C intensity, as a function of depth beneath the diamond surface.

4.3.2.2 Effect of grain boundaries on dopants

To understand the role of grain boundaries in diffusion of lithium into diamond, the same procedures were repeated using single-crystal HPHT type Ib diamond. Two films were grown, the first using N₂ with 20 μ l of Li₃N suspension and the other using NH₃ with 7 μ l of Li₃N suspension, and with different thicknesses of capping layers. A larger amount of Li₃N suspension was used for the N₂ growth because of the expected difficulty of dissociation of N₂ gas. The growth procedure was: HPHT substrate, ~0.5 μ m of N-doped diamond, Li₃N dropcast, N-doped capping layer (100 nm and 500 nm, respectively). Figure 4.13 shows the SIMS depth profile for the two films. As before (Section 4.3.1.4, above) there is ~10 times as much nitrogen present in the sample that was grown using NH₃ compared to the one grown using N₂. The total levels of N incorporated for both films are a

factor of ~100 lower than for the microcrystalline diamond case; indeed, for the N₂-grown sample the N content throughout the bulk of the film is below the detection limits except within the Li₃N layer. For Li it is interesting to compare the width of the Li peaks to gain insight into Li diffusion. For the microcrystalline films the Li peak had a spread of about 200 nm either side of the centre, whereas for single-crystal diamond the spread is much less (± 50 nm for the NH₃-grown sample) for the equivalent deposition time, of which ± 20 nm may be attributed to SIMS mixing. These findings suggest that grain boundaries play an important role in helping both N and Li diffuse through diamond, and they may even trap many of these species within the *sp*² grain boundaries.

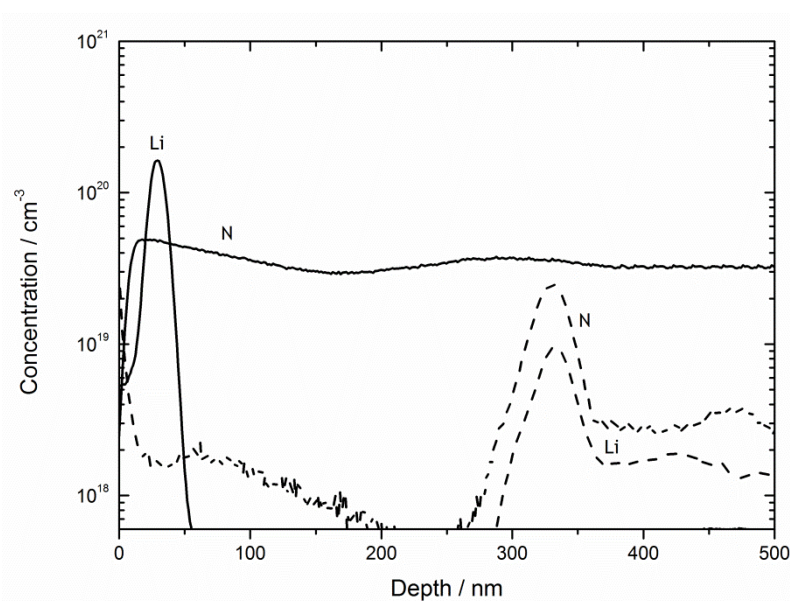


Figure 4.13: SIMS depth profile (top 500 nm only) of Li-N co-doped diamond films grown on HPHT type Ib substrates using NH₃ (solid lines) or N₂ (dashed lines) as the nitrogen precursors.

4.3.2.3 Lithium Saturation Point

In order to test whether it was possible to control the amount of Li incorporation, two deposition experiments were performed where the same procedure (Si substrate, growth of 2 μ m N-doped diamond, Li₃N drop cast,

deposition of ~150-200 nm of N-doped capping layer) was performed using (i) N₂ as the source of nitrogen and 100 μl of Li₃N in the first experiment, and (ii) NH₃ and 200 μl of Li₃N in the second. The results are shown in Figure 4.14(a) and (b). Doubling the amount of Li₃N had little effect upon either the maximum concentration of Li ($5 \times 10^{-19} \text{ cm}^{-3}$) or the total integrated amount of Li incorporated inside the films, which is $\sim 4.0 \times 10^{21}$ Li atoms in both cases. As before, the Li layer is localised ~200 nm below the surface, although diffusion has broadened the layer to a thickness ~300 nm. The diffusion profile is slightly asymmetric due to the longer diffusion time experienced by the Li atoms on the deeper side of the film.

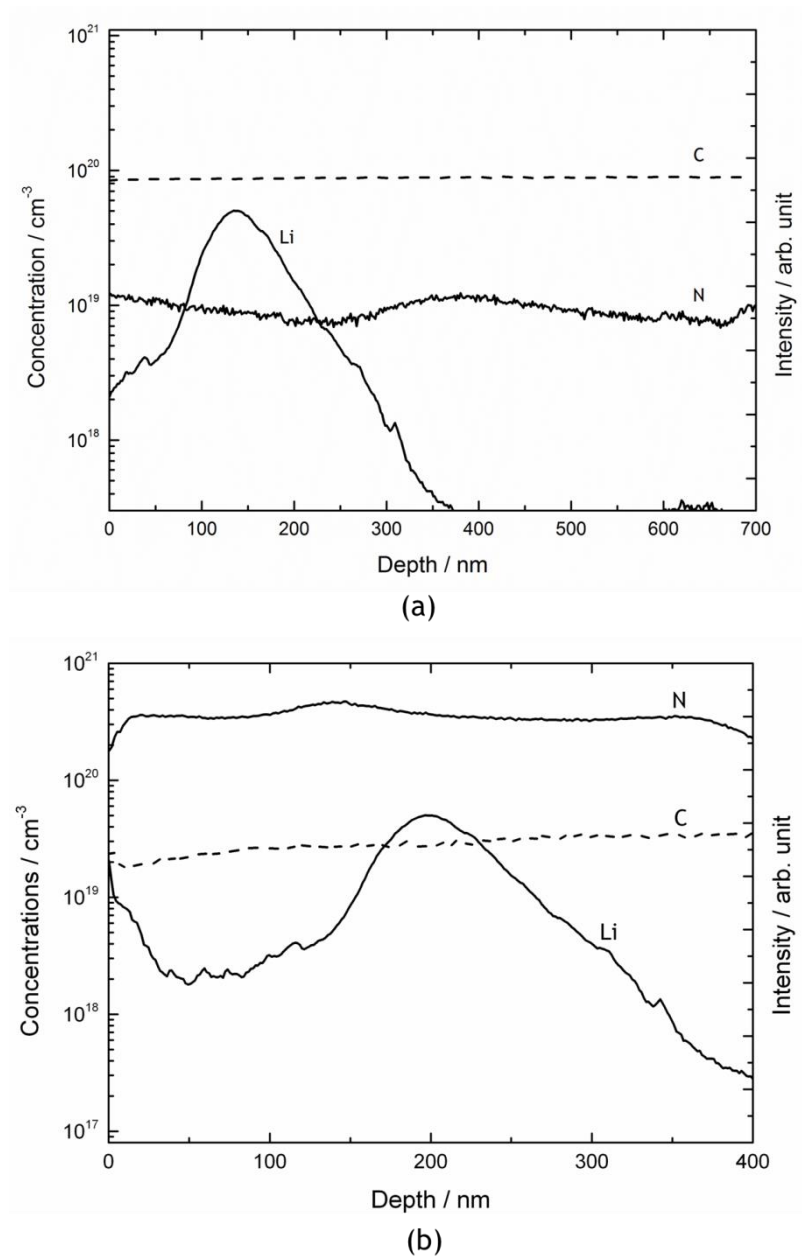


Figure 4.14: SIMS depth profiles (top 400 nm only) of samples grown with (a) N_2 gas and (b) NH_3 gas added to the CVD gas mixture. Li_3N was added after the film thickness was $\sim 2 \mu\text{m}$, and then a 200 nm capping layer was added using the same gas mixture as for the lower layer.

The fact that doubling the Li_3N amount did not change the Li content suggests that the amount of lithium has reached its solubility limit inside the diamond film. To confirm this, a third sample was grown using the same conditions as (ii) above (*i.e.* using NH_3), but with an even higher amount of Li_3N (300 μl). When attempting to grow the capping layer this instead produced a thin black flaky film which spontaneously delaminated

upon opening the chamber. The black flakes were analysed using laser Raman spectroscopy and no diamond or graphite peaks were observed, whilst SIMS showed them to be composed of Li and C. These findings are consistent with the black flakes being a form of a lithium carbide (Li_2C_2 , Li_4C , Li_6C_2 , etc.), although no further analysis was performed to identify them more precisely.

A fourth experiment was performed in which $2 \times 100 \mu\text{l}$ of Li_3N was added to the diamond surface sequentially, with an hour bake in H_2 in between. Again, subsequent diamond CVD resulted in the formation of the flaky lithium carbide. So we conclude that adding more Li to a diamond lattice that has reached its solid solution saturation point does not work, and the excess lithium reacts with the gas-phase carbon species to form lithium carbides, preventing further diamond deposition.

4.3.3 Electrical Resistance

Table 4.2: Electrical resistance of doped diamond films grown using various N and Li precursors.

Diamond	Dopant Precursors	Substrate	Resistance ($\text{M}\Omega$)
N-doped diamond	N_2 gas	Silicon Wafer	>200
	HMT		>200
	NH_3 gas		>200
Li-N co-doped diamond	Li_3N and N_2 gas	Silicon Wafer	25-75
	Li_3N and NH_3 gas		15-50
	Li_3N and N_2 gas	Type Ib HPHT	0.085
	Li_3N and NH_3 gas		0.250

Table 4.2 shows the electrical resistance measured using two-point probes on various diamond films grown using different N and Li precursors. All N-doped diamond samples grown in Section 4.2.1 showed high electrical resistance (>200 $\text{M}\Omega$). These were due to the compensation effect when

introducing a deep donor level in diamond lattice. A high activation energy is needed to excite electrons from the N-donor energy level into the conduction band minimum of diamond, which can be overcome at high temperatures leading to increased conductivity [18,36].

On the other hand, Li-N co-doped diamond films grown on silicon substrates had electrical resistance values ranging between 15 - 75 M Ω . There were no correlations between samples grown with N₂ or NH₃. Some samples were re-grown with similar conditions and the resistance values were not reproducible, the reasons for which are not fully understood. Interestingly, diamond films grown on HPHT substrates exhibited lower electrical resistance. The values were between 85 k Ω - 250 k Ω , although these values too were not reproducible when the samples were regrown under supposedly identical conditions. This may be due to the varying amount of N-content in the HPHT type Ib (see Section 4.2.3).

4.4 Conclusions

This chapter has demonstrated that it was possible to incorporate high concentrations of both dopants (Li, N) into different types of diamond films using solid Li₃N, NH₃, N₂ and solid HMT as sources of Li and N, respectively. The concentrations of both species are as high, or even higher, than those reported by other methods, such as in-diffusion or implantation, while not suffering from the lattice damage or poor process control that these other methods sometimes involve.

However, it appears that there is a solid solubility limit of around $5 \times 10^{19} \text{ cm}^{-3}$ for Li in diamond, above which the Li no longer incorporates but instead reacts with the gas-phase CVD species to form carbides. Below this limit, the Li content can be well controlled and localised into defined layers with a spread of $\pm 200 \text{ nm}$ for microcrystalline diamond and $\pm 50 \text{ nm}$ for single-crystal diamond.

This difference in diffusion between the two types of diamond has been attributed to the presence of grain boundaries which we suggest aid diffusion of both Li and N throughout the bulk. The fact that these species can be incorporated at concentrations 10-100 times higher in MCD than in SCD films also suggests that the grain boundaries act as sinks for these species. Thus, Li and N in grain boundaries may be mobile along and within the grain boundary network, but do not migrate into the grains themselves where the diffusion is much slower.

This model helps explain why the electrical conductivity of the Li-N co-doped films remained so low, despite the dopant concentrations being so high. Perhaps much of the Li and N is trapped as electrically inactive species within the sp^2 grain boundaries. Alternatively, it may be that the optimal ratio of Li:N was not obtained in these preliminary experiments, and a more exhaustive series of experiments needs to be performed with a wider range of Li:N ratios. Computer modelling of Li and N within the diamond lattice was performed to help identify optimal ratio that would give electrically active n-type diamond and discussed further in Chapter 5.

4.5 References

- [1] S.A. Kajihara, A. Antonelli, J. Bernholc, & R. Car, Phys. Rev. Lett. **66** (1991) 2010.
- [2] J.P. Goss, & P.R. Briddon, Phys. Rev. B **75** (2007) 75202.
- [3] A. Mainwood, J. Mater. Sci. Mater. Electron. **17** (2006) 453-458.
- [4] E.B. Lombardi, & A. Mainwood, Diamond Relat. Mater. **17** (2008) 1349-1352.
- [5] E.B. Lombardi, A. Mainwood, & K. Osuch, Phys. Rev. B **76** (2007) 155203.
- [6] E.B. Lombardi, & A. Mainwood, Phys. B Condens. Matter **401-402** (2007) 57-61.

- [7] A. Namba, Y. Yamamoto, H. Sumiya, Y. Nishibayashi, & T. Imai, *United States Pat.*, US 2006/1077962 A1, (2006).
- [8] J.E. Moussa, N. Marom, N. Sai, & J.R. Chelikowsky, *Phys. Rev. Lett.* **108** (2012) 226404.
- [9] A. Afzal, C.A. Rego, W. Ahmed, & R.I. Cherry, *Diamond Relat. Mater.* **7** (1998) 1033-1038.
- [10] R. Haubner, *Diam. Relat. Mater. Diam. 2004, 15th Eur. Conf. Diamond, Diamond-Like Mater. Carbon Nanotub. Nitrides Silicon Carbide* **14** (2005) 355-363.
- [11] A.J. Eccles, T.A. Steele, A. Afzal, C.A. Rego, W. Ahmed, P.W. May, & S.M. Leeds, *Thin Solid Films* **343-344** (1999) 627-631.
- [12] W. Ahmed, C.A. Rego, R. Cherry, A. Afzal, N. Ali, & I.U. Hassan, *Vacuum* **56** (2000) 153-158.
- [13] W. Muller-Sebert, E. Worner, F. Fuchs, C. Wild, & P. Koidl, *Appl. Phys. Lett.* **68** (1996) 759-760.
- [14] J.A. Smith, J.B. Wills, H.S. Moores, A.J. Orr-Ewing, M.N.R. Ashfold, Y.A. Mankelevich, & N. V Suetin, *J. Appl. Phys.* **92** (2002) 672-681.
- [15] S. Bohr, R. Haubner, & B. Lux, *Appl. Phys. Lett.* **68** (1996) 1075-1077.
- [16] P.W. May, P.R. Burrridge, C. A. Rego, R.S. Tsang, M.N.R. Ashfold, K.N. Rosser, R.E. Tanner, D. Cherns, & R. Vincent, *Diamond Relat. Mater.* **5** (1996) 354-358.
- [17] S. Jin, & T.D. Moustakas, *Appl. Phys. Lett.* **65** (1994) 403-405.
- [18] V. Baranauskas, B.B. Li, A. Peterlevitz, M.C. Tosin, & S.F. Durrant, *J. Appl. Phys.* **85** (1999) 7455-7458.
- [19] J. Mort, M.A. Machonkin, & K. Okumura, *Appl. Phys. Lett.* **59** (1991) 3148-3150.
- [20] J. A. Smith, M.A. Cook, S.R. Langford, S.A. Redman, & M.N.R. Ashfold, *Thin Solid Films* **368** (1999) 169-175.
- [21] V. Baranauskas, B.B. Li, A. Peterlevitz, M.C. Tosin, & S.F. Durrant, *J. Appl. Phys.* **85** (1999) 7455-7458.
- [22] L. Bergman, D. Alexson, P. Murphy, R. Nemanich, M. Dutta, M. Stroscio, C. Balkas, H. Shin, & R. Davis, *Phys. Rev. B* **59** (1999) 12977-12982.
- [23] L. Bergman, & R.J. Nemanich, *J. Appl. Phys.* **78** (1995) 6709.

- [24] P.W. May, & Y.A. Mankelevich, *J. Phys. Chem. C* **112** (2008) 12432-12441.
- [25] S. Matsumoto, Y. Sato, M. Tsutsumi, & N. Setaka, *J. Mater. Sci.* **17** (1982) 3106-3112.
- [26] E. Salgueiredo, M. Amaral, M.A. Neto, A.J.S. Fernandes, F.J. Oliveira, & R.F. Silva, *Vacuum* **85** (2011) 701-704.
- [27] P.W. May, *Philos. Trans. R. Soc. London. Ser. A Math. Phys. Eng. Sci.* **358** (2000) 473-495.
- [28] Z.M. Shah, & A. Mainwood, *Diamond Relat. Mater.* **17** (2008) 1307-1310.
- [29] S.J. Blanksby, & G.B. Ellison, *Acc. Chem. Res.* **36** (2003) 255-263.
- [30] J. Filik, *Spectrosc. Eur.* **17** (2005).
- [31] R.G. Buckley, T.D. Moustakas, L. Ye, & J. Varon, *J. Appl. Phys.* **66** (1989) 3595.
- [32] X. Jiang, & C. Jia, *Appl. Phys. Lett.* **1197** (1995) 13-16.
- [33] N. Jiang, A. Hatta, & T. Ito, *Japanes J. Appl. Phys.* **37** (1998) L1175-L1177.
- [34] N.A. Kaskhedikar, & J. Maier, *Adv. Mater.* **21** (2009) 2664-2680.
- [35] H. Sachdev, *Diamond Relat. Mater.* **10** (2001) 1390-1397.
- [36] J. Mort, K. Okumura, & M. Machonkin, *Philos. Mag. Part B* **63** (1991) 1031-1036.

Chapter 5: Theoretical Study of Li & N Clusters in Diamond

5.1 Introduction

Density Functional Theory (DFT) has been used in some form since the late 1920's to predict the electronic structure of various materials [1,2]. Advancement in past decades has allowed DFT functionality to evolve, allowing the Schrödinger equations to be solved to generally, a good degree of accuracy and thereby giving better understanding of bond energies, bond length of molecules and lattice structure. In addition, the properties of solids such as thermal conductivity, electrical conductivity, scattering and vibrations in solids (phonons) could also be understood.

By the early 1990's the DFT technique had advanced so that it could predict simple structures sufficiently accurately in reasonable computer time, and this instigated the first computational investigations of the diamond structure and its properties [3-9]. Soon after, computational studies moved on to investigate the effect of dopants in diamond. The detailed of boron-doped diamond were first studied using DFT techniques by Briddon and co-workers [10]. Nitrogen-doped diamond was first calculated using molecular-orbital (Hartree-Fock) techniques [11] and re-calculated using DFT by Kajihara. The nitrogen energy level in diamond was predicted at 1.7 eV below the CBM of diamond [12]. This high activation energy classified N atoms as deep donors in the diamond lattice. As computational calculations took less time compared to experiments, scientists started to calculate the effects of incorporation of various elements and combination of elements in pursuit of the elusive shallow donor for n-type diamond films [13].

Apart from N atoms as a potential donor in diamond, Kajihara and co-workers also reported that interstitial Li atoms will act as shallow donors in the diamond structure, with an activation energy of 0.1 eV to excite an electron from the Fermi level to the CBM of diamond [12]. However, the large formation energy required to substitute a C atom with a Li atom in the diamond lattice leads to low solubility of Li atoms in

diamond. In addition, under standard diamond growth conditions Li has a relatively high mobility in the diamond, leading to non-uniform concentration profiles and inhomogeneous doping. These findings, together with further experimental reports in the mid-1990s showing that incorporated Li resulted mainly in electrically inactive diamond, meant that interest in performing theoretical calculations on such an ‘unpromising’ dopant declined [14,15].

A decade passed, and with further advancement of the DFT technique it became possible to study the role of small dopant atoms in diamond in greater detail than before. As a result, interest in Li doping was rekindled. New studies by Mainwood’s group (King’s College London) and Goss’s group (Newcastle University) in the United Kingdom provided greater insight on how Li atoms behave in the diamond structure [16-22]. The effect of clustering that inhibits the ability of Li atoms to perform as shallow donors was also investigated.

The major challenge faced by experimentalists when producing Li-doped diamond was to make it behave as a shallow n-type semiconductor, but this was controlled by the position adopted by the Li atoms within the diamond lattice. Li is small enough to insert into an interstitial site, and when it does, calculations predict this leads to formation of a shallow donor (0.1 - 0.3 eV below the CBM of diamond) [16,23]. However, when Li substitutes for C in the lattice sites (or fills a vacancy site), it acts as a deep acceptor [18]. The two Li types compensate each other, which would not be a problem if the Li could be preferentially grown into one of the sites. Unfortunately, experimentally it proved extremely difficult to control the growth process to favour the interstitial position [22], and the resulting mixture of Li sites leads to uncontrolled, poor or zero electrical activity.

Li also plays an interesting role when at the diamond surface. Lithiation (adding LiO groups to the diamond surface) has been shown both experimentally and theoretically to increase the negative electron affinity (NEA) of the diamond surface, and remain stable at temperatures up to

1000 K. Such NEA surfaces enhance the emission of electrons from the bulk diamond into the vacuum [24-26]. Other groups have used DFT to explore the effects of other termination species, such as F, Cl, Br, Co, Cu, and Ti [27-31]. These enhancement effects are discussed further in Chapter 6 and Chapter 7.

These prior reports suggest that Li may hold the key to solving the issue of electrical conductivity in diamond, whether in bulk or at the surface. To complement the experimental work on Li+N doping discussed in Chapter 4, result of DFT calculations are reported in order to have better understanding of Li atoms in diamond. The major aims were to find shallow donor atom clusters (<0.3 eV energy level below the CBM of diamond) consisting of Li and N that could be formed inside the diamond lattice at particular concentrations of Li, and Li/N ratios. The Li within these clusters needs to remain as a shallow donor without having any compensation due to the presence of other Li nearby.

The Cambridge Serial Total Energy Package (CASTEP) codes were used in this study. The codes were developed by Mike Payne and his group in 1986 [32]. In these codes, plane-wave basis sets were used and pseudopotentials were used to replace the core electrons, and this approach is known as the plane-wave pseudopotential (PWP) method. For large numbers of atoms and electrons (>100 atoms), the PWP approach is sufficiently accurate, general, robust and efficient, and this makes it ideal for the study of condensed matter. Having PWP embedded in the CASTEP code reduced the computer time needed and made large-scale DFT calculations possible on a large unit cell of diamond.

In this study, the CASTEP codes were used to generate general information about the diamond lattice, including the formation energy of Li-N co-doped-diamond structures, the bond lengths between the dopants and the neighbouring C atoms, and the band structure of the material. While OptaDOS was used to calculate the density-of-states (DOS) [33].

5.2 Details of calculations

All calculations in this study were done using parallel computing facilities situated in the Advanced Computing Research Centre (ACRC), University of Bristol. The facility consists of two clusters; BlueCrystal Phase 1 and BlueCrystal Phase 2. Since the CASTEP codes can be run on parallel message passing interface (MPI) systems, BlueCrystal Phase 2 could be used in order to reduce the computational time needed.

The calculation started with geometry optimisation of a cubic supercell (see Section 5.2.1) consisting of 64 carbon atoms, using four nodes and eight processors in each node, with 24 hours wall time. Next, k-point optimisation (see Section 5.2.3) utilised only two nodes with eight processors in each nodes with 12 hours wall time. This was followed by the band structure calculation (see Section 5.2.4) consuming eight nodes with eight processors in each node with 48 hours wall time. Finally, the DOS calculations used 12 nodes with eight processors in each node with 72 hours wall time.

5.2.1 Geometry Optimisation

Various sizes of supercell were investigated ranging in size from 8 to 216 atoms. 8, 16 and 32 atom supercells provide inaccurate information due the convergence of energies with cell size. The supercell needs to be large enough so the defect introduced into the supercell will not be interacting between one another. The energy per unit carbon in each supercell should be similar with other supercell to determine the accuracy of the supercell used. 216 atoms supercell was not used in this study because of the extra computational time it requires. 64 atom supercell was deemed to be sufficient to be used as the basic supercell for the dopant in diamond calculations discussed in this chapter [18].

The generalised gradient approximation (GGA) with the Perdew-Burke-Ernzerhof (PBE) [34] exchange-correlation functional was used employing a 64-atom supercell constructed using 2×2×2 conventional f.c.c. diamond unit cells. The plane-wave basis-set cut-off energy was set at 391 eV. A 3×3×3 mesh of k-points was used for the integration over the Brillouin zone and further increasing the number of mesh points did not make a significant difference.

This calculation employed periodic boundaries. First, the undefective lattice parameter was determined by varying the size of the primitive unit cell and determining which value gave the lowest energy resulting unit cell parameter of 3.568 Å for the cubic diamond unit cell compares well with the experimental value of 3.567 Å [35,36]. The lattice parameter was then kept constant throughout the calculations on the defect (doped) diamond supercell while the positions of the atoms were optimised. The dopant was inserted into diamond lattice without any symmetry constraints.

Calculations were done using local density approximation (LDA) to compare with PBE. Two sets of supercells were used, 2×2×2 (64 atoms) and 3×3×3 (216 atoms) conventional f.c.c. diamond unit cells. The energy per atom must not change even larger supercell was used in the calculations. However, by using LDA as the exchange-correlation function, the energy per atom for 64 atom and 216 atom supercells differ by ~0.8 eV/atom while when using PBE for both supercells the energy per atom differ by <0.001 eV/atom. Thus, PBE was chosen as the best exchange-correlation function and used in all calculations discussed in this chapter.

5.2.2 Formation Energy

The formation energy, ΔE_f of doped diamond was calculated using:

$$\Delta E_f = E_{\text{tot}}^{\text{Def}} - E_{\text{tot}}^{\text{Perf}} - \sum n_i \mu_i + q(E_F + E_v + \Delta V) + 0.5q^2 \quad (5.1)$$

where

$$q = -\Delta n_e \quad (5.2)$$

$E_{\text{tot}}^{\text{Def}}$ is the energy of the doped diamond supercell, $E_{\text{tot}}^{\text{Perf}}$ is the energy of a perfect (undoped) diamond supercell, n is the number of atoms added (+) or removed (-) from the supercell and μ is the chemical potential of the atoms added to the diamond. The difference in number of electrons added or removed from the cell is Δn_e . E_F is the Fermi energy of the material, E_v is the energy of the valence band maximum (VBM) of the defective diamond structure and ΔV is the difference between the average electron potential of doped diamond and perfect (undoped) diamond. $0.5q^2$ is the correction term using the Madelung term [22] for a cubic supercell with a side length of $2a_0$, which is needed when the unit cell is non-neutral.

5.2.3 K-point Optimisation

Before any band structure calculation took place, k-point optimisation needed to be performed to ensure sufficient points in the Brillouin zone were used to ensure convergence while also minimising the computational time required. The geometry output file obtained from the geometry optimisation calculation of the diamond supercell was used as the input file in this optimisation. Single point energy calculations were done with different k-point values range from $2 \times 2 \times 2$ to $7 \times 7 \times 7$, and the energies obtained plotted in a graph as depicted in Figure 5.1. The optimum k-point condition was determined by a trade-off between the minimum energy obtained from the calculation and a reasonable computational time taken to complete the calculations. Most of the calculations employed $4 \times 4 \times 4$ k-point selection for their band structure calculations.

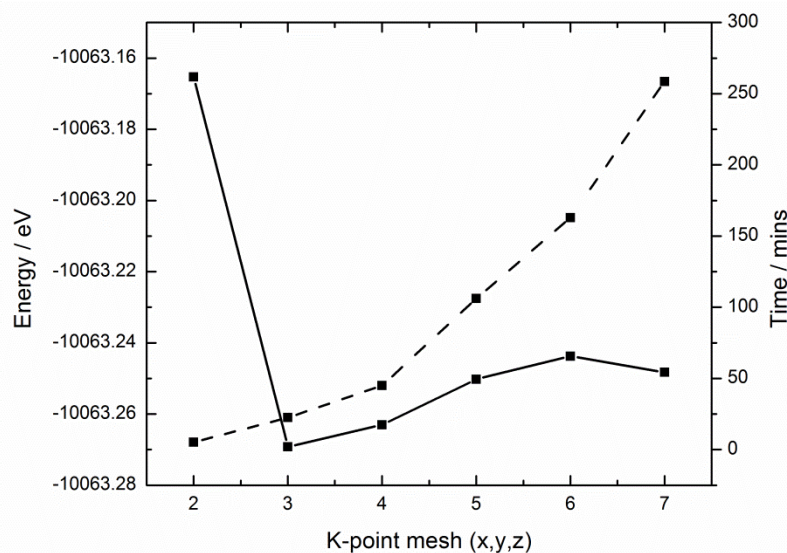


Figure 5.1: Energy of nitrogen defect in diamond 64 atom supercell and time taken for the calculations vs. the k-point mesh used. Solid line represents energy for the defective supercell while dashed line represents the time taken for the calculation to be completed.

5.2.4 Band Structure Calculation

After obtaining the optimised geometry and the optimum set of k-points for further calculating the calculations on the defective diamond were performed, it is customary to report dispersion curves particular high-symmetry direction in the Brillouin zone. The standard path for f.c.c. lattice was chosen: X-R- Γ -X-M- Γ [18] which fractional coordinate of Γ , X, R and M are (0.0, 0.0, 0.0), (0.5, 0.0, 0.0), (0.5, 0.5, 0.5) and (0.5, 0.5, 0.0). The output file then was analysed using the software ‘castep_utilities’ tools prepared by Dr. Kane O’Donnell in order to determine the band structure.

5.2.5 Density of State (DOS) Calculation

The DOS calculation was carried out using the CASTEP code ‘optics’. A later version of CASTEP renames the job code as ‘spectra’. Another series of convergence runs were done to optimise the ‘optics k-point’. The objective of the k-point optimisation was similar to that of the previous

optimisation; to ensure the data points in the calculation were sufficient while not jeopardising the computational time. The optimum ‘optics k-point’ was set to $10 \times 10 \times 10$.

The output files obtained from CASTEP then underwent further analysis using OptaDOS software in order to determine the DOS. OptaDOS average out over large number of k-points in the Brillouin zone to get the DOS.

5.2.6 Dopants in Diamond

Series of dopants such as Li, N and mixtures of both at different ratios were used in this study to search for a suitable shallow dopant that would enhance the n-type semiconducting properties of diamond material. The fractional positions of each dopant in the unit cell were summarised in Appendix E. Once the chosen undefective diamond unit cell had undergone a geometry optimisation calculation, the output file was used as the input file for dopant calculations. For substitutional dopants, the carbon atoms were directly replaced with the dopant of interest. However, for interstitial dopants the dopant atoms were placed in three possible interstitial sites, T_d (tetrahedral site), T_h (interstitial site on the hexagon plane of the diamond) and T_c (at the centre of the unit cell) as depicted in Figure 5.2. When the dopants were positioned on the interstitial site, care was taken that a special high symmetry point was not selected. After the series of calculations were complete, T_d was found to be the interstitial site with the lowest energy per unit cell, suggesting that this is the most stable and preferable such site for lithium dopants. This result agrees with previous researchers [16,17,22,23].

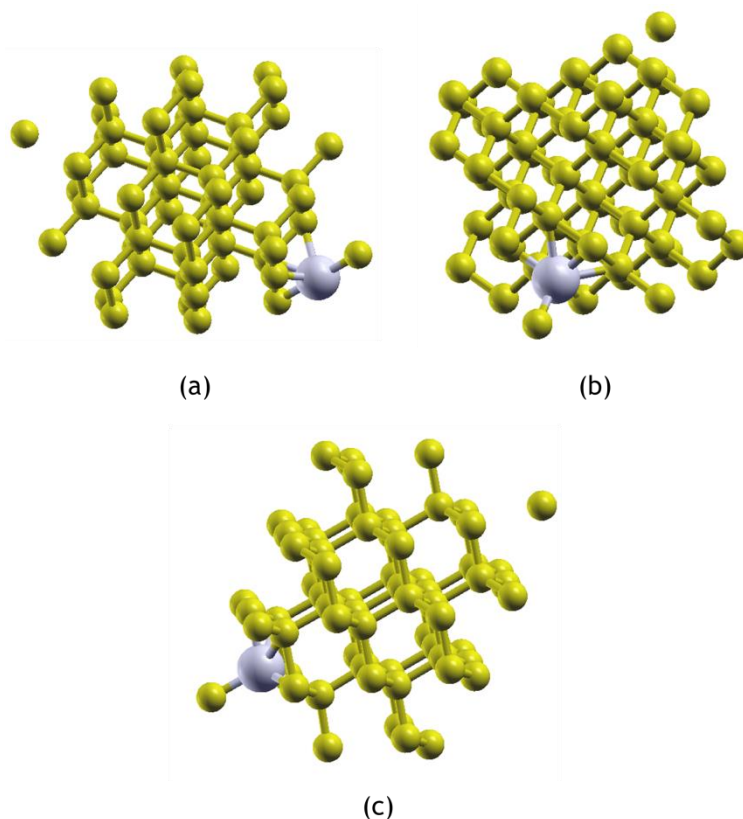


Figure 5.2: The possible interstitial sites of Li in diamond lattice, (a) T_d , tetrahedral site, (b) T_h , interstitial site on the hexagon plane of the diamond and (c) T_c , at the centre of the unit cell.

For co-doping, N atoms were also added to the diamond supercell along with the Li, and the Li:N ratio was varied depending on the type of cluster studied as illustrated in Figure 5.3. When adding two N atoms for the 1:2 ratio, the N atoms were placed opposite each other forming a N-Li-N arrangement. For a 1:3 ratio, the N atoms were bonded to Li atom as depicted in Figure 5.3(c). Lastly, for the 1:4 ratio of Li and N, the N atoms formed a cage-like structure encapsulating the Li in the middle of the N atoms. The fractional position for all clusters in the supercell were summarised in Appendix F.

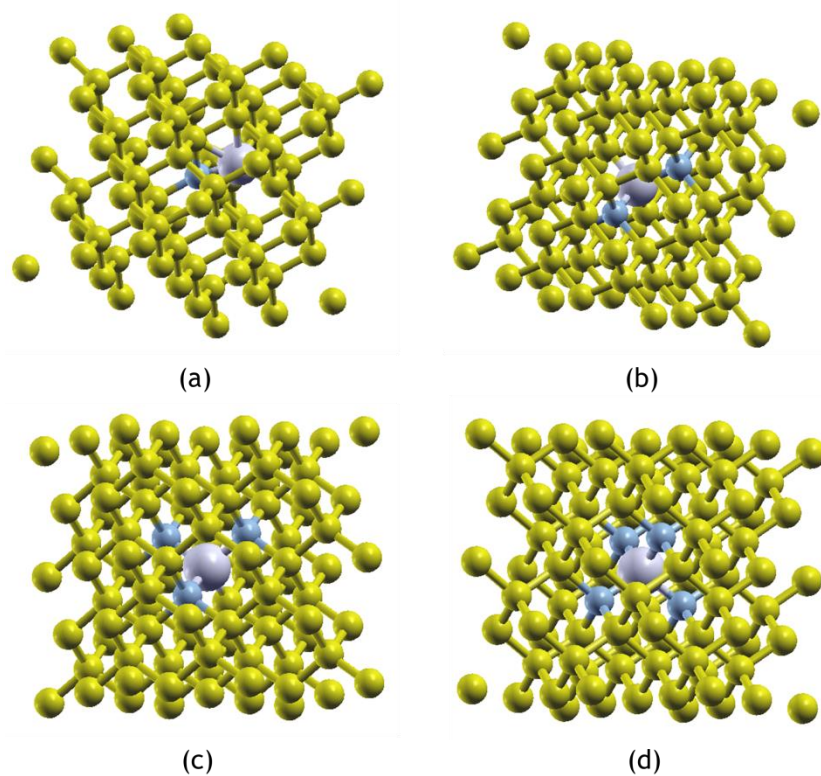


Figure 5.3: The Li-N clusters in substitutional sites with ratio of Li-to-N of (a) 1:1, (b) 1:2, (c) 1:3 and (d) 1:4.

5.3 Results and Discussion

5.3.1 Pure Diamond

To check that the model had been set up correctly, CASTEP was first used to simulate the structure and properties of pure diamond. The optimised diamond structure calculated had a carbon-carbon bond length of 1.55 Å, comparable with the experimental value and good lattice parameter as showed in Section 5.2.1 [35]. Figure 5.4 shows the GGA band structure of pure diamond and the DOS produced using the CASTEP code. The calculated band gap of diamond was 4.06 eV, which is in agreement with the values calculated using similar methods by the group at KCL [16] (~4.1 eV). However, this value is much lower than the experimental value, 5.4 eV [36]. The difference is due to the limitations arising from the theoretical model. Underestimation of band gap is a well-known failure of

DFT and due to the approximations in the exchange-correlation. Thus, the result produced from the calculations did not resemble the true value of the band structure of the diamond material and could not be used directly as quantitative analysis. Nevertheless, it was used qualitatively as a model to compare between pure diamond and doped-diamond structures. Based on Figure 5.4, the Fermi level of pure diamond (undoped) was observed near the valence band maximum (VBM) of the structure with the value of 0.80 eV above the VBM.

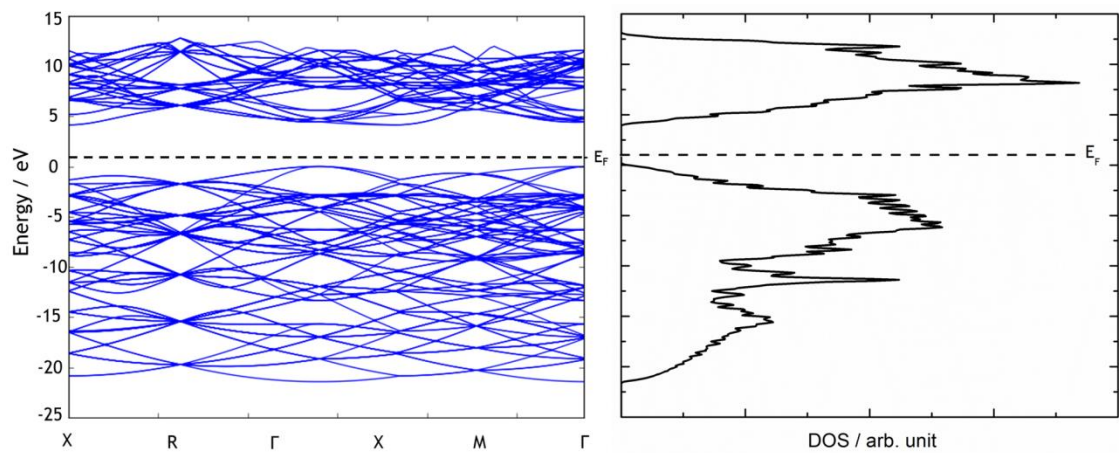


Figure 5.4: Band structure and DOS of pure diamond from the 64 atoms supercell calculated using CASTEP. From here onwards, E_F is the Fermi level and energy levels situated below the E_F are occupied with electrons while energy levels situated above the E_F are unoccupied.

5.3.2 Nitrogen in Diamond

When an atom of nitrogen was substituted for an existing carbon atom in the diamond structure, the formation energy, ΔE_f as defined in Equation 5.1 for the process was found to be 4.13 eV. The chemical equation for this process showed in Equation 5.3. The positive formation energy indicates that the process is not spontaneous and the substitution will not occur at room temperature or even at CVD diamond growth temperature (1100 K). The energy required is so large mainly due to the requirement of removing a strongly-bonded C atom from the structure.

Furthermore, strain is induced in the lattice since N atom has a covalent radius of 0.72 Å while the C atom has a covalent radius of 0.77 Å. Alternatively, if the N atom simply added into an existing vacancy site in the diamond structure, the formation energy is reduced to -2.62 eV. The chemical equation for this process showed in Equation 5.4. Negative formation energy indicates a spontaneous reaction which is thermodynamically favourable. When diamond films are prepared using CVD, the formation of vacancies are inevitable [37,38]. These energy values suggest that the addition of N atoms into the diamond structure will be dependent mainly on the availability of vacancy sites created during the CVD process which can spontaneously trap N atoms, rather than N displacing C atoms bonded in the lattice.

Formation of nitrogen-doped diamond from undefective diamond:



Formation of nitrogen-doped diamond from vacancies in diamond:



The calculated C-N bond length in the lattice was 1.59 Å, which is 0.04 Å longer than the C-C bond (1.55 Å). To compensate for this, the bond length of the next neighbouring carbons shortened to 1.53 Å. The lengths of C-C bonds situated far away from the dopant position remain unchanged. This indicates that the structure is strained only within a few atoms of the dopant position.

Figure 5.5 illustrates the band structure and DOS of nitrogen-doped diamond calculated using CASTEP. The calculation shows the nitrogen energy level situated right at the bottom of the CBM and the Fermi level lying within the bottom of CBM. The nitrogen energy level was 0.31 eV below the conduction band minimum (CBM) of the diamond structure. This indicates a deep donor level state in the diamond lattice [12].

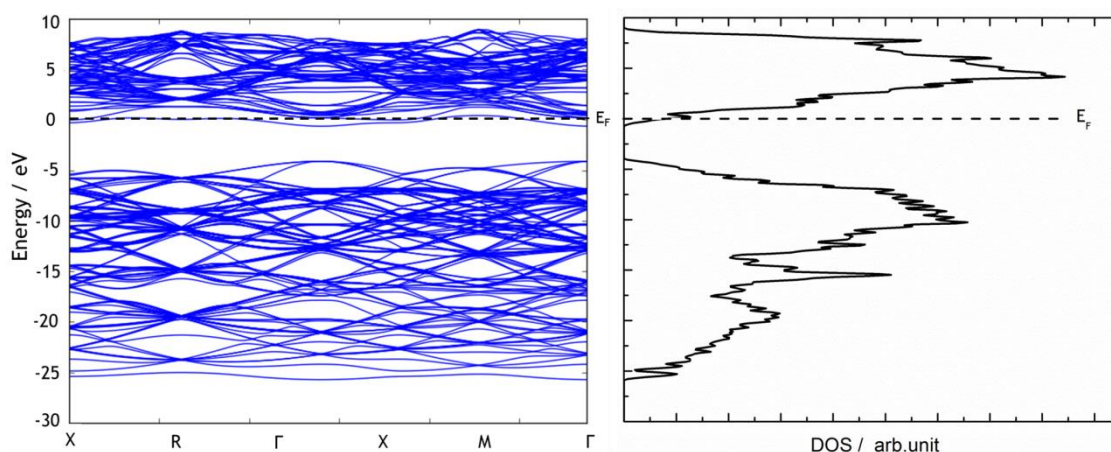
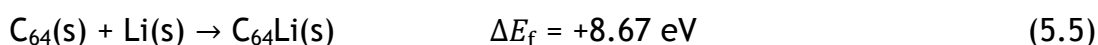


Figure 5.5: Band structure and DOS of nitrogen-doped diamond from the 64-atom supercell produced using CASTEP.

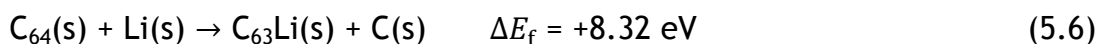
5.3.3 Lithium in Diamond

Using Equation 5.1, the formation energies for interstitial and substitutional lithium atoms were found to be 8.67 eV and 8.32 eV, respectively. The chemical equations for these processes are shown in Equation 5.5 and Equation 5.6. The difference between these values was small, and this implies that both locations are possible with roughly equal amounts in both. However, if the Li dopant sits in an existing vacancy site (in a similar way to N, discussed in section 5.3.2), the formation energy is only 1.57 eV. The chemical equation for this process is shown in Equation 5.7. Even though the formation energy is much less for this process, the reaction is still non-spontaneous due to its positive energy. The vast majority of CVD (and other) techniques used in growing diamond will produce vacancy sites in the structure during growth. As a result, Li introduced during a diamond growth process will predominantly occupy substitutional sites following the lower energy step of capture by a vacancy, although some Li will also remain in interstitial positions.

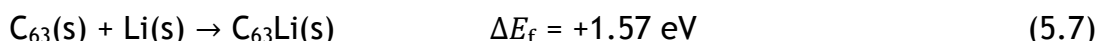
Formation of Li-doped diamond (interstitial) from undefective diamond:



Formation of Li-doped diamond (substitutional) from undefective diamond:



Formation of Li-doped diamond (substitutional) from vacancies in diamond:



The addition of lithium to an interstitial site reduces the C-C bond length of the neighbouring carbons to 1.49 Å, a 4% reduction in length compared with the C-C bond length in undoped diamond (1.55 Å). The calculations show that the lowest energy of Li interstitial site was the T_d interstitial site [17]. The Li-C bond length was 1.63 Å, similar to that obtained by Lombardi and Mainwood [17]. Changing the position of Li from interstitial to substitutional increases the Li-C bond length from 1.63 Å to 1.74 Å but the neighbouring C-C bond lengths remain unchanged. In both substitutional and interstitial sites, the C-C bond length for carbon atoms situated far away from the defect sites remains unchanged.

5.3.3.1 Interstitial Site

Figure 5.6 depicts the band structure and DOS of Li-doped diamond residing in an interstitial site. The Li energy level merges with the conduction band with the Fermi level lying within and just below the CBM. The value was smaller compared to previous calculations by other groups (0.1-0.3 eV) [12,23]. Furthermore, the Li 2s orbital energy level seems to be distributed just below the CBM of diamond, as in the band structure produced by Lombardi & Mainwood [16]. It is indeed a suitable shallow

donor candidate but due to the competition with the formation of lithium at the substitutional site, further improvement needs to be done.

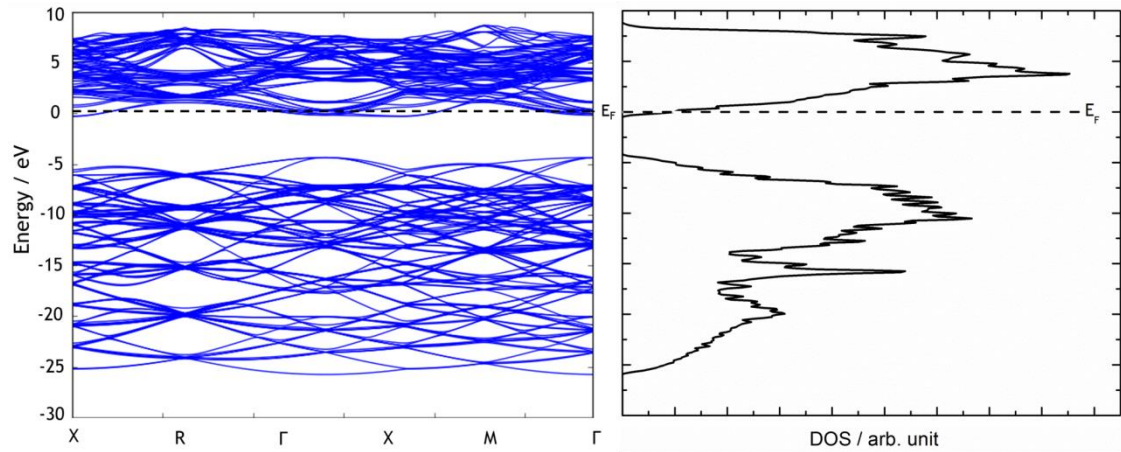


Figure 5.6: Band structure and DOS of Li-doped diamond (interstitial) from the 64-atom supercell produced using CASTEP.

5.3.3.2 Substitutional Site

Figure 5.7 shows the calculated band structure and DOS for lithium-doped diamond residing at a substitutional site. Both the band structure and DOS are different from that for interstitial Li (above). Firstly, the Fermi level for Li substitutional dopants is situated near the VBM, which indicates that the structure possesses p-type semiconducting properties in agreement with previous works [16-18]. The dopant will act as an acceptor rather than a donor. The acceptor energy level was calculated to be at 1.35 eV above the VBM of diamond.

With this p-type behaviour, the existence of both substitutional and interstitial sites simultaneously in diamond films will lead to compensation effects that will reduce its electronic activity. However, due to the ability of Li atoms to become trapped in vacancy sites, substitutional Li will be the dominant species. Thus, for any Li precursor being used and introduced into

diamond films during growth, a p-type semiconductor will be formed preferably.

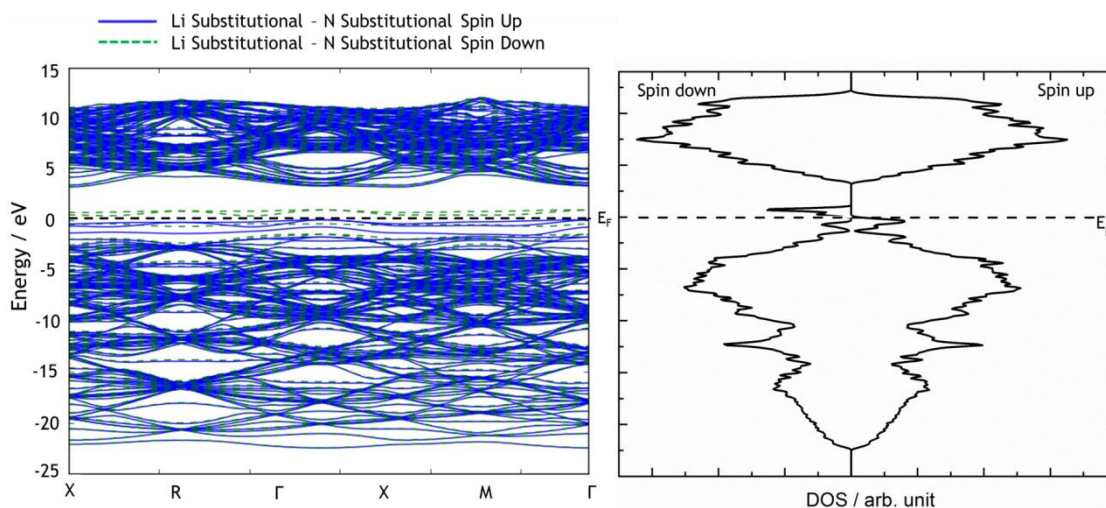


Figure 5.7: Band structure and DOS of Li-doped diamond (substitutional) from the 64-atoms supercell produced by CASTEP.

Secondly, in both the band structure and DOS there were new states observed near the Fermi level. These states were not visible in the calculation for pure diamond (Figure 5.4) because these new states were generated from removing C atoms and addition of Li atoms into the substitutional site. Figure 5.8 illustrates the band structure of substitutionally positioned Li-doped diamond near the Fermi level. There are new states observed near the VBM of diamond. When one C atom was removed from the unit cell, four dangling bonds were produced by the neighbouring C atoms. As Li atom substituted into the vacant position, Li supplies one extra electron into one of these dangling bonds. The other three dangling bonds remained unoccupied and denoted by three energy state above the Fermi level. The DOS depicted in Figure 5.7 is also in agreement with the band structure in Figure 5.8, as the spin-down peak showed above the Fermi level, indicating the unoccupied state, while both spin-down and spin-up peaks appear below the Fermi level, suggesting that

the energy levels were occupied with electrons from neighbouring carbon atoms and substitutional lithium atom.

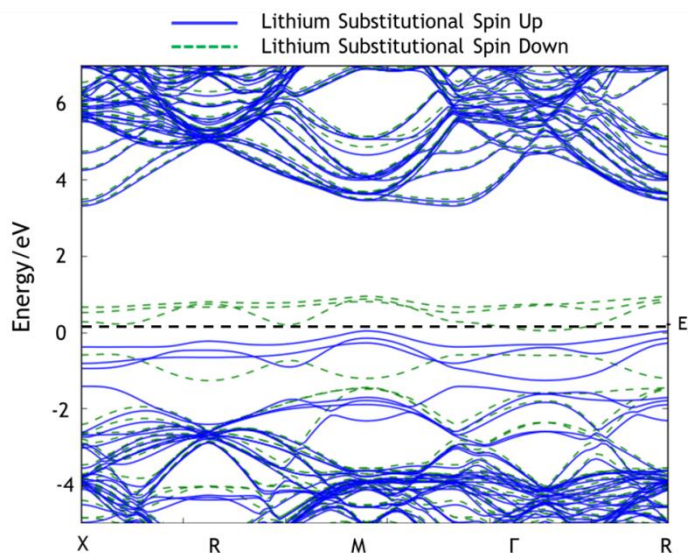


Figure 5.8: Band structure of Li-doped diamond (substitutional) near the Fermi Level.

After thorough analysis of the characteristic of both interstitial and substitutional Li in a diamond crystal lattice, it was concluded that a different experimental approach needed to be taken to produce electrically active Li-doped diamond. Simply adding Li to the growth process (e.g. as a gas-phase component in the CVD mixture) would result in both interstitial and substitutional Li in the diamond lattice, but with substitutional Li being the dominant species. Thus, such material would be weakly p-type semiconducting due to the substitutional Li acting as an acceptor [12,19]. Since substitutional Li atoms in diamond occupy a level in a higher than substitutional B dopants (0.37 eV above the VBM), the former will show higher electrical resistance at room temperature compared to B-doped diamond.

5.3.4 Li-N Co-Doped Diamond

The combination of N deep-donor properties and Li shallow-donor properties are predicted to overcome the uncertainty in formation of interstitial or substitutional Li in the diamond lattice. The semiconductor produced may not be as shallow a donor as interstitial Li alone, but it will help to eliminate the competition between both substitutional and interstitial incorporation. To model this in CASTEP, N atoms were introduced into the system as substitutional nitrogen. They acted as a trap for interstitial Li atoms, allowing the valence electron from the Li atoms to be donated into the diamond lattice structure through the substitutional N atoms. Both the effects of interstitial and substitutional Li were studied in this co-doped calculation.

5.3.4.1 1:1 Ratio of Li-to-N Atoms in Li-N Co-doped Diamond

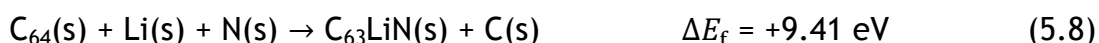
Initially, a ratio of one atom of N to one atom of Li (1:1) was investigated for simplicity.

5.3.4.1.1 Interstitial Lithium

Based on the formation energy equation (Equation 5.1), 9.41 eV is needed to form Li-N co-doped diamond from undoped diamond. The chemical equation for this process is shown in Equation 5.8. The calculated total energy includes the energy needed to remove one carbon atom and replace with a nitrogen atom. The formation energy could be further reduced if the N atoms are introduced into existing vacancies in the space lattice (see Section 5.3.2). By calculating the formation energy of Li-N co-doped diamond from the addition of Li atom into an interstitial site in nitrogen-doped diamond, the resulting formation energy was reduced to

5.28 eV. The chemical equation for this process showed in Equation 5.9. Even though the energy needed was reduced by 4.13 eV, the formation of Li-N co-doped diamond by using this approach remains very thermodynamically unfavourable.

Formation of Li-N co-doped diamond (interstitial) from undefective diamond:



Formation of Li-N co-doped diamond (interstitial) from N-doped diamond:



Another series of calculations were performed to investigate the capability of N atoms to act as a trap for pinning Li atoms. Putting a Li atom further away from a substitutional N site, the calculated formation energy was 11.32 eV. This suggests that once the Li atom has inserted into the diamond lattice, its most thermodynamically favourable position is as close as possible to an N atom as the formation energy will decrease from 11.32 eV to 9.41 eV.

For Li-N co-doped diamond, the strain in the structure was also greater as the Li-C bond lengths were calculated to be between 1.64 Å and 1.74 Å. The Li-C bond lengths increased by at least 0.01 Å compared to the nearest neighbour Li-C distance with the absence of N atom. Due to the elongation of the Li-C bond lengths, the N-C bond lengths were reduced greatly, varying greatly between 1.43 Å and 1.49 Å. The N-C bond length in Li-N co-doped diamond was smaller than that in nitrogen-doped diamond (1.59 Å). However, the expansion and compression of the bond lengths was only observed within a few atoms of the dopant location. All other independent carbon atoms situated further away from the dopants area maintained their C-C bond length at 1.55 Å.

Figure 5.9 shows the band structure and DOS of Li-N co-doped diamond produced using CASTEP. The energy level of the dopant was well separated from the diamond energy level. The dopant energy level is situated below the Fermi level suggesting the dopant energy level was fully occupied. For the N-doped diamond with its band structure depicted in Figure 5.5 (see Section 5.3.2), the nitrogen energy level lying within and close to the Fermi level because it is half-occupied. When a Li atom was introduced into the system, the valence electron from the Li atom was donated into the half-filled N energy level. The nitrogen energy level is completely occupied. The dopant energy level is 1.01 eV below CBM of diamond. If N atoms in diamond are considered as deep donors with energy 0.31 eV below the CBM of diamond, the combination of interstitial Li and substitutional N makes it a deeper donor compared to nitrogen itself. Thus, the introduction of single interstitial Li atom and single substitutional N atom in the diamond lattice will not lead to a successful production of shallower donor dopant in diamond.

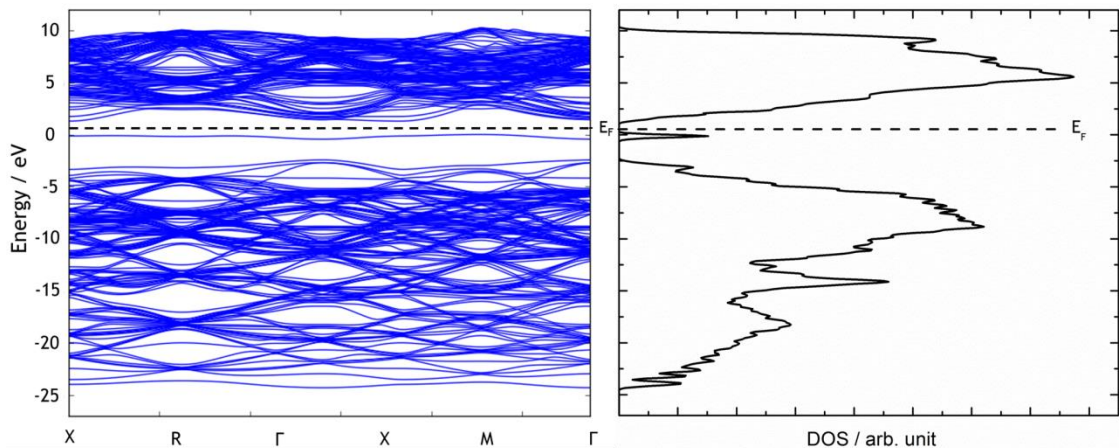
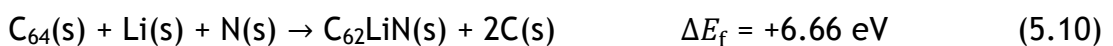


Figure 5.9: Band structure and DOS of Li-N co-doped diamond (interstitial) from the 65-atoms supercell produced by CASTEP.

5.3.4.1.2 Substitutional Lithium

The trend for formation energy of substitutional lithium in Li-N co-doped diamond follows its predecessor. The formation energy for insertion of both lithium and nitrogen atoms simultaneously in pure diamond into substitutional sites was 6.66 eV. The chemical equation for this process showed in Equation 5.10. The formation energy is 2.75 eV lower than the formation energy of Li in the interstitial site for Li-N co-doped diamond crystals. However, if the calculation started with nitrogen-doped diamond, then only a C atom is replaced by a Li atom, and the formation energy is 2.09 eV. The chemical equation for this process showed in Equation 5.11. Conversely, if the calculation started with a cell with a nitrogen vacancy (because nitrogen vacancy defect sites are easily formed at growth temperatures due to the mobility of vacancy sites at 850 °C [39,40]), the formation energy reduced even further to 1.16 eV. The chemical equation for this process showed in Equation 5.12. Even though the formation energy is still positive value, only a small amount of energy is required to form this type of Li-N co-doped diamond structure, with both dopants residing in the substitutional site compared to that for interstitial lithium with substitutional nitrogen.

Formation of Li-N co-doped diamond (substitutional) from undefective diamond:



Formation of Li-N co-doped diamond (substitutional) from N-doped diamond:



Formation of Li-N co-doped diamond (substitutional) from nitrogen vacancy diamond:



The Li-C bond elongated further to a value of 1.79 Å. Elongated Li-C bonds result in shortening the N-C bond to 1.48 Å. The four carbon atoms next to the carbon bonded directly to Li have C-C bonds length of 1.48 Å. The reduction in bond length not only occurred for N-C bonds next to Li-C but also to other next-neighbouring carbon atoms. Conversely, the neighbouring carbon atoms bonded to the carbon atom in the N-C bond have longer C-C bond lengths, 0.01 Å larger than the typical C-C distance of 1.55 Å.

Figure 5.10 depicts the band structure and DOS Li-N co-doped diamond where both dopants reside on the substitutional sites. The overall valence band and conduction band in the band structure and DOS look similar to that from the pure (undoped) diamond structure (Figure 5.4) indicating there are no significant changes being made to the structure by the addition of both dopants. However, the Fermi level of this particular structure resembles that for the substitutional lithium addition (see Section 5.3.3.2). The Fermi level is situated near to the VBM of diamond which indicates the structure formed is a p-type semiconductor.

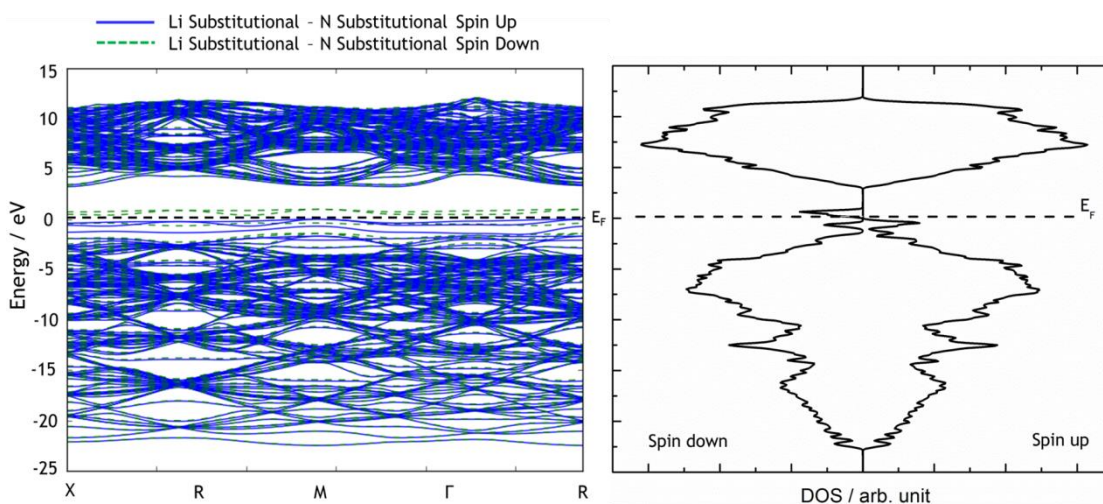


Figure 5.10: Band structure and DOS of Li-N co-doped diamond (substitutional) consist of a 64-atoms supercell calculated using CASTEP.

Figure 5.11 illustrates the band structure of Li-N co-doped diamond near the Fermi level with both dopants incorporated substitutionally. As previously discussed in Section 5.3.3.2, the Fermi level shifts from near the CBM to the VBM of diamond. When one C atom removed from the lattice, four dangling bonds were created by the neighbouring C atoms and substitutional Li sit in the vacant position supplies its electron to form Li-C bond with one of the dangling bonds. When another C atom is substituted with N atom, the extra electrons in N atom help to stabilise one of the dangling bonds. Hence, only two dangling bonds left unoccupied and their energy state were observed above the Fermi level depicted in Figure 5.11. By having unoccupied energy levels near the VBM of diamond, this lowers the Fermi level of the diamond structure. Thus, the Li-N co-doped diamond produces a p-type semiconductor.

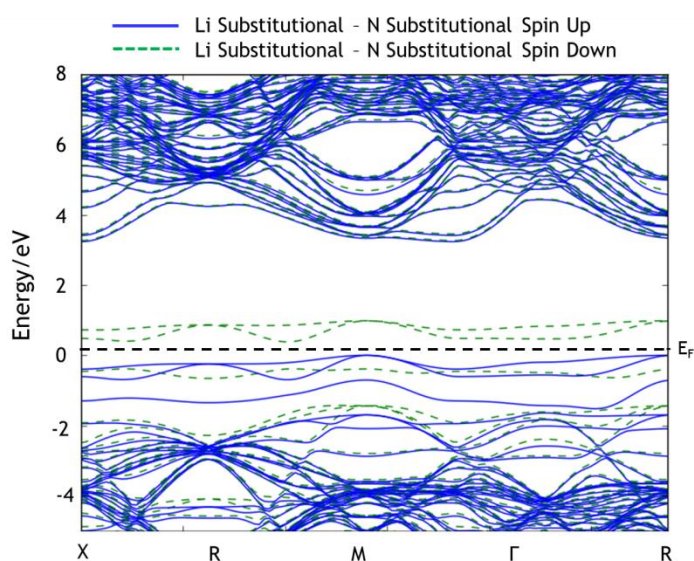


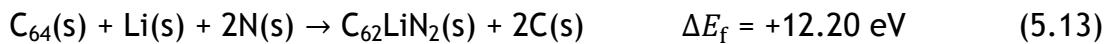
Figure 5.11: Band structure of Li-N co-doped diamond (substitutional) near the Fermi Level.

5.3.4.2 1:2 Ratio of Li:N atoms in Li-N Co-doped Diamond

The formation energies obtained from CASTEP for both interstitial and substitutional sites with a 1:2 ratio of Li-to-N atoms were 12.20 eV and

5.18 eV, respectively. The chemical equations for these processes showed in Equation 5.13 and Equation 5.14. The formation energy of the interstitial site increased by 2.79 eV compared to that for the 1:1 ratio. This suggests that the 1:2 interstitial lithium cluster will not be preferred in the diamond lattice. On the other hand, the formation energy of a Li atom in a substitutional site showed a reduction in formation energy by 1.48 eV compared to the Li substitutional cluster with 1:1 ratio of Li and N. Less energy indicates that the 1:2 cluster with Li in the substitutional site was preferable compared to 1:1 co-dopant clusters. Further analysis on the interstitial lithium cluster was not carried out due to the high formation energy needed to form this type of structure.

Formation of 1:2 ratio of Li-N co-doped diamond (interstitial) from undefective diamond:



Formation of 1:2 ratio of Li-N co-doped diamond (substitutional) from undefective diamond:



Figure 5.12 illustrates the band structure and DOS for a 1:2 ratio of Li:N in Li-N co-doped diamond. Both of the dopants reside at substitutional sites. The Fermi level of the material was situated near the VBM of the structure and results in a p-type material, with the dopants acting as acceptors. From the band structure and DOS, the existence of spin-up and spin-down electrons were nearly the same as in previous lithium substitutional dopant clusters (see Section 5.3.4.1.2).

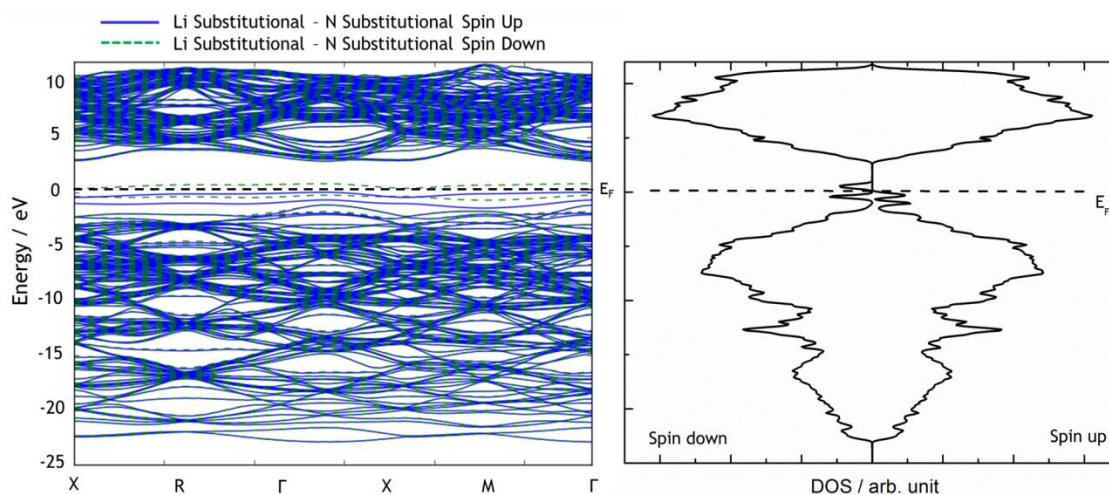


Figure 5.12: Band structure and DOS for a 1:2 ratio of Li:NN in Li-N co-doped diamond (substitutional) consisting of a 64-atoms supercell calculated using CASTEP.

Figure 5.13 depicts an expanded view of the band structure of the 1:2 ratio of Li:N cluster in Li-N co-doped diamond. In this structure only one unoccupied energy state was observed. The observation could be explained in the same manner as before. When one C atom removed from the lattice, the four neighbouring carbons possessed dangling bonds. The Li atom sits in the vacant position will supplies its electron to stabilise one dangling bonds while substituting two C atoms with two N atoms help to stabilise another two dangling bonds. Now, only one dangling bond remained unoccupied. Hence, the energy state that is denoted as spin-down (dashed line) above the Fermi level in Figure 5.13 belongs to the last dangling bond.

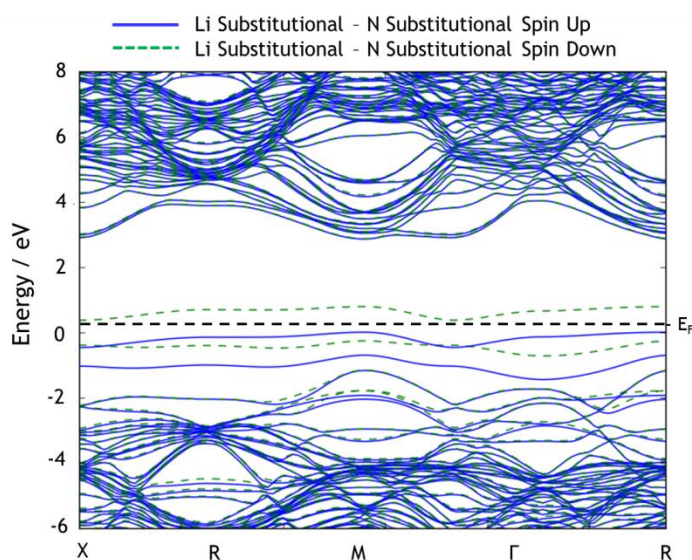


Figure 5.13: Band structure of 1:2 ratio of Li:N of Li-N co-doped diamond (substitutional) near the Fermi Level.

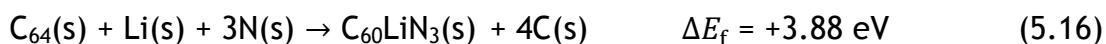
5.3.4.3 1:3 Ratio of Li:N Atoms in Li-N Co-doped Diamond

An additional N atom was added into the 1:2 dopant cluster to create a 1:3 dopant cluster (LiN_3). The formation energy for this cluster, assuming a Li atom is present at the interstitial site, increased to 13.69 eV. Conversely, the 1:3 cluster with the Li atom substitute for C atom showed the opposite effect, with a reduction in the formation energy to a new value of 3.88 eV. The chemical equations for these processes showed in Equation 5.15 and Equation 5.16. This is by far the lowest formation energy obtained without taking into account any effects from vacancy sites (see Section 5.3.4.1.2). Substituting five C atoms with one Li atom and four N atoms that bonds together have a lower formation energy compared to the energy needed to substitute one C atom with one N atom (4.13 eV) (see Section 5.3.2).

Formation of 1:3 ratio of Li-N co-doped diamond (interstitial) from undefective diamond:



Formation of 1:3 ratio of Li-N co-doped diamond (substitutional) from undefective diamond:



Only calculation of a substitutional Li atom in the 1:3 cluster was carried out due to its low formation energy. No further action was taken for the interstitial lithium atom in the 1:3 cluster due to its large formation energy. Figure 5.14 shows the band structure and DOS for 1:3 ratio Li:N of Li-N co-doped diamond with substitutional lithium. Both the band structure and DOS looks different from the previous substitutional lithium structures, but resemble the result produced by the 1:1 Li:N ratio cluster with interstitial Li (see Section 5.3.4.1.1). However, the dopant energy level differs by ~ 0.86 eV. This structure had a dopant energy level of 1.87 eV below the CBM while interstitial lithium in the 1:1 ratio cluster had a dopant energy level 1.01 eV below the CBM.

In this structure, there are no dangling bonds. This explains the non-existence of different spin electrons above and below the Fermi level, as seen in previous clusters with different ratios and substitutional Li. The dopant energy level lies below the Fermi level. This structure resembles the 1:1 ratio cluster interstitial lithium because they share one common property: there are no unpaired electrons in their system. All the original valence electrons possessed by the dopants have been (formally) used to form 2-electron- bonds. Thus, the occupied dopant energy levels lie below the Fermi level.

Even though this 1:3 ratio cluster had the lowest formation energy and was a possible n-type material, the dopant energy level was too deep for practical application at room temperature. The material would have

higher electrical resistance compared to nitrogen-doped diamond and phosphorus-doped diamond.

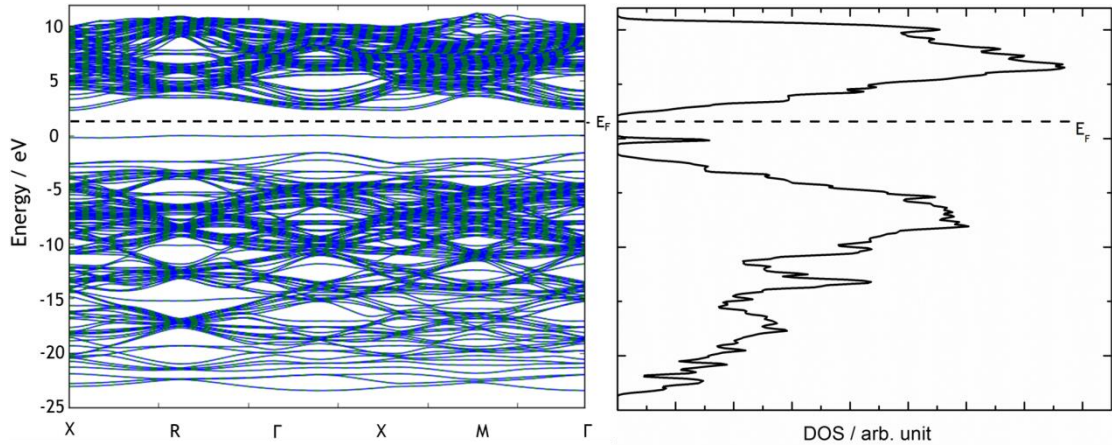
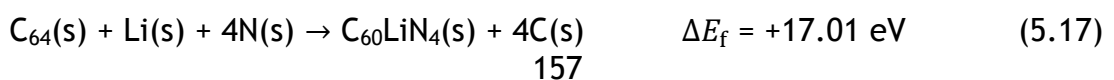


Figure 5.14: Band structure and DOS of 1:3 ratio of Li:N of Li-N co-doped diamond (substitutional) consisting of a 64-atom supercell calculated using CASTEP.

5.3.4.4 1:4 Ratio of Li:N Atoms in Li-N Co-doped Diamond

Finally, when all the neighbouring C atoms are substituted with nitrogen atoms, the 1:4 ratio cluster is formed (LiN_4). The formation energy of this cluster with interstitial Li atom remains high, with a value of 17.01 eV. However, the formation energy for the cluster with a substitutional Li atom also showed an increased to a value of 4.88 eV compared to 1:3 cluster. The structure gained 1 eV by replacing one more carbon with a nitrogen atom when compared with the formation energy of the 1:3 ratio cluster. This may be associated with the extra unpaired electron present due to the fourth nitrogen atom. The chemical equations for these processes showed in Equation 5.17 and Equation 5.18

Formation of 1:4 ratio of Li-N co-doped diamond (interstitial) from undefective diamond:



Formation of 1:4 ratio of Li-N co-doped diamond (substitutional) from undefective diamond:

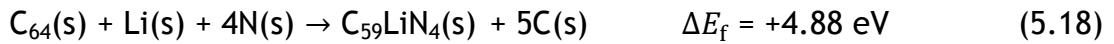


Figure 5.15 shows the band structure and DOS of the 1:4 ratio cluster of Li-N co-doped diamond with substitutional Li. The Fermi level is situated right below the CBM of the diamond structure suggesting that the material produced is a shallow n-type material. Both the band structure and DOS for this cluster resemble that of interstitially lithium-doped diamond. The dopant energy level merges with the conduction band, with the Fermi level lying within and just below the bottom of the CBM. The dopant energy level is shallower compared to that calculated by Moussa and co-workers (0.20 eV below the CBM) [41]. Hence, with lower formation energy and without any competition from the positioning of the Li atoms (i.e. interstitial substitutional sites), the structure with 1:4 ratio looks like being a promising n-type semiconducting material to be produced and tested.

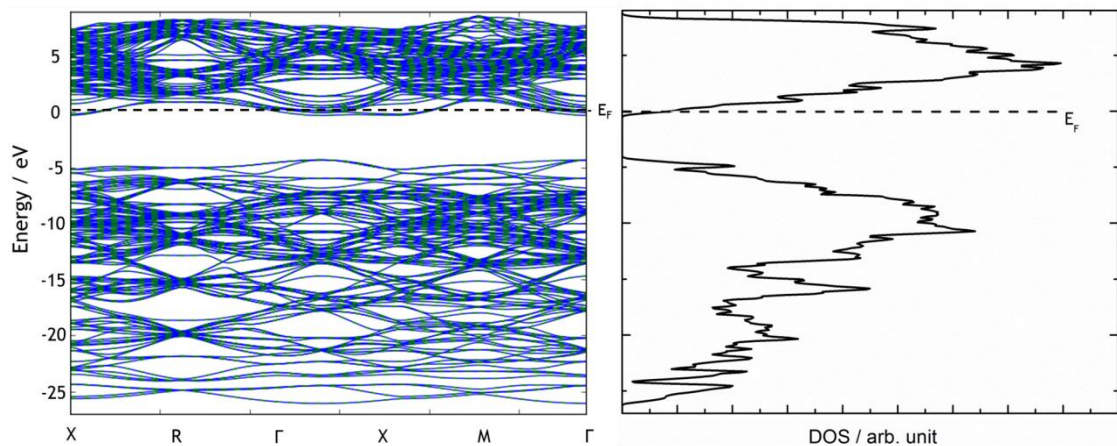


Figure 5.15: Band structure and DOS for the 1:4 ratio Li:N of Li-N co-doped diamond (substitutional) consisting of a 64-atoms supercell calculated using CASTEP.

5.4 Conclusions

Li atom alone as dopant has been shown to be not sufficient to be a candidate for a shallow donor to produce n-type semiconducting diamond. This is due to the ability of Li atom to be positioned either at interstitial sites or substituting for C atom. Li behaves differently at the two sites: interstitial Li acts as a donor while substitutional Li acts as an acceptor. This mixture will compensate each other and the dominant site (substitutional) will make the diamond act as a p-type semiconductor.

By the addition of a N atom to accompany a Li atom as a co-dopant, the effects vary depending upon the Li:N ratio. When a 1:1 ratio of Li and N is used, substitutional Li atoms had the lower formation energy. Unfortunately, the cluster formed with substitutional lithium acted as an acceptor. However, it was shown that Li and N stay close to each other due to strong association between the two dopants. This is an important finding, because it shows that N atoms act as traps to pin down Li atoms, and indirectly they reduce lithium atom mobility in diamond. In addition, this encourages further experimental analysis to determine the whereabouts of Li atoms in diamond.

Further analysis with different ratios of Li and N yielded other interesting results. By increasing the amount of N atoms in the system, Li atoms are less likely to reside in the interstitial site as the formation energies increased to values above 10 eV. With higher amounts of N atoms in the cluster, the energetically favourable position that Li atoms could adopt is at substitutional sites. 1:3 ratio clusters gave the lowest formation energy of 3.88 eV, but it acted as a deep donor in the diamond material.

However, a 1:4 cluster (LiN_4) behaved like a shallow donor with the donor energy level <0.10 eV below the CBM of diamond. The challenge in producing this type of material will be to overcome the higher formation energy of 1:4 cluster compared to 1:3 cluster with the difference of 1.0 eV in energy. Once the ratio is correct, there will be no competition between adding Li atom at interstitial or substitutional sites and there will be no

compensation effect due to the formation of both p-type and n-type dopant in the same material. Thus, the calculations predict that LiN_4 is a highly promising potential candidate as an n-type dopant in diamond, with excellent electrical properties.

Table 5.1: Summary of the electronic properties of doped diamond structures. ΔE_f is defined by Equation 5.1, dopant energy levels are stated with respect to VBM or CBM with (-) indicates it lies below the CBM/VBM or (+) indicates it lies above the CBM/VBM.

Dopants	Formation energy, ΔE_f	Dopant energy levels	Type of semiconductors
N - substitutional	4.13 eV	0.31 eV - CBM	n-type
Li - interstitial	8.67 eV	<0.10 eV - CBM	n-type
Li - substitutional	8.32 eV	1.35 eV + VBM	p-type
1:1 Li-to-N - interstitial	9.41 eV	1.01 eV - CBM	n-type
1:1 Li-to-N - substitutional	6.66 eV	1.10 eV + VBM	p-type
1:2 Li-to-N - substitutional	5.18 eV	0.96 eV + VBM	p-type
1:3 Li-to-N - substitutional	3.88 eV	1.87 eV - CBM	n-type
1:4 Li-to-N - substitutional	4.88 eV	<0.10 eV - CBM	n-type

5.5 References

- [1] L.H. Thomas, Math. Proc. Cambridge Philos. Soc. **23** (1927) 542.
- [2] E. Fermi, Zeitschrift fur Phys. **48** (1928) 73-79.
- [3] S. Yang, D. Drabold, & J. Adams, Phys. Rev. B **48** (1993) 5261-5264.
- [4] A. Scholze, W.G. Schmidt, P. Käckell, & F. Bechstedt, Mater. Sci. Eng. B **37** (1996) 158-161.
- [5] C.C. Battaile, D.J. Srolovitz, I.I. Oleinik, D.G. Pettifor, A.P. Sutton, S.J. Harris, & J.E. Butler, J. Chem. Phys. **111** (1999) 4291.
- [6] M. Hebbache, Solid State Commun. **110** (1999) 559-564.
- [7] F. Mauri, & R. Car, Phys. Rev. Lett. **75** (1995) 3166-3169.

- [8] W.E. Pickett, M.R. Pederson, & B.N. Davidson, *Nanotechnology* **5** (1994) 172-178.
- [9] S. Biernacki, & M. Scheffler, *Phys. Rev. Lett.* **63** (1989) 290-293.
- [10] S. Breuer, & P. Briddon, *Phys. Rev. B* **49** (1994) 10332-10336.
- [11] R. Messmer, & G. Watkins, *Phys. Rev. B* **7** (1973) 2568-2590.
- [12] S.A. Kajihara, A. Antonelli, J. Bernholc, & R. Car, *Phys. Rev. Lett.* **66** (1991) 2010.
- [13] J.P. Goss, R.J. Eyre, & P.R. Briddon, *Phys. Status Solidi B-Basic Solid State Phys.* **245** (2008) 1679-1700.
- [14] S. Praver, C. Uzan-Saguy, G. Braunstein, & R. Kalish, *Appl. Phys. Lett.* **63** (1993) 2502-2504.
- [15] R. Zeisel, C.E. Nebel, M. Stutzmann, H. Sternschulte, M. Schreck, & B. Stritzker, *Phys. Status Solidi* **181** (2000) 45-50.
- [16] E.B. Lombardi, A. Mainwood, & K. Osuch, *Phys. Rev. B* **76** (2007) 155203.
- [17] E.B. Lombardi, & A. Mainwood, *Diamond Relat. Mater.* **17** (2008) 1349-1352.
- [18] E.B. Lombardi, & A. Mainwood, *Phys. B Condens. Matter* **401-402** (2007) 57-61.
- [19] A. Mainwood, *J. Mater. Sci. Mater. Electron.* **17** (2006) 453-458.
- [20] J.P. Goss, B.J. Coomer, J. Jones, C.J. Fall, P.R. Briddon, & S. Öberg, *Phys. Rev. B* **67** (2003).
- [21] J.P. Goss, P.R. Briddon, R. Jones, & S. Sque, *Diamond Relat. Mater.* **13** (2004) 684-690.
- [22] J.P. Goss, & P.R. Briddon, *Phys. Rev. B* **75** (2007) 75202.
- [23] G. Popovici, & M.A. Prelas, *Diamond Relat. Mater.* **4** (1995) 1305-1310.
- [24] K.M. O'Donnell, M.T. Edmonds, J. Ristein, A. Tadich, L. Thomsen, Q.H. Wu, C.I. Pakes, & L. Ley, *Adv. Funct. Mater.* **23** (2013) 5608-5614.
- [25] K. M. O'Donnell, & T. L. Martin, *Mater. Res. Soc. Symp. Proc.* **1282** (2011).

- [26] K.M. O'Donnell, T.L. Martin, N.A. Fox, & D. Cherns, *Phys. Rev. B* **82** (2010) 115303.
- [27] A.K. Tiwari, J.P. Goss, P.R. Briddon, N.G. Wright, a. B. Horsfall, & M.J. Rayson, *Phys. Status Solidi* **209** (2012) 1703-1708.
- [28] A.K. Tiwari, J.P. Goss, P.R. Briddon, N.G. Wright, A.B. Horsfall, R. Jones, H. Pinto, & M.J. Rayson, *Phys. Rev. B* **84** (2011) 245305.
- [29] A.K. Tiwari, J.P. Goss, P.R. Briddon, N.G. Wright, A.B. Horsfall, & M.J. Rayson, *Phys. Status Solidi* **209** (2012) 1697-1702.
- [30] A.K. Tiwari, J.P. Goss, P.R. Briddon, N.G. Wright, A.B. Horsfall, & M.J. Rayson, *Phys. Rev. B* **86** (2012) 155301.
- [31] A.K. Tiwari, J.P. Goss, P.R. Briddon, N.G. Wright, a. B. Horsfall, R. Jones, H. Pinto, & M.J. Rayson, *Phys. Status Solidi* **209** (2012) 1709-1714.
- [32] S.J. Clark, M.D. Segall, C.J. Pickard, P.J. Hasnip, M.I.J. Probert, K. Refson, & M.C. Payne, *Zeitschrift für Krist.* **220** (2005) 567-570.
- [33] R.J. Nicholls, A.J. Morris, C.J. Pickard, & J.R. Yates, *J. Phys. Conf. Ser.* **371** (2012) 012062.
- [34] J.P. Perdew, K. Burke, & M. Ernzerhof, *Phys. Rev. Lett.* **77** (1996) 3865-3868.
- [35] R.W.G. Wyckoff, *Crystal Structures*, 2nd Edition, Interscience Publishers, (1963).
- [36] J.E. Field, *The Properties of Natural and Synthetic Diamond*, Academic Press, (1992).
- [37] Y. Bar-Yam, & T. Moustakas, *Nature* **342** (1989) 786-787.
- [38] W. Banholzer, *Surf. Coatings Technol.* **53** (1992) 1-12.
- [39] L. Allers, & A. Mainwood, *Diamond Relat. Mater.* **7** (1998) 261-265.
- [40] M.H. Nazare, & A.J. Neves, *Properties, Growth and Applications of Diamond*, INSPEC, (2001).
- [41] J.E. Moussa, N. Marom, N. Sai, & J.R. Chelikowsky, *Phys. Rev. Lett.* **108** (2012) 226404.

Chapter 6: Electron Emission Study of Li-N Co-Doped Diamond Films

6.1 Introduction

Detailed discussions on the preparation and characterisation methods of Li-N co-doped diamond films were discussed in Chapter 3 and Chapter 4. However, the films prepared did not exhibit any semiconductor properties and the 2-point electrical resistance observed in those films ($>10\text{ M}\Omega$) was extremely high at room temperature. Later, a computational approach was considered and discussed in Chapter 5 that investigated the possible arrangements of both Li and N atoms in a diamond lattice. The calculations suggested that certain Li-N clusters might form deep donor levels in diamond. Most of the Li-N co-doped diamond films prepared in Chapter 4 had a high content of N atoms with the ratio of Li to N being of the order of 1:18 indicating that the sample may behave similarly to N-doped diamond films. Previous studies also suggest that N-doped films start to exhibit low electrical resistance at high temperature [1-3]. Thus, the thermionic emission measurement technique was considered as a suitable choice to be used for electrical measurement of the N-rich Li-N co-doped diamond films prepared in this study.

Thermionic emission involves heating a material electrode such that electrons are emitted from the highest occupied energy level into the vacuum. If these electrons are captured by a second electrode possessing a lower work function called a collector, the electron gas streaming between the two electrodes acts as a fluid for transferring heat in the form of kinetic and potential energy. If the kinetic energy is rejected by the collector as heat, the electrons are able to utilise the potential energy to do electrical work in an external circuit. The thermionic conversion process effectively transforms thermal energy into electrical power. The main equation underlying the thermionic process is Richardson-Dushman's equation showed in Equation 6.1. Thermionic emission is characterized by two important properties of the material itself; the work function, ϕ and

the working temperature, T . The electron emission current density (J) produced is given by:

$$J = A_R T^2 e^{\frac{-\phi}{kT}} \quad (6.1)$$

In the 1950s, thermionic electron emission was considered as a possible means to generate electrical power from nuclear or solar thermal heat sources on account of the high theoretical power densities and lack of mechanical moving parts [4]. It works based on the principle of a temperature difference between a hot emitter and cold collector separated by a small vacuum gap. In this case there would be one-way stream of electrons emitted from the emitter into the collector, which forms thermionic emission current across the gap and indirectly converts heat into electricity. Many applications would benefit by emission of electrons thermionically, such as space propulsion, high power electronics and direct thermal-to-electrical energy conversion [5-9]. For example, many researchers have strived to produce solar panels for harvesting energy [10-15]. The light from the Sun can be concentrated and used as a heat source to heat the emitter and when it reaches the threshold temperature, electrons will start to be emitted into the vacuum region and collected by the collector. Such a thermionic solar convertor has no mechanically moving parts, thus lowering the maintenance cost.

The idea of thermionic emission as a tool for harvesting electrical energy is not new, the TOPAZ program in 1991 [5] developed by Soviet Union and United States, used thermionic emitters mainly for powering their satellites. At that time, most of the emitters used were made from transition metals such as Mo, Ni, Ta, Rh and W. Unfortunately, most of these thermionic emitters required working temperatures above 1000°C [16-21]. This high working temperature limited almost all usage of Earth-based applications. The research into thermionic emission applications started to take off when diamond began to be used as the emitter. A low

threshold temperature ($<700\text{ }^{\circ}\text{C}$) was recorded by Nemanich and co-workers when nanocrystalline N-doped diamond acted as the emitter in their thermionic emission setup [22,23]. Later, various parameters were explored to try to improve the current density yield and reduce the threshold temperature. Some of the key parameters behind the reason for using diamond structure were due to its large band gap and the ability of the diamond surface to exhibit negative electron affinity (NEA). However, some challenges need to be overcome to work at lower threshold temperature while harvesting high current density. Current research focuses on the resistance at the interface layer between diamond and the substrate, the contribution of the substrate work function and Fermi level to the total work function of the emitter, and the effect of dopants incorporated into diamond films [11,22,24,25].

In this chapter, a series of Li-N co-doped diamond films was tested to investigate the potential of these co-dopants in enhancing the thermionic emission from diamond. Previously, both theoretical calculations (Chapter 5) and two-point probe measurements (Chapter 4), suggested that Li-N co-doped diamond films might not act as good emitter due to their low room-temperature conductivity. However, at high temperature these materials are expected to become more conducting and may be useful in thermionic emissions.

6.2 Experimental

6.2.1 Preparation of Li-N Co-Doped Diamond

Li-N co-doped diamond films were prepared in the same manner discussed in Chapter 4. Li_3N powder and NH_3 gas were used as the dopant precursor. The substrates used in this experiment were 1 cm^2 Si wafers and W foils. W foils were used in this study to investigate the effect of different substrate conductivity on the thermionic emission of the diamond films. Nitrogen-doped diamond, as the initial diamond layer, was grown on top of

the chosen manually abraded substrate. The diamond films were grown using the optimised N-doped diamond growth conditions (0.33% NH₃/H₂ atmosphere) developed previously. Then, 100 µl of Li₃N suspension in chloroform were drop cast onto the surface of the nitrogen-doped diamond films. Next, the films underwent hydrogen treatment for an hour inside the HFCVD reactor. Finally, an undoped capping layer was overgrown on top of the films to ensure full encapsulation of Li and N atoms inside the films.

The films also underwent a MW-CVD hydrogen-plasma treatment at Arizona State University after the testing inside the thermionic emission kit. This procedure was done to compare the effect of hydrogen-terminated Li-N co-doped diamond films with the as-grown surface of the films. The films were exposed to hydrogen plasma at 50 torr for 15 minutes. The temperature recorded by the thermocouple was 550 °C.

6.2.2 Thermionic Emission Measurements of Li-N Co-doped Diamond Films

Thermionic emission measurements were done at Arizona State University (ASU) with the help from Mr. Franz Köeck. The electron emission characterisation was performed in an in-house custom-built ultra-high vacuum (UHV) system. The base pressure for all measurements was kept at 1.8×10^{-10} torr. The anode (collector) was made from mirror-polished Mo metal and moveable in all three spatial directions. The sample stage was heated radiatively by resistive heating of a W coil. Care was taken to ensure there would be no electrical contact between the W coil and sample stage to avoid current leakage. The leakage may lead to error of the recorded measurement up to 50%. The resistive heating could increase the temperature of the sample up to 1000°C but to prolong the life-time of the W coil, most of the measurements were kept below 800°C. The temperature readings were recorded using a 2-colour pyrometer. During the measurement, positive bias was applied on the anode (collector) to overcome the space-charge effect that occurred in the vacuum gap between the emitter and collector. The electron emission current and

applied bias was controlled by a Stanford Research I/V source. The sample was attached onto the sample stage using custom-made Mo sample holder as depicted in Figure 6.1. The distance between the emitter and the collector was fixed at 0.75 mm. The diamond films were tested up to maximum temperature of 620°C and the current measurements were recorded at every 10°C interval.



Figure 6.1: Custom-made sample holder used to hold Li-N co-doped diamond film grown on W substrate for thermionic emission experiment.

6.2.3 UPS and XPS Analysis of Li-N Co-doped Diamond Films

This study was done *in-situ* in ASU by using an integrated UHV system consisting of X-ray Photoelectron Spectroscopy (XPS) and Ultraviolet Photoelectron Spectroscopy (UPS) instruments that were connected with the UHV transfer line. These studies were done on a separate vacuum line to the Thermionic Emission kit. Hence, precautions were done to minimise possible surface contamination during transport. XPS analysis was done for core level analysis and elemental characterisation while UPS was done for electronic structure analysis. The annealing process was done in the UPS instrument with the UHV transfer line connected between both of the

instruments. This ensures that there was no surface contamination due to the limited exposure of air or other organic impurities during the transfer between both instruments.

UPS spectra were obtained using the He I line at 21.2 eV from a He discharge lamp. The spectra were recorded by a VSW HA50 hemispherical analyser and VSW HAC300 lens controller that operated at a resolution of 0.1 eV. A negative bias (8 V) was applied to the substrate to overcome the work function of the analyser.

XPS analysis was performed using the 1256.6 eV Mg K α line of a VG XR3E2 dual anode source and VG microtech Clam II analyser operated at a resolution of 0.1 eV.

Spectra collected by UPS and XPS were referenced to the Fermi level of the metallic sample holder which was calibrated against a standard gold sample. All characterisation and analysis was done in ASU with help from Dr. Tianyin Sun.

6.3 Results and Discussion

6.3.1 Thermionic Emission

The thermionic emission data were fitted to the Richardson-Dushman's equation (Equation 6.1). From the equation, the work function of each emitter was calculated. The effect of a hydrogen terminated surface, nitrogen content and the nature of the material used as a substrate are discussed in the following section.

6.3.1.1 Effect of a Hydrogen Terminated Diamond Surface

Figure 6.2 shows the thermionic emission data of Li-N co-doped diamond films with two different surfaces, the as-grown surface and after

hydrogen plasma treatment. The data were taken over a temperature range from 700 K to 910 K. The as-grown surface did not exhibit high current density. For this experiment, the threshold temperature was defined as that required to produce a current density of at $0.1 \mu\text{A cm}^{-2}$. The film started to emit thermionic electrons at 900 K. The maximum current density observed at 910 K was $1.15 \mu\text{A cm}^{-2}$.

After the same diamond film underwent hydrogen plasma treatment, the threshold temperature reduced to 800 K and the current increased exponentially to a value of $121.54 \mu\text{A cm}^{-2}$ at 900 K. The current density improved by more than 100 times after the diamond film was exposed to hydrogen plasma. The existence of hydrogen atoms on the diamond surface creates an NEA surface that enhance the dipole moment at the surface [26]. This dipole moment was responsible for attracting more electrons from the bulk of the diamond to the surface. From the Richardson fitting, the work function of the hydrogen-terminated Li-N co-doped diamond film was 3.62 eV. The work function calculated was the effective work function of the whole material, consisting of substrate (Si), SiC at the interface [27,28] and the diamond film. The thickness of the diamond film was $\sim 1 \mu\text{m}$ and the thickness of the substrate used was $\sim 550 \mu\text{m}$. In addition to that, the thickness of SiC layer was suggested by previous findings to be between 100 to 200 nm [27,28]. Typical n-type Si has a work function of ~ 4.70 eV [29] and deep n-type diamond with an NEA surface may exhibit a work function of ~ 1.6 eV [1,30,31]. Based on the Li-N co-doped diamond analysis in Chapter 4, the concentration of N atoms was much larger than that of Li atoms. Thus, the diamond film in this study can be classified as being similar to nitrogen-doped diamond films with deep-donor characteristics. From the work function obtained from the Richardson fitting to the data, we can see that the diamond film has had some effect in reducing the work function of the whole emitter structure even though the diamond layer was very small compared to the thickness of n-type silicon substrate.

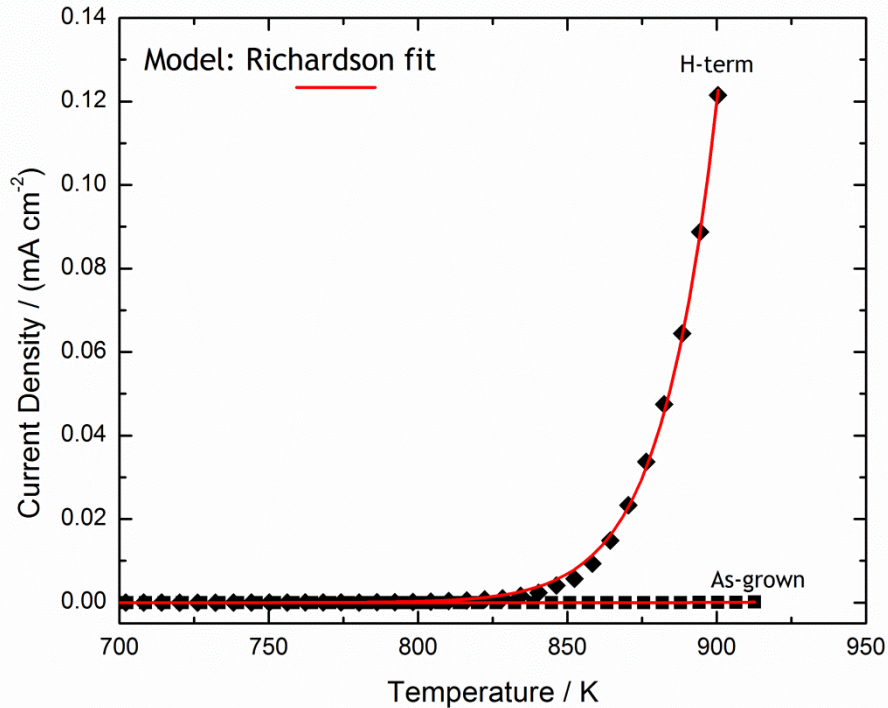


Figure 6.2: Thermionic emission data from a Li-N co-doped diamond film with an as-grown surface and after hydrogen plasma treatment. The diamond film was grown with 0.33% NH_3 gas present in the hydrogen atmosphere.

Figure 6.3 illustrates the I-V curve produced from the Li-N co-doped diamond film with a hydrogen terminated surface at 900 K. This plot is essential to ensure the space-charge effect was minimised throughout the experiment [32]. The presence of space-charge may give a pseudo-current reading from the thermionic emission kit. The electron cloud that exists near the surface of the diamond film will repel any incoming electron back to the diamond surface [33]. A positive potential across the collector will attract the electron to the collector and reduce the probability of formation of electron clouds. In Figure 6.3, a minimum of 1 V was needed to reduce the space-charge effect, which can be seen as the point at which the current detected first increased above the background level. With 12 V applied across the emitter and collector, the detected current started to saturate. This indicates that the space-charge effect was reduced to its minimum effect. For extra precautions, 20 V was applied in all subsequent measurements to ensure the space-charge effect did not interfere with

data collection and analysis. 20 V was applied across the 0.75 mm gap between the emitter and collector resulting in an electric field of 0.027 V/ μm . This electric field was small enough that there was no possibility of emission of electrons by field emission. For comparison, typical B-doped diamond and undoped diamond start to emit field emission electrons at electric fields of 10-15 V/ μm and 15-25 V/ μm , respectively [34-37].

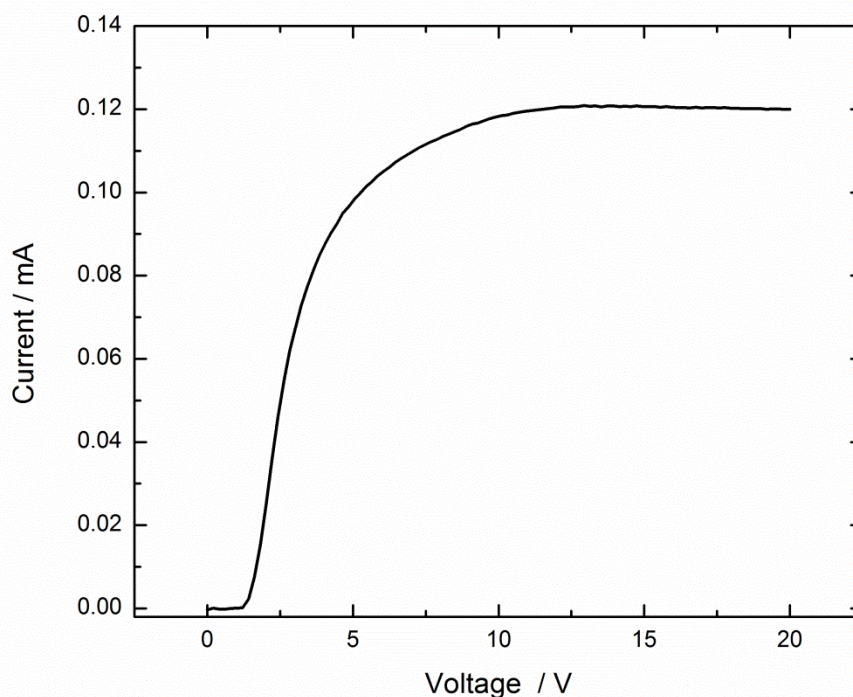


Figure 6.3: I-V curve of Li-N co-doped diamond film with hydrogen terminated surfaces at 900 K.

6.3.1.2 Effect of Different Nitrogen Content in Li-N Co-doped Diamond Films

Figure 6.4 shows the thermionic emission data from Li-N co-doped diamond films with two different N atom concentrations. The diamond films were grown with 0.33% of NH_3 gas and 0.26% of NH_3 gas, respectively. The 0.26% sample had a threshold temperature of 870 K with the maximum current density of 32.32 $\mu\text{A}/\text{cm}^2$ detected at 928 K. The higher-nitrogen-

content diamond film (0.33% NH₃) exhibit lower threshold temperature (800 K) and the current detected at 900 K for this film was 121.54 μA/cm². By having higher nitrogen content, the current produced from thermionic emission at 900 K was 70 times better. A similar pattern was observed in nanocrystalline nitrogen-doped diamond films grown by Suzuki and co-workers [22]. The highest current density emitted from their nitrogen-doped samples was 700 μA/cm² for a film with 2.7×10²⁰ of N atoms per cm³. For N concentrations lower than this the current density started to reduce. This may be due to the reduction of available donors in the diamond film to donate extra electrons into the diamond lattice. The reduction may also be due to there being fewer N atoms in the diamond grain boundaries that are believed to be essential in reducing the electrical resistance of the diamond. Previous researchers investigated the effect on thermionic emission of different crystallinities (SCD and NCD) of N-doped diamond, and it resulted in lower current density when the films had higher sp³ carbon fraction [12,22]. However, if the sample surface was reconstructed to produce a higher sp²/sp³ ratio with the formation of amorphous carbon, it decreased the thermionic emission current density [38]. Hence, grain boundaries do play a role in improving the thermionic emission of diamond films.

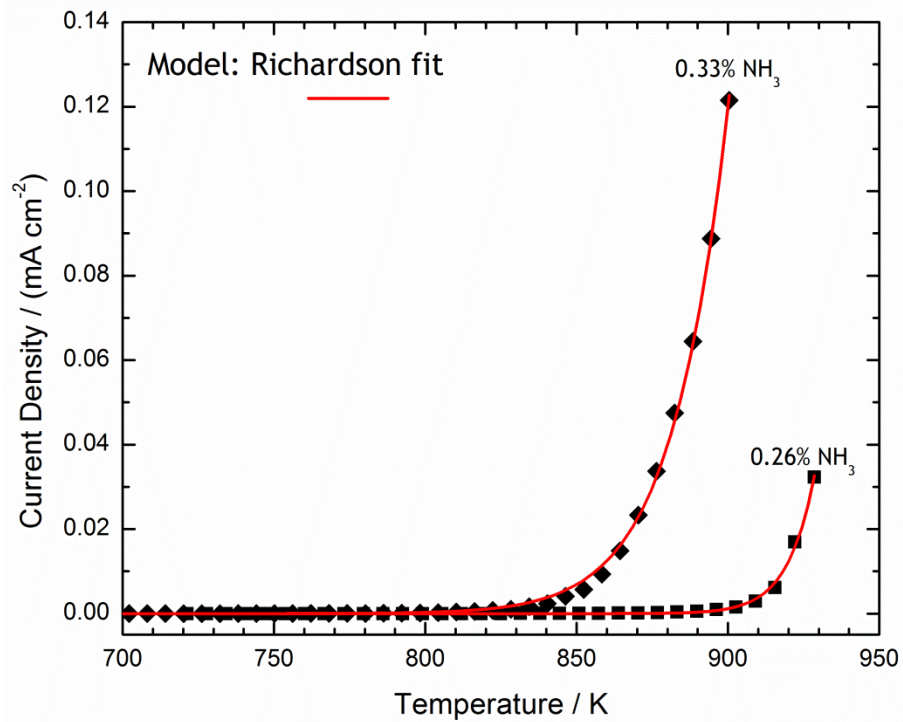


Figure 6.4: Thermionic emission from Li-N co-doped diamond films with hydrogen terminated surfaces grown with different amounts of NH₃ present in the hydrogen atmosphere.

6.3.1.3 Effect of Different Substrates Used for Growing Li-N Co-doped Diamond Films

Two types of substrate material with different conductivities were used as the substrate for the diamond film growth, a semiconductor and a metal. An N-type Si (100) wafer was used as the semiconductor substrate and W foil (Goodfellow, 99.9% purity, 0.25 mm) was used as the metallic substrate. W foil was used as a model in this study to investigate the effect of substrate conductivity. Various other metallic substrates such as Rh and Mo were used in previous work by other researchers [25]. Figure 6.5 illustrates the thermionic emission from Li-N co-doped diamond films with a hydrogen-terminated surface grown on the two types of substrate. The Li-N co-doped diamond films were grown using the standard procedure described in Chapter 4 and subsequently terminated with H atoms in the MW plasma system at ASU to obtain an NEA surface.

From Figure 6.5, at 900 K the diamond films grown on the Si substrate emitted 1.21×10^{-4} A/cm² current compared to 3.35×10^{-5} A/cm² emitted by the diamond films grown on W substrate. Interestingly, the threshold temperatures exhibited by both films were almost the same (~800 K). This indicates that there were no changes in the electron emission behaviour near the surface as the electrons started to be emitted into the vacuum at a similar energy. However, the total work function of both emitters was different. The diamond/Si emitter exhibited a work function of 3.62 eV while the diamond/W emitter exhibited a work function of 2.87 eV. The reduction of the overall work function of the emitter using a metallic substrate was in agreement with results from previous researchers [25] who suggested that this was due to the lower electrical resistance at the diamond-substrate interface .

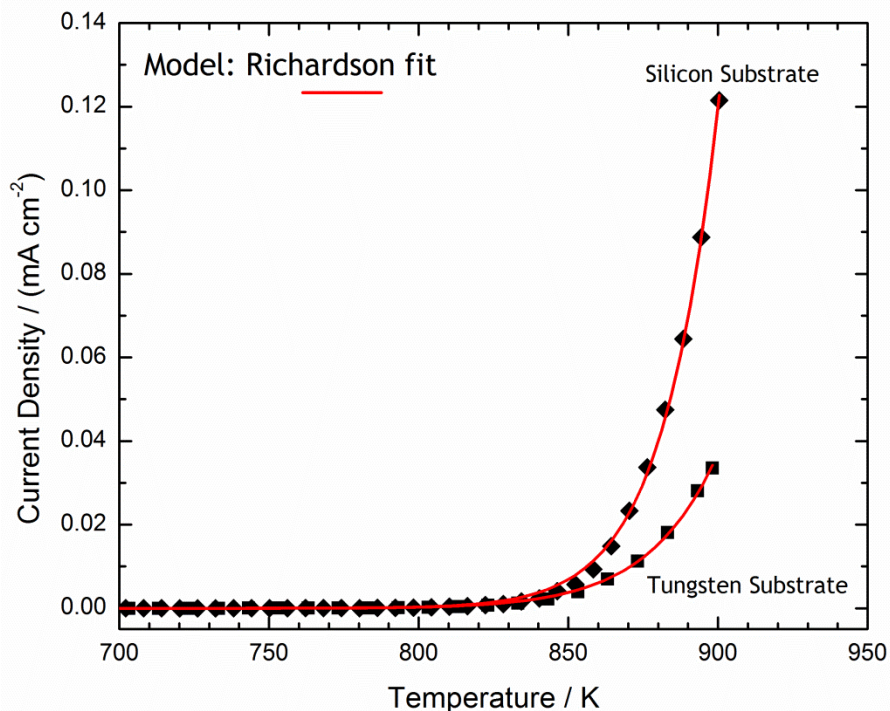


Figure 6.5: Thermionic emission of Li-N co-doped diamond films with hydrogen-terminated surface grown on 2 different substrates.

However, based on Richardson-Dushman's equation, when an emitter possesses a lower work function, the current density produced should be

higher than that from a higher-work-function emitter. In this study, this was not the case. This issue was probably due to the inhomogeneity and non-continuous nature of the diamond film grown on the W substrate, as depicted in Figure 6.6. The manual abrasion technique may not be a suitable seeding technique for diamond growth on metal substrates as it abrades the substrate non-uniformly. By having less diamond coverage on the substrate, it reduces the amount of carriers that were available in the emitter. Hence, this reduced the number of electrons emitted from the emitter i.e. the current density. This could be solved by using the electro spray method or the self-assembly technique during the seeding process to ensure better coverage of diamond seed prior to the diamond growth process.

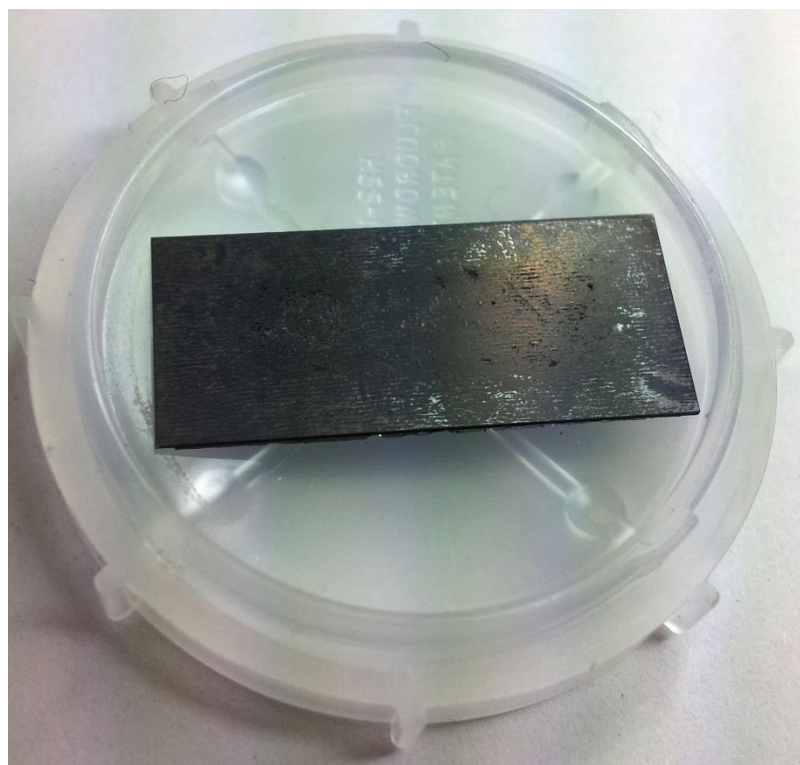


Figure 6.6: Li-N co-doped diamond film grown on a W substrate showing the non-uniformity of the diamond film across.

In addition, by changing the substrate from a semiconductor to a conductive metal, it eliminated the high resistance of Si. Lower resistance

substrate will improve the movement of the electrons throughout the material before the electrons reach the diamond and its surface. Nemanich and co-workers achieved low-work-function emitters by combining a molybdenum disk as the substrate, MoC carbide (a low resistance material) as the thin interface layer and mixture of UNCD/NCD films with an NEA surface as their emitter [39]. Other groups, such as Paxton and co-workers [11] also used Mo as their substrate and grew B-doped MCD for their emitter. With boron as the dopant, the emitter started to emit 0.2 - 0.6 nA current between 1313 K and 1393 K [11]. This suggests that p-type diamond was not a good candidate for an emitter due to the higher operating temperatures required. For a better comparison, Köeck and co-workers also studied the thermionic emission from phosphorus-doped MCD [24]. They achieved a lower work function (0.9 eV) compared to the Li-N co-doped diamond presented here, although at 900 K, the Li-N co-doped diamond exhibited higher electrical current density ($121 \mu\text{A cm}^{-2}$) compared to that from the phosphorus-doped diamond ($\sim 70 \mu\text{A cm}^{-2}$) [24].

Comparing Li-N co-doped diamond with B-doped, N-doped diamond and P-doped diamond, it is clear that Li-N co-doped diamond films provide similar performance as a thermionic emitter. This was only a preliminary study with a limited number of Li-N diamond films available for these thermionic tests. Further improvements to the deposition and doping processes should enable the thermionic emission properties to be improved, and perhaps become direct competition for the nanocrystalline emitters produced by Nemanich and co-workers [25,39,40].

The Li-N co-doped diamond film grown on Si using 0.33% NH_3 gas during growth process and terminated with H atoms, was chosen as the best sample for thermionic emitter application in this study. Further analysis was done using UPS and XPS instruments to determine the surface work function and elements that were present on the surface and sub-surface of the material.

6.3.2 Ultraviolet Photoemission of Li-N Co-doped Diamond Film

UPS measurement was done on Li-N co-doped diamond film to determine the value of its surface work function and the nature of the surface electron affinity. Figure 6.7 shows the UPS spectra from the Li-N co-doped diamond film with an H-terminated surface. The surface work function of the diamond film before any annealing treatment was 2.79 eV and the VBM value was 2.58 eV. Adding the work function to the VBM value, it gives information on the gap between the VBM and the vacuum level. For this particular diamond film, the gap was 5.37 eV. The band gap of diamond \sim 5.45 eV, which suggests that the surface possesses NEA of -0.08 eV as the vacuum level is situated lower than the CBM of diamond. In addition, the surface work function of 2.79 eV suggests that the dopant energy level near the surface was in a deep donor state. This can be explained by the undoped diamond capping layer of the material, as shown in the SIMS depth profile in Chapter 4, and the theoretical cluster calculation in Chapter 5. The surface of the Li-N co-doped diamond did not contain many dopant atoms compared to the bulk structure itself. Thus, it leads to the reduction in the amount of electrons that can act as carriers and reduce the Fermi level on the surface of diamond film.

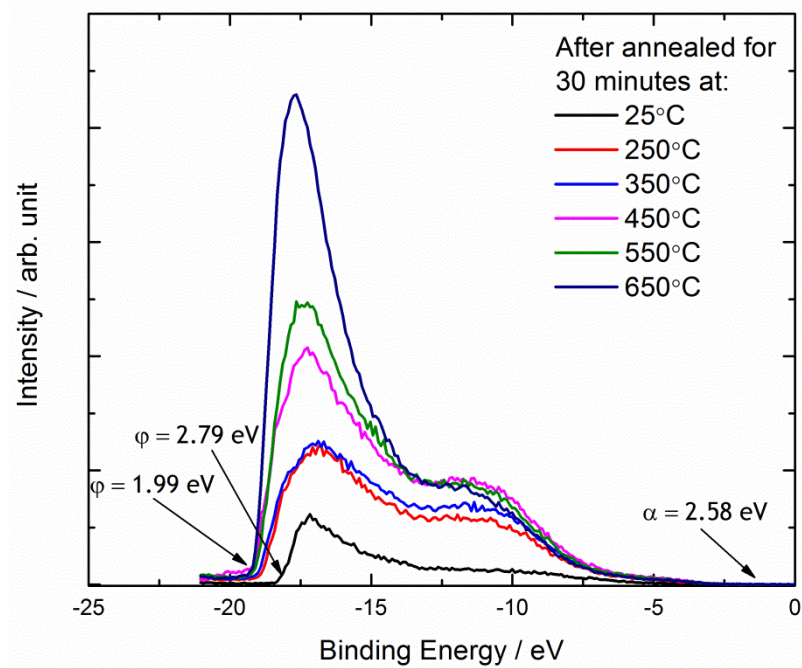


Figure 6.7: UPS spectra of Li-N co-doped diamond film (0.33% NH₃) with H-terminated species annealed at various temperatures. The spectra were taken after the temperature of the films reduced to less than 100°C.

After the annealing treatment, even as low as 250°C, changes in the surface work function started to be visible. The surface work function remained constant throughout the various annealing temperatures after being annealed at 250°C as depicted in Figure 6.7. In addition, the VBM of the material remained constant at 2.58 eV and had no temperature effect from the annealing process. The total gap between the vacuum level and the VBM reduced to 4.57 eV after the annealing process. The reduction of the surface work function may be due to desorption of surface impurities such as moisture, CO gas, CO₂ gas and other organic moieties that inhibit the NEA property. The intensity of the NEA increased with respect to the temperature. Thus, it is important to ensure that the surface of the diamond films were cleaned during the thermionic emission measurement as the effect may interrupt the interpretation of the result based on Richardson-Dushman's equation due to the changes of NEA intensity with respect to the temperature.

6.3.3 X-Ray Photoemission of Li-N Co-doped Diamond Film

XPS measurements were done to characterise the elements that were present on the surface and sub-surface (few atomic layers) of Li-N co-doped diamond. The diamond used in this section was similar with the diamond film examined by UPS (see Section 6.3.2). From the XPS survey scan illustrates in Figure 6.8, C 1s core and O 1s core were the only species present on the surface and sub-surface region. There was no metal contamination detected on the surface suggesting that was no cross-contamination from the steel growth chamber or from the Ta filament during growth process. This result supported the EDX analysis in Chapter 3 showing that previous contamination difficulties had been overcome. The N and Li elements were not detected due to the amount incorporated inside the diamond film were significantly smaller (~0.01% - 0.1%). In addition, XPS instrument could only detect element with atomic number, Z higher than 3 (Li). Hence, H and He elements were difficult to detect using this method.

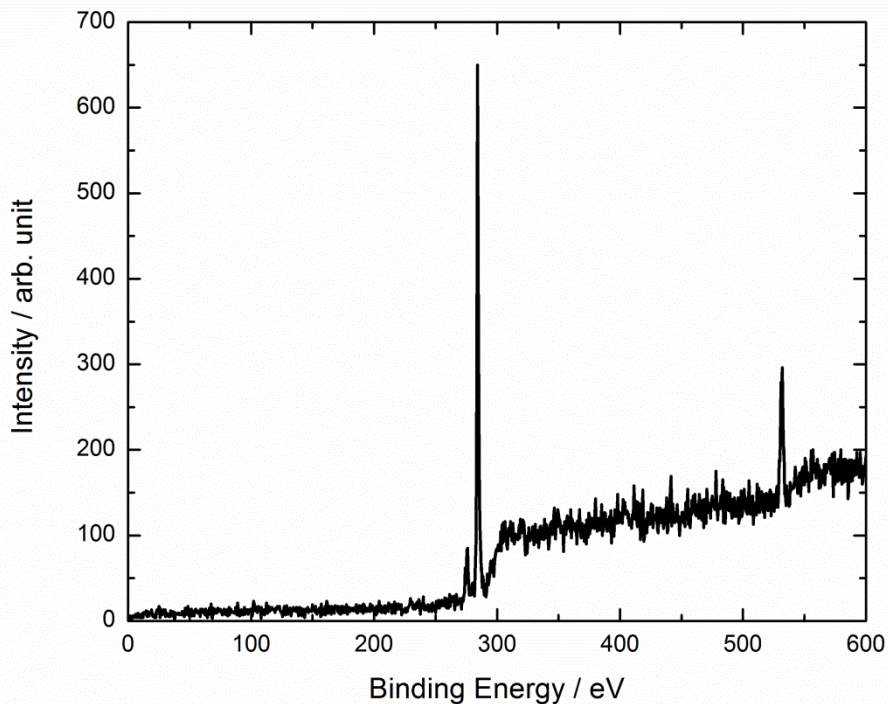
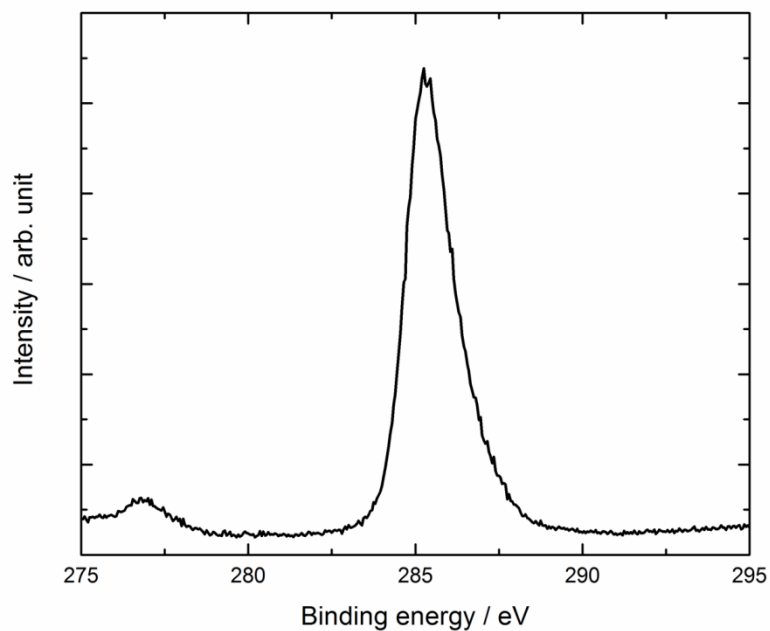


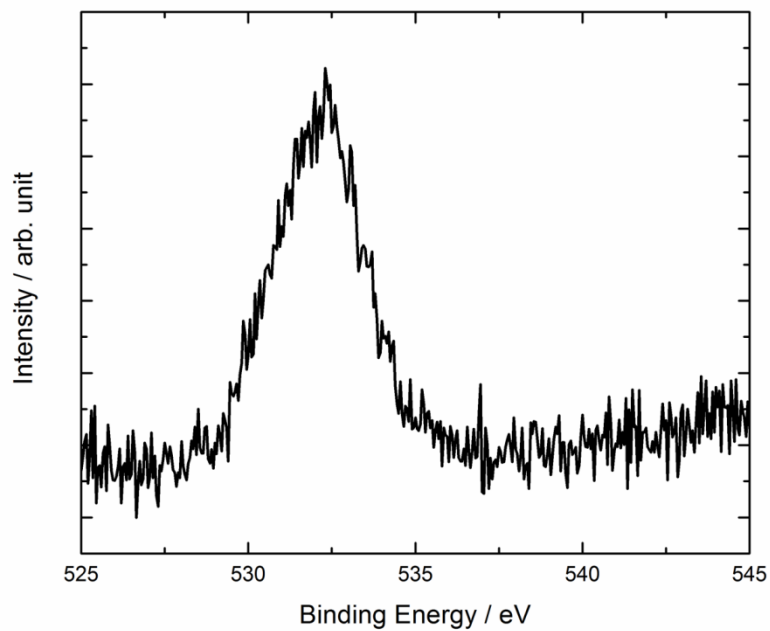
Figure 6.8: XPS survey scan of a Li-N co-doped diamond film (0.33% NH_3) with H-terminated surface.

Figure 6.9 illustrates the XPS spectra of C 1s core and O 1s core elements from Li-N co doped diamond film. There were only two elements detected on the diamond surface. The band offset for the 1s core level of carbon and the diamond VBM was approximately 282.8 eV. This value agreed with the XPS result upon investigation of an epitaxial diamond in which the band offset was recorded at 283.1 eV [41]. Surprisingly, there were O species present on the diamond film surface. The diamond film then underwent annealing treatment at 650°C in vacuum and XPS analysis on the O 1s core level was repeated. However, O was still present, eliminating the probability of water moieties or other O-species that were responsible for the initial signal before annealing process, as most of O-containing molecules would desorb at 650°C. This suggested that the O atoms were bonded directly onto the diamond surface. This was surprising as O should not be present on the surface during the growth process. The only possibility of the surface seeing O was during the transport from the

growth chamber in Bristol, UK to the analysis centre in Arizona, USA, due to the breaking of the vacuum system in between the two instruments.



(a)



(b)

Figure 6.9: XPS spectra of (a) C 1s core and (b) O 1s core element of a Li-N co-doped diamond film (0.33% NH_3) with H-terminated surface.

From the XPS observation, the UPS analysis discussed in Section 6.3.2 did not resemble a uniform H-termination but it consists of both H and O species. However, it is believed that the surface was dominated by H atoms due to the existence of the NEA surface. If O atoms dominated the surface, PEA behaviour should be observed from the spectrum taken from UPS instrument [42], which was not the case.

6.4 Conclusions

Electrical measurements were successfully obtained from Li-N co-doped diamond films using a Thermionic Emission System based at ASU. Li-N co-doped diamond films grown on top of Si substrates with high N content and NEA surface exhibit the highest current density with a value of 1.21×10^{-4} A/cm² at 900 K. Thus, these Li-N co-doped diamond films show great potential as thermionic emitters, and future development is needed to improve the doping procedure and optimise the emission properties.

From this study, it is essential to have an NEA surface compared to an as-grown diamond film, which failed to emit any electrons from its surface. Metallic substrates showed a lower work function compared to semiconductor substrate but due to the non-uniform and non-continuous surface, the current emitted from the surface of this film was smaller.

UPS analysis suggested that the Li-N co-doped diamond film prepared had a deep donor property near the surface of the material. The material possessed a NEA surface due to the termination by H atoms on the diamond surface. The NEA surface was thermally stable at high temperature (650°C). XPS analysis showed no cross-contamination from metals present in the growth chamber were observed. However, the surface was contaminated by O impurities. At the first, the impurities was suspected to be coming from water molecules or other organic moieties but the O atoms remained on the surface after undergo 650°C annealing process. This suggested that the O atoms were chemisorbed onto the diamond surface

and had formed strong bonds with the C atoms. Thus, the diamond surface consists of a mixture of H atoms and O atoms, but H atoms remain as the dominant species on the diamond surface due to the NEA property observed from UPS measurement.

6.5 References

- [1] N. Jiang, A. Hatta, & T. Ito, *Japanese J. Appl. Phys.* **37** (1998) L1175-L1177.
- [2] J. Mort, M.A. Machonkin, & K. Okumura, *Appl. Phys. Lett.* **59** (1991) 3148-3150.
- [3] V. Baranauskas, B.B. Li, A. Peterlevitz, M.C. Tosin, & S.F. Durrant, *J. Appl. Phys.* **85** (1999) 7455-7458.
- [4] V.C. Wilson, *J. Appl. Phys.* **30** (1959) 475.
- [5] I.P. Bogush, G.M. Gryaznov, E.E. Zhabotinskii, A.N. Makarov, V.. Serbin, & Y. L. Trukhanov, *At. Energy* **70** (1991) 263-266.
- [6] V. Granastein, R. Parker, & C. Armstrong, *Proc. IEEE*, May **87** (1999) 702-716.
- [7] P. Shefsiek, *IEEE Trans. Plasma Sci.* **38** (2010) 2041-2047.
- [8] S. Merkwowitz, & P. Maghami, *Class. Quantum Gravity* **19** (2002) 1745-1750.
- [9] P.J. Wilbur, R.G. Jahn, & F.C. Curran, *IEEE Trans. Plasma Sci.* **19** (1991) 1167-1179.
- [10] F.A.M. Köeck, J.M. Garguilo, & R.J. Nemanich, *Diamond Relat. Mater.* **14** (2005) 704-708.
- [11] W.F. Paxton, T. Wade, M. Howell, N. Tolk, W.P. Kang, & J.L. Davidson, *Phys. Status Solidi* **209** (2012) 1993-1995.
- [12] M. Kataoka, C. Zhu, F.A.M. Köeck, & R.J. Nemanich, *Diamond Relat. Mater.* **19** (2010) 110-113.
- [13] J.W. Schwede, I. Bargatin, D.C. Riley, B.E. Hardin, S.J. Rosenthal, Y. Sun, F. Schmitt, P. Pianetta, R.T. Howe, Z.-X. Shen, & N.A. Melosh, *Nat. Mater.* **9** (2010) 762-7.

- [14] K. Uppireddi, T.L. Westover, T.S. Fisher, B.R. Weiner, & G. Morell, J. Appl. Phys. **106** (2009) 043716.
- [15] S.H. Shin, T.S. Fisher, D.G. Walker, A.M. Strauss, W.P. Kang, & J.L. Davidson, 14th Int. Vac. Microelectron. Conf. **21** (2003) 587-592.
- [16] H. Shelton, Phys. Rev. **21** (1957) 1553-1557.
- [17] E.F. Redden, & A.E. Wallis, IEEE Trans. Aerosp. **1** (1963) 30-33.
- [18] A. Madjid, & J. Martinez, Phys. Rev. Lett. **28** (1972) 1313-1315.
- [19] J.G. DeSteele, Appl. Phys. Lett. **2** (1963) 25-27.
- [20] R.L. Aamodt, L.J. Brown, & B.D. Nichols, J. Appl. Phys. **33** (1962) 2080-2085.
- [21] M. Futamoto, M. Nakazawa, K. Usami, S. Hosoki, & U. Kawabe, J. Appl. Phys. **51** (1980) 3869-3876.
- [22] M. Suzuki, T. Ono, N. Sakuma, & T. Sakai, Diamond Relat. Mater. **18** (2009) 1274-1277.
- [23] F. Köck, J. Garguilo, & R. Nemanich, Diamond Relat. Mater. **10** (2001) 1714-1718.
- [24] F.A.M. Koeck, R.J. Nemanich, A. Lazea, & K. Haenen, Diamond Relat. Mater. **18** (2009) 789-791.
- [25] F. Koeck, & R. Nemanich, J. Appl. Phys. **112** (2012) 113707.
- [26] P.W. May, J.C. Stone, M.N.R. Ashfold, K.R. Hallam, W.N. Wang, & N.A. Fox, Diamond Relat. Mater. **7** (1998) 671-676.
- [27] X. Jiang, & C. Jia, Appl. Phys. Lett. **1197** (1995) 13-16.
- [28] B. Stoner, G. Ma, S. Wolter, & J. Glass, Phys. Rev. B. Condens. Matter **45** (1992) 11067-11084.
- [29] F. Allen, & G. Gobeli, Phys. Rev. **127** (1962).
- [30] K.M. O'Donnell, M.T. Edmonds, J. Ristein, A. Tadich, L. Thomsen, Q.H. Wu, C.I. Pakes, & L. Ley, Adv. Funct. Mater. **23** (2013) 5608-5614.
- [31] S.A. Kajihara, A. Antonelli, J. Bernholc, & R. Car, Phys. Rev. Lett. **66** (1991) 2010.
- [32] I. Langmuir, & K. Kingdon, Proc. R. Soc. London **107** (1925) 61-79.

- [33] F.A.M. Koeck, J.M. Garguilo, & R.J. Nemanich, *Diamond Relat. Mater.* **13** (2004) 2052-2055.
- [34] K. Okano, & K. Gleason, *Electron. Lett.* **31** (1995) 74-75.
- [35] M.W. Geis, J.C. Twichell, J. Macaulay, & K. Okano, *Appl. Phys. Lett.* **67** (1995) 1328.
- [36] M.W. Geis, J.C. Twichell, N.N. Efremow, K. Krohn, & T.M. Lyszczarz, *Appl. Phys. Lett.* **68** (1996) 2294.
- [37] F. Lacher, C. Wild, D. Behr, & P. Koidl, *Diamond Relat. Mater.* **6** (1997) 1111-1116.
- [38] O.R. Bar-Hama, & A. Hoffman, *Diamond Relat. Mater.* **32** (2013) 61-65.
- [39] N. Neugebohrn, T. Sun, F. A. Koeck, G. G. Hembree, R.J. Nemanich, T. Schmidt, & J. Falta, *Diamond Relat. Mater.* **40** (2013) 12-16.
- [40] J. Garguilo, F. Koeck, R. Nemanich, X. Xiao, J. Carlisle, & O. Auciello, *Phys. Rev. B* **72** (2005) 165404.
- [41] J.W. Liu, M.Y. Liao, M. Imura, & Y. Koide, *Appl. Phys. Lett.* **101** (2012) 252108.
- [42] P.K. Baumann, & R.J. Nemanich, *Surf. Sci.* **409** (1998) 320-335.

Chapter 7: Metal-Oxygen Termination on Boron-Doped Diamond Films

7.1 Introduction

Negative electron affinity (NEA) (see Section 1.8.1) has been proven theoretically and experimentally to be essential in activating a diamond surface for various purposes [1-4]. Without the presence of NEA, the electron from the diamond conduction band will experience a potential barrier which needs to be overcome (by heat, photons, or an applied bias) before the electron can be emitted into the vacuum. Normally, CVD diamond will have a hydrogen terminated surface after being exposed to an H-containing plasma [3,5-7], which imparts NEA to the surface. However the H atoms from the surface can be easily desorbed into the gas phase at higher temperature (650 °C and above) [8,9], and the NEA is lost as well. In addition, the H atoms could also be replaced by O atoms using various techniques such as wet-chemical oxidation (acid washing) [6,7,10,11], ozonolysis [12-14] and oxygen-plasma treatment [15,16]. When O atoms replaced H atoms on the diamond surfaces, the NEA characteristic will be converted to positive electron affinity (PEA). For an NEA surface, the usual requirement is that there is a surface dipole where the outer atomic layer is positively charged while the inner carbon layer is negatively charged. This is the case with C-H bonds. The opposite is true for PEA, such as the oxidised surfaces, where the outer O atoms are slightly negative whereas the inner carbon is positive. Thus, the relative electronegativity of an atom relative to that of C can be used as a guide to determine whether a surface termination might give PEA or NEA. For example, the halogens all have much greater electronegativity than C, and from experiments it is known that chlorinated and fluorinated diamond surfaces exhibit strong PEA [7]. The problem for NEA is that it requires strongly electropositive atoms to terminate the surface, and most of these are metals which do not form stable monovalent bonds with carbon. Nevertheless, a trick was found whereby the electropositive metal (such as Na or Cs) could be added to an

oxygenated diamond surface to form a 'salt' on the surface, such that the surface layer looked like -C-O-Cs [17,18]. Since the outermost layer is the electropositive metal, the structure still exhibits NEA. In this case the surface bonds contain quite a good deal of ionic character [15,19-21].

The problem with hydrogenated surfaces being unstable at high temperature jeopardises many promising applications involving electron emission from diamond, such as thermionic emission, field emission and secondary electron emission (where too much emitted current causes local heating which desorbs the H layer). In the case of thermionic emission, when the H atoms start to desorb from the diamond surface the thermionic current starts to drop and often the emitter will fail shortly afterwards [8,9,22-24]. Theoretical studies have searched for possible thermally stable alternatives to H atom termination. Following on from the early work using CsO and NaO salts, Cu, Ti, Ni and Co metals were studied by *ab initio* computational techniques to determine if they would produce an NEA surface. All four transition metals were found to induce a NEA surface. However, the results were dependent on the ability of the metals to form a carbide layer with the diamond surface. Due to the inability of Cu and Ni to form a carbide layer, their NEA were lower than Ti and V metals. Ni and Cu showed NEA properties when one atom layer of coverage of metal was applied on the diamond surface giving NEA values of 0.29 eV and 0.55 eV, respectively. In contrast with Ti and V metals, one atom layer coverage of metal will lead to low NEA value and the optimum metal coverage was predicted to be at 0.25 of atom layer coverage. At 0.25 layer coverage, Ti exhibits an NEA of 3.64 eV while V only produced 1.15 eV of NEA. These findings suggested that Ti metal will show a promising NEA surface [20,21].

One of the challenges in producing metal-oxygen terminated diamond films is to be able to produce thin coverage in the form of an atomic layer (<10 Å) of the chosen metal on top of the diamond surfaces. The standard way to achieve such thin layers is to use Atomic Layer Deposition (ALD) [25-27], however this is expensive and requires specialised apparatus that is not available in many laboratories.

In early 2010, Li-O-terminated diamond was proposed to possess NEA characteristic on C(100) surfaces with a work function shift of -4.52 eV with one mono atomic layer coverage of Li atoms [19]. Later O'Donnell and co-workers successfully prepared air-stable Li-O terminated diamond films with a controllable atomic layer coverage [15]. 0.4 Å and 2.8 Å of Li atoms were deposited on to O-terminated diamond films followed by annealing process at 800°C proven to provide sufficient energy to enhance the NEA characteristic on the diamond surface. However, during the analysis care needed to be taken before a conclusive NEA characteristic could be appointed to any diamond surface. Figure 7.1 depicts the band schematics of a 'true NEA' and an 'effective NEA'. An effective NEA describes the condition whereby the vacuum level is situated between the CBM of the bulk material and the CBM at the surface, and the electron affinity, X , (see Section 2.7.2) is between 0 and 0.7 eV [15]. Electrons at the CBM approaching to the surface have certain chance to be emitted into the vacuum level without encountering any energy barrier. However, a more efficient electron emission process is expected with a true NEA characteristic whereby the vacuum level lies below the CBM of the material at the surface.

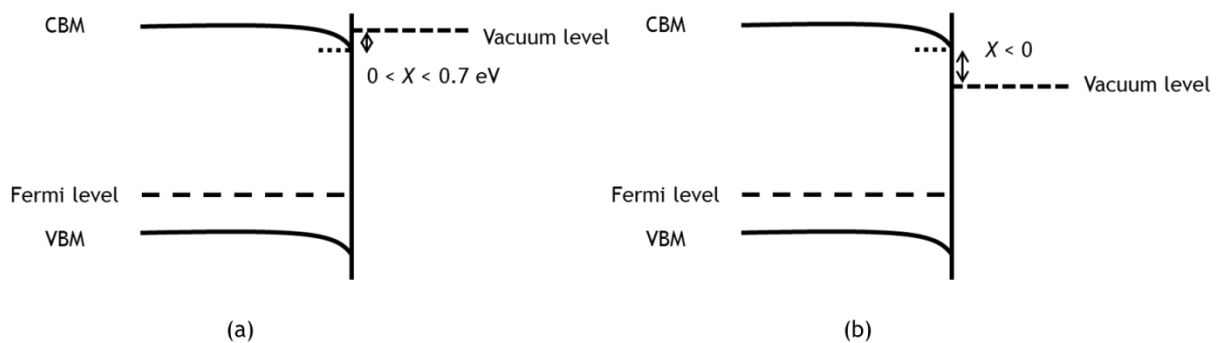


Figure 7.1: Band schematics of (a) an effective NEA and (b) a true NEA.

This study will investigate the potential of creating stable NEA surfaces by combining metal with oxygen-terminated diamond films. Once the optimum metal-oxygen termination was determined, the method was

applied to the Li-N co-doped diamond films (see Chapter 4) to compare their thermionic emission properties with those from a hydrogen-terminated diamond.

7.2 Experimental

The technique used in this investigation utilised the top-down approach. An initial thick (~20 nm) layer of the metal of interest was deposited onto a boron-doped diamond (BDD) substrate. Then, a series of washing techniques were developed to selectively wash the metal layer without removing the metal-oxygen layer. Next, the metal-oxygen terminated BDD underwent X-ray Photoelectron Spectroscopy (XPS) analysis to ensure the metal-oxygen layer was still present on the surface. Finally, the sample was annealed to chemically bond the metal-O-C together, and then analysed using Ultraviolet Photoelectron Spectroscopy (UPS) for electronic structure analysis.

Ideally, n-type diamond would be used for electron emission experiments, but these are not yet commercially available. Therefore, p-type BDD films were chosen because they were commercially available as free standing films with the appropriate thickness, and are electrically conducting [28]. The BDD used in this experiment were supplied by Element Six (electrochemistry grade) with dimensions of 10 mm × 10 mm × 0.6 mm and with one sided polished. Prior to use, these substrates were washed in a mixture of sulfuric acid and potassium nitrate at 180°C to remove any impurities including metallic particles and graphite that may be produced during the cutting & polishing process at the factory.

Then, the BDD films underwent ozonolysis treatment using a UVO cleaner 42A-220. The cleaned BDD films were placed on top of the metallic tray and were exposed to a UV lamp (220 nm) for 30 minutes to create oxygen-terminated surfaces. Dr. Tomas Martin confirmed the improvement of oxygen-terminated surface *via* this method by wettability experiment

[29]. The contact angle of the diamond reduced after the surface being exposed in ozone atmosphere by at least 10°.

7.2.1 Thermal Deposition of Metal on Oxygen-Terminated BDD Films

Cr, Al, Zn, Ti and Mg metals were used in this experiment. Zn and Ti was chosen because the semiconducting characteristics of their oxides [30]. The semiconducting property may lead to enhancement of the NEA on the diamond surface. Mg was chosen due to the success of lithium-oxygen termination in providing an NEA surface [1,15,19]. As Mg has a diagonal relationship with Li in the Periodic Table, it might react with a diamond surface in the same way as Li [31]. Cr was chosen to investigate the effect of transition metals, while Al was used to observe the effect of its amphoteric oxide properties.

Cr and Zn were used in chunks (~3 mm) while Al and Ti were used in the form of wires. All metals had 99% purity and were supplied by Goodfellow Metals. Mg strips (BDH, 99%) were used in the experiment with prior treatment using sandpaper to remove any unwanted oxide layer.

A bell-jar thermal evaporator (see Section 2.8) was used to deposit the metals of interest onto BDD substrates. Firstly, the metal chunks/wires/strips were placed into or wrapped around a tungsten filament, which was shaped into a coil. The BDD substrates were placed 10 cm below the filament. Then, the chamber was pumped down using a diffusion pump to a base pressure of 5×10^{-6} torr. Once it reached the pressure, 15 to 40 A of current (depending on the metal used) were passed through the filament, causing it to glow white hot. The metal in contact with the filament evaporated at a constant rate, the speed of which could be controlled by the current. The deposition ended when ~20 nm of metal was successfully deposited on the BDD surface. The thickness was monitored by Agar thickness monitor (quartz crystal) positioned next to the substrate.

Each set of metal deposition experiments was done separately to avoid any cross-contamination inside the chamber. After each deposition, the chamber was cleaned with methanol and acetone. Before next deposition began, layers of *Bell-Bright* polymer were sprayed inside the glass bell jar to create polymeric coating to ease the next cleaning process.

7.2.2 Removing Excess Metal

The evaporation procedure deposits a layer that is much too thick - ideally only a monolayer of metal is needed. Therefore the excess metal has to be removed. For Li this was done by simply washing with water - the Li was sufficiently soluble/reactive that any atoms that had not bonded to the oxygen were removed easily [29]. However, for other metals, acid needed to be used to remove them. To find out what type of acid, and at what concentration was required, a preliminary study was done. 0.5 g of each of the metals (chunks, wires or strips) were inserted into individual vials. Then, 10 ml of 1M HCl was pipetted into the vials. Next, the vials were heated in an oil bath at 100 °C. The time taken for all the metal to completely dissolve was taken. It was found that all the metals dissolved within 2 hours after the reaction started. However, extra precautions needed to be taken for Ti metal, which required a longer reaction time (4 hours) with more concentrated HCl acid (4 M) to dissolve the metal completely.

This process needed to be selective towards the removal of excess metal and not their oxide. Thus, the same procedure was repeated with their respective oxides. Ti_2O_3 (purple powder) and Cr_2O_3 was prepared by a calcination process of their parent metals for 1 hour at 550°C with a heating rate of 5°C/min. Al_2O_3 (Reidel-de Haën, 98%, <250 µm), ZnO (Sigma-Aldrich, 99.9%, <1 µm) and MgO (Fine Chemicals, 99%, <250 µm) were used without further treatment. When the same experiment was repeated, all the metal oxides dissolved instantly except Ti_2O_3 , Cr_2O_3 and Al_2O_3 . Thus, the selective etching method was deemed suitable to remove

Ti, Cr and Al selectively without removing their oxides but a different method was required for Mg and Zn metals.

Zn metal is known to dissolve in organic solvents such as methanol and glycerol but is insoluble in water [32]. When Iodine was added into the Zn-methanol mixture, ZnI_2 is formed, as shown in Equation 7.1.



In addition, ZnI_2 is soluble in water and this makes the washing process easier. 8.5% w/v of I_2 in ethanol was prepared by dissolving 0.85 g of iodine crystals (Fisher Scientific, 99.9%, <2 mm) in 100 ml of ethanol. The solution was sonicated for 10 minutes in the ultrasonic bath resulting in the formation of a brown solution. Then, 10 ml of this solution was pipetted into a vial filled with 0.5 g of Zn powder. This mixture was then sonicated for 1 hour and the time taken for the Zn metal to completely dissolve was written down, and any changes in the colour of the brown solution was noted. The same experiment was repeated with ZnO powder to ensure the selectivity of the reaction.

After an hour in the ultrasonic bath, the Zn metal dissolved completely and the colour intensity of the brown solution reduced greatly. This suggests that the concentration of iodine inside the solution was reduced due to the formation of ZnI_2 as shown in Equation 7.1. However, no change could be observed when Zn metal was replaced with ZnO powder. The white ZnO powder remained inside the solution and the colour intensity of iodine solution remain unchanged. Thus, this procedure was deemed to be successful for selectively removing Zn in the presence of ZnO.

The same experiment was repeated for Mg metal. It is known that Mg dissolves in organic solvents, especially in alcohol, as this is the basic step in preparing Grignard reagents. Iodine was still used but its role was

different. In this experiment, iodine acts as a catalyst and is not involved in the formation of the final product [32]. The expected final product is magnesium ethoxide ($\text{Mg}(\text{OCH}_3)_2$). After 1 hour of sonication, the Mg strip was still present and no significant change was observed. Thus, the experiment had failed, and a different method needed to be developed in order to selectively remove excess Mg metal from the diamond surfaces.

Various techniques were tried, such as dissolving Mg metal in double deionised water or using a variety of mineral acids with different concentrations. With double deionised water it took 72 hours for the Mg metal to start showing visible signs of dissolution but it was still not sufficient to etch away all remaining metal from diamond surfaces. Later, HNO_3 , H_2SO_4 and HCl with various concentrations ranging from 0.01 M up to 1 M were used to dissolve Mg. The higher the concentration used, the faster both Mg and its oxide dissolved in the acids at room temperature. Finally, a concentration of 0.005 M of H_2SO_4 at room temperature with less than 5 seconds washing time was chosen as the best method to selectively remove Mg metal and not its oxide.

Having developed a range of selective etching techniques to remove excess metal in the presence of their oxides using bulk metals, the next step was to use these methods on freshly deposited metal-oxygen BDD substrates. Because the quantities of metal involved were now so small, success of these etching processes on the metal and oxide films could not be determined by eye, and so XPS and UPS were used. This was done before and after thermal annealing to see if the C-O-Metal structure had been chemically bonded on the surface.

7.2.3 Elemental Analysis using XPS

All washed samples were analysed in the XPS instrument (see Section 2.7.1) at ASU, Arizona, USA, with the help from Professor Robert Nemanich and Dr. Tianyin Sun. Sample preparation, data recording and sample

analysis were done by Dr. Tianyin Sun with help from the author. The XPS measurements were done under high vacuum ($\sim 4.5 \times 10^{-9}$ torr) with Mg used as the X-ray source. XPS survey scans and elemental scans were taken before any annealing treatment for all samples, which were then followed up by UPS surface analysis. If changes were observed in the UPS scan after annealing, an additional XPS scan was done immediately to observe the changes in the binding energy of the surface species.

The sample transfer from the XPS instrument to the UPS instrument was done using UHV transfer line ($\sim 10^{-9}$ Torr) to make sure the vacuum environment was sustained and to avoid any contamination in air.

7.2.4 NEA Stability Determination using UPS

A home-built UPS spectrometer (see Section 2.7.2) with a He I UV light source based in ASU, Arizona, USA was used in this experiment. The working vacuum while measuring the photoemission was set at $\sim 1 \times 10^{-8}$ torr. A $\sim 10^\circ$ angle tolerance was measured between the detector and the sample. 8 V of bias voltage was applied to overcome the work function of the detector. The scan rate was set to 0.01 V/s and the resolution was tuned between 0.10 and 0.15 eV. The work function of the detector was set to 4.2 eV

After the 1st scan at room temperature ($\sim 25^\circ\text{C}$), the samples were annealed at various temperatures, starting from 250°C , 350°C , 450°C , 550°C and 650°C . All annealing processes were done for 30 minutes. The samples were then cooled down to $\sim 70^\circ\text{C}$ before being scanned with the UPS instrument. If any changes were observed during the scan, the sample was transferred to the XPS instrument for elemental analysis to observe any changes in the binding energy of the elements.

All sample preparation for measurements in the UPS system, data recording and sample analysis, were done by Dr. Tianyin Sun with help from the author.

7.3 Results and Discussion

An oxygen-terminated BDD substrate was used as a control sample. Any changes observed in both XPS and UPS spectra of metal-oxygen-terminated diamond samples were compared to those from this control sample. Figure 7.2 illustrates the XPS spectra recorded at room temperature, before and after the annealing process at 650°C. From the survey scan (not shown), only two elements (C and O) were present and no other impurities were observed. This suggests that the surface of the material was clean and contamination was minimised. Scans at specific binding energies were done to obtain higher resolution of C and O peaks. From Figure 7.2(a), the C 1s core peak with a binding energy of 284.7 eV was recorded. After the sample was annealed at 650°C, no change in binding energy was observed but the intensity of the carbon peak increased to twice its previous value. This may be due to the removal of surface impurities such as water molecules and adsorbed gases [33,34]. The band offset (Equation 2.3) between the 1s core level of carbon and the diamond valence band maximum (VBM) was approximately 282.7 eV. The value was smaller when compared with data recorded by other researchers who obtained an offset value of 283.1 eV [35]. This may be due to a different oxygen termination treatment used by their group. Oxygen plasma treatment has better oxygen-termination coverage compared to the ozonolysis treatment used in this study. Removing the impurities improved the signal received by the detector.

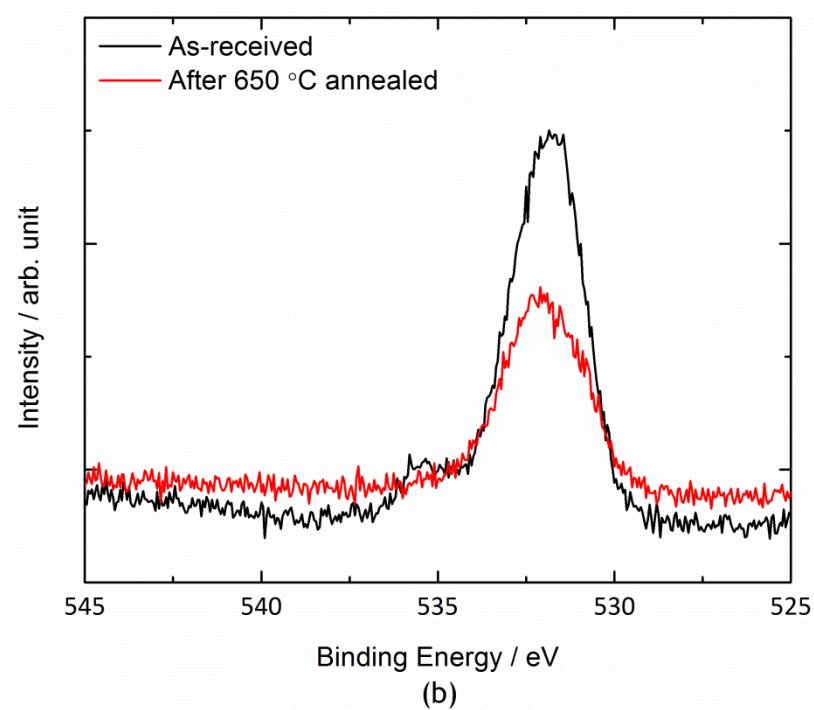
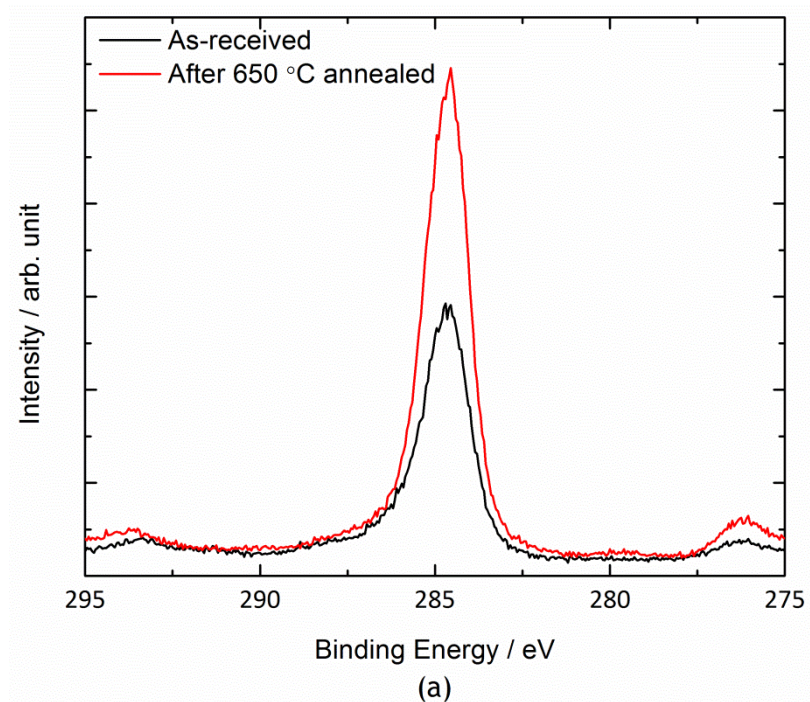


Figure 7.2: XPS spectra of (a) C 1s core and (b) O 1s core element of oxygen-terminated BDD substrate (the control sample). The measurements were recorded at room temperature, before and after annealing at 650°C.

The binding energy for the O 1s core peak was recorded at 532 eV. A small shoulder peak was also observed at a higher binding energy (535.4 eV). In contrast with C, after annealing the sample at 650°C the intensity

of O reduced by half. In addition to that, the small shoulder peak observed at room temperature disappeared after the annealing process. The disappearance of this shoulder peak and also the reduction in the intensity of the oxygen peak is consistent with the desorption of water moieties and other oxygen containing gases (CO and CO₂). By removing the oxygen containing molecules, the amount of O 1s core signal detected by the instrument was also reduced, hence decreasing the intensity of the O 1s core peak observed in the spectrum.

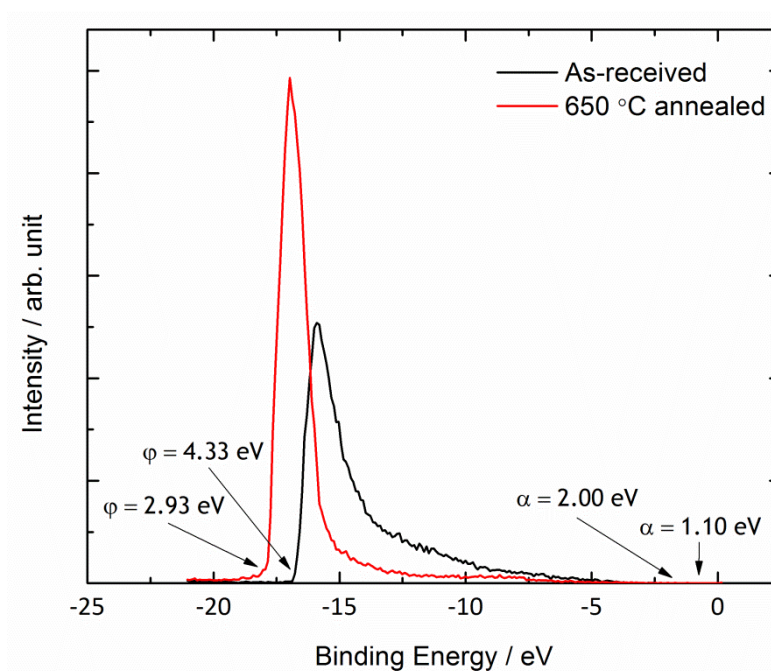


Figure 7.3: UPS spectra of oxygen-terminated BDD sample recorded at room temperature, before and after annealing.

Figure 7.3 depicts the UPS spectra of oxygen-terminated BDD control sample recorded at room temperature, before and after the annealing process. The work function calculated (see Section 2.7.2) for the sample before the annealing process was 4.33 eV while the energy gap between the VBM and the Fermi level was determined to be 2.00 eV. Hence, the distance from the VBM of diamond to the vacuum level is 6.33 eV. The band gap of diamond has the value of 5.45 eV [36]. By comparing both values,

this O-terminated BDD possessed a PEA surface because the vacuum level is situated 0.88 eV above the conduction band minimum (CBM) of the material. The Fermi level was nearer to the VBM compared to the CBM suggesting that the material was still a p-type material. However, after annealing, the cut-off energy shifted to give a lower work function (2.93 eV). In addition, the gap between the VBM and Fermi level also reduced to 1.10 eV and the total gap between the VBM and vacuum level decreased to 4.03 eV. This means that the vacuum level was now situated 1.42 eV below the CBM. This means that the surface had changed from PEA to NEA. O-terminated diamond is known to possess PEA [10], and the XPS spectrum in Figure 7.2 confirm the existence of the O species, suggesting that O species will still be responsible for any electron affinity properties on the surface.

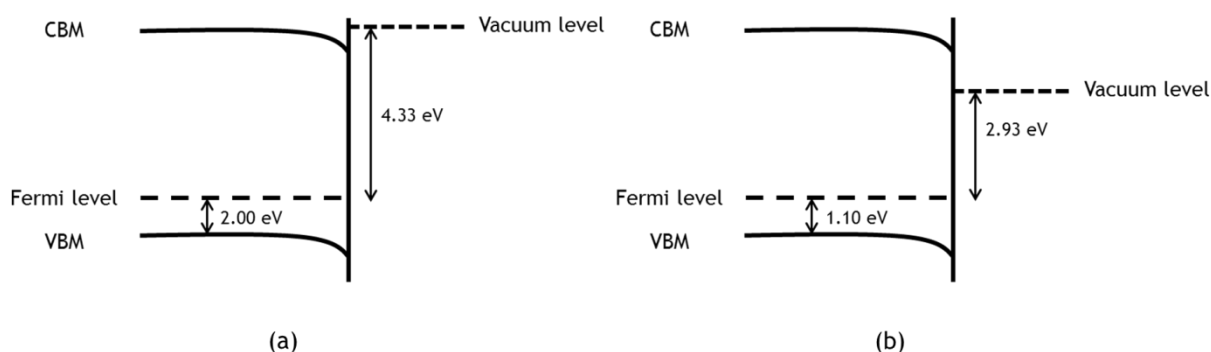


Figure 7.4: Band schematics of O-terminated BDD films (a) before and (b) after annealing. O-terminated BDD films before annealing exhibit PEA while after annealing exhibit NEA.

It should be noted that the NEA observed after annealing may not be a ‘true NEA’. O’Donnell’s group and Takeuchi’s group have discovered a variety of NEA behaviour on diamond surfaces, either the NEA behaves as an ‘effective NEA’ or a ‘true NEA’ [11,15].

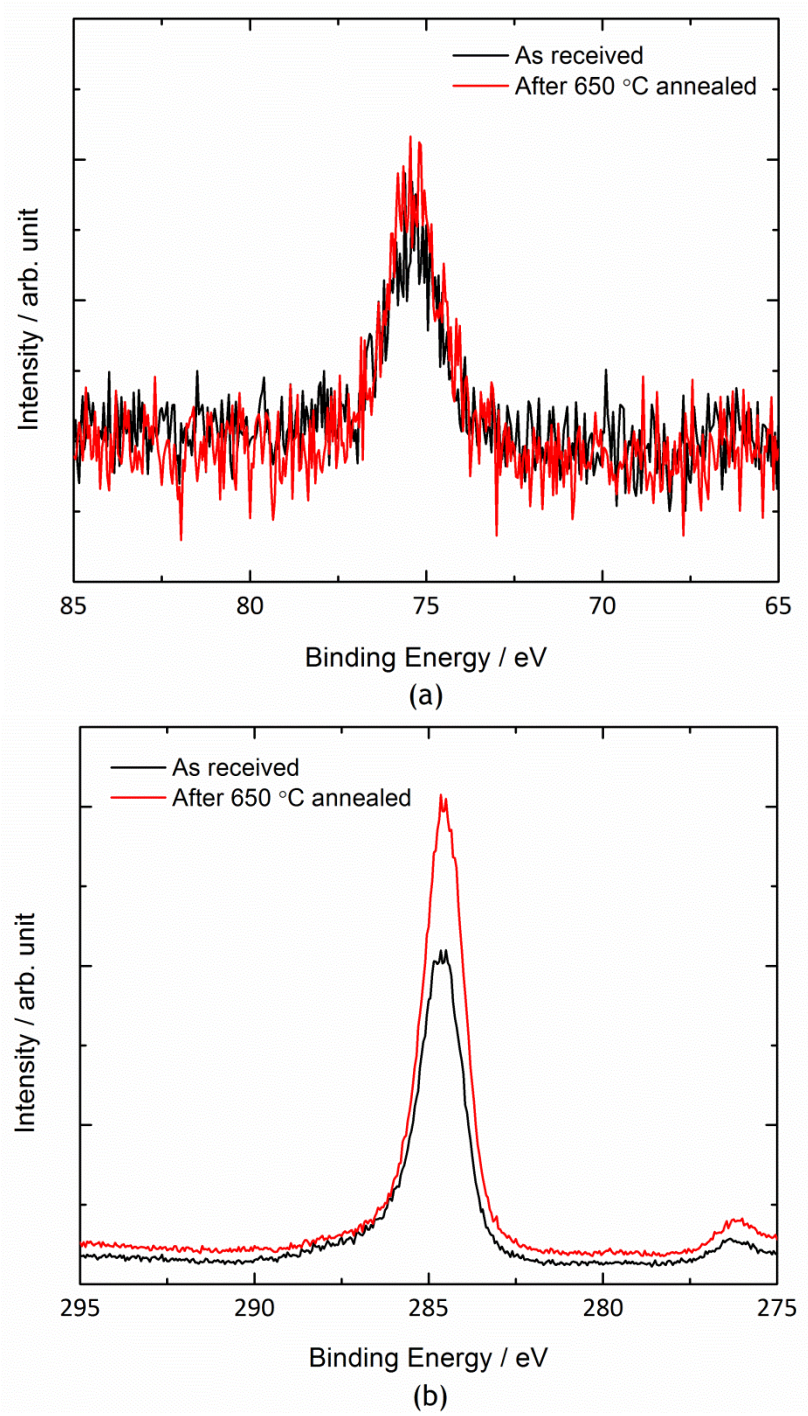
Takeuchi and co-workers also reported the possibility of oxygen-terminated diamond films recovering its NEA after high-temperature annealing due to replacement of O atoms with H atoms. The origin of the H atoms remained unknown. Either the H atoms were trapped in the grain

boundaries or it originates from the interstitial H atoms trapped in the diamond lattice during growth process. We have evidence for H trapped in polycrystalline CVD diamond from the SIMS spectra of the N-doped microcrystalline samples in Chapter 2.

The results suggest that annealed oxidised diamond exhibits an effective NEA surface. The reduced work function does not resemble the expected work function for oxidised diamond. However, it cannot be ruled out that the apparent NEA came from spurious sources, such as substitution of the O by H, or by inadvertent contamination by metals (although neither was seen in XPS).

7.3.1 Aluminium-Oxygen Termination

Figure 7.5 depicts the Al $2p_{3/2}$, C 1s and O 1s signals detected using the XPS instrument on an Al-O-terminated BDD sample. The measurements were taken at room temperature, before and after annealing at 650 °C. From the survey scan (not shown), only three elements were observed, which shows that the surface was clean from any contamination. The detection of Al metal (Figure 7.5 (a)) suggests that the selective etching method using HCl acid (Section 7.2.2) was successful. If none of the excess Al metal were removed from the diamond surface, a low signal-to-noise ratio spectrum would be observed compared to the spectrum shown in Figure 7.5(a). After annealing, the Al metal was still present suggesting that the layer was thermally stable at the annealing temperature. Because Al metal normally melts at 660 °C, this shows that the Al must be strongly bound to the surface, probably in the form of its oxide. Similar observations were made for both C 1s and O 1s (Figure 7.5(b) & (c)). After annealing, the C intensity increased while the O peak reduced. The peak position of the C 1s core remained unchanged after the annealing process with the maximum peak observed at 284.6 eV.



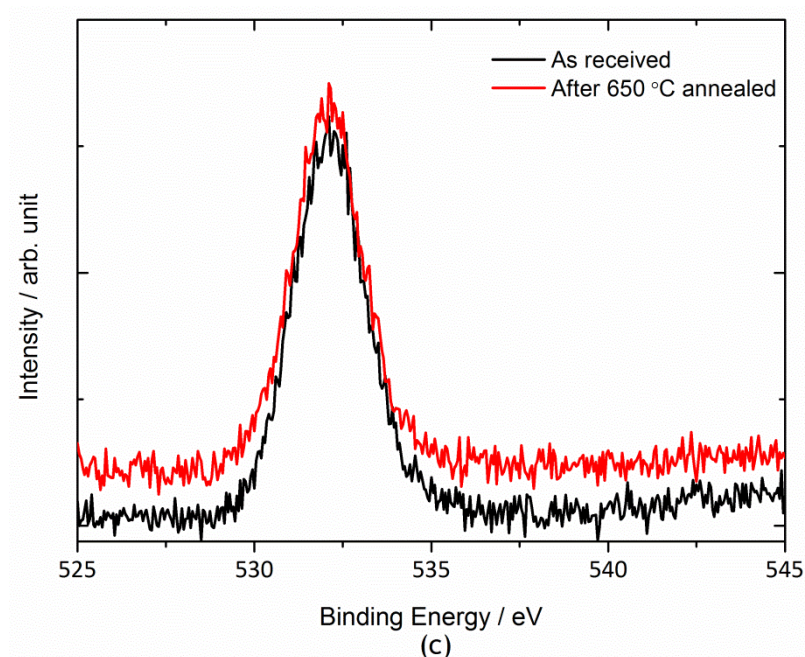


Figure 7.5: XPS spectra of (a) Al $2p_{3/2}$, (b) C $1s$ and (c) O $1s$ elements of Al-O-terminated BDD sample. The measurements were at room temperature, before and after annealing.

Figure 7.6 shows the UPS spectra of Al-O-terminated BDD sample measured at room temperature after series of annealing processes. The VBM of the diamond before annealing was 1.44 eV below the Fermi level and it did not change after the annealing process. However, the work function of the material reduced after the annealing process. The work function remained unchanged at 4.09 eV from room temperature up to the annealing temperature of 550°C. After annealing at 650°C for 30 minutes, the work function of the material reduced to 3.61 eV. Combined with the value of the VBM (1.44 eV), this indicates NEA occurs on the Al-O-terminated BDD surface, with a gap of 5.05 eV between the VBM and vacuum level. This suggests that 650°C is sufficient to allow Al to react with the O-termination surface, and reconstruct into a more stable structure. Similar observations were made on a Li-O surface after annealing under UHV conditions [15].

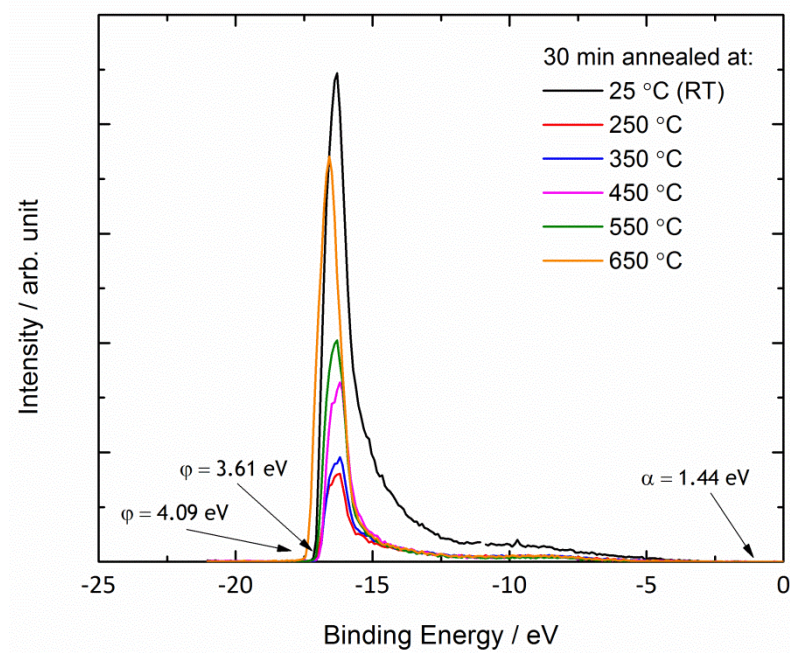


Figure 7.6: UPS spectra of Al-O-terminated BDD samples measured at room temperature after series of annealing processes.

From UPS measurement, UPS deduced Al-O-terminated BDD film possessed an NEA characteristic. However, further analysis was done to confirm whether it is an effective NEA or a true NEA. By applying the 282.7 eV valence band offset of diamond (Section 7.3), the VBM of Al-O terminated BDD sample was deduced to be at 1.90 eV below the Fermi level as depicted in Figure 7.7. With the band gap of diamond, $E_G = 5.45$ eV, this implies that as long as $\phi < E_G - 1.90$ eV, the surface has NEA. From this calculation, the vacuum level lies just above the CBM at the surface. Thus, Al-O-terminated BDD film exhibit effective NEA behaviour.

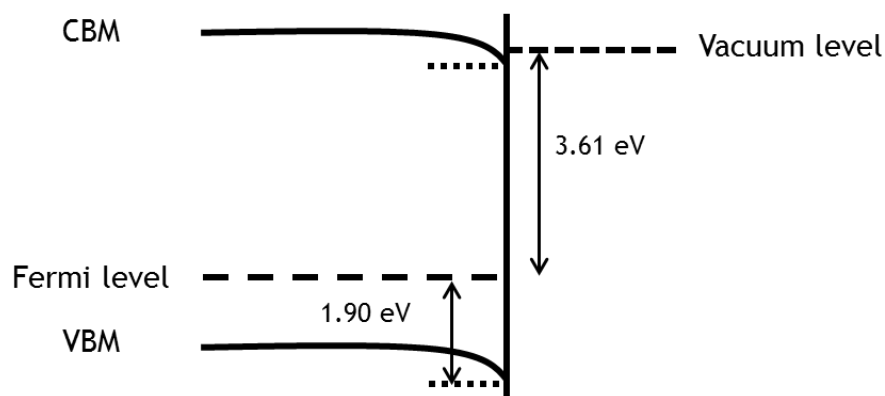


Figure 7.7: Band schematics of Al-O-terminated BDD film after annealing.

The measured binding energies of Al $2p_{3/2}$, C 1s, O 1s and work function of the Al-O-terminated BDD are summarised in Table 7.1.

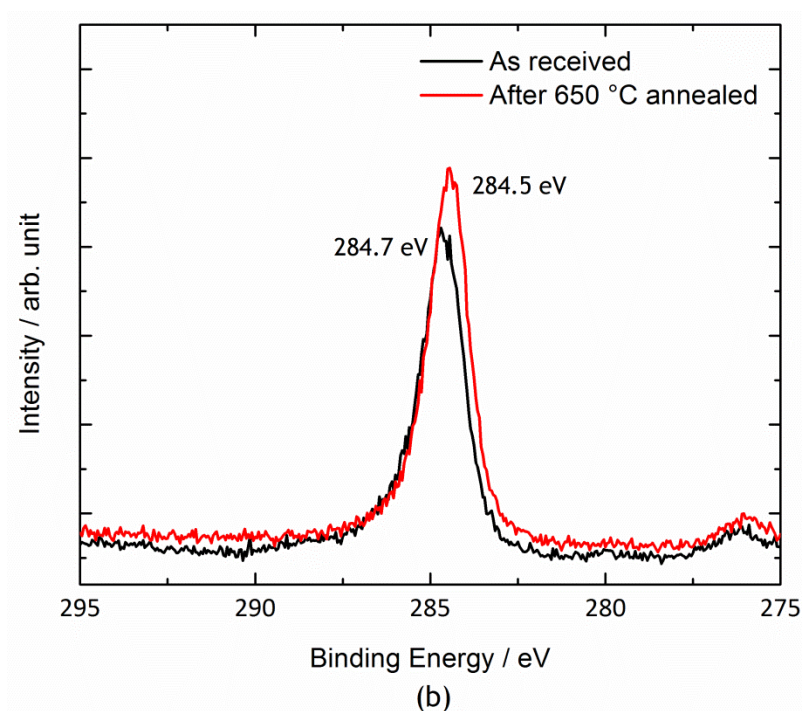
Table 7.1: Al $2p_{3/2}$, C 1s, O 1s core binding energies and work function of Al-O-terminated BDD.

Process	C 1s (eV)	O 1s (eV)	Al $2p_{3/2}$ (eV)	Work function (eV)
O-termination	284.7	531.7	--	4.33
Al deposition & washed	284.6	532.1	75.4	4.09
Annealed at 650°C	284.6	532.1	75.4	3.61

7.3.2 Chromium-Oxygen Termination

Figure 7.8 illustrates the core level of Cr $2p_{1/2}$ & $2p_{3/2}$, C 1s and O 1s of Cr-O-terminated BDD sample. From the XPS spectra, the selective etching process using HCl acid to remove excess Cr metal without removing Cr-O was a success due to the presence of Cr $2p_{1/2}$ & $2p_{3/2}$ core levels. From the survey scan spectrum (not shown), only three elements were present, thus eliminating any possible contamination of the surface. The core binding energies of all elements showed shifts from higher binding energy to lower binding energy after the annealing. The Cr $2p_{1/2}$ & $2p_{3/2}$ binding

energy reduced from 586.7 eV to 586.4 eV and from 576.9 to 576.8 eV, respectively. The C 1s binding energy reduced from 284.7 eV to 284.5 eV, and the O 1s binding energy reduced from 531.3 eV to 530.9 eV. This suggests that at high annealing temperature the surface species gained extra energy to reconstruct into a more stable formation that reduced the core level binding energies. In addition, the Cr-O-terminated surface was also thermally stable due to the presence of Cr even after high temperature annealing.



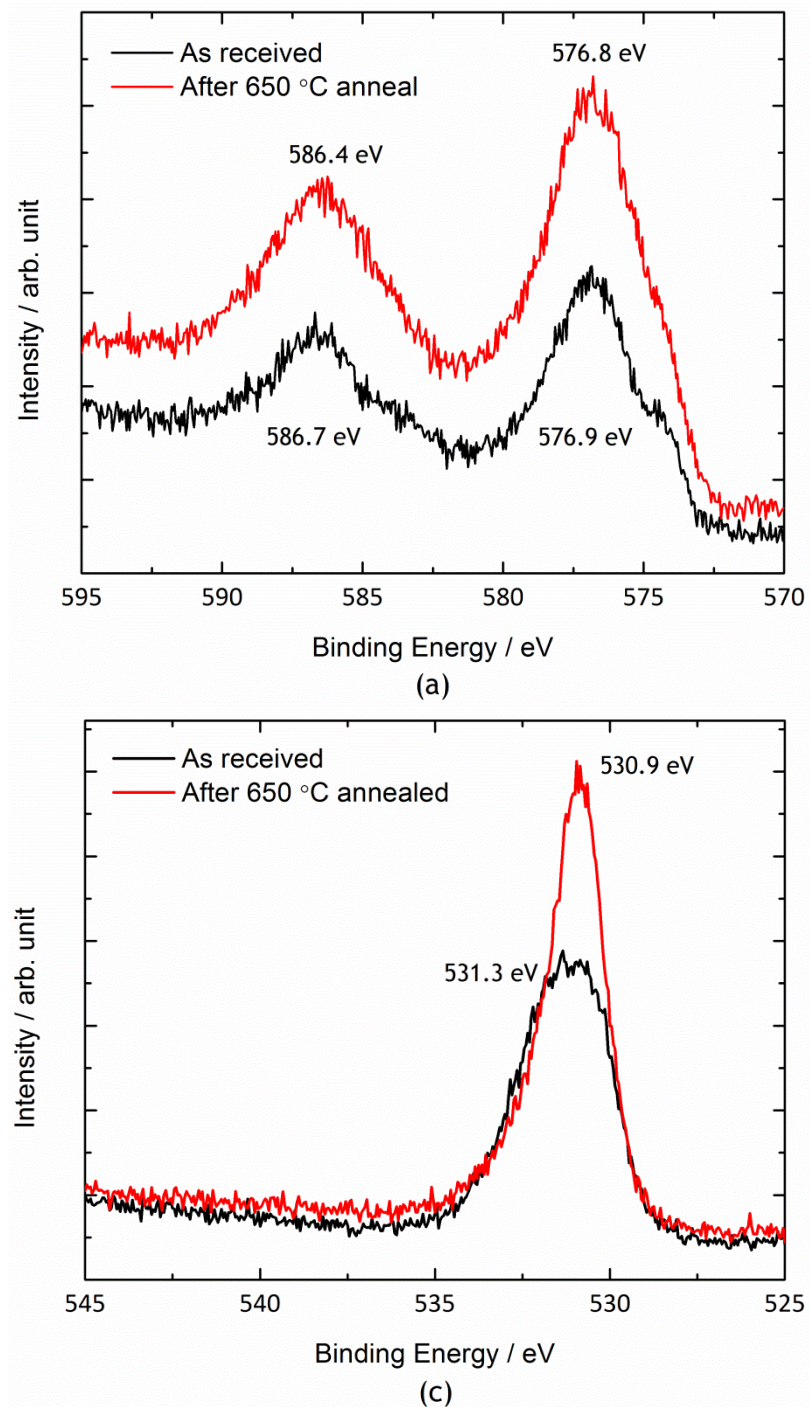


Figure 7.8 XPS spectra of (a) Cr $2p_{1/2}$ & $2p_{3/2}$, (b) C $1s$ and (c) O $1s$ elements of Cr-O-terminated BDD sample. The measurements were at room temperature, before and after annealing.

Figure 7.9 depicts the UPS spectra of Cr-O-terminated BDD sample measured at room temperature after annealing. The VBM of the diamond film remained unchanged at 1.57 eV below the Fermi level even after high temperature annealing. At first, the work function on the surface was

observed to be at 3.53 eV. After the 1st annealing cycle at 250 °C, the work function reduced to 3.25 eV. However, the work function returned to its original value after annealing at 350 °C and remained unchanged throughout the subsequent annealing steps. The change of work function was treated as an anomaly and repetition is required to confirm whether the change was due to instrumentation error during that measurement period. Combining both the VBM (1.57 eV) and the work function (3.53 eV), results in a 5.10 eV gap between the VBM and the vacuum level. Since we know that the band gap of pristine diamond ~5.45 eV, this means that the Cr-O-terminated surface exhibits NEA property.

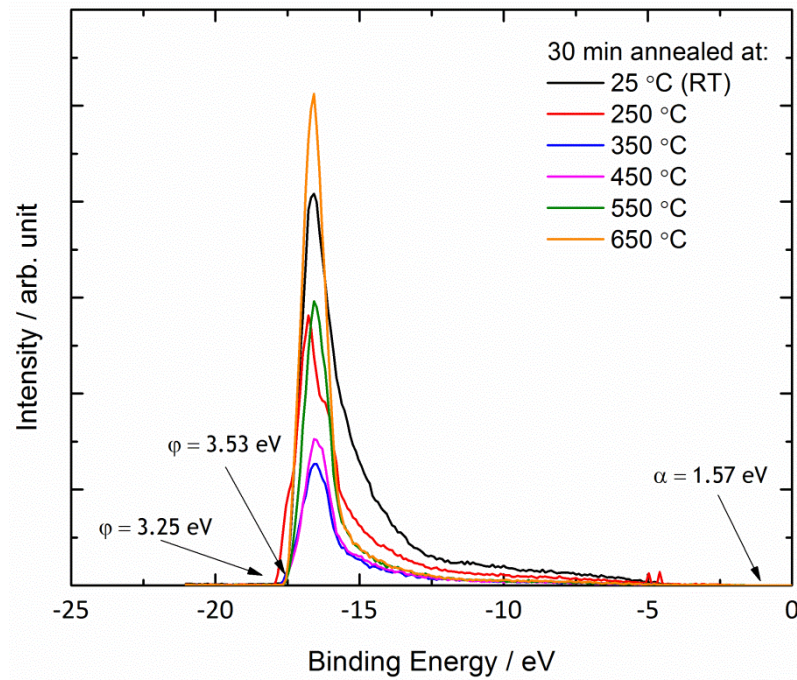


Figure 7.9: UPS spectra of Cr-O-terminated BDD sample measured at room temperature after annealing.

By applying the 282.7 eV valence band offset (Section 7.3), the VBM of the Cr-O terminated BDD sample was deduced to be 1.8 eV below the Fermi level as showed in Figure 7.10. With the band gap of diamond, $E_G = 5.45$ eV, this implies that as long as work function, $\phi < E_G - 1.80$ eV, the surface has NEA. From this calculation, the ϕ lies below the CBM at the

surface. Thus, Cr-O-terminated BDD film does exhibit a true NEA due to the $X < 0$ eV.

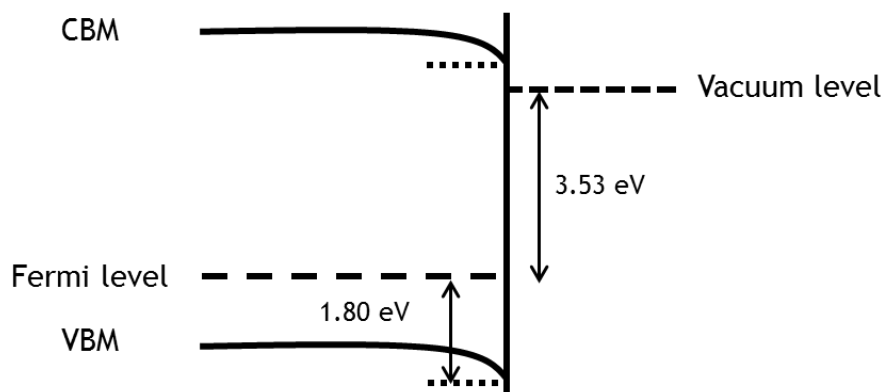


Figure 7.10: Band schematics of Cr-O-terminated BDD film after annealing.

The measured binding energies of Cr $2p_{1/2}$ & $2p_{3/2}$, C 1s, O 1s and the work function of the Cr-O-terminated BDD are summarised in Table 7.2.

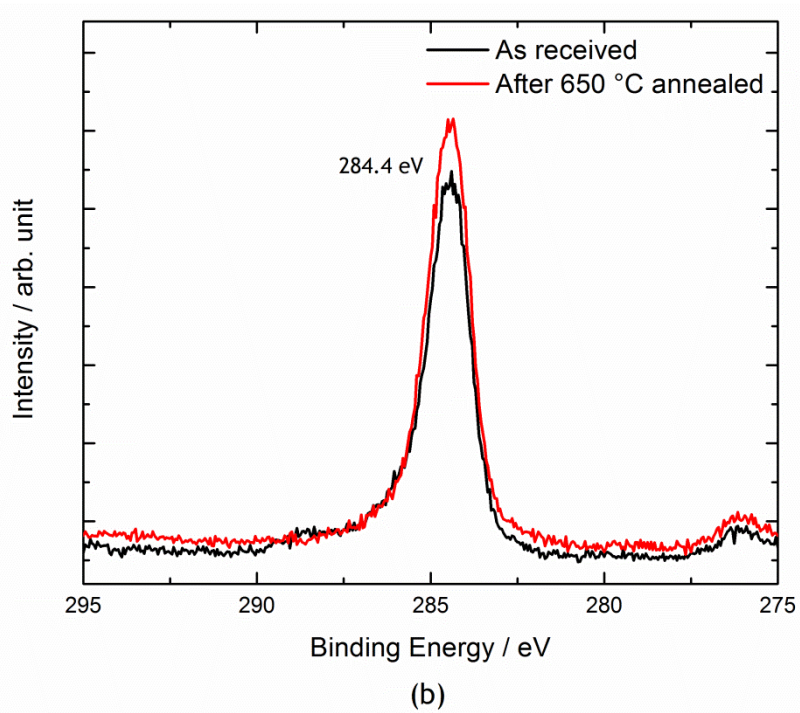
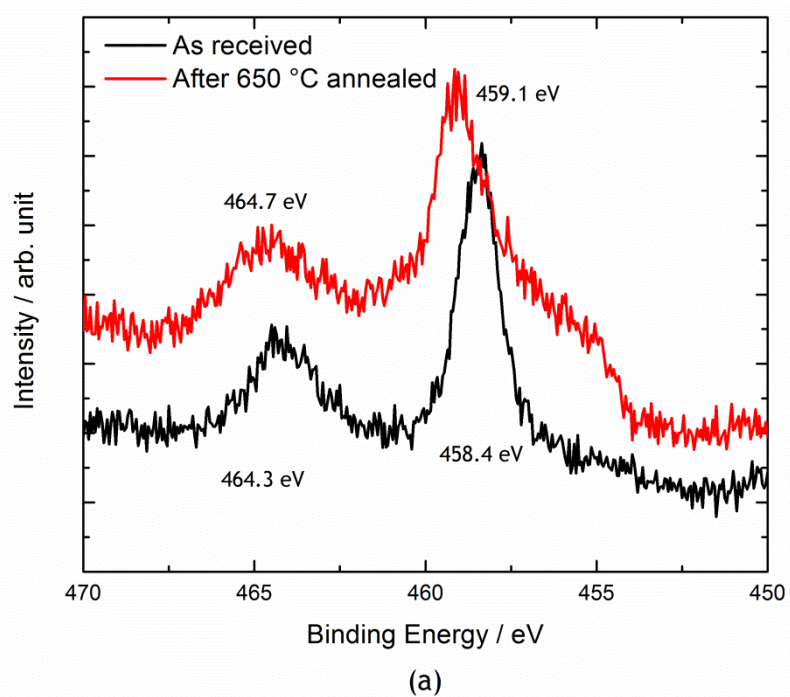
Table 7.2: Cr $2p_{1/2}$ & $2p_{3/2}$, C 1s, O 1s core binding energies and work function of Cr-O-terminated BDD.

Process	C 1s (eV)	O 1s (eV)	Cr $2p_{1/2}$ & $2p_{3/2}$ (eV)	Work function (eV)
O-termination	284.7	531.7	--	4.33
Cr deposition & washed	284.7	531.3	586.7, 576.9	3.53
Annealed at 650°C	284.5	530.9	586.4, 576.8	3.53

7.3.3 Titanium-Oxygen Termination

Figure 7.11 illustrates the XPS spectra of Ti $2p_{1/2}$ & $2p_{3/2}$, C 1s and O 1s from Ti-O-terminated BDD. The initial selective etching method using 4M of HCl acid for 4h was too vigorous as it removed all the Ti atoms, as

evidenced by the fact that Ti was not detected during the XPS survey scan. A milder version of the etching process was performed using 1M HCl for 30 minutes. This method was a success, evidenced by the presence of Ti in Figure 7.11(a). The XPS survey scan measurement (not shown) showed that the diamond surface was clean, and no contamination from other metals was detected. After 650°C annealing the Ti 2p_{1/2} core level shifted from 463.3 eV to 464.7 eV and the 2p_{3/2} core level shifted from 458.4 eV to 459.1 eV. Previously, Cr-O-termination showed a shift toward lower binding energy suggesting that the surface reconstructed to form a more stable surface with smaller binding energy. However, for Ti-O-termination the reason for the shift towards higher formation energy is unknown. To try to understand this, higher sensitivity XPS measurements are needed to determine the stoichiometry of the TiO species present. The change of stoichiometry of TiO was possible due to the disappearance of the O peak at 531.7 eV (Figure 7.11(c)). As a transition metal, Ti has various oxidation states available. When the metal was initially deposited onto the oxygen-terminated BDD film, a mixture of TiO stoichiometries may have been present with different Ti oxidation states. However, during annealing, it's possible that the Ti changed oxidation state, and thus its stoichiometry. On the other hand, the C 1s core level remained unchanged after the annealing process with a binding energy of 284.4 eV.



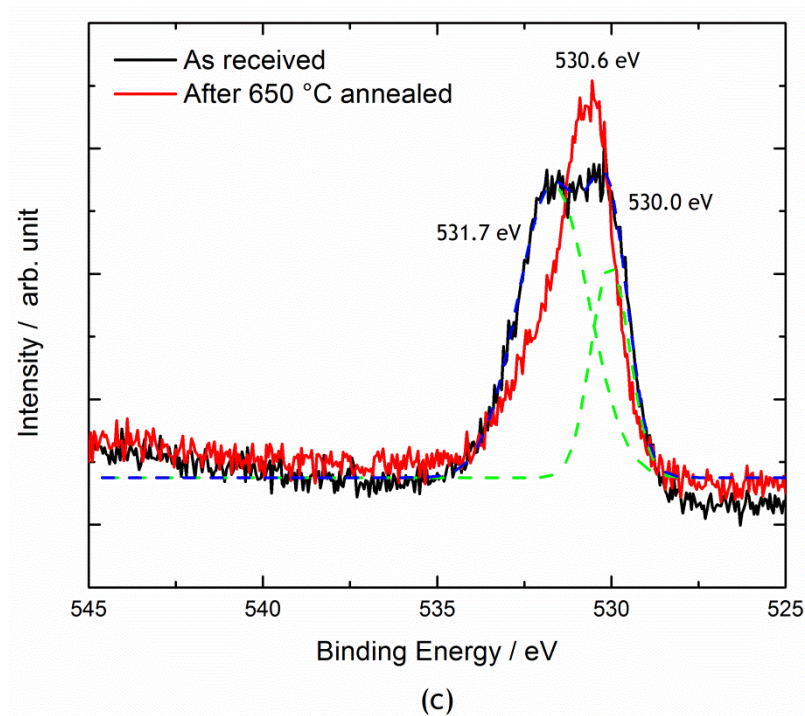


Figure 7.11: XPS spectra of (a) Ti $2p_{1/2}$ & $2p_{3/2}$, (b) C $1s$ and (c) O $1s$ elements of Ti-O-terminated BDD.

Figure 7.12 shows the UPS spectra of Ti-O-terminated BDD measured at room temperature after annealing. The work function for the Ti-O-terminated surface remained unchanged after the annealing process, and was constant at 3.75 eV throughout the experiment. The VBM showed similar behaviour with a value of 1.40 eV. The gap between the VBM of the diamond and the vacuum level was calculated to be 5.15 eV. Compared to standard band gap of diamond (5.45 eV), this suggests that the vacuum level is situated below the CBM and the surface exhibits NEA characteristic. The changes in the core energy levels of Ti and O measured by XPS did not affect the surface work function measured using UPS.

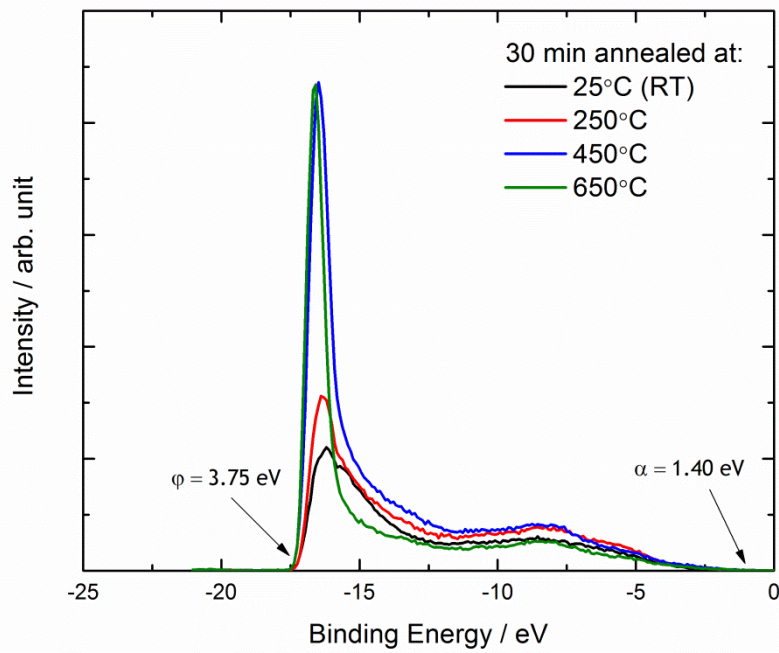


Figure 7.12: UPS spectra of Ti-O-terminated BDD measured at room temperature after annealing.

By applying the 282.7 eV valence band offset (Section 7.3), the VBM of Ti-O-terminated BDD was deduced to be 1.7 eV below the Fermi level as depicted in Figure 7.13. With the band gap of diamond, $E_G = 5.45$ eV, this implies that as long as work function, $\phi < E_G - 1.70$ eV, the surface has NEA. From this calculation, the ϕ lies at the same level as CBM at the surface ($X = 0$ eV). Thus, Ti-O-terminated BDD film exhibits an effective NEA characteristic.

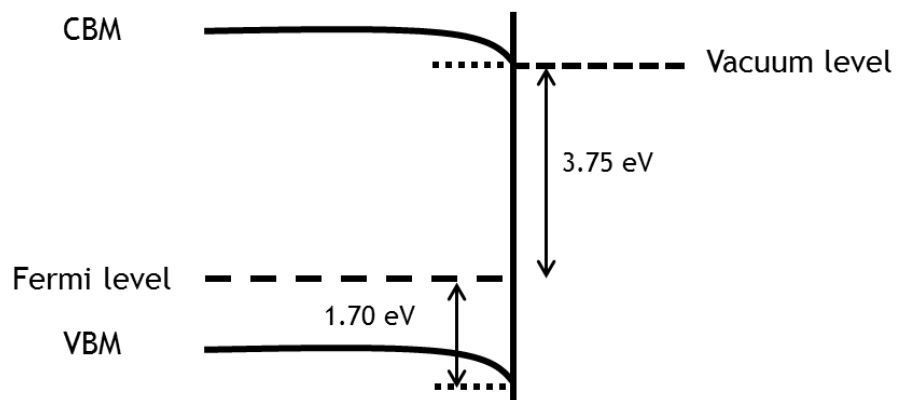


Figure 7.13: Band schematics of Ti-O-terminated BDD film after annealing.

The measured binding energies of Ti 2p_{1/2} & 2p_{3/2}, C 1s, O 1s and work function of the Ti-O-terminated BDD are summarised in Table 7.3.

Table 7.3: Ti 2p_{1/2} & 2p_{3/2}, C 1s, O 1s core binding energies and work function of Ti-O-terminated BDD.

Process	C 1s (eV)	O 1s (eV)	Ti 2p _{1/2} & 2p _{3/2} (eV)	Work function (eV)
O-termination	284.5	531.7	--	4.33
Ti deposition & washed	284.4	531.7, 530.0	464.3, 458.4	3.53
Annealed at 650 °C	284.4	530.6	464.7, 459.1	3.53

7.3.4 Zinc-Oxygen & Magnesium-Oxygen Termination

XPS measurement was done on both Zn-O-terminated and Mg-O-terminated BDD. Unfortunately, there were no Zn or Mg signals detected from the XPS wide scan spectrum. The UPS spectra of both samples (not shown) did show NEA properties but due to the absence of both elements on the surface conclusions are limited.

The Zn-O-terminated sample was repeated by annealing at 450 °C for one hour prior to the selective etching stage (washing in I₂/CH₃OH solution). The process was believed to provide extra energy to enhance the formation of Zn-O bonds between the Zn metal layers near the O-terminated layer. The formation of Zn-O bonds was crucial to avoid it being selectively etched during washing. However, this method resulted in the same results as before: no Zn was detected on the BDD surface using XPS.

The difficulty with detecting Mg on the Mg-O-terminated BDD was partly expected due to the reaction of both Mg metal and MgO with mineral acids. When H₂SO₄ was used as the washing reagent, it was not a selective

etchant as both Mg metal and MgO reacted with it to form MgSO_4 . Hence, a better selective etching method needs to be developed to investigate the effect of Mg-O-termination.

7.4 Conclusions

The selective etching technique was successfully developed for Al, Cr and Ti metals. The method creates a thermally stable metal-oxygen terminated diamond surface that can be exposed in air without changing its properties, and which was not contaminated during the exposure period. All three metal-oxygen-terminated BDD samples exhibited NEA indicating that the vacuum level was situated below the CBM of bulk diamond but only Cr-O-terminated BDD film exhibit true NEA characteristic. This is an important property if these materials are to be used for thermionic emission. Any electrons that are successfully excited into the CBM of the diamond will be spontaneously transferred into the vacuum level and emitted out of the material. The importance of NEA was demonstrated in the thermionic emission measurement discussed in Chapter 6.

This chapter is also in agreement with Takeuchi and co-workers on the effect of true NEA and effective NEA of oxygen-terminated BDD samples. In order to avoid misinterpretation, a proper characterisation of the metal-oxygen surface is essential. The surface of Ti-O, Cr-O and Al-O was confirmed using XPS, and were stable in vacuum up to 650°C . Even though the main purpose of this study was to identify potential surface species to replace H-termination, the annealing in this study needs to be performed at high temperatures. This is because H atoms start to desorb between 600°C to 700°C . Higher temperature annealing is essential before a solid conclusion can be drawn as to whether the metal-oxygen terminations can completely replace H-termination.

The p-doped BDD used in this study acted as a standard sample and due to the success of the selective etching technique, the method will be

replicated on n-doped or Li-N co-doped diamond films in the future. Similar systematic investigations using XPS and UPS measurements will be carried out to observe its effect on the electronic structure of n-type diamond films.

7.5 References

- [1] K. M. O'Donnell, & T. L. Martin, *Mater. Res. Soc. Symp. Proc.* **1282** (2011).
- [2] F.A.M. Koeck, & R.J. Nemanich, *Diam. Relat. Mater. Appl. Diam. Conf. 2005 - ADC/NanoCarbon 2005* **15** (2006) 217-220.
- [3] F.A.M. Koeck, R.J. Nemanich, A. Lazea, & K. Haenen, *Diamond Relat. Mater.* **18** (2009) 789-791.
- [4] V. Baranauskas, B.B. Li, A. Peterlevitz, M.C. Tosin, & S.F. Durrant, *J. Appl. Phys.* **85** (1999) 7455-7458.
- [5] J.B. Cui, J. Ristein, M. Stammer, K. Janischowsky, G. Kleber, & L. Ley, *Diamond Relat. Mater.* **9** (2000) 1143-1147.
- [6] D. Takeuchi, S.G. Ri, H. Kato, C.E. Nebel, & S. Yamasaki, *Phys. Status Solidi* **202** (2005) 2098-2103.
- [7] P.W. May, J.C. Stone, M.N.R. Ashfold, K.R. Hallam, W.N. Wang, & N.A. Fox, *Diamond Relat. Mater.* **7** (1998) 671-676.
- [8] F. Köck, J. Garguilo, & R. Nemanich, *Diamond Relat. Mater.* **10** (2001) 1714-1718.
- [9] M. Kataoka, C. Zhu, F.A.M. Koeck, & R.J. Nemanich, *Diamond Relat. Mater.* **19** (2010) 110-113.
- [10] P.K. Baumann, & R.J. Nemanich, *Surf. Sci.* **409** (1998) 320-335.
- [11] D. Takeuchi, S.G. Ri, N. Tokuda, & S. Yamasaki, *Diamond Relat. Mater.* **18** (2009) 206-209.
- [12] C.K. Fink, & S.J. Jenkins, *J. Phys. Condens. Matter* **21** (2009) 264010.
- [13] Y. Coffinier, S. Szunerits, B. Marcus, R. Desmet, O. Melnyk, L. Gengembre, E. Payen, D. Delabouglise, & R. Boukherroub, *Diamond Relat. Mater.* **16** (2007) 892-898.

- [14] T. Sakai, K. Song, & H. Kanazawa, *Diamond Relat. Mater.* **12** (2003) 1971-1975.
- [15] K.M. O'Donnell, M.T. Edmonds, J. Ristein, A. Tadich, L. Thomsen, Q.H. Wu, C.I. Pakes, & L. Ley, *Adv. Funct. Mater.* **23** (2013) 5608-5614.
- [16] Y. Mori, H. Kawarada, & A. Hiraki, *Appl. Phys. Lett.* **58** (1991) 940.
- [17] M.W. Geis, J.C. Twichell, J. Macaulay, & K. Okano, *Appl. Phys. Lett.* **67** (1995) 1328.
- [18] W. Pickett, *Phys. Rev. Lett.* **73** (1994).
- [19] K.M. O'Donnell, T.L. Martin, N.A. Fox, & D. Cherns, *Phys. Rev. B* **82** (2010) 115303.
- [20] A.K. Tiwari, J.P. Goss, P.R. Briddon, N.G. Wright, A.B. Horsfall, & M.J. Rayson, *Phys. Status Solidi* **209** (2012) 1697-1702.
- [21] A.K. Tiwari, J.P. Goss, P.R. Briddon, N.G. Wright, A.B. Horsfall, & M.J. Rayson, *Phys. Rev. B* **86** (2012) 155301.
- [22] F.A.M. Köck, J.M. Garguilo, B. Brown, & R.J. Nemanich, *Diamond Relat. Mater.* **11** (2002) 774-779.
- [23] W.F. Paxton, M. Howell, W.P. Kang, & J.L. Davidson, *J. Vac. Sci. Technol. B Microelectron. Nanom. Struct.* **30** (2012) 021202.
- [24] W.F. Paxton, A. Steigerwald, M. Howell, N. Tolk, W.P. Kang, & J.L. Davidson, *Appl. Phys. Lett.* **101** (2012) 243509.
- [25] P.K. Baumann, & R.J. Nemanich, *J. Appl. Phys.* **83** (1998) 2072.
- [26] J. Van der Weide, & R. Nemanich, *Phys. Rev. B* **49** (1994) 13629-13637.
- [27] J. Van der Weide, & R. Nemanich, *J. Vac. Sci. Technol. B Microelectron. Nanom. Struct.* **10** (1992) 1940-1943.
- [28] W.F. Paxton, T. Wade, M. Howell, N. Tolk, W.P. Kang, & J.L. Davidson, *Phys. Status Solidi* **209** (2012) 1993-1995.
- [29] T.L. Martin, Lithium oxygen termination as a negative electron affinity surface on diamond: a computational and photoemission study, University of Bristol, (2011).
- [30] P.J. Van der Put, *The Inorganic Chemistry Of Materials*, Plenum Press, New York, (1998).

- [31] K.M. MacKay, R.A. MacKay, & W. Henderson, *Introduction to Modern Inorganic Chemistry*, 6th ed., Nelson Thornes, Cheltenham, (2002).
- [32] N.N. Greenwood, & A. Earnshaw, *Chemistry of the Elements*, 2nd ed., Elsevier B.V., Oxford, (1997).
- [33] R.E. Thomas, R.A. Rudder, & R.J. Markunas, *J. Vac. Sci. Technol. A Vacuum, Surfaces, Film.* **10** (1992) 2451-2457.
- [34] A. Dandekar, R.T.K. Baker, & M.A. Vannice, *Carbon N. Y.* **36** (1998) 1821-1831.
- [35] J.W. Liu, M.Y. Liao, M. Imura, & Y. Koide, *Appl. Phys. Lett.* **101** (2012) 252108.
- [36] J.E. Field, *The Properties of Natural and Synthetic Diamond*, Academic Press, (1992).

Chapter 8: Thesis Summary

8.1 Summary

Li-N co-doped diamond films were successfully prepared using stable Li_3N suspension and NH_3 gas as Li and N precursors, respectively. High concentration of Li and N atoms were identified using SIMS in the same diffusion region. 5×10^{19} atoms/ cm^3 of Li and 3×10^{20} atoms/ cm^3 of N were detected in some of the diamond films as Li^+ and CN^- using SIMS. In addition, the solubility limit of Li was also confirmed ($\sim 5 \times 10^{19} \text{ cm}^{-3}$); above this amount the Li_3N molecules were reacted with the process gases to form Li_xC_x compounds.

Various types of diamond films were also investigated to observe different diffusion profile of both Li and N inside diamond films. For MCD films, the amount of Li and N atoms incorporated were much higher compared to SCD films. The existence of more grain boundaries in MCD films had been proven as one of the contributing factors in higher incorporation of Li and N inside diamond films. Perhaps much of the Li and N are trapped as electrically inactive species within the sp^2 grain boundaries due to higher resistance measured in Li-N co-doped diamond films.

Theoretical model of Li-N co-doped diamond films in Chapter 5 explained in detail the failure of 1:1 ratio of Li and N atoms in diamond structure to produce promising n-type semiconducting diamond films. Even though the 1:1 ratio was not the answer for n-type semiconductor, this calculation successfully proved the concept of N atoms as a trapping mechanism to immobilise Li atoms. The formation energy when both Li and N atoms positioned as neighbour (9.41 eV) was much lower compared to the energy when both of the atoms far apart (11.32 eV).

The formation of Li-N clusters with higher content of N atoms however lead to a shallow donor level in diamond structure with Li atoms residing in substitutional positions. It was found that 1:4 ratios of Li to N

atoms promote a donor level less than 0.1 eV is below the CBM of diamond with formation energy of 4.88 eV when the Li positioned in the substitutional site. Hence, these types of clusters eliminated the competition whether Li atoms would reside in interstitial or substitutional positions, as the corresponding of Li-N cluster with Li in an interstitial position had much higher formation energy (10 eV).

Even though the resistance of the Li-N co-doped diamond films prepared was measured above 10 M Ω , the sample exhibits a high current density value with the presence of NEA surface. 1.21×10^{-4} A/cm² was observed at 900 K and the threshold temperature recorded at 800 K. Thus, these Li-N co-doped diamond films show great potential as thermionic emitters, and future development is needed to improve the doping procedure and optimise the emission properties.

From XPS and UPS measurements, the Li-N co-doped diamond films produced exhibit a deep donor characteristic. It is consistent with some of the cluster models proposed using computational model. However, the Li:N ratio in Li-N co-doped diamond films was at 1:18 ratio. This ratio was never being modelled and in this case, the major donor contribution may be from N atoms alone. Even though the dopants in the diamond film are dominated by N atoms, the resistance measured from the Li-N co-doped diamond films showed lower resistance compared to a nitrogen-doped diamond at room temperature (200 M Ω). This suggests that Li atoms contribute in improving the conductivity of the film but further improvement in the film's resistance needs to be carried out to create a working n-type semiconductor device.

From the thermionic emission study in Chapter 6, NEA surface is deemed to be crucial for increasing the electron emission from diamond surface. However due to desorption of H atoms at high temperature, NEA property exhibited by an H-termination surface will be lost and thus, inhibit the emission of electrons at high temperature. Metal termination techniques were successfully developed for various metals including Cr-O, Al-O and Ti-O that can withstand high temperature annealing (650°C)

without changing their NEA characteristic. UPS analysis confirms the NEA characteristic of the metal-oxygen termination species while XPS analysis confirms the species remained intact throughout the annealing process.

8.2 Future work

For further development of N-type diamond films, magnesium could be used to replace Li in diamond lattice due to the diagonal relationship of Mg with Li in the Periodic Table. Mg consists of two valence electrons compared to Li. Hence, the carrier concentration in diamond lattice would be double when Mg used as a dopant compared to Li at the same dopant concentration. In addition, due to unknown behaviour of Mg in diamond lattice including the solubility of Mg in diamond and the mobility of Mg in diamond, wide research prospects are available to understand the behaviour of Mg through experiment and theoretical model.

Li-N co-doped diamond films were proven to be a potential shallow n-type semiconducting diamond material. Based on the theoretical models, the 1:4 ratios of Li and N atoms in diamond lattice suggest the formation this type of structure. Thus, it is essential to devised it experimentally by varying the amount of N atoms incorporated into the diamond films. Reducing the amount of NH_3 gas during growth process will be the initial step. However, it will be a challenge later on as MCD films consists of 5-10% grain boundaries and most of the N atoms may excreted into the grain boundaries, thus, exact Li:N cluster ratio deemed to be hard to determine.

The computational model could be improved further. The calculation of clusters formation energies were done from pure diamond and not from N-doped diamond films. The formation of 1:1 cluster of Li-to-N proved to reduce the formation energy when N-doped diamond used as starting material compared to pure diamond. Thus, it would be fruitful to understand the effect on substituting only C atoms with Li atoms in the N-doped diamond for the Li:N clusters calculations. It is also possible to

evaluate the pathway of Li substituting reaction when approaching the N atoms cluster. The possibility of the N-clusters to trap Li atoms and reduced the mobility of the Li atoms could also be investigated. Similar calculation could be implemented by replacing Li atoms with Mg atoms for further development of the theoretical models.

The sensitivity of thermionic emission measurement could be improved further by replacing resistive heater with laser heating instrument to reduce the current leakage due to electrons escape from the heater's filament into the emitter or collector. In addition to that, spacing between the collector and emitter should be reduced further until the space charge effect is kept to minimum without having external bias to overcome it. This is important for the practicality of the device made in the future. The solar panel device should be able to produce energy independently without having any external energy supplied to the collector.

Air stable metal-oxygen termination of Cr-O can be applied on the Li-N co-doped diamond films and any other future N-type semiconducting diamond for thermally stable NEA surface to replace weakly bonded H-termination. However, higher temperature ($>800^{\circ}\text{C}$) investigations using XPS and UPS are essential before any conclusive remark could be made to replace H-termination with Cr-O termination or other potential metal-oxygen termination such as V-O or other lanthanide elements that have lower work function than Cr.

SIMS Calibration of Li Concentration in Diamond

Etch rate measurement

Etch rate measurements were made using the FIB to etch holes in the diamond at known beam current and area. The SIMS etch pits areas were also measured on the FIB. Figure shows the example of SIMS etch pit. The area of the pit is estimated to be $1370 \mu\text{m}^2$.

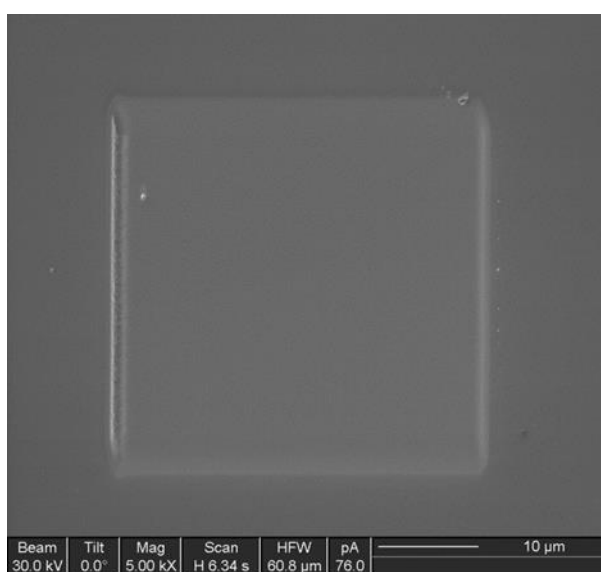


Figure 1: The etch pit produced after SIMS depth profile.

The etch rate (volume removed per unit charge) was estimated by etching a deep pit with the FIB, measuring its area, then filling with platinum and measuring the depth by cutting and imaging in the FIB. Figure 2 shows the resulting pit after etching at 2.89nA for 10 min 57s at 45°.

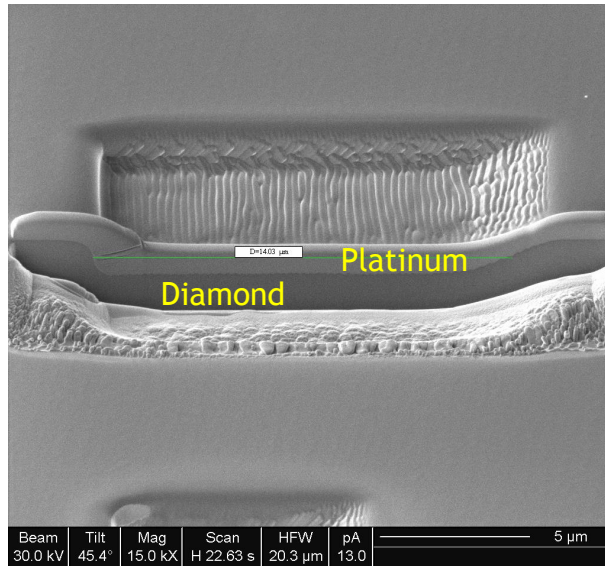


Figure 2: Cross-section view of the FIB etch pit

The area of the pit (viewed from the top) was $140 \mu\text{m}^2$. The depth, measured from the section, was $1.61 \mu\text{m}$. The volume removed was therefore $225.4 \mu\text{m}^3$. The charge imparted to the sample during etching was

$$2.89 \text{ nA} \times 615 \text{ s} = 1777 \text{ nC}$$

The volume etch rate of the material was therefore:

$$225.4 / 1777 = 0.127 \mu\text{m}^3/\text{nC}.$$

With an etch area of $1370 \mu\text{m}^2$ and a beam current of 3.0 nA in the SIMS depth profiles, the depth erosion rate was therefore:

$$0.127 \times 3 / 1370 = 2.8 \times 10^{-4} \mu\text{m}/\text{s} = 0.28 \text{ nm}/\text{s}$$

This value has been used in determining the profile depths for all SIMS analysis in this study.

SIMS Depth Profiles

A typical SIMS depth profile of the $8 \times 10^{14} \text{ cm}^{-2}$ lithium implanted sample is shown in Figure 3.

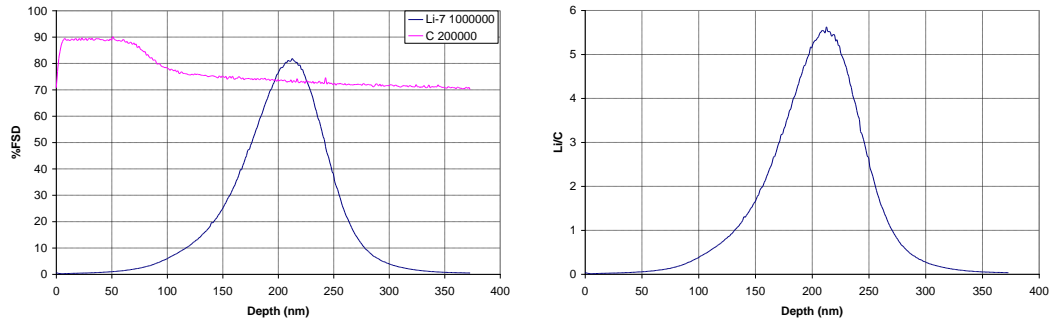


Figure 1: SIMS depth profile analysis of $5 \times 10^{14} \text{ cm}^{-2}$ nitrogen implanted sample. Left: CN^- and C^- signals from SIMS. Right: CN^-/C^- ratio.

The profile of the lithium signal is approximately Gaussian, as expected from an implantation of this type. The small drop in carbon signal at 60-70nm is not understood.

A typical SIMS depth profile of the $8 \times 10^{12} \text{ cm}^{-2}$ lithium implanted sample is shown in Figure 2.

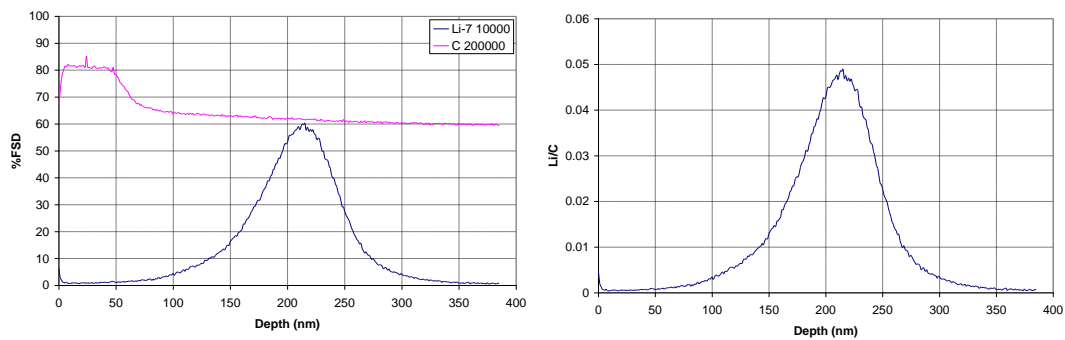


Figure 2: SIMS depth profile analysis of $8 \times 10^{12} \text{ cm}^{-2}$ lithium implanted sample. Left: Li^+ and C^+ signals from SIMS. Right: Li^+/C^+ ratio.

Concentration Calculations

For each region, three depth profiles were used to compile depth and concentration information. Gaussian curves were fitted to each profile, using the usual equation for a Gaussian curve:

$$y = \frac{K}{(\sqrt{2\pi})\sigma} e^{-\frac{(x-\mu)^2}{2\sigma^2}}$$

where μ is the peak depth, K is a measure of the magnitude (height), and σ is a measure of the Gaussian width. The integral of this form equates to K

The values of CN^-/C^- were used for the fit. The results are presented in the Table below:

Table 4: Gaussian parameters for lithium implanted sample.

Sample		K	μ (nm)	σ (nm)
8×10^{14} Li sample a		461.2	209.4	38.1
8×10^{14} Li sample b		435.9	207.2	35.7
8×10^{14} Li sample c		489.3	207.6	36.5
	AVE	462.3	208.07	36.77
8×10^{12} Li sample a		3.82	212.7	35.9
8×10^{12} Li sample b		4.19	209.5	35.7
8×10^{12} Li sample c		4.1	210.4	35.8
	AVE	4.04	209.5	36.3

$$8 \times 10^{14} \text{ Li sample: } C(x = \mu) = \frac{8 \times 10^{14}}{(\sqrt{2\pi}) \times 36.8 \times 10^{-7}} = 8.8 \times 10^{19} \text{ cm}^{-3}$$

Similarly, the peak concentrations for the other samples are:

$$8 \times 10^{12} \text{ Li: } 8.8 \times 10^{17} \text{ cm}^{-3}$$

The SIMS sensitivities to the materials can be obtained by using the K values from the Gaussian fits, and the area concentrations (calculating A/K).

From these results, the following calibration factors are obtained:

From 8×10^{14} Li sample, Li concentration $[\text{Li}] = 1.73 \times 10^{19} \times (\text{Li}^+/\text{C}^+ \text{ ratio})$.

From 8×10^{12} Li sample, Li concentration $[\text{Li}] = 1.98 \times 10^{19} \times (\text{Li}^+/\text{C}^+ \text{ ratio})$.

Evidently there are small discrepancies between the results obtained from the high concentration and the low concentration samples. It appears that the SIMS is slightly non-linear in its response over the two orders of magnitude of concentration used, assuming that the implantation doses were accurate. It is therefore proposed that the average values be taken as follows:

$$[\text{Li}] = (\text{Li}^+/\text{C}^+) \times 1.8 \times 10^{19} \text{ cm}^{-3}$$

SIMS Calibration of N Concentration in Diamond

SIMS Depth Profiles

A typical SIMS depth profile of the $5 \times 10^{14} \text{ cm}^{-2}$ nitrogen implanted region is shown in Figure 3.

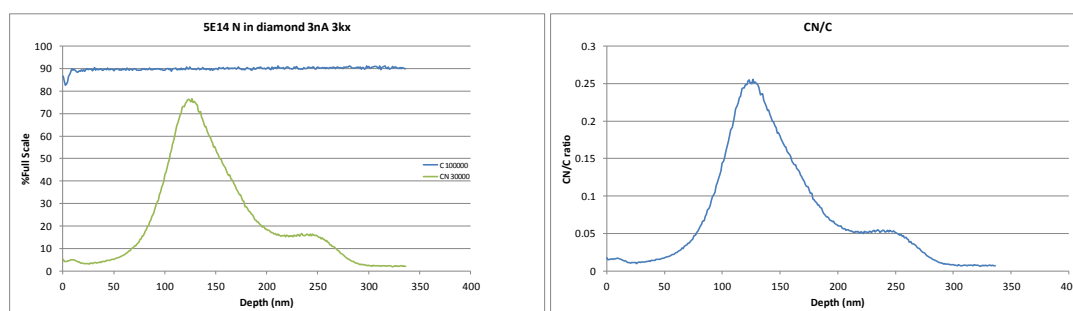


Figure 14: SIMS depth profile analysis of $5 \times 10^{14} \text{ cm}^{-2}$ nitrogen implanted sample. Left: CN^- and C^- signals from SIMS. Right: CN^-/C^- ratio.

The profile of the CN^- signal is approximately Gaussian, as expected from an implantation of this type. The secondary peak is not understood, but may be a channelling effect.

A typical SIMS depth profile of the $5 \times 10^{12} \text{ cm}^{-2}$ nitrogen implanted sample is shown in Figure 4.

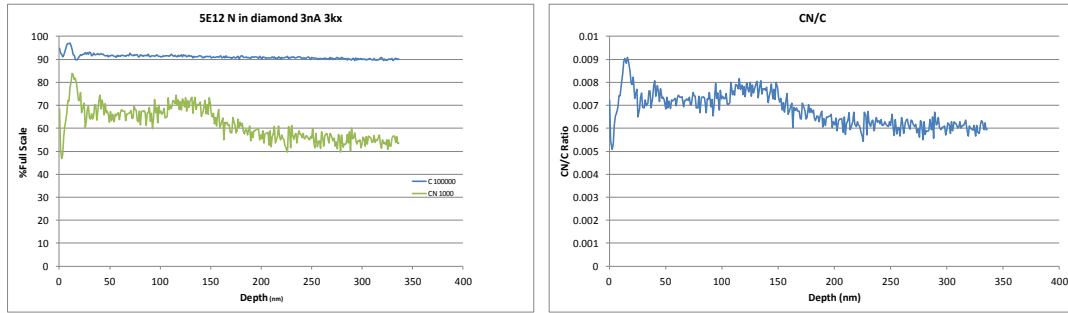


Figure 4: SIMS depth profile analysis of $5 \times 10^{12} \text{ cm}^{-2}$ nitrogen implanted sample. Left: CN^- and C^- signals from SIMS. Right: CN^-/C^- ratio.

Concentration Calculations

For each region, three depth profiles were used to compile depth and concentration information. Gaussian curves were fitted to each profile, using the usual equation for a Gaussian curve:

$$y = \frac{K}{(\sqrt{2\pi})\sigma} e^{-\frac{(x-\mu)^2}{2\sigma^2}}$$

where μ is the peak depth, K is a measure of the magnitude (height), and σ is a measure of the Gaussian width. The integral of this form equates to K :

The values of CN^-/C^- were used for the fit. The results are presented in the Table 1 below:

Table 5: Gaussian parameters for nitrogen implanted sample.

Sample		K	μ (nm)	σ (nm)
$5 \times 10^{14} \text{ cm}^{-2}$ sample a		16.5	127	26.2
$5 \times 10^{14} \text{ cm}^{-2}$ sample b		14.6	119	21.4
$5 \times 10^{14} \text{ cm}^{-2}$ sample c		13.4	131	26.4
	AVE	14.8	126	24.7

These values can be used to calculate the volume concentration of the implanted material with depth. Again assuming the implantation depth profile to be Gaussian, the concentration of implant material (cm^{-3}), $C(x)$, where x is depth, can be given as:

$$C(x) = \frac{A}{(\sqrt{2\pi})\sigma} e^{-\frac{(x-\mu)^2}{2\sigma^2}}$$

where A is the area concentration (i.e. $5 \times 10^{14} \text{ cm}^{-2}$). We now know σ , so we can calculate C . The peak concentration is therefore:

$$C(x = \mu) = \frac{5 \times 10^{14}}{(\sqrt{2\pi}) \times 24.7 \times 10^{-7}} = 8.1 \times 10^{19} \text{ cm}^{-3}$$

The SIMS sensitivities to the materials can be obtained by using the K values from the Gaussian fits, and the area concentrations (calculating A/K).

From these results, the following calibration factor is obtained:

N concentration $[N] = 3.4 \times 10^{20} \times (CN^-/C^- \text{ ratio})$.

From the $5 \times 10^{12} \text{ cm}^{-2}$ implanted sample, the minimum detectable concentration is about 10^{18} cm^{-3} .

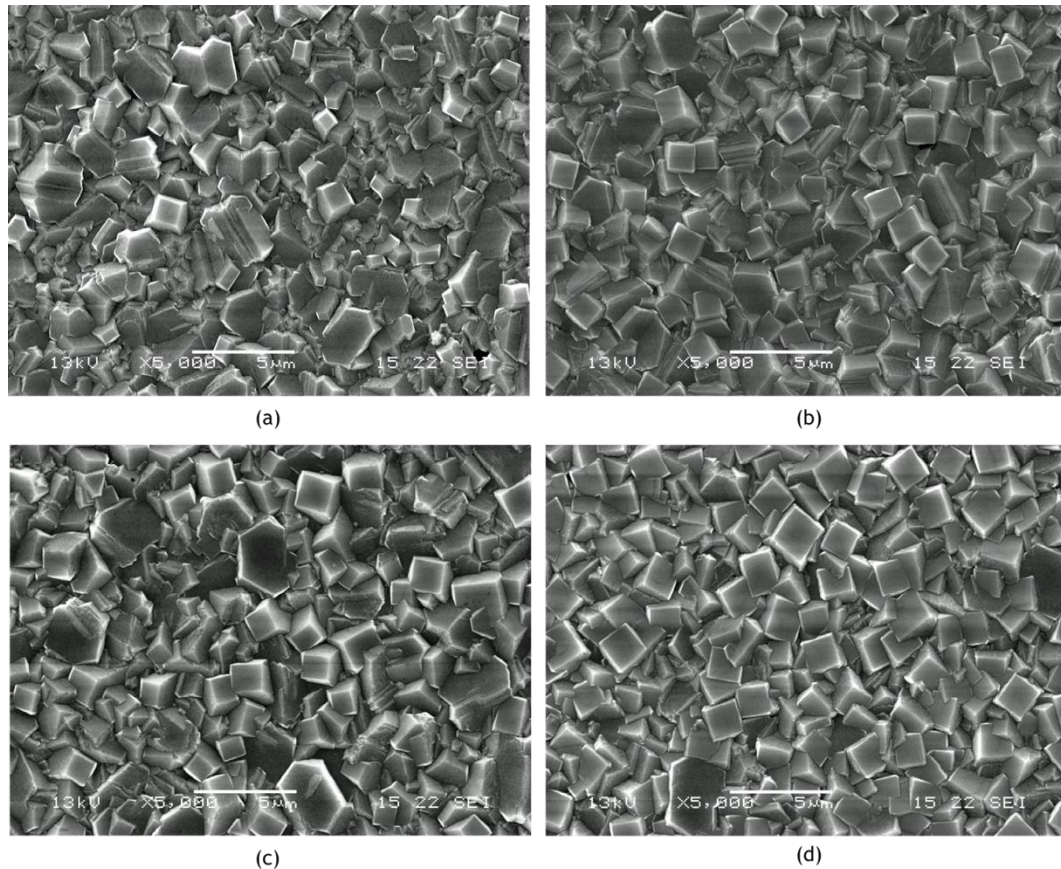
SEM Micrograph of HMT addition into MCD films

Figure 1: SEM micrographs of diamond films grown with addition of HMT sandwiched in between two diamond layers grown with (a) underlying undoped diamond with undoped diamond capping layer (MCD-HMT-MCD), (b) underlying undoped diamond with N-doped diamond capping layer (MCD-HMT-MCD-N), (c) underlying N-doped diamond with undoped diamond capping layer (MCD-N-HMT-MCD) and (d) underlying N-doped diamond with N-doped diamond capping layer (MCD-N-HMT-MCD), with N_2 gas used as the N precursor.

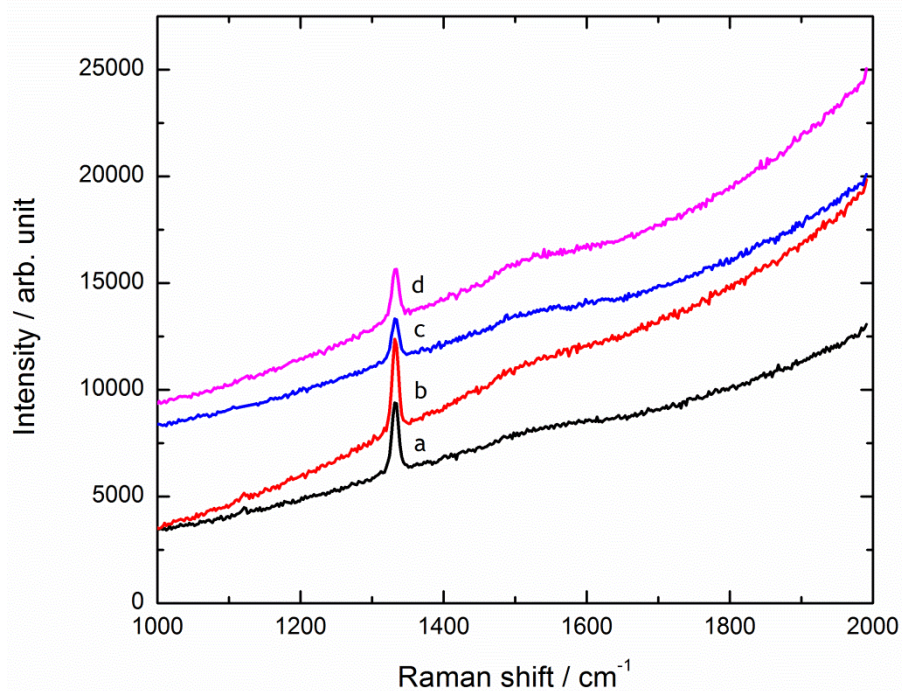
SEM Micrograph of HMT addition into MCD films

Figure 1: Raman spectrum (512 nm He-Cd laser excitation) of diamond films grown with addition of HMT sandwiched in between two diamond layers grown with (a) underlying undoped diamond with undoped diamond capping layer (MCD-HMT-MCD), (b) underlying undoped diamond with N-doped diamond capping layer (MCD-HMT-MCD-N), (c) underlying N-doped diamond with undoped diamond capping layer (MCD-N-HMT-MCD) and (d) underlying N-doped diamond with N-doped diamond capping layer (MCD-N-HMT-MCD), with N₂ gas used as the N precursor.

Fractional Position of Interstitial Li in 64 atom supercellTable 1: Fractional position of T_d of interstitial Li in 64 atom supercell.

Atom	Coordinate (x,y,z)		
Li	0.325	0.075	0.075
C	0.000	0.000	0.000
C	0.500	0.000	0.000
C	0.250	0.250	0.000
C	0.750	0.250	0.000
C	0.000	0.500	0.000
C	0.500	0.500	0.000
C	0.250	0.750	0.000
C	0.750	0.750	0.000
C	0.125	0.125	0.125
C	0.625	0.125	0.125
C	0.375	0.375	0.125
C	0.875	0.375	0.125
C	0.125	0.625	0.125
C	0.625	0.625	0.125
C	0.375	0.875	0.125
C	0.875	0.875	0.125
C	0.250	0.000	0.250
C	0.750	0.000	0.250
C	0.000	0.250	0.250
C	0.500	0.250	0.250
C	0.250	0.500	0.250
C	0.750	0.500	0.250
C	0.000	0.750	0.250
C	0.500	0.750	0.250

C	0.375	0.125	0.375
C	0.875	0.125	0.375
C	0.125	0.375	0.375
C	0.625	0.375	0.375
C	0.375	0.625	0.375
C	0.875	0.625	0.375
C	0.125	0.875	0.375
C	0.625	0.875	0.375
C	0.000	0.000	0.500
C	0.500	0.000	0.500
C	0.250	0.250	0.500
C	0.750	0.250	0.500
C	0.000	0.500	0.500
C	0.500	0.500	0.500
C	0.250	0.750	0.500
C	0.750	0.750	0.500
C	0.125	0.125	0.625
C	0.625	0.125	0.625
C	0.375	0.375	0.625
C	0.875	0.375	0.625
C	0.125	0.625	0.625
C	0.625	0.625	0.625
C	0.375	0.875	0.625
C	0.875	0.875	0.625
C	0.250	0.000	0.750
C	0.750	0.000	0.750
C	0.000	0.250	0.750
C	0.500	0.250	0.750
C	0.250	0.500	0.750
C	0.750	0.500	0.750
C	0.000	0.750	0.750
C	0.500	0.750	0.750
C	0.375	0.125	0.875

C	0.875	0.125	0.875
C	0.125	0.375	0.875
C	0.625	0.375	0.875
C	0.375	0.625	0.875
C	0.875	0.625	0.875
C	0.125	0.875	0.875
C	0.625	0.875	0.875

Table 2: Fractional position of T_h of interstitial Li in 64 atom supercell.

Atom	Coordinate (x,y,z)		
Li	0.363	0.263	0.238
C	0.000	0.000	0.000
C	0.500	0.000	0.000
C	0.250	0.250	0.000
C	0.750	0.250	0.000
C	0.000	0.500	0.000
C	0.500	0.500	0.000
C	0.250	0.750	0.000
C	0.750	0.750	0.000
C	0.125	0.125	0.125
C	0.625	0.125	0.125
C	0.375	0.375	0.125
C	0.875	0.375	0.125
C	0.125	0.625	0.125
C	0.625	0.625	0.125
C	0.375	0.875	0.125
C	0.875	0.875	0.125
C	0.250	0.000	0.250
C	0.750	0.000	0.250
C	0.000	0.250	0.250
C	0.500	0.250	0.250
C	0.250	0.500	0.250

C	0.750	0.500	0.250
C	0.000	0.750	0.250
C	0.500	0.750	0.250
C	0.375	0.125	0.375
C	0.875	0.125	0.375
C	0.125	0.375	0.375
C	0.625	0.375	0.375
C	0.375	0.625	0.375
C	0.875	0.625	0.375
C	0.125	0.875	0.375
C	0.625	0.875	0.375
C	0.000	0.000	0.500
C	0.500	0.000	0.500
C	0.250	0.250	0.500
C	0.750	0.250	0.500
C	0.000	0.500	0.500
C	0.500	0.500	0.500
C	0.250	0.750	0.500
C	0.750	0.750	0.500
C	0.125	0.125	0.625
C	0.625	0.125	0.625
C	0.375	0.375	0.625
C	0.875	0.375	0.625
C	0.125	0.625	0.625
C	0.625	0.625	0.625
C	0.375	0.875	0.625
C	0.875	0.875	0.625
C	0.250	0.000	0.750
C	0.750	0.000	0.750
C	0.000	0.250	0.750
C	0.500	0.250	0.750
C	0.250	0.500	0.750
C	0.750	0.500	0.750

C	0.000	0.750	0.750
C	0.500	0.750	0.750
C	0.375	0.125	0.875
C	0.875	0.125	0.875
C	0.125	0.375	0.875
C	0.625	0.375	0.875
C	0.375	0.625	0.875
C	0.875	0.625	0.875
C	0.125	0.875	0.875
C	0.625	0.875	0.875

Table 3: Fractional position of T_c of interstitial Li in 64 atom supercell.

Atom	Coordinate (x,y,z)		
Li	0.200	0.200	0.200
C	0.000	0.000	0.000
C	0.500	0.000	0.000
C	0.250	0.250	0.000
C	0.750	0.250	0.000
C	0.000	0.500	0.000
C	0.500	0.500	0.000
C	0.250	0.750	0.000
C	0.750	0.750	0.000
C	0.125	0.125	0.125
C	0.625	0.125	0.125
C	0.375	0.375	0.125
C	0.875	0.375	0.125
C	0.125	0.625	0.125
C	0.625	0.625	0.125
C	0.375	0.875	0.125
C	0.875	0.875	0.125
C	0.250	0.000	0.250
C	0.750	0.000	0.250

C	0.000	0.250	0.250
C	0.500	0.250	0.250
C	0.250	0.500	0.250
C	0.750	0.500	0.250
C	0.000	0.750	0.250
C	0.500	0.750	0.250
C	0.375	0.125	0.375
C	0.875	0.125	0.375
C	0.125	0.375	0.375
C	0.625	0.375	0.375
C	0.375	0.625	0.375
C	0.875	0.625	0.375
C	0.125	0.875	0.375
C	0.625	0.875	0.375
C	0.000	0.000	0.500
C	0.500	0.000	0.500
C	0.250	0.250	0.500
C	0.750	0.250	0.500
C	0.000	0.500	0.500
C	0.500	0.500	0.500
C	0.250	0.750	0.500
C	0.750	0.750	0.500
C	0.125	0.125	0.625
C	0.625	0.125	0.625
C	0.375	0.375	0.625
C	0.875	0.375	0.625
C	0.125	0.625	0.625
C	0.625	0.625	0.625
C	0.375	0.875	0.625
C	0.875	0.875	0.625
C	0.250	0.000	0.750
C	0.750	0.000	0.750
C	0.000	0.250	0.750

C	0.500	0.250	0.750
C	0.250	0.500	0.750
C	0.750	0.500	0.750
C	0.000	0.750	0.750
C	0.500	0.750	0.750
C	0.375	0.125	0.875
C	0.875	0.125	0.875
C	0.125	0.375	0.875
C	0.625	0.375	0.875
C	0.375	0.625	0.875
C	0.875	0.625	0.875
C	0.125	0.875	0.875
C	0.625	0.875	0.875

Fractional Position of Li:N Cluster in 64 atom supercell

Table 1: Fractional position of atoms in 1:1 Li-N cluster in 64 atom supercell.

Atom	Coordinate (x,y,z)		
C	0.000	0.000	0.000
C	0.500	0.000	0.000
C	0.250	0.250	0.000
C	0.750	0.250	0.000
C	0.000	0.500	0.000
C	0.500	0.500	0.000
C	0.250	0.750	0.000
C	0.750	0.750	0.000
C	0.125	0.125	0.125
C	0.625	0.125	0.125
C	0.375	0.375	0.125
C	0.875	0.375	0.125
C	0.125	0.625	0.125
C	0.625	0.625	0.125
C	0.375	0.875	0.125
C	0.875	0.875	0.125
C	0.250	0.000	0.250
C	0.750	0.000	0.250
C	0.000	0.250	0.250
C	0.500	0.250	0.250
C	0.250	0.500	0.250
C	0.750	0.500	0.250
C	0.000	0.750	0.250
C	0.500	0.750	0.250
C	0.375	0.125	0.375

C	0.875	0.125	0.375
C	0.125	0.375	0.375
C	0.625	0.375	0.375
C	0.375	0.625	0.375
C	0.875	0.625	0.375
C	0.125	0.875	0.375
C	0.625	0.875	0.375
C	0.000	0.000	0.500
C	0.500	0.000	0.500
C	0.250	0.250	0.500
C	0.750	0.250	0.500
C	0.000	0.500	0.500
N	0.500	0.500	0.500
Li	0.700	0.500	0.500
C	0.250	0.750	0.500
C	0.750	0.750	0.500
C	0.125	0.125	0.625
C	0.625	0.125	0.625
C	0.375	0.375	0.625
C	0.875	0.375	0.625
C	0.125	0.625	0.625
C	0.625	0.625	0.625
C	0.375	0.875	0.625
C	0.875	0.875	0.625
C	0.250	0.000	0.750
C	0.750	0.000	0.750
C	0.000	0.250	0.750
C	0.500	0.250	0.750
C	0.250	0.500	0.750
C	0.750	0.500	0.750
C	0.000	0.750	0.750
C	0.500	0.750	0.750
C	0.375	0.125	0.875

C	0.875	0.125	0.875
C	0.125	0.375	0.875
C	0.625	0.375	0.875
C	0.375	0.625	0.875
C	0.875	0.625	0.875
C	0.125	0.875	0.875
C	0.625	0.875	0.875

Table 2: Fractional position of atom in 1:2 Li-N cluster in 64 atom supercell.

Atom	Coordinate (x,y,z)		
C	0.000	0.000	0.000
C	0.500	0.000	0.000
C	0.250	0.250	0.000
C	0.750	0.250	0.000
C	0.000	0.500	0.000
C	0.500	0.500	0.000
C	0.250	0.750	0.000
C	0.750	0.750	0.000
C	0.125	0.125	0.125
C	0.625	0.125	0.125
C	0.375	0.375	0.125
C	0.875	0.375	0.125
C	0.125	0.625	0.125
C	0.625	0.625	0.125
C	0.375	0.875	0.125
C	0.875	0.875	0.125
C	0.250	0.000	0.250
C	0.750	0.000	0.250
C	0.000	0.250	0.250
C	0.500	0.250	0.250
C	0.250	0.500	0.250
C	0.750	0.500	0.250

C	0.000	0.750	0.250
C	0.500	0.750	0.250
C	0.375	0.125	0.375
C	0.875	0.125	0.375
C	0.125	0.375	0.375
C	0.625	0.375	0.375
C	0.375	0.625	0.375
C	0.875	0.625	0.375
C	0.125	0.875	0.375
C	0.625	0.875	0.375
C	0.000	0.000	0.500
C	0.500	0.000	0.500
C	0.250	0.250	0.500
C	0.750	0.250	0.500
C	0.000	0.500	0.500
Li	0.500	0.500	0.500
C	0.250	0.750	0.500
C	0.750	0.750	0.500
C	0.125	0.125	0.625
C	0.625	0.125	0.625
N	0.375	0.375	0.625
C	0.875	0.375	0.625
C	0.125	0.625	0.625
N	0.625	0.625	0.625
C	0.375	0.875	0.625
C	0.875	0.875	0.625
C	0.250	0.000	0.750
C	0.750	0.000	0.750
C	0.000	0.250	0.750
C	0.500	0.250	0.750
C	0.250	0.500	0.750
C	0.750	0.500	0.750
C	0.000	0.750	0.750

C	0.500	0.750	0.750
C	0.375	0.125	0.875
C	0.875	0.125	0.875
C	0.125	0.375	0.875
C	0.625	0.375	0.875
C	0.375	0.625	0.875
C	0.875	0.625	0.875
C	0.125	0.875	0.875
C	0.625	0.875	0.875

Table 3: Fractional position of atom in 1:3 Li-N cluster in 64 atom supercell.

Atom	Coordinate (x,y,z)		
C	0.000	0.000	0.000
C	0.500	0.000	0.000
C	0.250	0.250	0.000
C	0.750	0.250	0.000
C	0.000	0.500	0.000
C	0.500	0.500	0.000
C	0.250	0.750	0.000
C	0.750	0.750	0.000
C	0.125	0.125	0.125
C	0.625	0.125	0.125
C	0.375	0.375	0.125
C	0.875	0.375	0.125
C	0.125	0.625	0.125
C	0.625	0.625	0.125
C	0.375	0.875	0.125
C	0.875	0.875	0.125
C	0.250	0.000	0.250
C	0.750	0.000	0.250
C	0.000	0.250	0.250
C	0.500	0.250	0.250

C	0.250	0.500	0.250
C	0.750	0.500	0.250
C	0.000	0.750	0.250
C	0.500	0.750	0.250
C	0.375	0.125	0.375
C	0.875	0.125	0.375
C	0.125	0.375	0.375
C	0.625	0.375	0.375
N	0.375	0.625	0.375
C	0.875	0.625	0.375
C	0.125	0.875	0.375
C	0.625	0.875	0.375
C	0.000	0.000	0.500
C	0.500	0.000	0.500
C	0.250	0.250	0.500
C	0.750	0.250	0.500
C	0.000	0.500	0.500
Li	0.500	0.500	0.500
C	0.250	0.750	0.500
C	0.750	0.750	0.500
C	0.125	0.125	0.625
C	0.625	0.125	0.625
N	0.375	0.375	0.625
C	0.875	0.375	0.625
C	0.125	0.625	0.625
N	0.625	0.625	0.625
C	0.375	0.875	0.625
C	0.875	0.875	0.625
C	0.250	0.000	0.750
C	0.750	0.000	0.750
C	0.000	0.250	0.750
C	0.500	0.250	0.750
C	0.250	0.500	0.750

C	0.750	0.500	0.750
C	0.000	0.750	0.750
C	0.500	0.750	0.750
C	0.375	0.125	0.875
C	0.875	0.125	0.875
C	0.125	0.375	0.875
C	0.625	0.375	0.875
C	0.375	0.625	0.875
C	0.875	0.625	0.875
C	0.125	0.875	0.875
C	0.625	0.875	0.875

Table 4: Fractional position of atom in 1:4 Li-N cluster in 64 atom supercell.

Atom	Coordinate (x,y,z)		
C	0.000	0.000	0.000
C	0.500	0.000	0.000
C	0.250	0.250	0.000
C	0.750	0.250	0.000
C	0.000	0.500	0.000
C	0.500	0.500	0.000
C	0.250	0.750	0.000
C	0.750	0.750	0.000
C	0.125	0.125	0.125
C	0.625	0.125	0.125
C	0.375	0.375	0.125
C	0.875	0.375	0.125
C	0.125	0.625	0.125
C	0.625	0.625	0.125
C	0.375	0.875	0.125
C	0.875	0.875	0.125
C	0.250	0.000	0.250
C	0.750	0.000	0.250

C	0.000	0.250	0.250
C	0.500	0.250	0.250
C	0.250	0.500	0.250
C	0.750	0.500	0.250
C	0.000	0.750	0.250
C	0.500	0.750	0.250
C	0.375	0.125	0.375
C	0.875	0.125	0.375
C	0.125	0.375	0.375
N	0.625	0.375	0.375
N	0.375	0.625	0.375
C	0.875	0.625	0.375
C	0.125	0.875	0.375
C	0.625	0.875	0.375
C	0.000	0.000	0.500
C	0.500	0.000	0.500
C	0.250	0.250	0.500
C	0.750	0.250	0.500
C	0.000	0.500	0.500
Li	0.500	0.500	0.500
C	0.250	0.750	0.500
C	0.750	0.750	0.500
C	0.125	0.125	0.625
C	0.625	0.125	0.625
N	0.375	0.375	0.625
C	0.875	0.375	0.625
C	0.125	0.625	0.625
N	0.625	0.625	0.625
C	0.375	0.875	0.625
C	0.875	0.875	0.625
C	0.250	0.000	0.750
C	0.750	0.000	0.750
C	0.000	0.250	0.750

C	0.500	0.250	0.750
C	0.250	0.500	0.750
C	0.750	0.500	0.750
C	0.000	0.750	0.750
C	0.500	0.750	0.750
C	0.375	0.125	0.875
C	0.875	0.125	0.875
C	0.125	0.375	0.875
C	0.625	0.375	0.875
C	0.375	0.625	0.875
C	0.875	0.625	0.875
C	0.125	0.875	0.875
C	0.625	0.875	0.875